

**STRENGTH AND FATIGUE FAILURE OF SPOT FRICTION WELDS
BETWEEN SIMILAR AND DISSIMILAR SHEET MATERIALS**

by

Van-Xuan Tran

A dissertation submitted in partial fulfillment
of the requirements for the degree of
Doctor of Philosophy
(Mechanical Engineering)
in The University of Michigan
2009

Doctoral Committee:

Professor Jwo Pan, Chair
Professor Amit K. Ghosh
Professor Emeritus William F. Hosford, Jr.
Professor Elijah Kannatey-Asibu, Jr.
Associate Professor Wei Lu

© Van - Xuan Tran 2009
All Rights Reserved

To my mom, Ms. Pham Thi Thua,
my wife, Phuong Thao and
my little princess, Phuong Ha
for their love, understanding, support and encouragement.

ACKNOWLEDGMENTS

I wish to express my sincere appreciation and gratitude to my advisor, Professor Jwo Pan, for his constant advice, support and unlimited patience throughout my study. His guidance were essential to the completion of this dissertation. I would also like to thank my doctoral committee, Professor Amit K. Ghosh, Professor William F. Hosford, Jr., Professor Elijah Kannatey-Asibu, Jr. and Professor Wei Lu for their efforts on providing advices and suggestions.

In addition, the support of my study by the Ford University Research Program and the National Science Foundation under Grant No. DMI-0456755 is appreciated. The financial support for my first two years from Vietnam Education Foundation is also appreciated. The support of the research work from Dr. C. Wu, Dr. C. Johnson and Dr. T. Pan of Ford Motor Company, and from Mr. T. Gendo, Mr. K. Tanaka and Mr. T. Ezaki of Mazda Motor Corporation is greatly appreciated. The help with my research work from Dr. P.-C. Lin of National Chung Cheng University, Taiwan is also greatly appreciated. I would like to thank Professors Vu-Quoc Loc, Nguyen Thien Tong, Truong Nguyen-Tran, Dang Van-Ky, Nguyen Quoc-Son and Habibou Maitournam for their help and supports.

Finally, I wish to express my deepest gratitude to my mother and mother-in-law, my family and family-in-law, and friends for their love, encouragement and support.

TABLE OF CONTENTS

DEDICATION	ii
ACKNOWLEDGMENTS	iii
LIST OF FIGURES	viii
CHAPTER	
I	INTRODUCTION.....1
	References.....7
II	FATIGUE BEHAVIOR OF ALUMINUM 5754-O AND 6111-T4 SPOT FRICTION WELDS IN LAP-SHEAR SPECIMENS.....8
	2.1 Introduction9
	2.2 Aluminum 5754 and 6111 spot friction welds before testing 11
	2.3 Experiments.....14
	2.4 Failure modes of aluminum 5754 welds under quasi-static and cyclic loading conditions.....16
	2.4.1 A two-dimensional overview of failure modes16
	2.4.2 Failure mode under quasi-static loading conditions 19
	2.4.3 Failure mode under low-cycle loading conditions ..19
	2.4.4 Failure mode under high-cycle loading conditions .21
	2.5 Failure modes of aluminum 6111 welds under quasi-static and cyclic loading conditions.....23
	2.5.1 A two-dimensional overview of failure modes23
	2.5.2 Failure mode under quasi-static loading conditions 26
	2.5.3 Failure mode under low-cycle loading conditions ..26
	2.5.4 Failure mode under high-cycle loading conditions .28
	2.6 Fatigue life estimation models29
	2.6.1 A kinked fatigue crack growth model30
	2.6.2 A structural stress model32
	2.7 Fatigue life estimations34
	2.8 Discussions.....37
	2.9 Conclusions40
	References56
III	EFFECTS OF PROCESSING TIME ON STRENGTHS AND FAILURE MODES OF DISSIMILAR SPOT FRICTION WELDS BETWEEN ALUMINUM 5754-O AND 7075-T6 SHEETS59
	3.1 Introduction60

3.2 Experiments	63
3.3 Micrographs of spot friction welds before testing	65
3.4 Failure loads of spot friction welds	72
3.5 Failure modes of 5754/7075 spot friction welds	73
3.6 Failure modes of 7075/5754 spot friction welds	79
3.7 Discussions	84
3.8 Conclusions	88
Table 3.1	90
References	109

IV	INVESTIGATION OF FATIGUE BEHAVIORS OF SPOT FRICTION WELDS BETWEEN DISSIMILAR SHEET MATERIALS IN LAP-SHEAR AND CROSS-TENSION SPECIMENS PART 1: WELDS BETWEEN ALUMINUM 5754-O AND 7075-T6 SHEETS	111
	4.1 Introduction	112
	4.2 Micrographs of 5754/7075 and 7075/5754 spot friction welds	116
	4.3 Specimens and experiments	119
	4.4 Failure modes of spot friction welds in lap-shear specimens	121
	4.4.1 Failure modes of 5754/7075 welds in lap-shear specimens	121
	4.4.2 Failure modes of 7075/7075 welds in lap-shear specimens	125
	4.5 Failure modes of spot friction welds in cross-tension specimens	128
	4.5.1 Failure modes of 5754/7075 welds in cross-tension specimens	128
	4.5.2 Failure modes of 7075/7075 welds in cross-tension specimens	132
	4.6 Fatigue life estimations for 5754/7075 and 7075/5754 welds in lap-shear specimens.....	136
	4.6.1 A kinked fatigue crack growth model	136
	4.6.2 A structural stress model	138
	4.6.3 Fatigue life estimations	139
	4.7 Fatigue life estimations for 5754/7075 and 7075/5754 welds in cross-tension specimens	142
	4.7.1 A through-nugget fatigue crack growth model	142
	4.7.2 Fatigue life estimations	144
	4.8 Correlations of the experimental fatigue data	147
	4.9 Discussions	150
	4.10 Conclusions	155
	References	177

V	INVESTIGATION OF FATIGUE BEHAVIORS OF SPOT FRICTION WELDS BETWEEN DISSIMILAR SHEET
----------	---

MATERIALS IN LAP-SHEAR AND CROSS-TENSION SPECIMENS PART 2: WELDS BETWEEN ALUMINUM AND STEEL SHEETS	180
5.1 Introduction	181
5.2 Micrographs of Al/Fe spot friction weld before testing	184
5.3 Specimens and experiments	186
5.4 Failure modes of Al/Fe spot friction welds under cyclic loading conditions	188
5.4.1 Failure modes of Al/Fe welds in lap-shear specimens	188
5.4.2 Failure modes of Al/Fe welds in cross-tension specimens	191
5.5 Three-dimensional finite element analyses	194
5.6 Correlations of the experimental fatigue data	202
5.7 Discussions	204
5.8 Conclusions	209
References	222

VI EFFECTS OF WELD GEOMETRY AND SHEET THICKNESS ON FRACTURE MECHANICS PARAMETERS FOR RESISTANCE SPOT WELDS AND SPOT FRICTION WELDS BETWEEN SIMILAR AND DISSIMILAR SHEET MATERIALS IN LAP-SHEAR SPECIMENS	224
6.1 Introduction	225
6.2 Analytical stress intensity factor and J integral solutions for spot welds in lap-shear specimens.....	233
6.2.1 J integral solutions for a strip model	234
6.2.2 Stress intensity factor solutions for spot welds between joining two sheets of different materials and thicknesses in lap-shear specimens.....	240
6.3 Closed-form structural stress solutions along nugget circumferences of spot welds in lap-shear specimens.....	243
6.3.1 For spot welds with ideal geometry in lap-shear specimens	244
6.3.2 For spot welds with gaps and bends in lap-shear specimens	248
6.4 Three-dimensional finite element models	253
6.5 Validation of analytical stress intensity factor and J integral solutions for spot welds with ideal geometry in lap-shear specimens.....	256
6.6 Effects of weld geometry on fracture mechanics parameters for resistance spot welds and spot friction welds in lap-shear specimens	263
6.6.1 Aluminum 6111 resistance spot welds	263
6.6.2 Aluminum 5754 spot friction welds	267
6.6.3 Dissimilar Al/Fe spot friction welds	271
6.7 Discussions	279

	6.8 Conclusions	286
	References	310
VII	CONCLUSIONS	314
	References	322

LIST OF FIGURES

- Figure 2.1 (a) An optical micrograph of the cross section along the symmetry plane of a 5754 spot friction weld made by the concave tool before testing,
(b) a close-up optical micrograph of region I,
(c) a close-up optical micrograph of region II,
(d) a close-up scanning electron micrograph of the crack tip region as shown in (c).42
- Figure 2.2 (a) An optical micrograph of the cross section along the symmetry plane of a 6111 spot friction weld made by the flat tool before testing,
(b) a close-up optical micrograph of region I,
(c) a close-up optical micrograph of region II,
(d) a close-up scanning electron micrograph of the crack tip region as shown in (c).43
- Figure 2.3 (a) A lap-shear specimen with a 5754 spot friction weld made by the concave tool,
(b) a lap-shear specimen with a 6111 spot friction weld made by the flat tool,
(c) experimental results for the 5754 spot friction welds made by the concave tool and the 6111 spot friction welds made by the flat tool in lap-shear specimens under cyclic loading conditions.44
- Figure 2.4 (a) A schematic plot of a lap-shear specimen with a 5754 spot friction weld made by the concave tool with the sheet thickness $t = 2$ mm under applied resultant shear loads (shown as the bold arrows),
(b) a schematic plot of the cross section along the symmetry plane of the 5754 spot friction weld made by the concave tool,
(c) failure modes of the 5754 spot friction welds in lap-shear specimens under quasi-static, low-cycle and high-cycle loading conditions.45
- Figure 2.5 An optical micrograph of the cross section along the symmetry plane of a failed 5754 spot friction weld made by the concave tool in a lap-shear specimen under quasi-static loading conditions.46
- Figure 2.6 Optical micrographs of the cross sections along the symmetry plane of

	(a) a partially failed 5754 spot friction weld made by the concave tool at the fatigue life of 3.5×10^3 cycles,	
	(b) a failed 5754 spot friction weld made by the concave tool at the fatigue life of 4.7×10^3 cycles under a load range of 2.45 kN.....	47
Figure 2.7	Optical micrographs of the cross sections along the symmetry plane of	
	(a) a partially failed 5754 spot friction weld made by the concave tool at the fatigue life of 4.2×10^4 cycles	
	(b) a failed 5754 spot friction weld made by the concave tool at the fatigue life of 5.5×10^4 cycles under a load range of 1.43 kN.....	48
Figure 2.8	(a) A schematic plot of a lap-shear specimen with a 6111 spot friction weld made by the flat tool with the upper sheet thickness of $t = 0.94$ mm and the lower sheet thickness $t' = 1.04$ mm under applied resultant shear loads (shown as the bold arrows),	
	(b) a schematic plot of the cross section along the symmetry plane of the 6111 spot friction weld made by the flat tool,	
	(c) failure modes of the 6111 spot friction welds in lap-shear specimens under quasi-static, low-cycle and high-cycle loading conditions.	49
Figure 2.9	An optical micrograph of the cross section along the symmetry plane of a failed 6111 spot friction weld made by the flat tool in a lap-shear specimen under quasi-static loading conditions.....	50
Figure 2.10	Optical micrographs of the cross sections along the symmetry plane of	
	(a) a partially failed 6111 spot friction weld made by the flat tool at the fatigue life of 2.0×10^3 cycles,	
	(b) a failed 6111 spot friction weld made by the flat tool at the fatigue life of 2.7×10^3 cycles under a load range of 2.13 kN.	51
Figure 2.11	Optical micrographs of the cross sections along the symmetry plane of	
	(a) a partially failed 6111 spot friction weld made by the flat tool at the fatigue life of 1.2×10^5 cycles,	
	(b) a failed 6111 spot friction weld made by the flat tool at the fatigue life of 1.6×10^5 cycles under a load range of 0.85 kN.....	52
Figure 2.12	(a) A schematic plot of the cross section along the symmetry plane of the 5754 spot friction weld under statically equivalent combined tensile and bending loads (shown as the bold arrows),	

	(b) a schematic plot of the cross section along the symmetry plane of the 6111 spot friction weld under statically equivalent combined tensile and bending loads (shown as the bold arrows).....	53
Figure 2.13	(a) Experimental results and fatigue life estimations for the 5754 spot friction welds made by the concave tool in lap-shear specimens, (b) experimental results and fatigue life estimations for the 6111 spot friction welds made by the flat tool in lap-shear specimens. The symbols represent the experimental results. The solid and dash lines represent the fatigue life estimations based on the kinked fatigue crack growth model and the structural stress model, respectively.	54
Figure 2.14	An optical micrograph of the cross section along the symmetry plane of a partially failed 5754 spot friction weld made by the concave tool under a load range of 3.38 kN at the fatigue life of 3.6×10^2 cycles which is 90% of the fatigue life of 4.0×10^2 cycles of another failed weld under the same load range.....	55
Figure 3.1	A schematic illustration of the spot friction welding process.....	91
Figure 3.2	(a) A lap-shear specimen with a 5754/7075 spot friction weld, (b) a lap-shear specimen with a 7075/5754 spot friction weld.	92
Figure 3.3	(a) A schematic plot of the tool rotational speed and the tool downward force as functions of the time, (b) a schematic plot of an extracted tool and two welded sheets after spot friction welding.....	93
Figure 3.4	(a) Optical micrographs of the cross sections along the symmetry planes of the 5754/7075 spot friction welds at the processing times of 1.8 sec, 2.8 sec and 3.8 sec before testing, (b) close-up optical micrographs of regions Ia, Ib and Ic, (c) scanning electron micrographs of the crack tip regions as marked in (b), (d) a scanning electron micrograph of crack C0 as marked in (a) and (b)....	94
Figure 3.5	(a) Optical micrographs of the cross sections along the symmetry planes of the 7075/5754 spot friction welds at the processing times of 1.0 sec, 3.5 sec and 6.5 sec before testing, (b) close-up optical micrographs of regions IIa, IIb and IIc, (c) scanning electron micrographs of the crack tip regions as marked in (b).	96

Figure 3.6	The weld diameters as functions of the processing time for the 5754/7075 and 7075/5754 spot friction welds in lap-shear specimens.	98
Figure 3.7	The failure loads as functions of the processing time for both 5754/7075 and 7075/5754 spot friction welds in lap-shear specimens under quasi-static loading conditions.....	99
Figure 3.8	Optical micrographs of the cross sections along the symmetry planes of the failed 5754/7075 spot friction welds at the processing times of (a) 1.8 sec, (b) 2.8 sec, (c) 3.8 sec.....	100
Figure 3.9	Close-up top views of the lower sheets and close-up top and bottom views of the upper sheets of the failed 5754/7075 spot friction welds at the processing times of 1.8 sec, 2.8 sec and 3.8 sec.	101
Figure 3.10	Scanning electron micrographs of (a) a fracture surface on the lower sheet obtained from another failed 5754/7075 spot friction weld made at 3.8 sec, (b) fracture surfaces of A, B, C, D, E, F, G, H, I and J, (c) a fracture surface of crack U3 as marked in Figure 3.8(c).	102
Figure 3.11	Optical micrographs of the cross sections along the symmetry planes of the failed 7075/5754 spot friction welds at the processing times of (a) 1.0 sec, (b) 3.5 sec, (c) 6.5 sec.....	104
Figure 3.12	Close-up top views of the lower sheets and close-up top and bottom views of the upper sheets of the failed 7075/5754 spot friction welds at the processing times of 1.0 sec, 3.5 sec and 6.5 sec.	105
Figure 3.13	Scanning electron micrographs of (a) a fracture surface on the lower sheet obtained from another failed 7075/5754 spot friction weld made at 6.5 sec, (b) fracture surfaces of A, B, C, D, E, F, G, H, I, J, K, L, M and N, (c) a fracture surface of crack U3a as marked in Figure 3.11(c).	106

Figure 3.14	Typical load-displacement curves of the 5754/7075 and 7075/5754 spot friction welds at the optimal processing times under lap-shear loading conditions.....	108
Figure 4.1	(a) An optical micrograph of the cross section along the symmetry plane of a 5754/5754 spot friction weld before testing, (b) a close-up optical micrograph of region I, (c) a scanning electron micrograph of the crack tip region as marked in (b). ..	159
Figure 4.2	(a) An optical micrograph of the cross section along the symmetry plane of a 7075/5754 spot friction weld before testing, (b) a close-up optical micrograph of region II, (c) a scanning electron micrograph of the crack tip region as marked in (b). ..	160
Figure 4.3	(a) A lap-shear specimen with a 5754/7075 spot friction weld, (b) a lap-shear specimen with a 7075/5754 spot friction weld, (c) a cross-tension specimen with a 5754/7075 spot friction weld, (d) a cross-tension specimen with a 7075/5754 spot friction weld.....	161
Figure 4.4	(a) Typical load-displacement curves for the 5754/7075 spot friction welds in lap-shear and cross-tension specimens under quasi-static loading conditions, (b) typical load-displacement curves for the 7075/5754 spot friction welds in lap-shear and cross-tension specimens under quasi-static loading conditions, (c) experimental results for the 5754/7075 spot friction welds in lap-shear and cross-tension specimens under cyclic loading conditions, (d) experimental results for the 7075/5754 spot friction welds in lap-shear and cross-tension specimens under cyclic loading conditions.....	162
Figure 4.5	(a) A schematic plot of a lap-shear specimen with a 5754/7075 spot friction weld with the upper sheet thickness $t_u = 2.0$ mm and the lower sheet thickness $t_l = 1.6$ mm under applied resultant loads (shown as the bold arrows), (b) a schematic plot of the cross section along the symmetry plane of the 5754/7075 spot friction weld in a lap-shear specimen, (c) failure modes of the 5754/7075 spot friction welds in lap-shear specimens under quasi-static and cyclic loading conditions.....	163
Figure 4.6	Optical micrographs of the cross sections along the symmetry planes of	

- (a) a partially failed 5754/7075 spot friction weld in a lap-shear specimen at the fatigue life of 3.7×10^4 cycles,
- (b) a failed 5754/7075 spot friction weld in a lap-shear specimen at the fatigue life of 4.3×10^4 cycles under a load range of 1.17 kN.164

Figure 4.7 (a) A schematic plot of a lap-shear specimen with a 7075/5754 spot friction weld with the upper sheet thickness $t_u = 1.6$ mm and the lower sheet thickness $t_l = 2$ mm under applied resultant loads (shown as the bold arrows),
 (b) a schematic plot of the cross section along the symmetry plane of the 7075/5754 spot friction weld in a lap-shear specimen,
 (c) failure modes of the 7075/5754 spot friction welds in lap-shear specimens under quasi-static and cyclic loading conditions.....165

Figure 4.8 (a) An optical micrograph of the cross section along the symmetry plane of a partially failed 7075/5754 spot friction weld in a lap-shear specimen at the fatigue life of 3.4×10^3 cycles,
 (b) close-up optical micrographs of regions I and II as marked in (a),
 (c) an optical micrograph of the cross section along the symmetry plane of a failed 7075/5754 spot friction weld in a lap-shear specimen at the fatigue life of 4.0×10^3 cycles under a load range of 3.24 kN.....166

Figure 4.9 (a) A schematic plot of a cross-tension specimen with a spot weld under applied resultant loads (shown as the bold arrows),
 (b) schematic plots of cross sections A-B and A'-B' for the 5754/7075 spot friction weld in a cross-tension specimen,
 (c) failure modes of the 5754/7075 spot friction welds in cross-tension specimens under quasi-static and cyclic loading conditions.....167

Figure 4.10 Optical micrographs of the cross sections along symmetry planes
 (a) A-B,
 (b) A'-B' of failed 5754/7075 spot friction welds in cross-tension specimens at the atigue life of 2.7×10^3 cycles under a load range of 0.83 kN. The cross sections A-B and A'-B' are schematically marked in Figure 4.11(a).
168

Figure 4.11 (a) A schematic plot of a cross-tension specimen with a spot weld under applied resultant loads (shown as the bold arrows),
 (b) schematic plots of cross sections C-D and C'-D' for the 7075/5754 spot friction weld in a cross-tension specimen,

(c) failure modes of the 7075/5754 spot friction welds in cross-tension specimens under quasi-static and cyclic loading conditions.....169

Figure 4.12 Optical micrographs of the cross sections along symmetry planes
(a) C-D
(b) C'-D' of failed 7075/5754 spot friction welds in cross-tension specimens at the fatigue life of 1.7×10^4 cycles under a load range of 0.55 kN. The cross sections C-D and C'-D' are schematically marked in Figure 4.11(a).
.....170

Figure 4.13 (a) A schematic plot of the cross section along the symmetry plane of a 5754/7075 spot friction weld in a lap-shear specimen under cyclic loading conditions,
(b) a schematic plot of the cross section along the symmetry plane of a 7075/5754 spot friction weld in a lap-shear specimen under cyclic loading conditions.171

Figure 4.14 (a) Experimental results and fatigue life estimations for the 5754/7075 spot friction welds in lap-shear specimens,
(b) experimental results and fatigue life estimations for the 7075/5754 spot friction welds in lap-shear specimens.
The symbols represent the experimental results. The solid and dash lines represent the fatigue life estimations based on the kinked fatigue crack growth model and the structural stress model, respectively.172

Figure 4.15 (a) A schematic plot of cross section A'-B' of a 5754/7075 spot friction weld in a cross-tension specimen under cyclic loading conditions,
(b) a schematic plot of cross section C-D of a 7075/5754 spot friction weld in a cross-tension specimen under cyclic loading conditions.173

Figure 4.16 (a) Experimental results and fatigue life estimations for the 5754/7075 spot friction welds in cross-tension specimens,
(b) experimental results and fatigue life estimations for the 7075/5754 spot friction welds in cross-tension specimens.
The symbols represent the experimental results. The solid and dash lines represent the fatigue life estimations based on the through-nugget fatigue crack growth model with the nominal thicknesses and effective thicknesses, respectively.174

Figure 4.17 (a) The load range as a function of the fatigue life for the 5754/7075 and 7075/5754 spot friction welds in lap-shear and cross-tension specimens under cyclic loading conditions,

(b) the effective stress intensity range as a function of the fatigue life for the 5754/7075 and 7075/5754 spot friction welds in lap-shear and cross-tension specimens under cyclic loading conditions,
(c) the J integral range as a function of the fatigue life for the 5754/7075 and 7075/5754 spot friction welds in lap-shear and cross-tension specimens under cyclic loading conditions.175

Figure 4.18 (a) The front and side views of the left half of the strip model. The normal stresses σ_{ui} , σ_{uo} , σ_{li} and σ_{lo} represent the normal stresses for line \overline{FG} and line \overline{AB} , the normal stresses σ_{ui}^* , σ_{uo}^* , σ_{li}^* and σ_{lo}^* represent the normal stresses for line \overline{DE} and line \overline{CD} at the inner (i) and outer (o) surfaces of the upper (u) and lower (l) strips, respectively,
(b) a schematic plot of a top view of the weld nugget (idealized as a rigid inclusion) in the upper sheet of the spot weld specimen with the cylindrical and Cartesian coordinate systems centered at the center of the upper half of the weld nugget.176

Figure 5.1 A schematic illustration of the spot friction welding process used to join an aluminum sheet to a coated steel sheet.210

Figure 5.2 (a) An optical micrograph of the cross section along the symmetry plane of an Al/Fe spot friction weld before testing,
(b) a scanning electron micrograph of the crack tip region as marked in (a).
.....211

Figure 5.3 (a) A lap-shear specimen with an Al/Fe spot friction weld,
(b) a cross-tension specimen with an Al/Fe spot friction weld.....212

Figure 5.4 (a) Typical load-displacement curves for the Al/Fe spot friction welds in lap-shear and cross-tension specimens under quasi-static loading conditions,
(b) the load range as a function of the fatigue life for the Al/Fe spot friction welds in lap-shear and cross-tension specimens under cyclic loading conditions.213

Figure 5.5 (a) A schematic plot of a lap-shear specimen with an Al/Fe spot friction weld and with the upper sheet thickness $t_u = 1.3$ mm and the lower sheet thickness $t_l = 0.8$ mm under applied resultant loads (shown as the bold arrows),
(b) a schematic plot of the cross section along the symmetry plane of the Al/Fe spot friction weld in a lap-shear specimen,

	(c) failure modes of the Al/Fe spot friction welds in lap-shear specimens under quasi-static and cyclic loading conditions.	214
Figure 5.6	(a) An optical micrograph of the cross section along the symmetry plane of a partially failed Al/Fe spot friction weld in a lap-shear specimen at the fatigue life of 6.5×10^3 cycles under a load range of 2.08 kN, (b) a scanning electron micrograph of the crack tip region as marked in (a), (c) a close-up top view of the lower sheet and a close-up bottom view of the upper sheet of a failed lap-shear specimen under cyclic loading conditions.	215
Figure 5.7	(a) A schematic plot of a top view of a cross-tension specimen with a spot weld under applied resultant loads (shown as the bold arrows), (b) schematic plots of cross sections A-B and C-D for the Al/Fe spot friction weld in a cross-tension specimen, (c) failure modes of the Al/Fe spot friction welds in cross-tension specimens under quasi-static and cyclic loading conditions.	216
Figure 5.8	Optical micrographs of cross sections (a) A-B, (b) C-D of failed Al/Fe spot friction welds in cross-tension specimens at the fatigue life of 10^4 cycles under a load range of 0.16 kN, (c) a close-up top view of the lower sheet and a close-up bottom view of the upper sheet of a failed cross-tension specimen under cyclic loading conditions.	217
Figure 5.9	(a) A schematic plot of a half of a lap-shear specimen with a spot weld and the boundary conditions of a finite element analysis, (b) a three-dimensional finite element mesh for a half of a lap-shear specimen, (c) a close-up view of the mesh near the weld.	218
Figure 5.10	(a) A schematic plot of a cross-tension specimen with a spot weld under applied loads shown as the bold arrows and clamped parts shaded, (b) a schematic plot of an equivalent cross-tension specimen without the clamped parts and the boundary conditions of a finite element analysis, (c) a three-dimensional finite element mesh for a quarter of an equivalent cross-tension specimen, (d) a close-up view of the mesh near the weld.	219

Figure 5.11	(a) A schematic plot of a top view of the weld nugget (idealized as a rigid inclusion) in the upper sheet of the spot weld specimen with the cylindrical and Cartesian coordinate systems centered at the center of the upper half of the weld nugget, (b) the K_1 , K_2 , K_3 and K_e stress intensity factor solutions as functions of θ for the crack front along the nugget circumference of the Al/Fe spot friction weld in a lap-shear specimen, (c) the K_1 , K_2 , K_3 and K_e stress intensity factor solutions as functions of θ for the crack front along the nugget circumference of the Al/Fe spot friction weld in a cross-tension specimen.....	220
Figure 5.12	(a) The J integral range as a function of the fatigue life for the Al/Fe spot friction welds in lap-shear and cross-tension specimens under cyclic loading conditions, (b) the effective stress intensity factor range as a function of the fatigue life for the Al/Fe spot friction welds in lap-shear and cross-tension specimens under cyclic loading conditions.	221
Figure 6.1	Schematic plots of (a) a spot weld with ideal geometry, (b) a resistance spot weld with electrode indentation, gap and bend, (c) an aluminum spot friction weld with complex geometry, gap and bend, (d) a dissimilar Al/Fe spot friction weld with complex geometry, gap and bend under lap-shear loading conditions.	290
Figure 6.2	A schematic plot of a lap-shear specimen with a spot weld idealized as a circular cylinder under the resultant applied forces shown as the bold arrows.	291
Figure 6.3	A schematic plot of a top view of the weld nugget (modeled as a rigid inclusion) in the upper sheet of the spot weld specimen with the cylindrical and Cartesian coordinate systems centered at the center of the upper half of the weld nugget.	292
Figure 6.4	A two-dimensional model of two infinite strips made of different materials and thicknesses with the connection under plane strain loading conditions.....	293
Figure 6.5	(a) A crack with contour Γ surrounding a crack tip, (b) the front and side views of the left half of the strip model.	

The normal stresses σ_{ui} , σ_{uo} , σ_{li} and σ_{lo} represent the normal stresses for line \overline{FG} and line \overline{AB} , the normal stresses σ_{ui}^* , σ_{uo}^* , σ_{li}^* and σ_{lo}^* represent the normal stresses for line \overline{DE} and line \overline{CD} at the inner (i) and outer (o) surfaces of the upper (u) and lower (l) strips, respectively. The shear stresses τ_u and τ_l represent the shear stress τ_{zx}^u of the upper (u) and lower (l) strips for line \overline{FG} and line \overline{AB} , respectively. The outside boundary line $\overline{ABCDEFG}$ is considered as the contour Γ for the J integral.294

Figure 6.6 The decomposition process of the general out-of-plane shear stress distribution of a strip model.
 Model A represents a spot weld under general out-of-plane shear loading conditions. The general out-of-plane shear loading conditions of model A are decomposed into the two loading conditions shown in models G and H.
295

Figure 6.7 (a) The decomposition process of the lap-shear loading condition of a lap-shear specimen,
 (b) the decomposition process of the general normal structural stress distributions of a strip model.
 The gray-shaded areas represent the rigid inclusions. Model A represents a spot weld under lap-shear loading conditions. Model B represents a spot weld under an equivalent loading condition of model A. The forces, moments and general distributions of the normal structural stress of model B are decomposed into four simple loading conditions: counter bending, central bending, shear, and tension, marked as models C, D, E, and F, respectively.296

Figure 6.8 (a) A schematic plot of a spot weld with a gap and a bend in a lap-shear specimen under the applied forces F marked as the bold arrows,
 (b) a schematic plot of the applied loading condition near the right edge surface of the specimen,
 (c) the decomposition process of the loading conditions for the spot weld with the gap and bend in a lap-shear specimen,
 (d) the decomposition process of the general lap-shear loading conditions. Model R^* represents a spot weld with the gap and bend in a lap-shear specimen under the applied forces of F_1 and F_2 .
 The forces in model R^* are decomposed into the two loading conditions as shown in models S^* and T^* . The forces and moments in model S^* are decomposed into three simple loading conditions: lap-shear loading, counter bending and central bending, marked as models A^* , C^* and D^* , respectively.
298

- Figure 6.9 A schematic plot of a half of a lap-shear specimen with a spot weld and the boundary conditions employed in the finite element models.300
- Figure 6.10 (a) A three-dimensional finite element mesh for a half of a lap-shear specimen with a spot weld joining two sheets of equal thickness of $t_u = t_l = 0.65$ mm,
 (b) a close-up view of the mesh near the weld,
 (c) the normalized K_I , K_{II} and K_{III} solutions as functions of θ for the crack front along the nugget circumference of the Fe/Fe-0.65/0.65 weld,
 (d) the normalized K_1 , K_2 and K_3 solutions as functions of θ for the crack front along the nugget circumference of the Al/Fe-0.65/0.65 weld,
 (e) the normalized J integral solutions as functions of θ for the crack fronts along the nugget circumferences of the Fe/Fe-0.65/0.65 weld and the Al/Fe-0.65/0.65 weld.301
- Figure 6.11 (a) A three-dimensional finite element mesh for a half of a lap-shear specimen with a spot weld joining two sheets of thicknesses $t_u = 0.65$ mm and $t_l = 1.3$ mm,
 (b) a close-up view of the mesh near the weld,
 (c) the normalized K_I , K_{II} and K_{III} solutions as functions of θ for the crack front along the nugget circumference of the Fe/Fe-0.65/1.30 weld,
 (d) the normalized K_1 , K_2 and K_3 solutions as functions of θ for the crack front along the nugget circumference of the Al/Fe-0.65/1.30 weld,
 (e) the normalized K_1 , K_2 and K_3 solutions as functions of θ for the crack front along the nugget circumference of the Fe/Al-0.65/1.30 weld,
 (f) the normalized J integral solutions as functions of θ for the crack fronts along the nugget circumferences of the Fe/Fe-0.65/1.30 weld, the Al/Fe-0.65/1.30 weld and the Fe/Al-0.65/1.30 weld.....303
- Figure 6.12 (a) An optical micrograph of the cross section along the symmetry plane of an aluminum 6111 resistance spot weld before testing,
 (b) a close-up view of a three-dimensional finite element mesh near the weld,
 (c) the normalized K_I , K_{II} and K_{III} solutions as functions of θ for the aluminum 6111 resistance spot weld and for the equivalent spot weld joining two aluminum sheets of $t'_u = 1.3$ mm and $t'_l = 1.5$ mm based on the finite element computations,
 (d) a close-up view of a modified finite element mesh near the weld,
 (e) the normalized K_I , K_{II} and K_{III} solutions obtained from the finite element computations based on the original and modified meshes as functions of θ305

Figure 6.13 (a) An optical micrograph of the cross section along the symmetry plane of an aluminum 5754 spot friction weld before testing,
 (b) a close-up view of a three-dimensional finite element mesh near the weld,
 (c) the normalized K_I , K_{II} and K_{III} solutions as functions of θ for the aluminum 5754 spot friction weld, for the equivalent spot weld joining two aluminum sheets of $t'_u = 1.70$ mm and $t'_l = 2.06$ mm based on the finite element computations, and the results based on the analytical solutions for the equivalent spot weld,
 (d) a close-up view of a modified finite element mesh near the weld,
 (e) the normalized K_I , K_{II} and K_{III} solutions obtained from the finite element computations based on the original and modified meshes as functions of θ306

Figure 6.14 (a) An optical micrograph of the cross section along the symmetry plane of a dissimilar Al/Fe spot friction weld between an aluminum sheet and a coated steel sheet,
 (b) a close-up view of a three-dimensional finite element mesh near the weld,
 (c) the normalized J integral solutions as functions of θ for the Al/Fe spot friction weld, for the equivalent spot weld joining an aluminum sheet of $t'_u = 0.83$ mm to a steel sheet $t'_l = 0.78$ mm based on the finite element computations, and the results based on the analytical solutions for the equivalent spot weld.307

Figure 6.15 (a) Three-dimensional finite element meshes for the Al/Fe spot friction welds in lap-shear specimens,
 (b) the normalized J integral solutions for the Al/Fe welds obtained from the finite element computations based on meshes A, B, C, D and E. Mesh A is used to model the Al/Fe spot friction weld based on the micrograph shown in Figure 6.14(a). Mesh B is obtained from mesh A by removing the flashes and rises. Mesh C is obtained from mesh A by removing the flashes and by filling the gap between the upper and lower sheets. Mesh D is obtained from mesh C by straightening the upper and lower sheets. Mesh E is used to model an ideal spot weld joining an aluminum sheet to a steel sheet.....308

Figure 6.16 (a) The normalized J integral solutions,
 (b) the normalized K_1 , K_2 and K_3 solutions,
 (c) the in-plane phase angle ω as functions of θ for the Al/Fe spot friction weld based on the finite element computation and the analytical solutions for the equivalent spot weld based on the structural stress solutions with consideration of the gap and bend.309

CHAPTER I

INTRODUCTION

Aluminum alloys are becoming widely used in the automotive industry. Recently, vehicles made of hybrid body structures which combine parts made of steel and various aluminum alloys have been produced in the automotive companies. Efficient joining methods are therefore needed to join different components made of different aluminum alloys and steel sheets. A new spot friction welding technology is a solid-state joining process recently developed by Mazda Motor Corporation and Kawasaki Heavy Industry [1,2] to join aluminum sheets with high quality and strength performance. This new welding technology leads to a clean and economical working environment and, most importantly, significant saving in energy since the melting of base metals is avoided.

Accurate models for the static and fatigue strengths of spot friction welds under complex loading conditions are needed to enhance the product development for the structural integrity and durability of the automotive components. However, most of the current literature is for spot friction welds joining two identical aluminum sheets under quasi-static loading conditions based on experimental observations. Therefore, in this thesis, the strength and fatigue failure of spot friction welds between similar and dissimilar sheet materials are investigated. During the spot friction welding process, the tool contacts the upper sheet and penetrates the upper sheet to weld together the upper and lower sheets. The dissimilar spot friction welds are denoted as 5754/7075 when

aluminum alloys 5754-O and 7075-T6 were used as the upper and lower sheets, respectively, and as 7075/5754 when aluminum alloys 7075-T6 and 5754-O were used as the upper and lower sheets, respectively. Also, the dissimilar spot friction welds are denoted as Al/Fe when aluminum 6000 series alloy and aluminum 6000 series alloy were used as the upper and lower sheets. In this thesis, the strength and fatigue failure of aluminum 5754-O, 6111-T4, 5754/7075, 7075/5754 and Al/Fe spot friction welds in lap-shear and cross-tension specimens are investigated based on experimental observations, fatigue life estimation models and three-dimensional finite element analyses.

Recently, closed-form structural stress and stress intensity factor solutions for spot welds with ideal geometry joining two sheets of identical material and equal thickness in commonly used specimens have been developed by Lin and Pan [3]. Therefore, in this thesis, new analytical stress intensity factor and J integral solutions for spot welds with ideal geometry, gap and bend joining two sheets of different materials and thicknesses in lap-shear specimens are developed and validated by three-dimensional finite element analyses. Finally, the effects of the weld geometry and sheet thickness on the fracture mechanics parameters for resistance spot welds and spot friction welds between similar and dissimilar sheet materials in lap-shear specimens are investigated based on a combined theoretical and numerical approach.

Research results are written in five chapters. Chapter II represents a paper to examine the fatigue behavior of aluminum 5754-O and 6111-T4 spot friction welds in lap-shear specimens based on the experimental results and the theoretical fracture mechanics and structural stress approaches. Chapter III represents a paper to examine the effects of the processing time on the strengths and failure modes of dissimilar 5754/7075

and 7075/5754 spot friction welds between aluminum 5754-O and 7075-T6 sheets. Chapters IV and V represent two papers to investigate the fatigue behaviors of dissimilar 5754/7075, 7075/5754 and Al/Fe spot friction welds in lap-shear and cross-tension specimens based on experiments, three-dimensional finite element analyses and three fatigue life estimation models. Finally, Chapter VI represents a paper to examine the effects of the weld geometry and sheet thickness on the fracture mechanics parameters for resistance spot welds and spot friction welds between similar and dissimilar sheet materials in lap-shear specimens based on a combined theoretical and numerical approach

In Chapter II, the fatigue behavior of aluminum 5754 and 6111 spot friction welds in lap-shear specimens is investigated based on experimental observations and two fatigue life estimation models. Optical micrographs of the welds before and after failure under quasi-static and cyclic loading conditions are examined to investigate the fracture and failure mechanisms of both types of welds. Based on the experimental observations of the paths of the dominant kinked fatigue cracks, the kinked fatigue crack growth model with the global stress intensity factor solutions for the main cracks obtained from three-dimensional finite element analyses is adopted to estimate the fatigue lives of the welds. The structural stress model based on the closed-form structural stress solutions at the critical locations of the spot welds as reported in Lin and Pan [3] and the experimental stress-life fatigue data is developed to estimate the fatigue lives of the welds. Finally, the estimated fatigue lives based on the kinked fatigue crack growth model and the structural stress model are compared with the experimental results for both types of welds.

In Chapter III, the effects of the processing time on the strengths and failure modes of dissimilar 5754/7075 and 7075/5754 spot friction welds between aluminum 5754-O and 7075-T6 sheets are investigated by experiments. Dissimilar spot friction welds were first made at different processing conditions. The failure loads of the 5754/7075 and 7075/5754 welds in lap-shear specimens under quasi-static loading conditions are obtained from the experiments. The optimal processing times to maximize the failure loads of the 5754/7075 and 7075/5754 welds under lap-shear loading conditions are identified. Selected optical and scanning electron micrographs of the 5754/7075 and 7075/5754 welds made at different processing times before and after failure are examined to investigate the weld geometries and the failure modes. Finally, the mechanical behaviors and failure modes of the 5754/7075 and 7075/5754 welds made at the optimal processing times are compared and discussed.

In Chapter IV, the fatigue behavior of dissimilar 5754/7075 and 7075/5754 spot friction welds made at the optimal processing times (as identified in Chapter III) in lap-shear and cross-tension specimens is investigated based on experimental observations and three fatigue life estimation models. Optical micrographs of the welds before and after failure under quasi-static and cyclic loading conditions are examined to understand the fracture and failure mechanisms of the welds under different loading conditions. Based on the experimental observations of the paths of the dominant fatigue cracks, three fatigue life estimation models are adopted and developed to estimate the fatigue lives of the welds. The kinked fatigue crack growth model and the structural stress model developed in Chapter II are adopted to estimate the fatigue lives of the 5754/7075 and 7075/5754 welds in lap-shear specimens. A through-nugget fatigue crack growth model

based on the closed-form stress intensity factor solutions for the through-nugget cracks and the Paris law for the fatigue crack propagation is developed to estimate the fatigue lives of the 5754/7075 and 7075/5754 welds in cross-tension specimens. The fatigue life estimations based on the kinked fatigue crack growth model, the structural stress model and the through-nugget fatigue crack growth model are compared with the experimental results. Finally, the effective stress intensity factor and J integral solutions at the critical locations of the welds obtained from three-dimensional finite element analyses are used to correlate the experimental fatigue data for the 5754/7075 and 7075/5754 spot friction welds in lap-shear and cross-tension specimens under cyclic loading conditions.

In Chapter V, the fatigue behavior of dissimilar Al/Fe spot friction welds between aluminum 6000 series alloy and coated mild steel sheets in lap-shear and cross-tension specimens is investigated based on experiments and three-dimensional finite element analyses. Optical micrographs of the Al/Fe welds after failure under quasi-static and cyclic loading conditions are examined to understand the fracture and failure mechanisms of the welds. Three-dimensional finite element analyses based on the micrograph of the cross section along the symmetry plane of the weld before testing were conducted to obtain accurate stress intensity factor and J integral solutions for the crack fronts along the nugget circumferences of the welds under lap-shear and cross-tension loading conditions. The results obtained from the finite element computations are correlated with those obtained from the experimental observations. Finally, the in-plane effective stress intensity factor and J integral solutions at the critical locations of the welds obtained from three-dimensional finite element analyses are used to correlate the experimental fatigue data for the Al/Fe welds in lap-shear and cross-tension specimens.

In Chapter VI, the effects of weld geometry and sheet thickness on the fracture mechanics parameters for the crack fronts along the nugget circumferences of resistance spot welds and spot friction welds between similar and dissimilar sheet materials in lap-shear specimens are investigated based on a combined theoretical and numerical approach. The analytical stress intensity factor and J integral solutions for spot welds with ideal geometry, gap and bend joining two sheets of different materials and thicknesses in lap-shear specimens are first developed based on the new closed-form structural stress solutions for a rigid inclusion in a finite square plate subjected to a lap-shear load and a coach-peel load (Lin and Pan [3]). Three-dimensional finite element analyses for spot welds with ideal geometry in lap-shear specimens are then developed to validate the analytical solutions. Three-dimensional finite element models based on the micrographs of the cross sections along the symmetry planes of an aluminum 6111 resistance spot weld, an aluminum 5754 spot friction weld, and a dissimilar Al/Fe spot friction weld before testing are then conducted to obtain accurate stress intensity factor and J integral solutions for the crack fronts along the nugget circumferences of the welds under lap-shear loading conditions. Different three-dimensional finite element models based on the meshes that represent different features of the weld geometry are conducted to identify important geometric parameters that strongly affect the fracture mechanics parameters for the Al/Fe spot friction weld. The analytical stress intensity factor and J integral solutions for the spot welds with the gap and bend in lap-shear specimens are used to correlate with the results obtained from the finite element analyses for the Al/Fe spot friction weld. Finally, the results obtained from the analytical and finite element models and the experimental observations are correlated.

References

- [1] Sakano R, Murakami K, Yamashita K, Hyoe T, Fujimoto M, Inuzuka M, Nagao Y, Kashiki H. Development of spot FSW robot system for automobile body members. In: Proceedings of the 3rd international symposium of friction stir welding, Kobe, Japan, September 27-28, 2001.
- [2] Iwashita T. Method and apparatus for joining. US Patent 6601751 B2, August 5, 2003.
- [3] Lin P-C, Pan J. Closed-form structural stress and stress intensity factor solutions for spot welds in commonly used specimens. Eng Fract Mech 2008;75:5187-5206.

CHAPTER II

FATIGUE BEHAVIOR OF ALUMINUM 5754-O AND 6111-T4 SPOT FRICTION WELDS IN LAP-SHEAR SPECIMENS¹

Abstract

Fatigue behavior of aluminum 5754-O and 6111-T4 spot friction welds in lap-shear specimens is investigated based on experimental observations and two fatigue life estimation models. Optical micrographs of the 5754 and 6111 welds made by a concave tool and a flat tool, respectively, before and after failure under quasi-static and cyclic loading conditions are examined. The micrographs show that the failure modes of the 5754 and 6111 welds under quasi-static and cyclic loading conditions are quite different. Under quasi-static loading conditions, both types of welds mainly fail from the nearly flat fracture surface through the nugget. Under low-cycle loading conditions, both types of welds mainly fail from the kinked crack through the upper sheet thickness and the fracture surface through the nugget. Under high-cycle loading conditions, both types of welds mainly fail from the kinked cracks through the upper and lower sheet thicknesses. A kinked fatigue crack growth model based on the stress intensity factor solutions for finite kinked cracks and a structural stress model based on the closed-form structural stress solutions at the critical locations of the welds are adopted to estimate the fatigue lives of both types of welds. The fatigue life estimations based on the kinked fatigue crack growth model and the structural

¹ Published in International Journal of Fatigue, 2008;3:2175-2190.

stress model appear to agree well with the experimental results for both types of welds.

Keywords: Spot friction weld; Friction stir spot weld; Failure mode; Fatigue life; Kinked crack; Structural stress

2.1. Introduction

Resistance spot welding is the most commonly used joining technique for body-in-white parts made of steel sheets. However, resistance spot welding of aluminum sheets is likely to produce poor welds as reported by Thornton et al. [1] and Gean et al. [2]. Recently, a spot friction welding technology for joining aluminum sheets has been developed by Mazda Motor Corporation and Kawasaki Heavy Industry [3,4]. The most significant advantage of the spot friction welding process comparing to the conventional welding processes is that the joint can be made without melting the base metal. A schematic illustration of the spot friction welding process was presented, for example, in Lin et al. [5].

The mechanical behavior of aluminum spot friction welds under quasi-static loading conditions was studied, for example, see Lin et al. [5], Pan et al. [6], Fujimoto et al. [7,8] and Hinrichs et al. [9]. The metallurgical aspects of 6111 spot friction welds were investigated by Mitlin et al. [10]. Tran et al. [11] investigated the failure loads of spot friction welds in aluminum 6111 lap-shear specimens under quasi-static and dynamic loading conditions. Recently, Lin et al. [12-15] investigated the fatigue behavior of spot friction welds made by different tools in aluminum 6111 sheets based on experimental observations and fracture mechanics. A comprehensive

literature review for spot friction welds can be found in Pan [16]. Note that most of the literature is for spot friction welds between similar aluminum sheets. However, dissimilar spot friction welds between aluminum 2017-T6 and 5052 sheets, between aluminum 5754 and 6111 sheets, and between aluminum 5754-O and 7075-T6 sheets were investigated by Tozaki et al. [17], Su et al. [18] and Tran et al. [19], respectively.

It should be noted that aluminum 5754 alloys are widely employed in the automotive industry to produce parts such as internal door stiffeners or the entire body-in-white as reported in Kaufman [20]. However, the fatigue behavior of aluminum 5754 spot friction welds has not been extensively studied. In this paper, we investigate the fatigue behavior of aluminum 5754 and 6111 spot friction welds in lap-shear specimens based on experimental observations and two fatigue life estimation models. Optical micrographs of the welds before and after failure under quasi-static and cyclic loading conditions are examined to investigate the fracture and failure mechanisms of both types of welds. Based on the experimental observations of the paths of the dominant kinked fatigue cracks, the kinked fatigue crack growth model as discussed in Lin et al. [12-15] with the global stress intensity factor solutions for the main cracks obtained from three-dimensional finite element analyses is adopted to estimate the fatigue lives of the welds. The structural stress model based on the closed-form structural stress solutions at the critical locations of the spot welds as reported in Lin and Pan [21] and the experimental stress-life fatigue data is also adopted to estimate the fatigue lives of the welds. Finally, the estimated fatigue lives based on the kinked fatigue crack growth model and the structural stress model are compared with the experimental results for both types of welds.

2.2. Aluminum 5754 and 6111 spot friction welds before testing

For the spot friction welding process under load-controlled conditions, the important welding processing parameters are the tool geometry, the tool rotational speed, the tool downward force and the processing time. In this investigation, a tool with a concave shoulder and a threaded probe pin was used to make spot friction welds in lap-shear specimens of aluminum 5754-O sheets of the thickness of 2.0 mm. A tool rotational speed of 3000 RPM and a tool downward force of 5.88 kN were specified to make the 5754 spot friction welds. The 5754 welds were first made under different processing times and tested under lap-shear loading conditions. The optimal processing time for the maximum failure strength of the 5754 welds in lap-shear specimens under this particular set of the welding processing parameters was identified. This optimal processing time and the welding processing parameters specified above were then used to make the 5754 spot friction welds tested in this investigation.

In this investigation, another tool with a flat shoulder was used to make spot friction welds in lap-shear specimens of aluminum 6111-T4 sheets. For the 6111 welds, the thicknesses of the upper and lower sheets are 0.94 mm and 1.04 mm, respectively. The 6111 welds tested in this investigation were made based on a DOE (design of experiments) method to determine the optimal tool rotational speed, tool downward force and processing time for the maximum failure strength of the 6111 welds in lap-shear specimens. Note that the 6111 lap-shear specimens used in this investigation and those used in Tran et al. [11] are identical. The 6111 lap-shear specimens used in this investigation were made of the upper and lower sheets of

unequal thicknesses while the 6111 lap-shear specimens used in Lin et al. [13,15] were made of the upper and lower sheets of equal thickness. We first present some optical and scanning electron micrographs of the cross sections along the symmetry planes of the 5754 and 6111 spot friction welds before testing.

Figure 2.1(a) shows an optical micrograph of the cross section along the symmetry plane of a 5754 spot friction weld made by the concave tool before testing. As shown in the figure, the indentation profile reflects the general shape of the threaded probe pin and the concave shoulder of the tool. The bottom surface of the lower sheet is almost flat. The area near the central hole represents the fine grain stir zone where the upper and lower sheets are well bonded possibly due to high pressure and large plastic deformation. Two notches, marked as N1 and N2, can be seen in the figure. Figure 2.1(b) shows a close-up optical micrograph of region I in Figure 2.1(a), where the notch, marked as N2, extends and becomes a crack. The location of the crack tip is marked in the figure. Figure 2.1(c) shows a close-up optical micrograph of region II in Figure 2.1(b). As shown in Figure 2.1(c), the interfacial surface between the two deformed sheet materials near the crack tip slightly rises up outside the stir zone. The location of the crack tip is also marked in the figure. The location of the crack tip can be identified by a scanning electron micrograph of the crack tip region as shown in Figure 2.1(d). As shown in the figure, some part of the crack surface near the tip becomes vague and may be bonded by the welding process.

As shown in Figure 2.1(a), the thickness of the weld nugget near the central hole is slightly larger than that near the outer circumference of the tool shoulder indentation due to the concave geometry of the tool shoulder. The concave tool

shoulder squeezed out some upper sheet material but maintained some upper sheet material near the central hole. As suggested in Figure 2.1(a), the material under the tool shoulder indentation flowed outward and resulted in a radial expansion of the upper sheet material along the outer circumference of the tool shoulder indentation. However, due to the constraint of the neighboring material, the upper sheet was therefore slightly bent along the outer circumference of the tool shoulder indentation.

Figure 2.2(a) shows an optical micrograph of the cross section along the symmetry plane of a 6111 spot friction weld made by the flat tool before testing. As shown in the figure, the indentation profile reflects the shape of the probe pin and the flat shoulder of the tool. The bottom surface of the lower sheet is almost flat. The area near the central hole represents the fine grain stir zone where the upper and lower sheets are well bonded possibly due to high pressure and large plastic deformation. Two notches, marked as N1 and N2, can be seen in the figure. Figure 2.2(b) shows a close-up optical micrograph of region I in Figure 2.2(a), where the notch, marked as N2, extends and becomes a crack. The location of the crack tip is marked in the figure. Figure 2.2(c) shows a close-up optical micrograph of region II in Figure 2.2(b) where the interfacial surface, marked by two small arrows, becomes vague and disappears into the stir zone. As shown in Figure 2.2(c), the interfacial surface between the two deformed sheets near the crack tip remained almost planar outside the stir zone. The location of the crack tip is also marked in the figure. The location of the crack tip can also be identified by a scanning electron micrograph of the crack tip region as shown in Figure 2.2(d). As shown in the figure, some part of

the crack surface near the tip becomes vague and may be bonded by the welding process.

As shown in Figure 2.2(a), the flat tool shoulder squeezed out a portion of the upper sheet material and, consequently, the thickness of the upper sheet decreased under the shoulder indentation. As suggested in Figure 2.2(a), the material under the tool shoulder indentation flowed outward and resulted in a radial expansion of the upper sheet material along the outer circumference of the shoulder indentation. However, due to the constraint of the neighboring material, the upper sheet was therefore slightly bent along the outer circumference of the tool shoulder indentation.

2.3. Experiments

The lap-shear specimens were made by using two 25.4 mm \times 101.6 mm aluminum sheets with a 25.4 mm \times 25.4 mm overlap area. Figures 2.3(a) and 2.3(b) show a lap-shear specimen with a 5754 spot friction weld made by the concave tool and a lap-shear specimen with a 6111 spot friction weld made by the flat tool, respectively. As shown in Figure 2.3(a), two square doublers of 25.4 mm \times 25.4 mm made of aluminum 5754 sheets are attached to the ends of the 5754 lap-shear specimen. As shown in Figure 2.3(b), two doublers are made by folding two square parts of the sheets near the ends (25.4 mm \times 25.4 mm) of the 6111 lap-shear specimen. Note that the doublers are used to align the applied load to avoid the initial realignment of the specimen under lap-shear loading conditions and to reinforce the sheet materials near the holes. Due to the load-controlled welding process, the actual plunge depths of the tool penetration and the geometries of the spot friction welds

may not be controlled precisely under the same welding processing parameters. In order to minimize the effects of the weld geometry on the experimental results, we selected the specimens with the spot friction welds that have nearly the same actual plunge depths of the tool penetration for the quasi-static and fatigue tests. Before testing, all 6111 specimens were baked in an oven at 170°C for 20 minutes and cooled in the ambient air to simulate the paint bake cycles in automotive assembly plants.

Lap-shear specimens were first tested under quasi-static loading conditions by using an Instron testing machine at a monotonic displacement rate of 1.0 mm per minute. The load and displacement were simultaneously recorded during each test. The average failure loads, defined as the maximum loads of the load-displacement curves, obtained from three tested 5754 and 6111 lap-shear specimens are 4.34 kN and 3.38 kN, respectively. These failure loads were used as the reference loads to determine the loads applied in the fatigue tests. The lap-shear specimens were then tested under cyclic loading conditions by using an Instron servo-hydraulic fatigue testing machine with the load ratio R of 0.2. The test frequency was 10 Hz. The tests were terminated when specimens were separated, or nearly separated when the displacement of the two grips of specimens exceeded 5 mm. Some tests were stopped before the final failures of the specimens to examine the fatigue crack growth patterns. Figure 2.3(c) shows the experimental results for the 5754 spot friction welds made by the concave tool and the 6111 spot friction welds made by the flat tool in lap-shear specimens under cyclic loading conditions. The number of specimens available for fatigue testing is limited.

2.4. Failure modes of aluminum 5754 welds under quasi-static and cyclic loading conditions

2.4.1. A two-dimensional overview of failure modes

We conducted experiments for the 5754 spot friction welds in lap-shear specimens under quasi-static and cyclic loading conditions. Based on the experimental observations, the failed 5754 spot friction welds under quasi-static loading conditions show one failure mode. The failed 5754 spot friction welds under cyclic loading conditions with the fatigue lives from 10^3 cycles to 10^4 cycles (low-cycle fatigue) show a different failure mode. The failed 5754 spot friction welds under cyclic loading conditions with the fatigue lives from 10^4 cycles to 2×10^5 cycles (high-cycle fatigue) show another failure mode. Note that we define low-cycle fatigue and high-cycle fatigue loading conditions only for convenient presentation in this paper. The fatigue life and the load range for the transition of the failure mode from low-cycle fatigue to high-cycle fatigue for the 5754 spot friction welds are about 1.46×10^4 cycles and 2.01 kN, respectively, as shown in Figure 2.3(c). Since the failure modes of the 5754 spot friction welds are quite complex under quasi-static and cyclic loading conditions, a two-dimensional general overview of the failure modes under quasi-static, low-cycle and high-cycle loading conditions is first presented.

Figure 2.4(a) shows a schematic plot of a lap-shear specimen with a 5754 spot friction made by the concave tool with the sheet thickness $t = 2$ mm under applied resultant shear loads (shown as the bold arrows). Figure 2.4(b) shows a schematic plot of the cross section along the symmetry plane of the 5754 spot friction weld made by the concave tool. In this figure, the short dash lines near the two notches represent the unwelded interfacial surfaces and the thin solid lines represent either the

fracture surfaces or fatigue cracks. Figure 2.4(c) summarizes the failure modes of the 5754 spot friction welds in lap-shear specimens under quasi-static, low-cycle and high-cycle loading conditions.

As shown in Figure 2.4(b) and as summarized in Figure 2.4(c), under quasi-static loading conditions, cracks A and B appear to emanate from the original crack tips of the weld. Crack A propagates upward a bit possibly along the interfacial surface and then into the upper sheet thickness while crack B propagates a bit along the interfacial surface. When the load continues to increase, the upper and lower sheets are eventually separated by fracture surfaces C and D. Under low-cycle loading conditions, fatigue cracks B and E appear to emanate from the original crack tips of the weld and propagate upward a bit possibly along the interfacial surface and through the upper sheet thickness, respectively. A shear failure, marked by F, occurs at the end of fatigue crack E. Then, the failure propagates along the nugget circumference. Near the final stage of the specimen failure, crack B becomes crack G that propagates partially into the lower sheet thickness. Eventually, the stir zone is separated by fracture surfaces H and D. Finally, the upper sheet is torn off.

Under high-cycle loading conditions, fatigue cracks E and I appear to emanate from the original crack tips of the weld and propagate through the upper and lower sheet thicknesses, respectively. A shear failure, marked by F, occurs at the end of fatigue crack E. Under high-cycle loading conditions with higher load ranges, after propagating through the upper and lower sheet thicknesses, fatigue crack E becomes a circumferential crack that propagates along the nugget circumference while fatigue crack I becomes a transverse through crack that propagates in the width direction of

the specimen. These two cracks finally cause the failure of the specimen. Under high-cycle loading conditions with lower load ranges, after propagating through the upper and lower sheet thicknesses, both fatigue cracks E and I become transverse through cracks that propagate in the width direction of the specimen. These two cracks finally cause the failure of the specimen.

As shown in Figure 2.1(a), the interfacial surface between the two deformed sheet materials of the 5754 spot friction weld in the stir zone can hardly be seen. Note that the welding processing parameters used to make the 5754 welds tested in this investigation are nearly the same as those used to make the dissimilar 5754/7075 welds at the optimal processing time tested in Tran et al. [19]. Note also that the upper aluminum 5754 sheets used in this investigation and in Tran et al. [19] are identical. Therefore, the geometry of the interfacial surface between the two deformed sheet materials of the 5754 welds tested in this investigation may be similar to that of the dissimilar 5754/7075 welds at the optimal processing time as shown in Tran et al. [19]. According to Tran et al. [19], the lower sheet material of the dissimilar 5754/7075 welds at the optimal processing time rises and extends significantly into the upper sheet near the central hole. Therefore, it seems that fracture or crack surfaces C, D, G and H in Figure 2.4(b) may not separate along the interfacial surface between the two deformed sheet materials of the 5754 welds. In the following, the micrographs to show the details of the failure modes of the 5754 welds in lap-shear specimens under different loading conditions are presented.

2.4.2. Failure mode under quasi-static loading conditions

Figure 2.5 shows an optical micrograph of the cross section along the symmetry plane of a failed 5754 spot friction weld made by the concave tool in a lap-shear specimen under quasi-static loading conditions. The bold arrows in Figure 2.5 schematically show the direction of the applied load. Due to the large deformation in the final stage of the specimen failure, the nugget rotated clockwise. Therefore, the sheets near the nugget are slightly bent. The loads are marked schematically parallel to the legs of the specimens as shown. The applied load stretches the upper right sheet (marked as Leg 2) and the lower left sheet (marked as Leg 1). As shown in Figure 2.5, two cracks, marked as crack 1 and crack 2, appear to emanate from the original crack tips of the weld. Crack 1 propagates a bit along the interfacial surface while crack 2 propagates upward a bit possibly along the interfacial surface (see Figure 2.1) and then into the upper sheet thickness due to the favorable stress condition. When the load continues to increase, the upper and lower sheets are eventually separated by the nearly flat fracture surface through the nugget, marked as S1 and S2, in Figure 2.5. In summary, the 5754 welds mainly fail from the nearly flat fracture surface through the nugget under quasi-static loading conditions.

2.4.3. Failure mode under low-cycle loading conditions

Figures 2.6(a) and 2.6(b) show optical micrographs of the cross sections along the symmetry plane of a partially failed 5754 spot friction weld made by the concave tool at the fatigue life of 3.5×10^3 cycles and a failed 5754 spot friction weld made by the concave tool at the fatigue life of 4.7×10^3 cycles under a load range of 2.45 kN, respectively. Note that the lap-shear specimen with the partially failed spot friction

weld was subjected to the same load range as the lap-shear specimen with the failed spot friction weld. However, we stopped the test for the partially failed spot friction weld at about 75% of the fatigue life of the failed spot friction weld under the same load range to examine the fatigue crack growth pattern before the final failure. Therefore, the spot friction weld in Figure 2.6(a), marked with $0.75N_f$, was partially failed and not separated while the spot friction weld in Figure 2.6(b), marked with N_f , was failed and separated. We will follow the same notation for other figures presented later in the paper. The bold arrows in Figures 2.6(a) and 2.6(b) schematically show the direction of the applied load. Near the lower left portions of the welds, fatigue cracks, marked as crack 1 in Figures 2.6(a) and 2.6(b), appear to emanate from the original crack tips and propagate upward a bit possibly along the interfacial surface (see Figure 2.1). Near the upper right portions of the welds, fatigue cracks, marked as crack 2 in Figures 2.6(a) and 2.6(b), appear to emanate from the original crack tips and propagate upward a bit possibly along the interfacial surface and then into the upper sheet thickness due to the favorable stress condition. As shown in Figure 2.6(a), another small crack, marked as crack 3, appears to be initiated near the fatigue life of 3.5×10^3 cycles. As shown in Figures 2.6(a) and 2.6(b), a shear failure, marked by S2, occurs at the end of fatigue crack 2. The failure then propagates along the nugget circumference. After fatigue crack 2 propagates through the upper sheet thickness and around the nugget circumference, without the support of the upper sheet near the stretching side of the nugget, the nugget is rotated clockwise and the sheets near the nugget are therefore bent. As shown in Figure 2.6(b), crack 1 does not grow but the original crack becomes crack 1a that propagates

downward into the lower sheet thickness and then through the nugget near the final stage of the specimen failure. Eventually, the stir zone is separated first by a fracture surface through the left portion of the nugget marked as S1 due to crack 1a as shown in Figure 2.6(b) and then by a fracture surface through the right portion of the nugget marked as S3 due to crack 3 as shown in Figure 2.6(b). The upper sheet is finally torn off. As shown in Figures 2.6(a) and 2.6(b), fatigue crack 2 can be considered as a kinked crack emanating from the original crack tip on the right side of the weld. As suggested in Figures 2.6(a) and 2.6(b), fatigue crack 2 appears to be the dominant kinked fatigue crack that causes the failure of the 5754 welds under low-cycle loading conditions. In summary, the 5754 welds mainly fail from the kinked crack through the upper sheet thickness and the nearly flat fracture surface through the nugget under low-cycle loading conditions.

2.4.4. Failure mode under high-cycle loading conditions

Figures 2.7(a) and 2.7(b) show optical micrographs of the cross sections along the symmetry plane of a partially failed 5754 spot friction weld made by the concave tool at the fatigue life of 4.2×10^4 cycles and a failed 5754 spot friction weld made by the concave tool at the fatigue life of 5.5×10^4 cycles under a load range of 1.43 kN, respectively. Note that the spot friction welds in Figures 2.7(a) and 2.7(b) were not separated. The bold arrows in Figures 2.7(a) and 2.7(b) schematically show the direction of the applied load. In Figures 2.7(a) and 2.7(b), two fatigue cracks, marked as crack 1' and crack 2' in each of the figures, appear to emanate from the original crack tips of the welds and propagate into the lower and upper sheet thicknesses,

respectively. As shown in Figure 2.7(a), fatigue crack 1' propagates partially into the lower sheet thickness while fatigue crack 2' propagates through the upper sheet thickness (with a reduced thickness). Note that the length of fatigue crack 1' is smaller than that of fatigue crack 2' at the fatigue life of 4.2×10^4 cycles as indicated in Figure 2.7(a). As shown in Figure 2.7(b), both fatigue cracks 1' and 2' propagate through the lower and upper sheet thicknesses, respectively. A shear failure, marked by S2, occurs at the end of fatigue crack 2' as shown in Figures 2.7(a) and 2.7(b). Note that another crack, marked as crack 3' in Figure 2.7(b), was likely formed during the welding process or introduced at the cross-sectional cutting of the failed specimen since no similar crack was found in the partially failed specimen as shown in Figure 2.7(a). Note also that this crack should not affect the fatigue behavior of the 5754 welds since the crack is subjected to an unfavorable stress condition for crack propagation.

Under high-cycle loading conditions with higher load ranges, after propagating through the lower and upper sheet thicknesses, fatigue crack 1' becomes a transverse through crack that propagates in the width direction of the specimen while fatigue crack 2' becomes a circumferential crack that propagates along the nugget circumference. These two cracks finally cause the failure of the specimen. Under high-cycle loading conditions with lower load ranges, after propagating through the lower and upper sheet thicknesses, both fatigue cracks 1' and 2' become transverse through cracks that propagate in the width direction of the specimen. These two cracks finally cause the failure of the specimen. As shown in Figures 2.7(a) and 2.7(b), both fatigue cracks 1' and 2' can be considered as kinked cracks emanating

from the original crack tips of the welds. As suggested in Figures 2.7(a) and 2.7(b), fatigue crack 2' appears to be the dominant kinked fatigue crack that causes the failure of the 5754 welds under high-cycle loading conditions. In summary, the 5754 welds mainly fail from the kinked cracks through the upper and lower sheet thicknesses under high-cycle loading conditions.

2.5. Failure modes of aluminum 6111 welds under quasi-static and cyclic loading conditions

2.5.1. A two-dimensional overview of failure modes

We conducted experiments for the 6111 spot friction welds in lap-shear specimens under quasi-static and cyclic loading conditions. Based on the experimental observations, the failed 6111 spot friction welds under quasi-static loading conditions show one failure mode. The failed 6111 spot friction welds under cyclic loading conditions with the fatigue lives from 10^3 cycles to 3×10^3 cycles (low-cycle fatigue) show a different failure mode. The failed 6111 spot friction welds under cyclic loading conditions with the fatigue lives from 3×10^3 cycles to 1.6×10^5 cycles (high-cycle fatigue) show another failure mode. Note that we define low-cycle fatigue and high-cycle fatigue loading conditions only for convenient presentation in this paper. The fatigue life and the load range for the transition of the failure mode from low-cycle fatigue to high-cycle fatigue for 6111 spot friction welds are about 3×10^3 cycles and 1.99 kN, respectively, as shown in Figure 2.3(c). Since the failure modes of the 6111 spot friction welds are quite complex under quasi-static and cyclic loading conditions, a two-dimensional general overview of the failure modes under quasi-static, low-cycle and high-cycle loading conditions is first presented.

Figure 2.8(a) shows a schematic plot of a lap-shear specimen with a 6111 spot friction weld made by the flat tool with the upper sheet thickness $t = 0.94$ mm and the lower sheet thickness $t' = 1.04$ mm under applied resultant shear loads (shown as the bold arrows). Figure 2.8(b) shows a schematic plot of the cross section along the symmetry plane of the 6111 spot friction weld made by the flat tool. In this figure, the short dash lines near the two notches represent the unwelded interfacial surfaces and the thin solid lines represent either the fracture surfaces or fatigue cracks. Figure 2.8(c) summarizes the failure modes of the 6111 welds in lap-shear specimens under quasi-static, low-cycle and high-cycle loading conditions.

In general, the failure modes of the 6111 welds made by the flat tool in lap-shear specimens under quasi-static and cyclic loading conditions as shown in Figure 2.8(b) and as summarized in Figure 2.8(c) are similar to those of the 5754 welds made by the concave tool in lap-shear specimens as discussed earlier. Under quasi-static loading conditions, cracks A' and B' appear to emanate from the original crack tips of the weld and propagate upward a bit into the upper sheet thickness and a bit along the interfacial surface, respectively. When the load continues to increase, the upper and lower sheets are eventually separated by fracture surfaces B' and C'. Under low-cycle loading conditions, fatigue cracks D' and F' appear to emanate from the original crack tips of the weld and propagate through the upper sheet thickness and partially into the lower sheet thickness, respectively. A shear failure, marked by E', occurs at the end of fatigue crack D'. The failure then propagates along the nugget circumference. After fatigue crack D' propagates through the upper sheet thickness

and along the nugget circumference, the stir zone is eventually separated by fracture surface B'. Finally, the upper sheet is torn off.

Under high-cycle loading conditions, fatigue cracks D' and F' appear to emanate from the original crack tips of the weld and propagate into the upper and lower sheet thicknesses, respectively. Under high-cycle loading conditions with higher load ranges, after propagating through the upper and lower sheet thicknesses, both fatigue cracks D' and F' become circumferential cracks that propagate along the nugget circumference. The upper sheet is finally torn off. Under high-cycle loading conditions with lower load ranges, after propagating through the upper and lower sheet thicknesses, both fatigue cracks D' and F' become transverse through cracks that propagate in the width direction of the specimen. These two cracks finally cause the failure of the specimen.

As shown in Figure 2.2(a), the interfacial surface between the two deformed sheet materials of the 6111 spot friction weld in the stir zone can hardly be seen. Note that Figure 2 in Lin et al. [15] shows a deformed shape of a 6111 spot friction weld made by a flat tool based on an axisymmetric thermal-mechanical finite element modeling of the spot friction welding process. As shown in the figure, the lower sheet material is pushed upward near the central hole. Therefore, it seems that fracture surfaces B' and C' in Figure 2.8(b) may not separate along the interfacial surface between the two deformed sheet materials of the 6111 spot friction welds tested in this investigation. In the following, the micrographs to show the details of the failure modes of aluminum 6111 spot friction welds in lap-shear specimens under different loading conditions are presented.

2.5.2. Failure mode under quasi-static loading conditions

Figure 2.9 shows an optical micrograph of the cross section along the symmetry plane of a failed 6111 spot friction weld made by the flat tool in a lap-shear specimen under quasi-static loading conditions. The bold arrows in Figure 2.9 schematically show the direction of the applied load. The applied load stretches the upper right sheet (marked as Leg 2) and the lower left sheet (marked as Leg 1). As shown in Figure 2.9, two cracks, marked as crack 1 and crack 2, appear to emanate from the original crack tips of the weld. Crack 1 propagates a bit along the interfacial surface while crack 2 propagates upward a bit into the upper sheet thickness possibly due to the favorable stress condition. When the load continues to increase, the upper and lower sheets are eventually separated with the nearly flat fracture surface through the nugget, marked as S1 and S2, in Figure 2.9. Similar to the 5754 welds, the 6111 welds mainly fail from the nearly flat fracture surface through the nugget under quasi-static loading conditions.

2.5.3. Failure mode under low-cycle loading conditions

Figures 2.10(a) and 2.10(b) show optical micrographs of the cross sections along the symmetry plane of a partially failed 6111 spot friction weld made by the flat tool at the fatigue life of 2.0×10^3 cycles and a failed 6111 spot friction weld made by the flat tool at the fatigue life of 2.7×10^3 cycles under a load range of 2.13 kN, respectively. Note that the spot friction weld in Figure 2.10(b) was separated. The bold arrows in Figures 2.10(a) and 2.10(b) schematically show the direction of the applied load. As shown in Figures 2.10(a) and 2.10(b), two fatigue cracks, marked as

crack 1 and crack 2 in each of the figures, appear to emanate from the original crack tips of the welds and propagate into the lower and upper sheet thicknesses, respectively. As shown in Figure 2.10(a), both fatigue cracks propagate partially into the lower and upper sheet thicknesses at the fatigue life of 2.0×10^3 cycles. Note that the lengths of both fatigue cracks are nearly the same at the fatigue life of 2.0×10^3 cycles as indicated in Figure 2.10(a). As shown in Figure 2.10(b), fatigue crack 1 propagates partially into the lower sheet thickness while fatigue crack 2 propagates through the upper sheet thickness at the fatigue life of 2.7×10^3 cycles. A shear failure, marked by S2, occurs at the end of fatigue crack 2. The failure then propagates along the nugget circumference. After fatigue crack 2 propagates through the upper sheet thickness and around the nugget circumference, without the support of the upper sheet, the nugget is rotated clockwise and the sheets near the nugget are therefore bent. Eventually, the stir zone is separated by a fracture surface through the left portion of the nugget, marked as S1, in Figure 2.10(b). The upper sheet is finally torn off. As shown in Figures 2.10(a) and 2.10(b), both fatigue cracks 1 and 2 can be considered as kinked cracks emanating from the original crack tips of the welds. As suggested in Figures 2.10(a) and 2.10(b), fatigue crack 2 appears to be the dominant kinked fatigue crack that causes the failure of the 6111 welds under low-cycle loading conditions. In summary, the 6111 welds mainly fail from the kinked crack through the upper sheet thickness and the fracture surface through the nugget under low-cycle loading conditions.

2.5.4. Failure mode under high-cycle loading conditions

Figures 2.11(a) and 2.11(b) show optical micrographs of the cross sections along the symmetry plane of a partially failed 6111 spot friction weld made by the flat tool at the fatigue life of 1.2×10^5 cycles and a failed 6111 spot friction weld made by the flat tool at the fatigue life of 1.6×10^5 cycles under a load range of 0.85 kN, respectively. The bold arrows in Figures 2.11(a) and 2.11(b) schematically show the direction of the applied load. In Figures 2.11(a) and 2.11(b), two fatigue cracks, marked as crack 1' and crack 2' in each of the figures, appear to emanate from the original crack tips of the welds and propagate into the lower and upper sheet thicknesses, respectively. As shown in Figure 2.11(a), both fatigue cracks propagate partially into the lower and upper sheet thicknesses at the fatigue life of 1.2×10^5 cycles. As shown in Figure 2.11(a), the length of fatigue crack 1' is much larger than that of fatigue crack 2' at the fatigue life of 1.2×10^5 cycles. As shown in Figure 2.11(b), both fatigue cracks propagate through the lower and upper sheet thicknesses at the fatigue life of 1.6×10^5 cycles. As shown in Figure 2.11(b), the length of fatigue crack 1' is slightly larger than that of fatigue crack 2' at the fatigue life of 1.6×10^5 cycles. Note that another crack, marked as crack 3' in Figure 2.11(b), appears to emanate from the original crack tip on the left side of the weld and propagates first a bit along the interfacial surface and then through the left portion of the nugget. This crack appears to be initiated near the final stage of the specimen failure since no similar crack was seen in Figure 2.11(a).

Under high-cycle loading conditions with higher load ranges, after propagating through the lower and upper sheet thicknesses, both fatigue cracks 1' and 2' become

circumferential cracks that propagate along the nugget circumference. Finally, the upper sheet is torn off. Under high-cycle loading conditions with lower load ranges, after propagating through the lower and upper sheet thicknesses, both fatigue cracks 1' and 2' become transverse through cracks that propagate in the width direction of the specimen. These two cracks finally cause the failure of the specimen. As shown in Figures 2.11(a) and 2.11(b), both fatigue cracks 1' and 2' can be considered as kinked cracks emanating from the original crack tips of the welds. As suggested in Figures 2.11(a) and 2.11(b), fatigue crack 1' appears to be the dominant kinked fatigue crack that causes the failure of the 6111 welds under high-cycle loading conditions. Similarly to the 5754 welds, the 6111 welds mainly fail from the kinked cracks through the upper and lower sheet thicknesses under high-cycle loading conditions.

2.6. Fatigue life estimation models

In order to develop engineering fatigue life estimation models, we idealize the three-dimensional spot friction weld problem as a two-dimensional crack problem as in Newman and Dowling [22] and Lin et al. [23]. Figures 2.12(a) and 2.12(b) show schematic plots of the cross sections along the symmetry plane of the 5754 and 6111 spot friction welds, respectively, under statically equivalent combined tensile and bending loads shown as the bold arrows in the figures. In Figures 2.12(a) and 2.12(b), the short dash lines near the notches represent the unwelded interfacial surfaces and the thin solid lines represent the fatigue cracks. According to Lin et al. [14,15,23,24], the global stress intensity factors solutions K_I and K_{II} are maximum at the original

crack tips on the cross section along the symmetry plane of the spot weld in lap-shear specimens. These critical locations are marked as a and b in Figures 2.12(a) and 2.12(b) (and also in Figures 2.4(a) and 2.8(a)).

2.6.1. A kinked fatigue crack growth model

As discussed earlier, the fatigue crack growth behaviors of the 5754 spot friction welds made by the concave tool under low-cycle and high-cycle loading conditions are quite similar, whereas the final failure modes of the welds under loading conditions of low-cycle fatigue and high-cycle fatigue are different, as shown in Figures 2.6 and 2.7. As schematically shown in Figure 2.12(a), two kinked fatigue cracks, marked as kinked crack 1 and kinked crack 2, are initiated from the original crack tips of the weld with the kink angles α_1 and α_2 , respectively. Based on the experimental observations, the failures of the 5754 spot friction welds made by the concave tool under cyclic loading conditions appear to be dominated by kinked crack 2 that propagates through the upper sheet thickness (with a reduced thickness). Note that the kink angle α_2 of kinked crack 2 is estimated from Figures 2.6 and 2.7 to be 69° for the 5754 welds under cyclic loading conditions.

As discussed earlier, the fatigue crack growth behavior and the final failure mode of 6111 spot friction welds made by the flat tool under low-cycle loading conditions are quite similar to those under high-cycle loading conditions as shown in Figures 2.10 and 11. As schematically shown in Figure 2.12(b), two kinked fatigue cracks, marked as kinked crack 1 and kinked crack 2, are initiated from the original crack tips of the weld with the kink angles α_1 and α_2 , respectively. Based on the experimental

observations, the failure of the 6111 welds made by the flat tool under low-cycle loading conditions appears to be dominated by kinked crack 2 that propagates through the upper sheet thickness (with a reduced thickness). Note that the kink angle α_2 of kinked crack 2 is estimated to be 75° from Figure 2.10 for the 6111 welds under low-cycle loading conditions. However, the failure of the 6111 welds made by the flat tool under high-cycle loading conditions appears to be dominated by kinked crack 1 that propagates through the lower sheet thickness. Note that the kink angle α_1 of kinked crack 1 is estimated to be 75° from Figure 2.11 for the 6111 welds under high-cycle loading conditions.

Here, we adopt the kinked fatigue crack growth model with consideration of the local stress intensity factor solutions for finite kinked cracks as discussed in details in Lin et al. [12-15]. It should be emphasized that the theoretical solutions for the global stress intensity factors K_I and K_{II} for the main cracks used in Lin et al. [12-15] are based on the works of Lin et al. [23] and Zhang [25] for resistance spot welds in lap-shear specimens, respectively. Due to the complex geometries of the 5754 and 6111 spot friction welds, three-dimensional finite element analyses based on the micrographs of the cross sections along the symmetry planes of the 5754 and 6111 spot friction welds shown in Figures 2.1(a) and 2.2(a), respectively, were employed to obtain the accurate global stress intensity factors along the crack front of the weld nuggets. The global stress intensity factors K_I and K_{II} solutions at the critical locations obtained from the finite element analyses are then used to estimate the fatigue lives of both types of spot friction welds. The local stress intensity factor

solutions k_I and k_{II} for the finite kinked cracks in this investigation are determined as in Lin et al. [12-15] with consideration of the finite kink length.

2.6.2. A structural stress model

Radaj [26] and Radaj and Zhang [27-29] established the foundation to use the structural stresses to determine the stress intensity factors for spot welds under various types of loading conditions. Zhang [25,30] presented closed-form stress intensity factor solutions at the critical locations of spot welds in various types of specimens based on the analytical stress solutions for a plate with a rigid inclusion under various types of loading conditions, and correlated the solutions with the experimental results. It should be emphasized that the authors mentioned above used the structural stresses to estimate the stress intensity factor solutions at the critical locations of spot welds to correlate with the experimental results under cyclic loading conditions. In the following, we present a structural stress model based on the closed-form structural stress solutions at the critical locations of the welds and the experimental stress-life fatigue data to estimate the fatigue lives of the spot friction welds in lap-shear specimens.

Lin and Pan [21] recently derived closed-form structural stress solutions for spot welds under lap-shear loading conditions based on the stress function approach and the Kirchoff plate theory for linear elastic materials. The closed-form structural stress solutions for spot welds under lap-shear loading conditions were developed from the analytical closed-form stress solutions for a plate with a rigid inclusion subjected to a resultant lap-shear load. This resultant lap-shear load was decomposed into four

types of symmetric and anti-symmetric loads of counter bending, central bending, in-plane shear and tension. The total structural stress σ_{total} at the critical locations of a spot weld in a lap-shear specimen under a resultant shear load F is presented here as a function of the radius a of the spot weld (idealized as a rigid inclusion), the relevant sheet thickness t , the half width b of the lap-shear specimen and the Poisson's ratio ν as

$$\sigma_{total} = \frac{-3F}{8btXY} \left[2b^2X + 4Y(a^4b^4 + b^8) \right] + \frac{3F}{2\pi at} + \frac{F}{2\pi at} + \frac{F}{4bt} \left[\frac{1}{1+\nu} - \frac{2}{\nu-3} \right] \quad (2.1)$$

where X and Y are defined as

$$X = (-1+\nu)(a^4 + b^4)^2 - 4a^2b^6(1+\nu) \quad (2.2)$$

$$Y = a^2(-1+\nu) - b^2(1+\nu) \quad (2.3)$$

Note that the four terms on the right hand side of Equation (2.1) correspond to the structural stresses at the critical locations for a finite plate with a rigid inclusion under counter bending, central bending, in-plane shear and tension loading conditions, respectively. Note also that Lin and Pan [21] idealized the spot weld nugget as a rigid inclusion and assumed that the inclusion is perfectly bonded to the neighboring plate material in their theoretical models to derive Equation (2.1). Note that the geometries of the spot friction welds shown in Figures 2.1(a) and 2.2(a) are slightly different but in general similar to those of resistance spot welds. Note also that the material strength of the stir zone in the weld nugget of the spot friction weld should be much larger than that of the base material due to the small grain size as reported in Lin et al. [5]. As discussed earlier, the dominant kinked fatigue cracks were initiated at the critical locations a and b . Therefore, Equation (2.1) can be adopted to estimate the

structural stress range at the critical locations a and b of the spot friction welds for a given load range. By using Equation (2.1) for the structural stress range at the critical locations a and b for the two-dimensional crack model and the experimental stress-life fatigue data of the aluminum 5754-O and 6111-T4 sheets, we can estimate the fatigue lives of the 5754 and 6111 spot friction welds in lap-shear specimens, respectively.

2.7. Fatigue life estimations

As discussed in Lin et al. [12-15], the spot weld radius a , the relevant sheet thickness t , the half width b of the lap-shear specimen, the Poisson's ratio ν and the kinked angle α are used to determine the global and local stress intensity factor solutions for the dominant kinked fatigue crack, and the material constants C and m in the Paris law are needed to estimate the fatigue lives of the spot friction welds in lap-shear specimens based on the kinked fatigue crack growth model. However, due to the complex geometries of the 5754 and 6111 spot friction welds, three-dimensional finite element analyses are used to determine the global stress intensity factors K_I and K_{II} solutions at the critical locations of the welds. As indicated in Equation (2.1), the spot weld radius a , the relevant sheet thickness t , the half width b of the lap-shear specimen, the Poisson's ratio ν and the stress-life fatigue data are needed to estimate the fatigue lives of the spot friction welds in lap-shear specimens based on the structural stress model. It should be emphasized that the relevant sheet thickness t is the thickness of the sheet through which the dominant kinked fatigue crack propagates.

Figure 2.13(a) shows the experimental results and fatigue life estimations based on the kinked fatigue crack growth model and the structural stress model for the 5754 spot friction welds made by the concave tool in lap-shear specimens. The fatigue life estimations shown in Figure 2.13(a) were obtained from the reduced thickness of the upper sheet $t = 1.75$ mm under the tool shoulder indentation, the weld nugget radius $a = 3.6$ mm based on the micrograph shown in Figure 2.1(a), the half width $b = 12.7$ mm of the lap-shear specimen and the Poisson's ratio $\nu = 0.33$. For the kinked fatigue crack growth model, the kink angle $\alpha_2 = 69^\circ$, estimated from the micrographs shown in Figures 2.6 and 2.7, was used to estimate the fatigue lives of the 5754 welds. Since the material constants for the Paris law for aluminum 5754-O sheets are not available, the material constants $C = 2.0244 \times 10^{-9} \frac{\text{mm/cycle}}{(\text{MPa} \sqrt{\text{m}})^m}$ and $m = 4.64$ for aluminum 5083-O sheets, determined from Figure 2.5.24 in Campbell et al. [31], were used to estimate the fatigue lives of the 5754 welds. For the structural stress model, the experimental stress-life fatigue data of aluminum 5754-O sheets supplied by Friedman [32] were used. As shown in Figure 2.13(a), the estimated fatigue lives of the 5754 spot friction welds in lap-shear specimens based on the kinked fatigue crack growth model and the structural stress model agree well with the experimental results.

Figure 2.13(b) shows the experimental results and fatigue life estimations based on the kinked fatigue crack growth model and the structural stress model for the 6111 spot friction welds made by the flat tool in lap-shear specimens. The fatigue life estimations shown in Figure 2.13(b) were obtained from the weld nugget radius $a = 3.35$ mm based on the micrograph shown in Figure 2.2(a), the half width

$b = 12.7$ mm of the lap-shear specimen and the Poisson's ratio $\nu = 0.33$. For the 6111 welds, the dominant kinked fatigue crack propagates through the upper sheet thickness (with a reduced thickness) under low-cycle loading conditions and through the lower sheet thickness under high-cycle loading conditions as discussed earlier. The reduced thickness of the upper sheet of $t = 0.85$ mm under the tool shoulder indentation and the thickness of the lower sheet $t = 1.04$ mm were therefore used as the relevant sheet thickness t in both fatigue life estimation models for the 6111 welds under low-cycle and high-cycle loading conditions, respectively. For the kinked fatigue crack growth model, the kink angles $\alpha_2 = \alpha_1 = 75^\circ$, estimated from the micrographs shown in Figures 2.10 and 2.11, for the 6111 welds under low-cycle and high-cycle loading conditions, respectively, were used to estimate the fatigue lives of the 6111 welds. Since the material constants for the Paris law for aluminum 6111-T4 sheets are not available, the material constants $C = 1.35 \times 10^{-7} \frac{\text{mm/cycle}}{(\text{MPa} \sqrt{\text{m}})^m}$ and $m = 2.55$ for aluminum 6014-T4 sheets (Bergner and Zouhar [33]) were used to estimate the fatigue lives of the 6111 spot friction welds as in Lin et al. [12-15]. For the structural stress model, the experimental stress-life fatigue data of baked aluminum 6111-T4 sheets supplied by Friedman [32] were used. It should be noted that the fatigue life estimations in Figure 2.13(b) are plotted as thin lines and thick lines that correspond to the estimated fatigue lives of the 6111 welds under low-cycle and high-cycle loading conditions, respectively, due to the different values of the relevant sheet thickness t . Note that the load range for the transition of the failure mode from low-cycle fatigue to high-cycle fatigue is about 1.99 kN as shown in Figures 2.3(c) and 2.13(b). As shown in Figure 2.13(b), the estimated fatigue lives of

the 6111 spot friction welds based on the kinked fatigue crack growth model and the structural stress model agree well with the experimental results.

2.8. Discussions

Figure 2.14 shows an optical micrograph of the cross section along the symmetry plane of a partially failed 5754 spot friction weld made by the concave tool under a load range of 3.38 kN at the fatigue life of 3.6×10^2 cycles which is 90% of the fatigue life of 4.0×10^2 cycles of another failed weld under the same load range. Note that this spot friction weld was not separated. It should be noted that the specimen with this partially failed weld was tested under the applied load range with a maximum load of 4.225 kN, which is about 97% of the average failure load of the 5754 lap-shear specimens under quasi-static loading conditions. As shown in Figure 2.14, fatigue cracks, marked as crack 1 and crack 2, appear to emanate from the original crack tips of the welds.

Two local kinked cracks, marked as crack 2a and crack 2b, appear to emanate from kinked fatigue crack 2 after fatigue crack 2 propagates partially into the upper sheet thickness. As shown in the figure, crack 2a has a tendency to propagate through the right portion of the nugget while crack 2b has a tendency to propagate into the upper sheet thickness (with a reduced thickness). Under this very high applied load range, during the final stage of the specimen failure, crack 2a can grow faster than crack 2b and the weld can be separated in the failure mode with the nearly flat fracture surface through the nugget (similar to the failure mode shown in Figure 2.5), or crack 2b can grow faster than crack 2a and the weld can be separated in the failure

mode with the fracture surfaces through the upper sheet thickness and the nugget (similar to the failure mode shown in Figure 2.6(b)). Therefore, this load range and this fatigue life can be considered as the load range and the fatigue life corresponding to the transition of the failure mode from the failure mode with the nearly flat fracture surface through the nugget to the failure mode with the fracture surfaces through the upper sheet thickness and the nugget. A micrograph indicating the similar transition of the failure mode was also observed for the 6111 welds and is not discussed here. Note that the load ranges and the fatigue lives for the transitions of the failure mode from the failure mode with the fracture surfaces through the upper sheet thickness and the nugget under low-cycle loading conditions to the failure mode with the fracture surfaces through the upper and lower sheet thicknesses under high-cycle loading conditions for the 5754 and 6111 welds are presented in Figure 2.3(c).

It should be noted that for the kinked fatigue crack growth model, we used the global stress intensity factor solutions obtained from the finite element analyses for the 5754 and 6111 welds based on the micrographs shown in Figures 2.1(a) and 2.2(a), respectively. In general, finite element computations are also needed to determine the accurate local stress intensity factor solutions for the kinked cracks emanating from the original crack tips of the welds with the exact weld geometries and loading conditions. However, the computational effort is quite extensive since the computations are three-dimensional in nature and the number of the cases for the weld geometries and the loading conditions are quite large. Therefore, the local stress intensity factor solutions k_I and k_{II} for finite kinked cracks in this investigation were determined as in Lin et al. [12-15] with consideration of the finite kink length. This

model is therefore approximate in nature by considering that the geometry of the spot friction welds is different from that of the resistance spot welds. Note also that no effort is attempted to select the material constants C and m in the Paris law to fit the experimental results. Since the material constants C and m of aluminum 5754-O and 6111-T4 sheets are not available, the material constants C and m of aluminum 5083-O and 6014-T4 sheets were used to estimate the fatigue lives of the 5754 and 6111 welds, respectively. When the material constants of aluminum 5754-O and 6111-T4 sheets are available, it will be straightforward to estimate the fatigue lives of these welds.

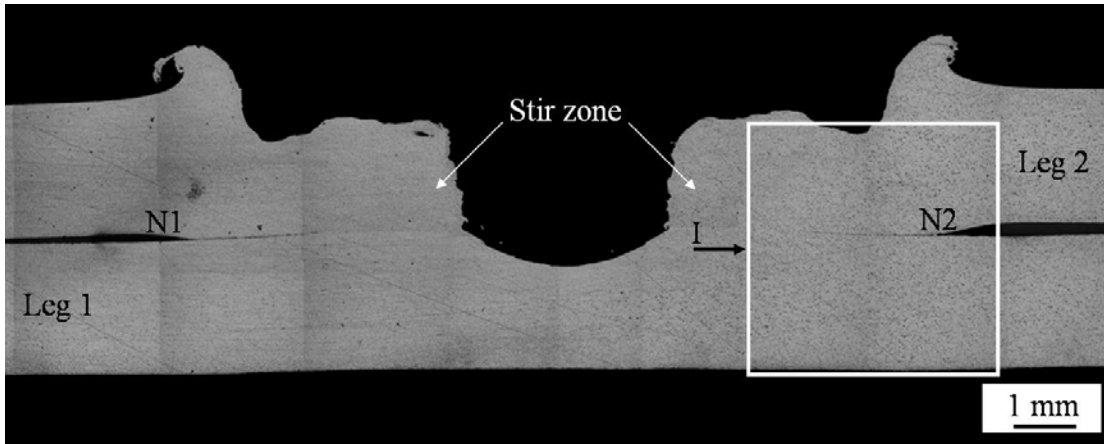
It should be emphasized that the closed-form structural stress solutions used in the structural stress model were obtained from a linear elastic analysis. Under high-cycle loading conditions, the estimated structural stress ranges based on Equation (2.1) are smaller than $2\sigma'_0$ for both types of welds where σ'_0 represents the initial cyclic yield strength of the corresponding sheet materials. The cyclic behavior of materials at the critical locations a and b of the welds can be therefore considered as linear elastic under high-cycle loading conditions. Under low-cycle loading conditions, the estimated structural stress ranges based on Equation (2.1) can be as high as $2.65\sigma'_0$ and $2.53\sigma'_0$ for the 5754 and 6111 welds, respectively. Neuber's type of life estimation methods can be used to improve the life estimations since the life estimations are based on the experimental stress-life fatigue data here. As shown in Figures 2.13(a) and 2.13(b), the structural stress model appears to give good estimations of the fatigue lives of both types of spot friction welds in lap-shear specimens without detailed information on the initiation and propagation of the

kinked cracks emanating from the original crack tips of the welds under cyclic loading conditions. Note also that the structural stress was used to estimate the stress intensity factor solutions at the critical locations of the spot welds to correlate with the experimental results under cyclic loading conditions (Zhang [25,30]). The effects of the mean stress intensity factors on the fatigue lives of the welds may not be significant. Therefore, the mean structural stress has not been considered in the structural stress model. Further investigation is needed to fully investigate the effects of the mean stress in the structural stress model.

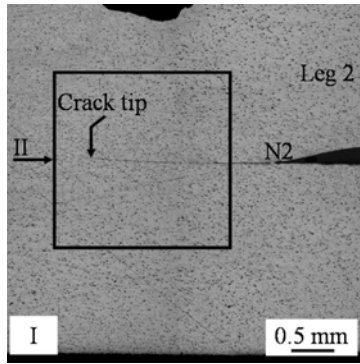
2.9. Conclusions

Fatigue behavior of aluminum 5754-O and 6111-T4 spot friction welds in lap-shear specimens is investigated based on experimental observations and two fatigue life estimation models. Optical micrographs of the 5754 and 6111 welds made by a concave tool and a flat tool, respectively, before and after failure under quasi-static and cyclic loading conditions are examined. The micrographs show that the failure modes of the 5754 and 6111 welds under quasi-static and cyclic loading conditions are quite different. Under quasi-static loading conditions, both types of welds mainly fail from the nearly flat fracture surface through the nugget. Under low-cycle loading conditions, both types of welds mainly fail from the kinked crack through the upper sheet thickness and the fracture surface through the nugget. Under high-cycle loading conditions, both types of welds mainly fail from the kinked cracks through the upper and lower sheet thicknesses. A kinked fatigue crack growth model based on the stress intensity factor solutions for finite kinked cracks and a structural stress

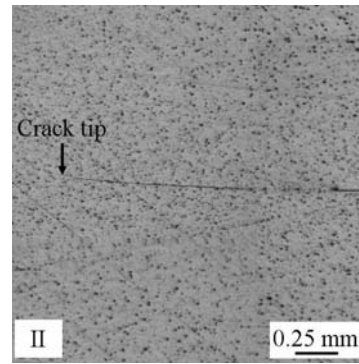
model based on the closed-form structural stress solutions at the critical locations of the welds are adopted to estimate the fatigue lives of both types of welds. The fatigue life estimations based on the kinked fatigue crack growth model and the structural stress model appear to agree well with the experimental results for both types of welds.



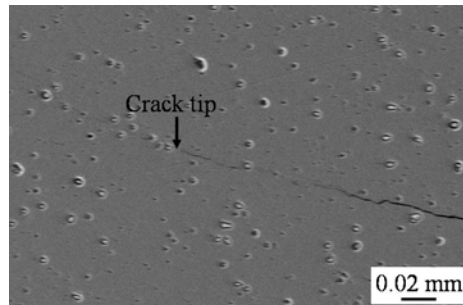
(a)



(b)

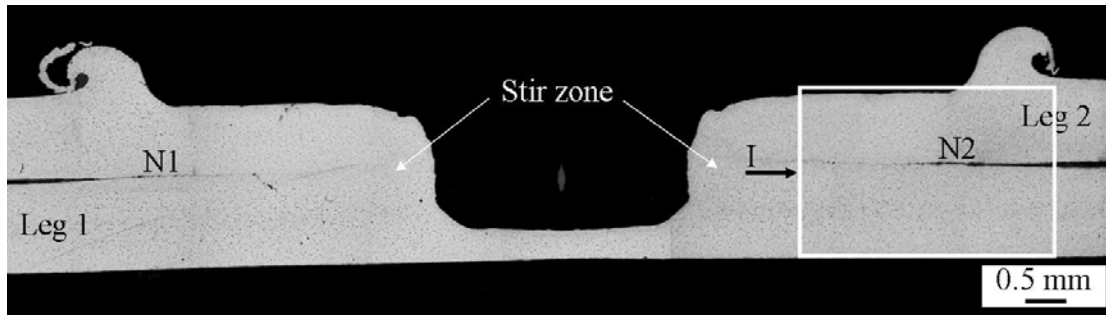


(c)

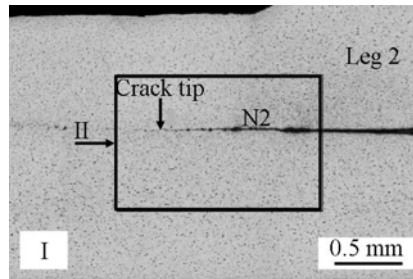


(d)

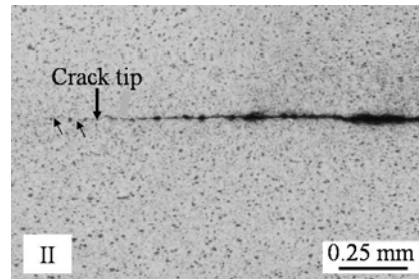
Figure 2.1 (a) An optical micrograph of the cross section along the symmetry plane of a 5754 spot friction weld made by the concave tool before testing, (b) a close-up optical micrograph of region I, (c) a close-up optical micrograph of region II, (d) a close-up scanning electron micrograph of the crack tip region as shown in (c).



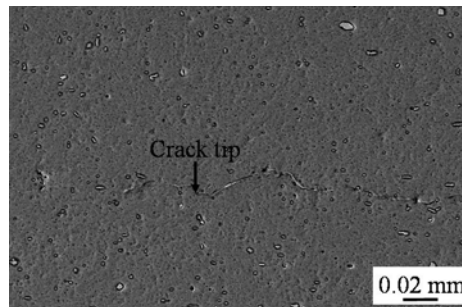
(a)



(b)

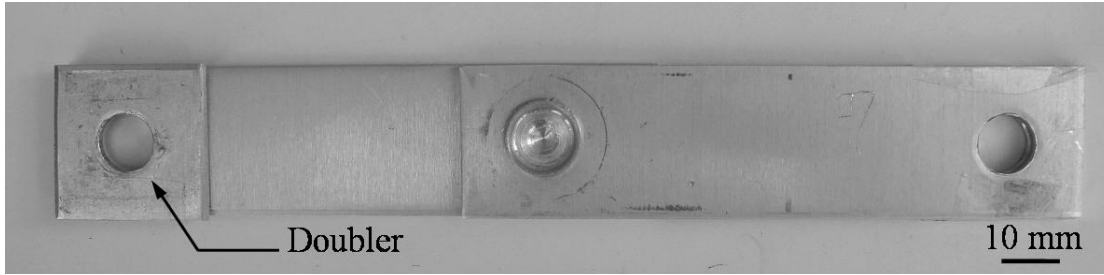


(c)

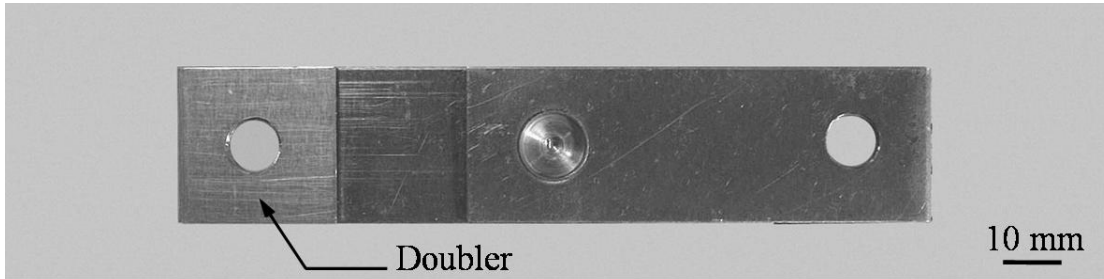


(d)

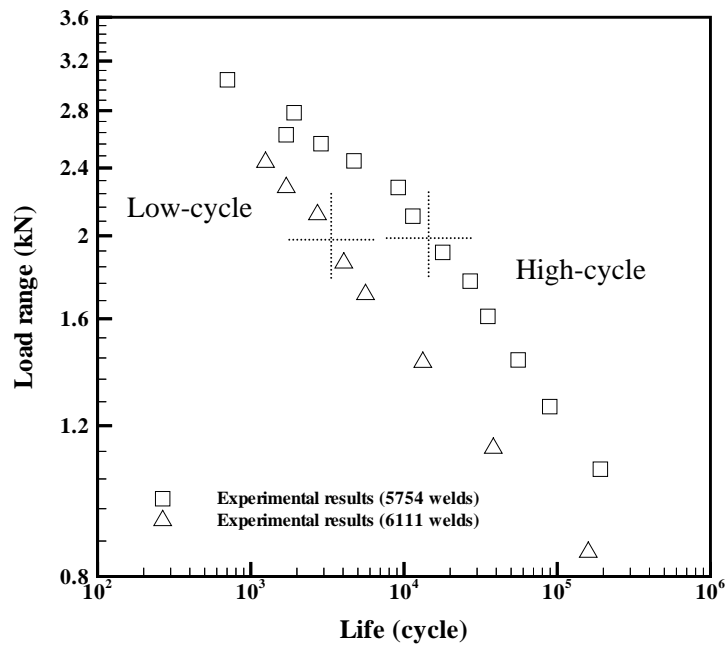
Figure 2.2 (a) An optical micrograph of the cross section along the symmetry plane of a 6111 spot friction weld made by the flat tool before testing, (b) a close-up optical micrograph of region I, (c) a close-up optical micrograph of region II, (d) a close-up scanning electron micrograph of the crack tip region as shown in (c).



(a)

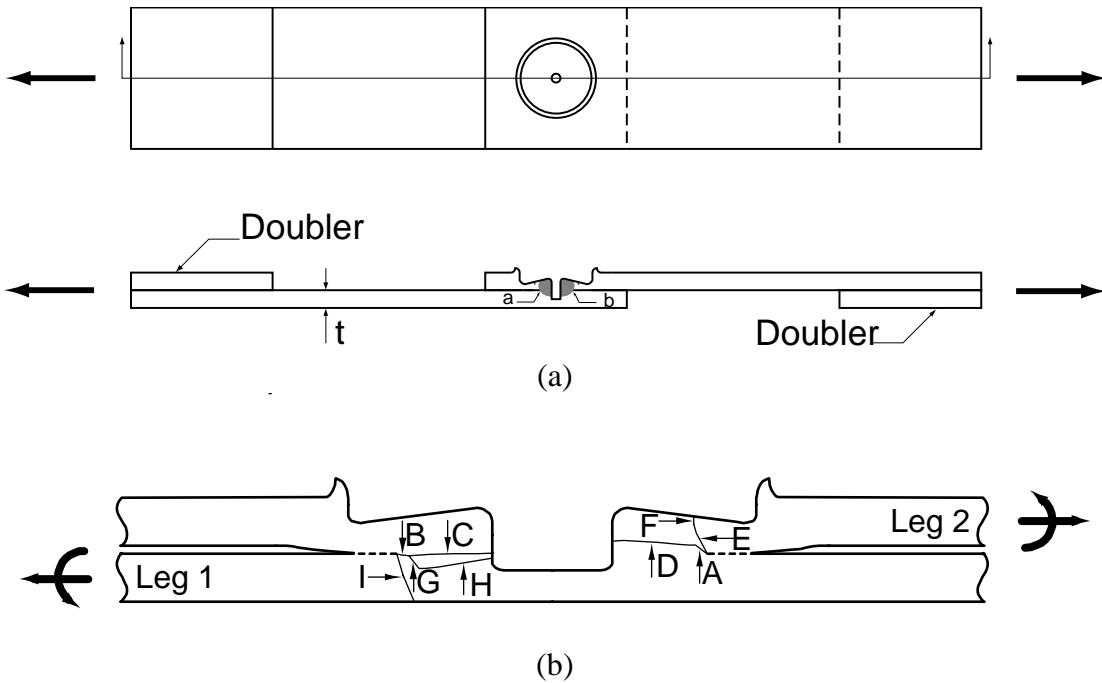


(b)



(c)

Figure 2.3 (a) A lap-shear specimen with a 5754 spot friction weld made by the concave tool, (b) a lap-shear specimen with a 6111 spot friction weld made by the flat tool, (c) experimental results for the 5754 spot friction welds made by the concave tool and the 6111 spot friction welds made by the flat tool in lap-shear specimens under cyclic loading conditions.



		Failure mode
Quasi-static		A, B → C, D
Low-cycle		E → F → Circumferential crack B → G → H, D
High-cycle	Higher load ranges	E → F → Circumferential crack I → Transverse through crack
	Lower load ranges	E → F → Transverse through crack I → Transverse through crack

(c)

Figure 2.4 (a) A schematic plot of a lap-shear specimen with a 5754 spot friction weld made by the concave tool with the sheet thickness $t = 2$ mm under applied resultant shear loads (shown as the bold arrows), (b) a schematic plot of the cross section along the symmetry plane of the 5754 spot friction weld made by the concave tool, (c) failure modes of the 5754 spot friction welds in lap-shear specimens under quasi-static, low-cycle and high-cycle loading conditions.

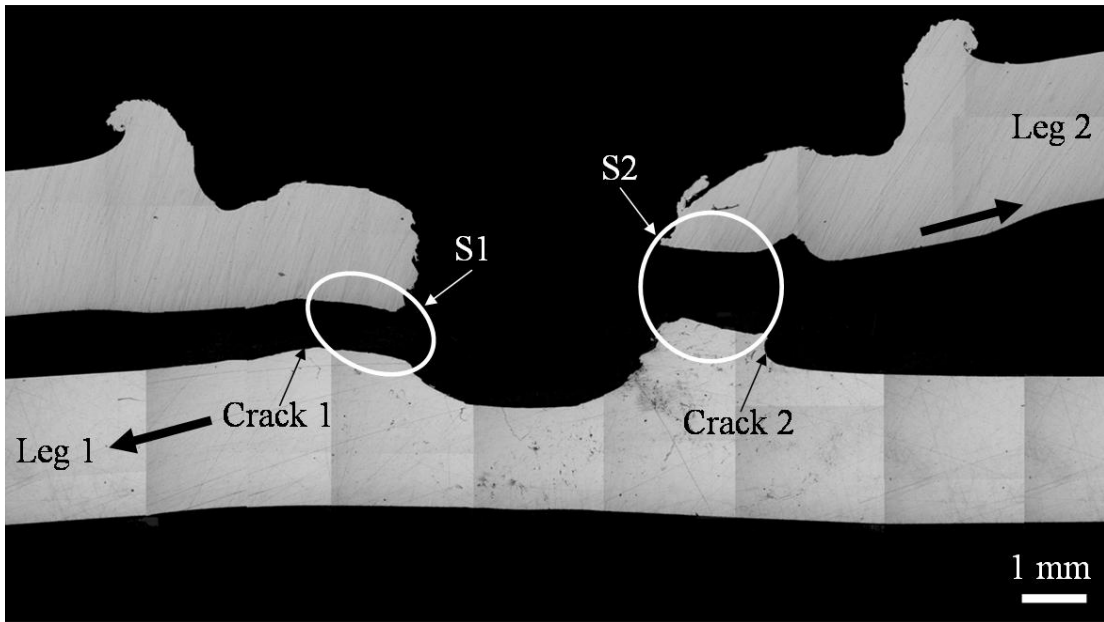
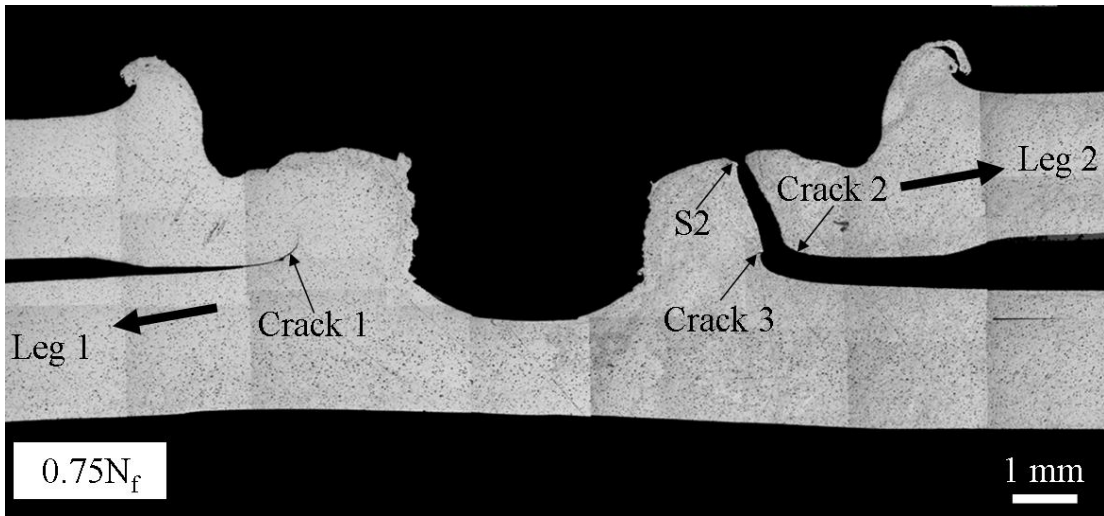
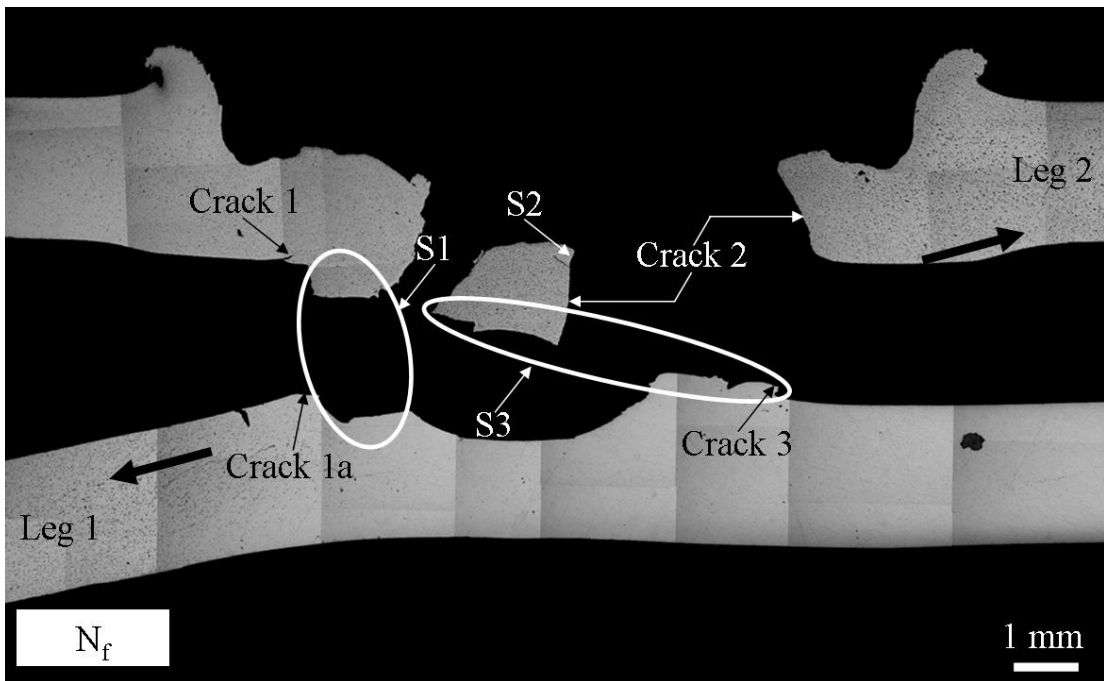


Figure 2.5 An optical micrograph of the cross section along the symmetry plane of a failed 5754 spot friction weld made by the concave tool in a lap-shear specimen under quasi-static loading conditions.

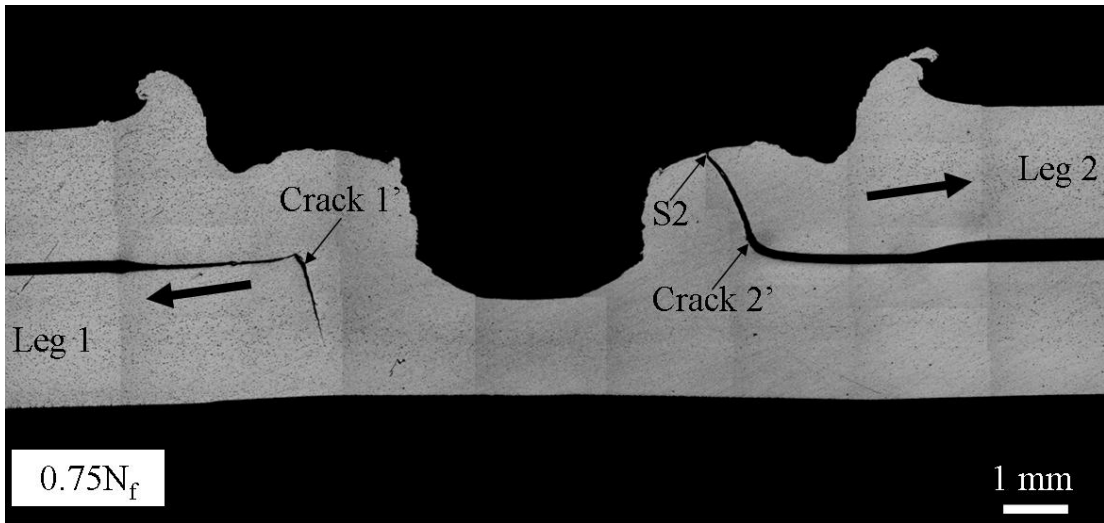


(a)

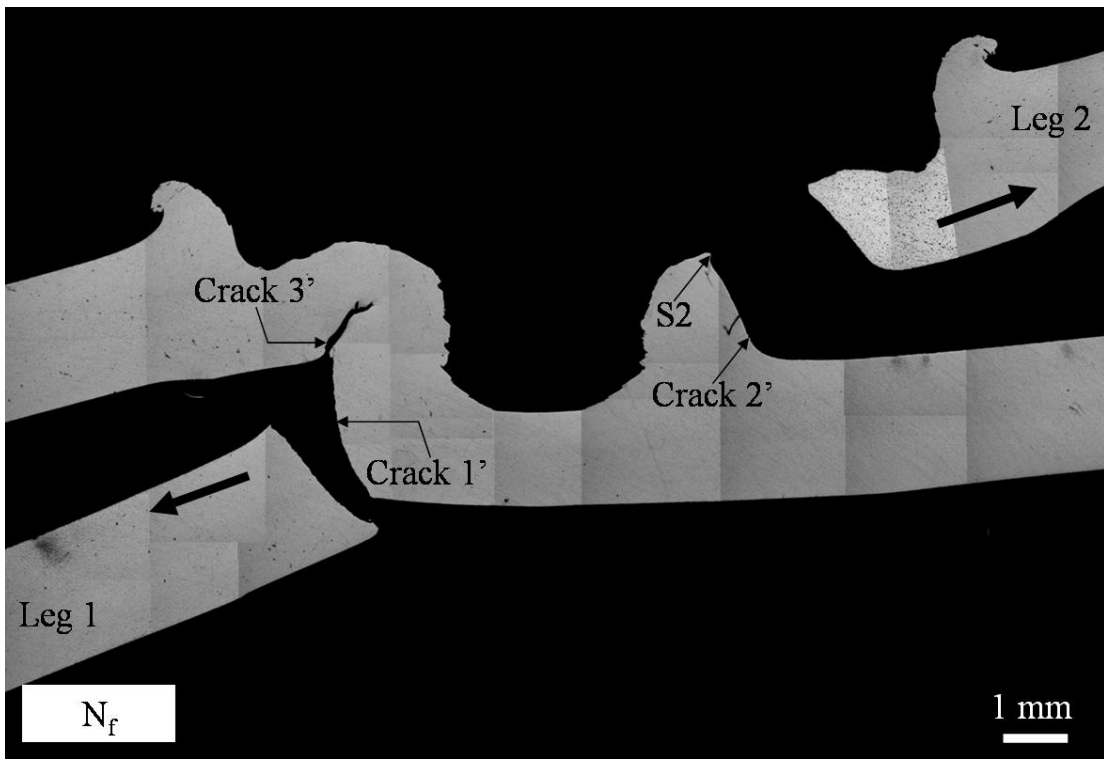


(b)

Figure 2.6 Optical micrographs of the cross sections along the symmetry plane of (a) a partially failed 5754 spot friction weld made by the concave tool at the fatigue life of 3.5×10^3 cycles, (b) a failed 5754 spot friction weld made by the concave tool at the fatigue life of 4.7×10^3 cycles under a load range of 2.45 kN.

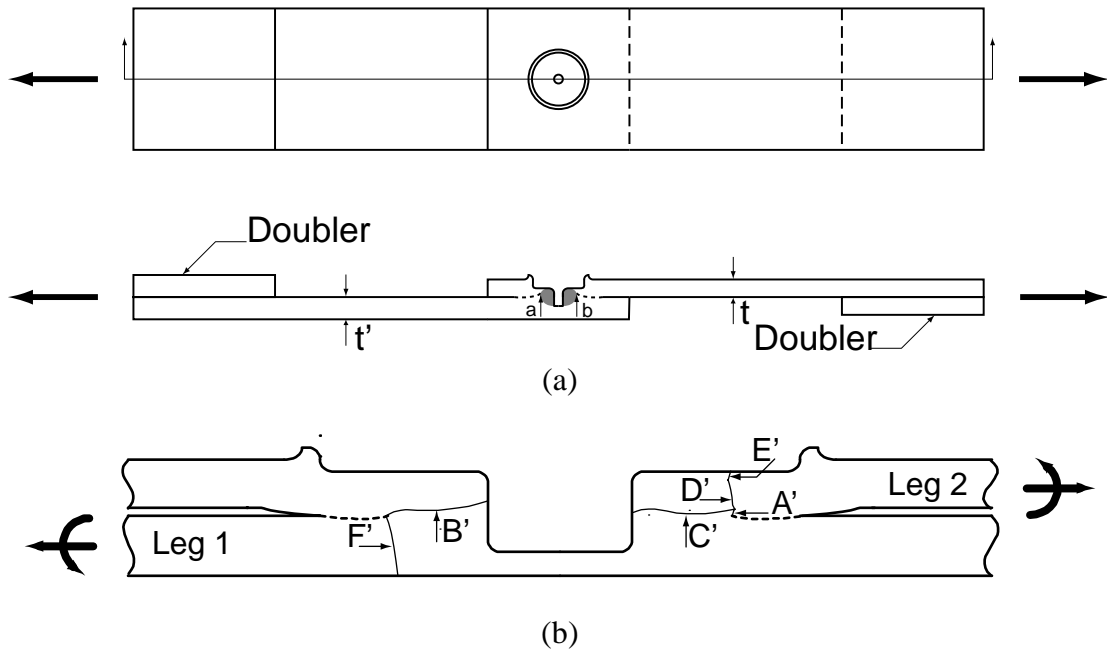


(a)



(b)

Figure 2.7 Optical micrographs of the cross sections along the symmetry plane of (a) a partially failed 5754 spot friction weld made by the concave tool at the fatigue life of 4.2×10^4 cycles and (b) a failed 5754 spot friction weld made by the concave tool at the fatigue life of 5.5×10^4 cycles under a load range of 1.43 kN.



		Failure mode
Quasi-static		A', B' → C'
Low-cycle		D' → E' → Circumferential crack F' → B'
High-cycle	Higher load ranges	D', F' → Circumferential cracks
	Lower load ranges	D', F' → Transverse through cracks

(c)

Figure 2.8 (a) A schematic plot of a lap-shear specimen with a 6111 spot friction weld made by the flat tool with the upper sheet thickness of $t = 0.94$ mm and the lower sheet thickness $t' = 1.04$ mm under applied resultant shear loads (shown as the bold arrows), (b) a schematic plot of the cross section along the symmetry plane of the 6111 spot friction weld made by the flat tool, (c) failure modes of the 6111 spot friction welds in lap-shear specimens under quasi-static, low-cycle and high-cycle loading conditions.

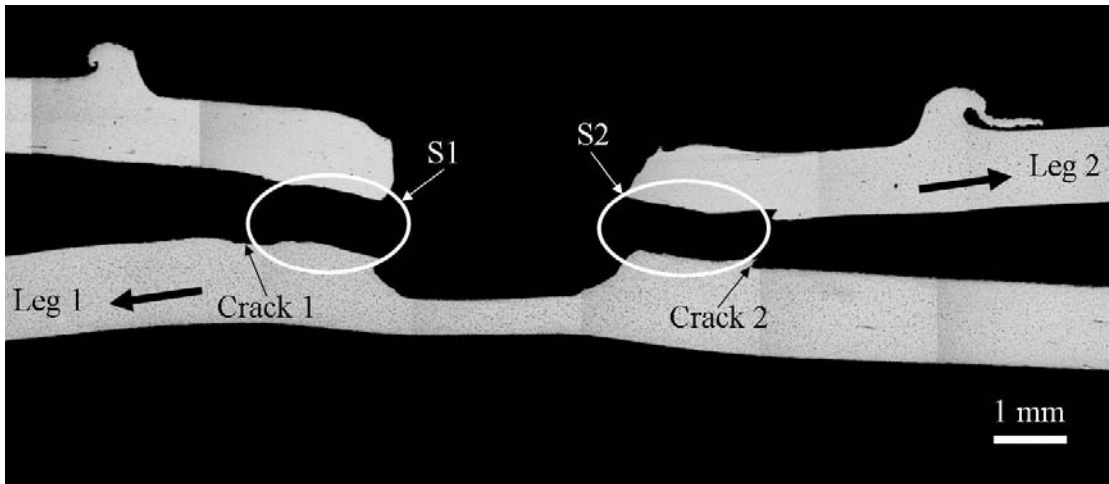
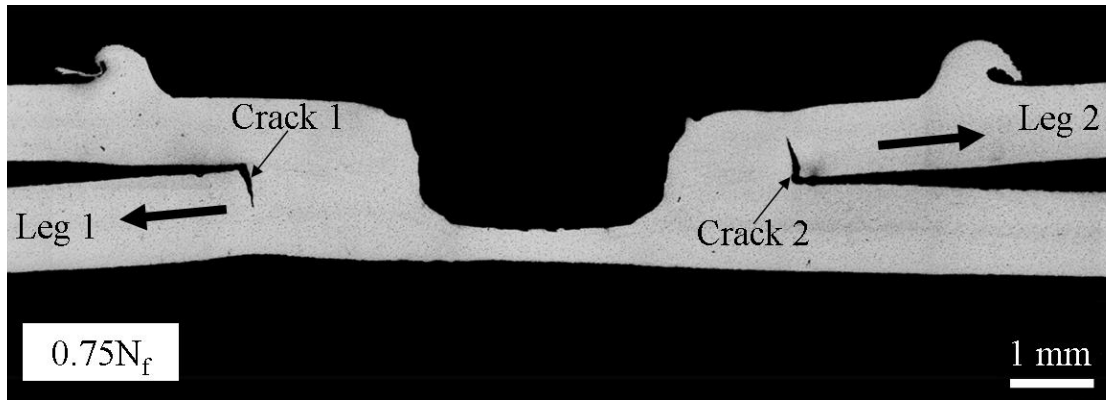
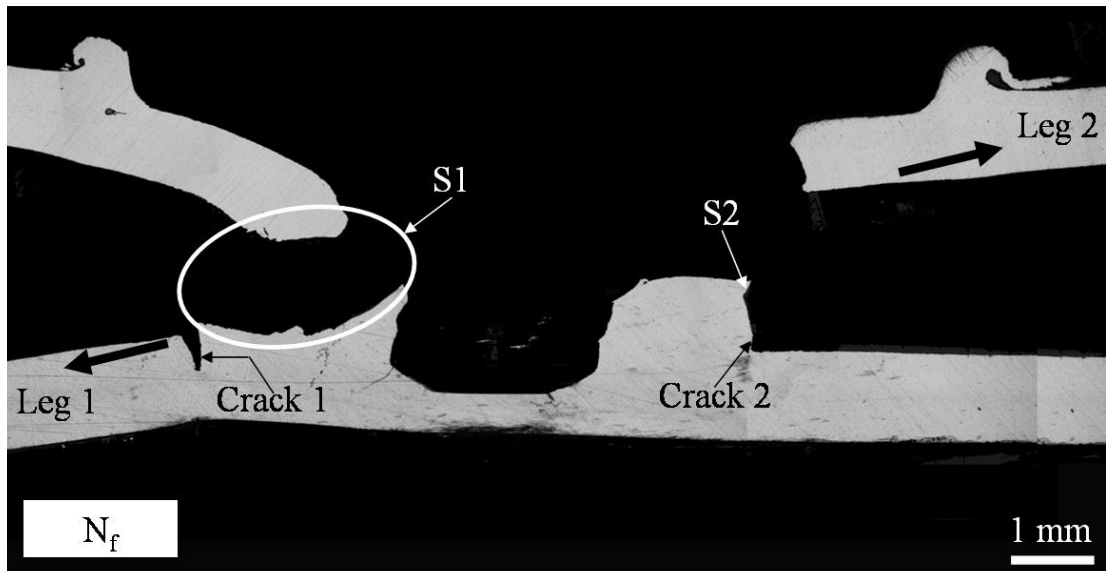


Figure 2.9 An optical micrograph of the cross section along the symmetry plane of a failed 6111 spot friction weld made by the flat tool in a lap-shear specimen under quasi-static loading conditions.

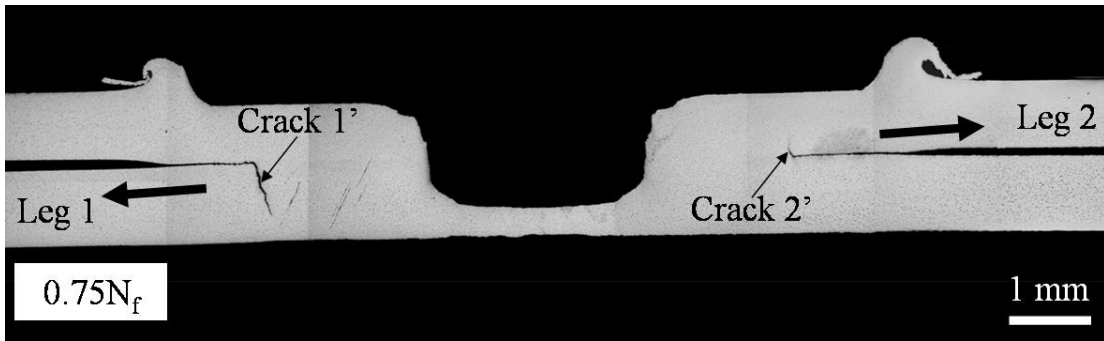


(a)

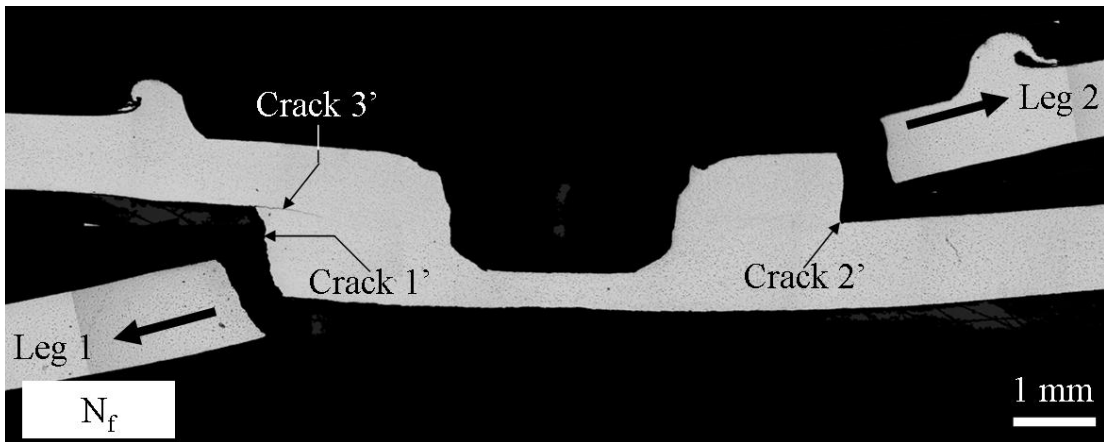


(b)

Figure 2.10 Optical micrographs of the cross sections along the symmetry plane of (a) a partially failed 6111 spot friction weld made by the flat tool at the fatigue life of 2.0×10^3 cycles, (b) a failed 6111 spot friction weld made by the flat tool at the fatigue life of 2.7×10^3 cycles under a load range of 2.13 kN.



(a)



(b)

Figure 2.11 Optical micrographs of the cross sections along the symmetry plane of (a) a partially failed 6111 spot friction weld made by the flat tool at the fatigue life of 1.2×10^5 cycles, (b) a failed 6111 spot friction weld made by the flat tool at the fatigue life of 1.6×10^5 cycles under a load range of 0.85 kN.

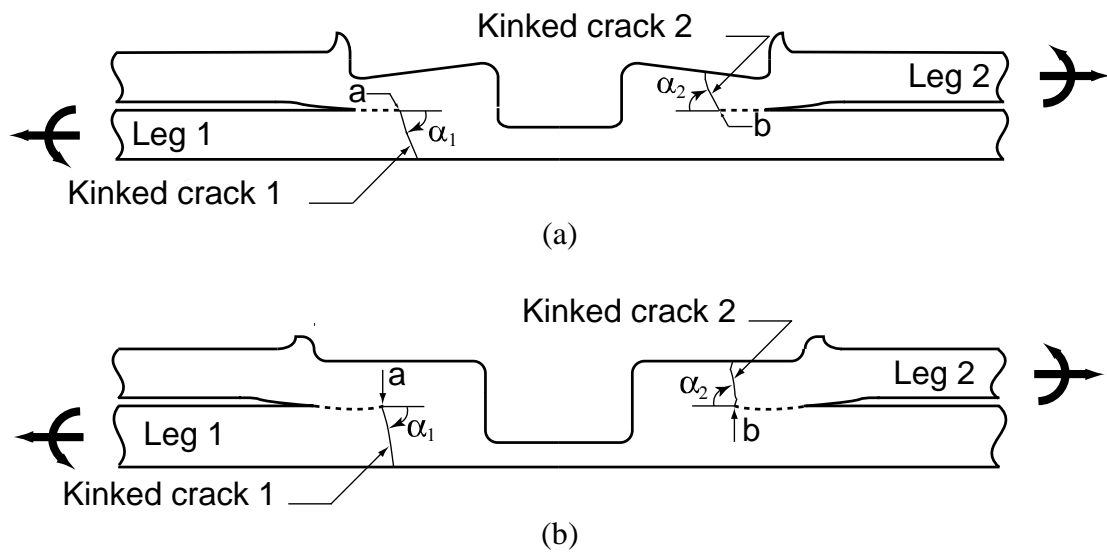
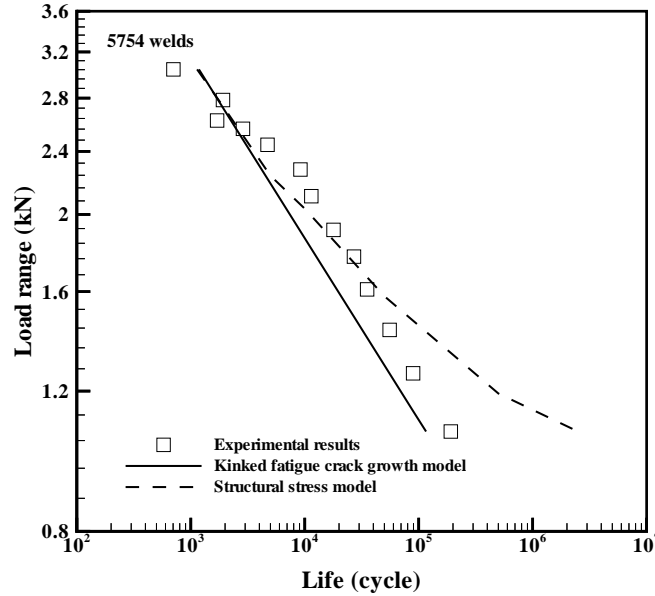
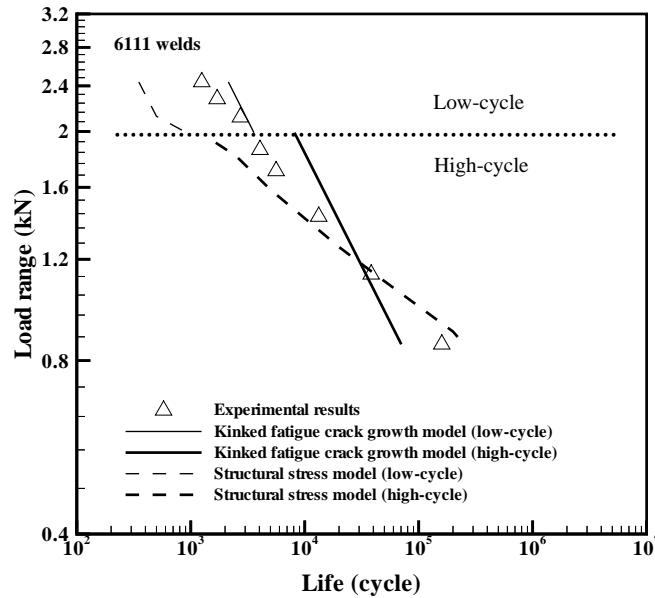


Figure 2.12 (a) A schematic plot of the cross section along the symmetry plane of the 5754 spot friction weld under statically equivalent combined tensile and bending loads (shown as the bold arrows), (b) a schematic plot of the cross section along the symmetry plane of the 6111 spot friction weld under statically equivalent combined tensile and bending loads (shown as the bold arrows).



(a)



(b)

Figure 2.13 (a) Experimental results and fatigue life estimations for the 5754 spot friction welds made by the concave tool in lap-shear specimens, (b) experimental results and fatigue life estimations for the 6111 spot friction welds made by the flat tool in lap-shear specimens. The symbols represent the experimental results. The solid and dash lines represent the fatigue life estimations based on the kinked fatigue crack growth model and the structural stress model, respectively.

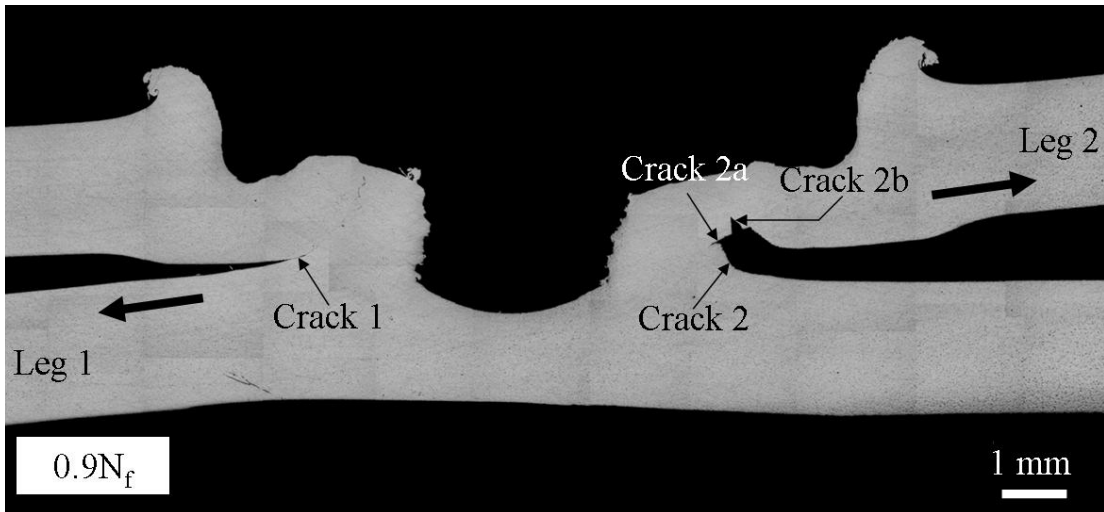


Figure 2.14 An optical micrograph of the cross section along the symmetry plane of a partially failed 5754 spot friction weld made by the concave tool under a load range of 3.38 kN at the fatigue life of 3.6×10^2 cycles which is 90% of the fatigue life of 4.0×10^2 cycles of another failed weld under the same load range.

References

- [1] Thornton PH, Krause, AR, Davies, R G. The aluminum spot weld. *Welding J* 1996;75:101s-108s.
- [2] Gean A, Westgate SA, Kucza JC, Ehrstrom JC. Static and fatigue behavior of spot-welded 5182-O aluminum alloy sheet. *Welding J* 1999;78:80s-86s.
- [3] Sakano R, Murakami K, Yamashita K, Hyoe T, Fujimoto M, Inuzuka M, Nagao Y, Kashiki H. Development of spot FSW robot system for automobile body members. In: *Proceedings of the 3rd international symposium of friction stir welding*, Kobe, Japan, September 27-28, 2001.
- [4] Iwashita T. Method and apparatus for joining. US Patent 6601751 B2, August 5, 2003.
- [5] Lin P-C, Lin S-H, Pan J, Pan T, Nicholson JM, Garman, MA. Microstructures and failure modes of spot friction welds in lap-shear specimens of aluminum 6111-T4 sheets. SAE Technical Paper No. 2004-01-1330, Society of Automotive Engineers, Warrendale, PA: 2004.
- [6] Pan T, Joaquin A, Wilkosz DE, Reatherford L, Nicholson JM. Spot friction welding for sheet aluminum joining. In: *Proceedings of the 5th international symposium of friction stir welding*, Metz, France, September 14-16, 2004.
- [7] Fujimoto M, Inuzuka M, Nishio M, Nakashima Y. Development of friction spot joining (Report 1) - Cross sectional structures of friction spot joints. *The National Meeting of Japan Welding Society*, No. 74, 2004, pp. 4-5.
- [8] Fujimoto M, Inuzuka M, Nishio M, Nakashima Y. Development of friction spot joining (Report 2) - Mechanical properties of friction spot joints. *The National Meeting of Japan Welding Society*, No. 74, 2004, pp. 6-7.
- [9] Hinrichs JF, Smith CB, Orsini BF, DeGeorge RJ, Smale BJ, Ruehl PC. Friction stir welding for the 21st century automotive industry. In: *Proceedings of the 5th international symposium of friction stir welding*, Metz, France, September 14-16, 2004.
- [10] Mitlin D, Radmilovic V, Pan T, Chen J, Feng Z, Santella ML. Structure-properties relations in spot friction welded (also known as friction stir spot welded) 6111 aluminum. *Mater Sci Eng A* 2006;441:79-96.
- [11] Tran V-X, Lin P-C, Pan J, Pan T, Tyan T. Failure loads of aluminum 6111 spot friction welds under quasi-static and dynamic loading conditions. SAE Technical Paper No. 2007-01-0983, Society of Automotive Engineers, Warrendale, PA:2007.

- [12] Lin P-C, Pan J, Pan T. Fracture and fatigue mechanisms of spot friction welds in lap-shear specimens of aluminum 6111 sheets. SAE Technical Paper No. 2005-01-1247, Society of Automotive Engineers, Warrendale, PA:2005.
- [13] Lin P-C, Pan J, Pan T. Fatigue failures of aluminum 6111 spot friction welds under cyclic loading conditions. SAE Technical Paper No. 2006-01-1207, Society of Automotive Engineers, Warrendale, PA:2006.
- [14] Lin P-C, Pan J, Pan T. Failure modes and fatigue life estimations of spot friction welds in lap-shear specimens of aluminum 6111-T4 sheets, Part 1: Welds made by a concave tool. *Int J Fatigue* 2008;30:74-89.
- [15] Lin P-C, Pan J, Pan T. Failure modes and fatigue life estimations of spot friction welds in lap-shear specimens of aluminum 6111-T4 sheets, Part 2: Welds made by a flat tool. *Int J Fatigue* 2008;30:90-105.
- [16] Pan T. Friction stir spot welding (FSSW) - A literature review. SAE Technical Paper No. 2007-01-1702, Society of Automotive Engineers, Warrendale, PA:2007.
- [17] Tozaki Y, Uematsu Y, Tokaji K. Effect of welding condition on tensile strength of dissimilar friction stir spot welds between different aluminum alloys. In: Proceedings of 6th international symposium on friction stir welding, Saint-Sauveur, Nr Montreal, Canada, October 10 - 13, 2006.
- [18] Su P, Gerlich A, North TH, Bendzsak GJ. Intermixing in dissimilar friction stir spot welds. *Metall Mater Trans A* 2007;38A:584-595.
- [19] Tran V-X, Pan J, Pan T. Effects of processing time on strengths and failure modes of dissimilar spot friction welds between aluminum 5754-O and 7075-T6 sheets. SAE Technical Paper No. 2008-01-1138, Society of Automotive Engineers, Warrendale, PA:2008.
- [20] Kaufman J-G. Introduction to Aluminum Alloys and Tempers. The Materials Information Society - ASM International, Materials Park, OH:2000.
- [21] Lin P-C, Pan J. Closed-form structural stresses and stress intensity factor solutions for spot welds in commonly used specimens. Submitted for publication in *Eng Fract Mech*, 2008.
- [22] Newman JA, Dowling NE. A crack growth approach to life estimation of spot-welded lap joints. *Fatigue Fract Eng Mater Struct* 1998;21:1123-1132.
- [23] Lin S-H, Pan J, Wung P, Chiang J. A fatigue crack growth model for spot welds in various types of specimens under cyclic loading conditions. *Int J Fatigue* 2006;28:792-803.

- [24] Lin P-C, Wang D-A, Pan J. Mode I stress intensity factor solutions for spot welds in lap-shear specimens. *Int J Solids Struct* 2007;44:1013-1037.
- [25] Zhang S. Stress intensities at spot welds. *Int J Fract* 1997;88:167-185.
- [26] Radaj D. Stress singularity, notch stress and structural stress at spot-welded joints. *Eng Fract Mech* 1989;34:495-506.
- [27] Radaj D, Zhang S. Stress intensity factors for spot welds between plates of unequal thickness. *Eng Fract Mech* 1991;39:391-413.
- [28] Radaj D, Zhang S. Simplified formulae for stress intensity factors of spot welds. *Eng Fract Mech* 1991;40:233-236.
- [29] Radaj D, Zhang S. Stress intensity factors for spot welds between plates of dissimilar materials. *Eng Fract Mech* 1992;42:407-426.
- [30] Zhang S. Fracture mechanics solutions to spot welds. *Int J Fract* 2001;112:247-274.
- [31] Campbell EJ, Gerberich WW, Underwood JH. Application of fracture mechanics for selection of metallic structural materials. American Society for Metals, Metals Parks, OH:1982.
- [32] Friedman P. Private communication, 2007.
- [33] Bergner F, Zouhar G. A new approach to the correlation between the coefficient and the exponent in the power law equation of fatigue crack growth. *Int J Fatigue* 2000;22:229-239.

CHAPTER III

EFFECTS OF PROCESSING TIME ON STRENGTHS AND FAILURE MODES OF DISSIMILAR SPOT FRICTION WELDS BETWEEN ALUMINUM 5754-O AND 7075-T6 SHEETS¹

Abstract

The effects of the processing time on the strength and failure mode of two types of dissimilar spot friction welds between aluminum 5754-O and 7075-T6 sheets are investigated by experiments. Dissimilar 5754/7075 and 7075/5754 spot friction welds made at different processing conditions were tested under lap-shear loading conditions. The experimental results indicate that the failure loads of both types of welds in lap-shear specimens increase when the processing time increases for the given ranges of the processing time. The optimal processing times to maximize the failure loads of the 5754/7075 and 7075/5754 welds under lap-shear loading conditions are identified. The maximum failure load of the 7075/5754 welds is about 40% larger than that of the 5754/7075 welds. Selected optical and scanning electron micrographs of both types of welds made at different processing times before and after failure are examined. The micrographs show different weld geometries and different failure modes of the welds made at different processing times. The failure modes of the dissimilar 5754/7075 and 7075/5754 spot friction welds are quite

¹ Published in Journal of Materials Processing Technology 2009; 209:3724-3739.

complex and appear to strongly depend on the geometry and strength of the interfacial surface between the two deformed sheet materials.

Keywords: Processing parameters; Dissimilar spot friction weld; Friction stir spot weld; Failure mode; Failure load

3.1. Introduction

Resistance spot welding is the most commonly used joining method for body-in-white parts made of steel sheets. However, resistance spot welding of aluminum sheets is likely to produce poor welds as reported by Thornton et al. [1] and Gean et al. [2]. Recently, a spot friction welding technology to join aluminum sheets has been developed by Mazda Motor Corporation and Kawasaki Heavy Industry [3,4]. The most significant advantage of the spot friction welding process comparing to the conventional welding processes is that the joint can be made without melting the base metals.

A schematic illustration of the spot friction welding process is shown in Figure 3.1. The process is applied to join the two metal sheets as shown. A rotating tool with a probe pin is first plunged into the upper sheet. When the rotating tool contacts the upper sheet, a tool downward force is applied. A backing tool beneath the lower sheet is used to support the tool downward force. The tool downward force and the tool rotational speed are maintained for an appropriate time to generate frictional heat. Then, heated and softened material adjacent to the tool deforms plastically, and a

solid-state bond is made between the surfaces of the upper and lower sheets. Finally, the tool is drawn out of the sheets as shown.

The mechanical behavior of aluminum spot friction welds under quasi-static loading conditions was studied, for example, see Fujimoto et al. [5,6], Hinrichs et al. [7], Lin et al. [8] and Pan et al. [9]. The metallurgical aspects of aluminum 6111-T4 spot friction welds were investigated by Mitlin et al. [10]. Tran et al. [11] investigated the failure loads of spot friction welds in aluminum 6111-T4 lap-shear specimens under quasi-static and dynamic loading conditions. Recently, Lin et al. [12-15] and Tran et al. [16,17] investigated the fatigue behaviors of spot friction welds in aluminum 6111-T4 and 5754-O sheets based on experimental observations, fracture mechanics, and the structural stress approach. A comprehensive literature review for spot friction welds can be found in Pan [18]. Note that most of the literature is for spot friction welds between similar aluminum sheets. However, dissimilar spot friction welds between aluminum 2017-T6 and 5052 sheets, and between aluminum 7075-T6 and 2024-T3 sheets were investigated by Tozaki et al. [18] and Tweedy et al. [19], respectively. Also, Su et al. [20] investigated the intermixing of dissimilar spot friction welds between aluminum 5754 and 6111 sheets by experiments and numerical simulations.

It should also be noted that many types of aluminum alloys are currently used to make different components of vehicles in the automotive industry. For example, the aluminum alloys are widely employed to produce different parts such as internal door stiffeners, entire body-in-white, and inner body panels as reported in Kaufman [21]. An efficient joining method is needed to join different components made of different

types of aluminum alloys. Therefore, dissimilar spot friction welds between different aluminum sheets need to be explored.

In this paper, the effects of the processing time on the strengths and failure modes of two types of dissimilar spot friction welds between aluminum 5754-O and 7075-T6 sheets are investigated by experiments. In this investigation, dissimilar spot friction welds were first made at different processing conditions. During the spot friction welding process of the two aluminum sheets, the tool contacts the upper sheet and penetrates the upper sheet to weld together the upper and lower sheets. The dissimilar spot friction welds are denoted as 5754/7075 when aluminum alloys 5754-O and 7075-T6 were used as the upper and lower sheets, respectively, and as 7075/5754 when aluminum alloys 7075-T6 and 5754-O were used as the upper and lower sheets, respectively. The failure loads of the 5754/7075 and 7075/5754 welds in lap-shear specimens under quasi-static loading conditions are obtained from the experiments. The optimal processing times to maximize the failure loads of the 5754/7075 and 7075/5754 welds under lap-shear loading conditions are identified. Selected optical and scanning electron micrographs of the 5754/7075 and 7075/5754 welds made at different processing times before and after failure are examined to investigate the weld geometries and the failure modes. Finally, the mechanical behaviors and failure modes of the 5754/7075 and 7075/5754 welds made at the optimal processing times are compared and discussed.

3.2. Experiments

Lap-shear specimens were used to investigate the mechanical behavior of spot friction welds under shear dominant loading conditions. The materials used in this investigation are aluminum 5754-O and 7075-T6 sheets. Table 3.1 lists the mechanical properties of the aluminum 5754-O and 7075-T6 sheets. As listed in Table 3.1, the yield and tensile strengths of the aluminum 7075-T6 sheets are about five and three times of those of the aluminum 5754-O sheets, respectively. Also, the elongation of the aluminum 5754-O sheets is about twice of that of the aluminum 7075-T6 sheets as listed in Table 3.1. The lap-shear specimens were made by using two 25.4 mm \times 101.6 mm aluminum sheets with a 38.1 mm \times 25.4 mm overlap area. The thicknesses of the aluminum 5754-O and 7075-T6 sheets are 2.0 mm and 1.6 mm, respectively. Figures 3.2(a) and 3.2(b) show a lap-shear specimen with a 5754/7075 spot friction weld and a lap-shear specimen with a 7075/5754 spot friction weld, respectively. One doubler made of the upper sheet and another doubler made of the lower sheet with a dimension of 25.4 mm \times 25.4 mm are attached to the ends of the upper and lower sheets, respectively, of the lap-shear specimens during testing. Note that the doublers are used to align the applied load to avoid the initial realignment of the specimen under lap-shear loading conditions. The welds were made by using a spot friction welding gun manufactured by Kawasaki Robotics, USA.

For the spot friction welding process under load-controlled conditions, the important processing parameters are the tool geometry, the tool rotational speed, the tool downward force and the tool holding time. Figure 3.3(a) shows a schematic plot of the tool rotational speed and the tool downward force as functions of the time. As

schematically shown in Figure 3.3(a), during the spot friction welding process, the tool rotational speed is kept constant. Initially, the tool downward force increases linearly for a period of time. Then the tool downward force is kept constant for another period of time and finally decreases linearly to zero. The rise and fall times of the tool downward force are about a fraction of a second based on a recent research investigation at Ford Motor Company. As shown in the figure, t_i represents the time that the tool contacts the top surface of the upper sheet and t_f represents the time that the tool extracts from the top surface of the upper sheet. The time interval between t_i and t_f represents the total tool holding time or the processing time.

Figure 3.3(b) shows a schematic plot of an extracted tool and two welded sheets after spot friction welding. As shown in the figure, the anvil is used to support the tool downward force during the welding process. As shown in Figure 3.3(b), the diameters of the tool shoulder and the tool probe pin are denoted as D_t and D_p , respectively. The actual bonding diameter for the weld or the weld diameter is denoted as D_c . The weld diameter D_c is determined as the distance between the locations of the two crack tips identified by the optical and scanning electron micrographs of the welds before testing. In this figure, the thick dashed line represents the interfacial surface between the two deformed sheet materials. It should be noted that the interfacial surface was well bonded as discussed later. In the figure, the reduced thickness of the central part of the nugget due to the tool probe pin penetration at the bottom of the central hole is denoted as t_c . The thinnest thickness of the upper sheet outside the weld nugget due to the indentation of the concave tool

shoulder geometry is denoted as t_u . The weld diameter D_c and the thicknesses t_c and t_u depend upon the processing parameters, and the thicknesses and mechanical properties of the upper and lower sheets.

3.3. Micrographs of spot friction welds before testing

In this investigation, a tool with a concave shoulder and a threaded probe pin was used to make dissimilar 5754/7075 and 7075/5754 spot friction welds. A tool rotational speed of 3000 RPM and a tool downward force of 5.88 kN were specified to make both types of welds used in this investigation. The 5754/7075 welds were made at the processing time ranging from 1.6 sec to 4.0 sec with a time increment of 0.2 sec. The 7075/5754 welds were made at the processing time ranging from 1.0 sec to 8.0 sec with a time increment of 0.5 sec. For both types of welds, at least two samples are made at each processing time. One sample is reserved for cross-sectioning before testing and the other samples are tested under lap-shear loading conditions. Note that the weld made at the processing time shorter than the minimum processing time of the range was not bonded while the weld made at the processing time longer than the maximum processing time of the range had a hole in the central portion of the weld due to the excessive tool penetration. Only the experimental results within the ranges were considered and investigated since there was no bonding between two sheets when the processing time was shorter than the minimum processing time, while a welded sample with a hole should be rejected from the manufacturing viewpoint when the processing time was longer than the maximum processing time. In the following, some optical and scanning electron micrographs of

the cross sections along the symmetry planes of the 5754/7075 and 7075/5754 spot friction welds made at different processing times before testing are presented to examine the weld geometries.

Figure 3.4(a) shows optical micrographs of the cross sections along the symmetry planes of the 5754/7075 spot friction welds at the processing times of 1.8 sec, 2.8 sec and 3.8 sec before testing. Figure 3.5(a) shows optical micrographs of the cross sections along the symmetry planes of the 7075/5754 spot friction welds at the processing times of 1.0 sec, 3.5 sec and 6.5 sec before testing. As shown in Figures 3.4(a) and 3.5(a), different weld geometries can be seen for both types of welds made at different processing times. Note that the aluminum 5754-O and 7075-T6 polished surfaces have different gray levels due to different chemical compositions as shown in the figures. In Figures 3.4(a) and 3.5(a), the indentation profile reflects the general shape of the threaded probe pin and the concave shoulder of the tool. The bottom surfaces of the lower sheets are almost flat for the 5754/7075 weld at the processing time of 1.8 sec and for the 7075/5754 welds at the processing times of 1.0 sec and 3.5 sec. At the processing times of 2.8 sec and 3.8 sec for the 5754/7075 welds and 6.5 sec for the 7075/5754 weld, the bottom surfaces of the lower sheets are slightly dented as shown in Figures 3.4(a) and 3.5(a).

As shown in Figures 3.4(a) and 3.5(a), a layer of the upper sheet material, pushed and deformed by the threaded probe pin, can be seen near the outer area of the central hole. The interfacial surface between the two deformed sheet materials can be seen near the outer area of the central hole. Due to the rotating pin penetration, the heated and softened upper sheet material was pushed down near the probe pin. Also, the

heated and softened lower sheet material rose upward and outward due to the probe pin penetration. As the processing time increases, the lower sheet material appears to flow upward, outward and then toward the central hole as shown in Figures 3.4(a) and 3.5(a). The notch tips are marked by points C and D in Figures 3.4(a) and 3.5(a). The notches extend into the welds and become cracks. The locations of the crack tips are marked in the figures. As shown in Figures 3.4(a) and 3.5(a), the location of the crack tip extends further out toward the outer circumference of the tool shoulder indentation when the processing time increases.

As shown in Figures 3.4(a) and 3.5(a), the thicknesses t_c and t_u (as defined in Figure 3.3(b)) decrease when the processing time increases since the tool indents deeper at the longer processing times. Note that the concave tool shoulder squeezed out some upper sheet material but maintained some upper sheet material near the central hole. The tool shoulder indentation resulted in a radial expansion of the upper sheet material along the outer circumference of the tool shoulder indentation. However, due to the constraint of the neighboring material, the sheet was therefore slightly bent along the outer circumference of the tool shoulder indentation. As shown in Figures 3.4(a) and 3.5(a), the bend along the outer circumference of the tool shoulder indentation becomes larger at longer processing times and consequently the notch gap between the upper and lower sheets increases when the processing time increases. As shown in Figures 3.4(a) and 3.5(a), the cross-sectional area of the squeezed out ring on the top surface of the upper sheet increases when the processing time increases for both types of welds

Figure 3.4(b) shows close-up optical micrographs of regions Ia, Ib and Ic as marked in Figure 3.4(a). Figure 3.5(b) shows close-up optical micrographs of regions IIa, IIb and IIc as marked in Figure 3.5(a). The locations of the crack tips are also marked in the figures. As shown in Figure 3.4(b), the lower sheet material rises and extends into the upper sheet material when the processing time increases from 1.8 sec to 2.8 sec. At the processing time of 3.8 sec, the lower sheet material extends significantly into the upper sheet material. As shown in Figure 3.5(b), the lower sheet material rises and extends into the upper sheet material when the processing time increases from 1.0 sec to 3.5 sec. At the processing time of 6.5 sec, the lower sheet material extends significantly into the upper sheet material and reaches the rim of the central hole. For both types of welds, as the processing time increases, the lower sheet material appears to flow upward and then toward the rim of the central hole. Note that the interfacial surfaces between the two deformed sheet materials near the central holes appear to be well bonded possibly due to high pressure and large plastic deformation.

Figure 3.4(c) shows scanning electron micrographs of the crack tip regions of the 5754/7075 spot friction welds as marked in Figure 3.4(b). Figure 3.5(c) shows scanning electron micrographs of the crack tip regions of the 7075/5754 spot friction welds as marked in Figure 3.5(b). The small arrows are used to mark the interfacial surfaces between the two deformed sheet materials. The locations of the crack tips can be identified by the scanning electron micrographs of the crack tip regions as shown in the figures. As shown in the figures, some part of the crack surfaces near the tips become vague and may be bonded by the welding process. A large crack,

marked as C0 in Figures 3.4(a) and 3.4(b) for the 5754/7075 weld at 3.8 sec, is shown near the central hole on the deformed upper sheet. Figure 3.4(d) shows a scanning electron micrograph of crack C0 as marked in Figures 3.4(a) and 3.4(b). The small arrows are used to mark the interfacial surface between the deformed 5754 and 7075 sheet materials. Crack C0 was likely formed during the welding process.

Figure 3.6 shows the weld diameters D_c , measured as the distance between the locations of the two crack tips of the cross section along the symmetry plane of the weld, as functions of the processing time for both 5754/7075 and 7075/5754 spot friction welds. Note that the location of the crack tip is identified by the optical and scanning electron micrographs. Note also that the welds made at short, medium or long processing times, as defined later, show different failure modes under lap-shear loading conditions. Therefore, for a given range of the processing time, only few representative welds were cross-sectioned before testing to examine the weld geometries. For this reason, the number of the available data presented in Figure 3.6 is smaller than the number of specimens tested in this investigation as shown later in Figure 3.7. As shown in Figure 3.6, the weld diameter D_c increases as the processing time increases for both types of welds. When the processing time is longer, the frictional heat generated between the rotating tool and the upper sheet material is larger. This leads to more tool penetration and larger extent of the plastic deformation of the sheet materials near the interfacial surface and therefore the weld diameter D_c increases. In order to obtain the trends of the dependence of the weld diameters on the processing time based on the available experimental data, the weld diameters are fitted as functions of the processing time by using the second-order

polynomials. The results based on the fitted curves are also shown in Figure 3.6. The second-order polynomial curves fitted very well the available experimental data for the given ranges of the processing time. The only purpose of fitting the experimental data is to determine approximately the processing time at the intersection of the two fitted curves within the ranges. Based on the fitted curves shown in Figure 3.6, at the processing times shorter than 2.1 sec, the diameter of the 7075/5754 welds is slightly larger than that of the 5754/7075 welds at the same processing time. In contrast, at the processing times longer than 2.1 sec, the diameter of the 5754/7075 welds is larger than that of the 7075/5754 welds at the same processing time.

It should be noted that the frictional heat is first generated from the contact of the rotating tool and the upper sheet, and the heat is then conducted through the interfacial surface to the lower sheet. At the same processing time, the upper and lower sheet materials near the interfacial surface will be heated and softened more, consequently bonded with a larger area, for the weld made of a thinner upper sheet thickness and a softer upper sheet material. This will lead to a larger weld diameter. Note that the upper sheet thickness of the 5754/7075 welds is 25% larger than that of the 7075/5754 welds but the upper sheet material of the 5754/7075 welds is softer than that of the 7075/5754 welds as indicated in Table 3.1. As shown in Figures 3.4(a) and 3.5(a), at the processing times shorter than 2.1 sec, the tool shoulder slightly indented the upper sheet. Therefore, the effect of the upper sheet thickness is possibly more dominant than the effect of the material strength of the upper sheet. The thinner thickness of the upper sheet of the 7075/5754 welds will consequently result in a larger weld diameter compared to that of the 5754/7075 welds at the same

processing time for the welds made at the processing times shorter than 2.1 sec. As shown in Figures 3.4(a) and 3.5(a), at the processing times longer than 2.1 sec, the tool shoulder deeply indented the upper sheet. Therefore, the effect of the material strength of the upper sheet is possibly more dominant than the effect of the upper sheet thickness. The softer material of the upper sheet of the 5754/7075 welds will consequently result in a larger weld diameter compared to that of the 7075/5754 welds at the same processing time for the welds made at the processing times longer than 2.1 sec.

It should be noted that no criterion to control the quality of the spot friction welds in aluminum sheets is available due to the recently developed technology. Therefore, a criterion which has been widely used in the automotive industry to control the quality of the resistance spot welds in steel sheets with the yield strength ranging from 140 MPa to 420 MPa and the thickness ranging from 0.6 mm to 3.0 mm as suggested by the Auto Steel Partnership [22] is adopted to examine the quality of the spot friction welds used in this investigation. The criterion for a normal weld is

$$D \geq 4\sqrt{t} \quad (3.1)$$

where D and t denote the average weld button size and the sheet thickness, respectively, in millimeter. The value of $4\sqrt{t}$ is defined as the minimum weld button size for a normal weld. Any weld fails in the interfacial failure mode under a peeling test will be considered as a bad weld.

Note that the geometries of the spot friction welds as shown in Figures 3.4(a) and 3.5(a) are similar to those of the resistance spot welds in general. Note also that the material strength of the stir zone in the weld nugget of the spot friction weld should

be much larger than that of the base material due to the small grain size as reported in Lin et al. [8]. Therefore, for lack of further information on the quality control of the spot friction welds in aluminum sheets, the criterion in Equation (3.1) is tentatively used to evaluate the quality of the spot friction welds before testing. Since the thicknesses of the upper and lower sheets for both 5754/7075 and 7075/5754 welds are not equal, the smaller thickness of $t = 1.6$ mm of the 7075 sheet is used in the criterion in Equation (3.1). For the weld diameters as indicated in Figure 3.6, all the 5754/7075 and 7075/5754 spot friction welds used in this investigation are tentatively considered as the normal welds according to the criterion in Equation (3.1).

3.4. Failure loads of spot friction welds

In this investigation, lap-shear specimens with dissimilar spot friction welds made at different processing times were tested under quasi-static loading conditions by using an Instron testing machine at a monotonic displacement rate of 10 mm per minute. The tests were terminated when the specimens were separated. The load and displacement were simultaneously recorded during each test.

Figure 3.7 shows the failure loads as functions of the processing time for both 5754/7075 and 7075/5754 spot friction welds in lap-shear specimens under quasi-static loading conditions. Here, the failure load is determined as the maximum load of the load-displacement curve obtained from the experiment. In this figure, the vertical dashed and solid lines represent the estimated upper limits of the processing time based on the experimental results for the 5754/7075 and 7075/5754 welds tested in this investigation. Note that the welds made at the processing times longer than

these limits would have holes in the central portions of the welds due to excessive tool penetration and should be rejected from manufacturing pointview. As shown in Figure 3.7, the trend of the experimental results indicates that the failure load of the 5754/7075 welds increases when the processing time increases from 1.6 sec to 3.8 sec and then decreases at 4.0 sec. The trend of the experimental results indicates that the failure load of the 7075/5754 welds also increases when the processing time increases from 1.0 sec to 6.5 sec, and then remains nearly the same when the processing time increases from 6.5 sec to 8.0 sec. As shown in Figure 3.6, the weld diameter D_c is larger when the processing time is longer for both types of welds. Therefore, the bonding area which can sustain the applied load is larger at the longer processing time. This consequently leads to a larger failure load. However, as the processing time increases, the upper sheet thickness near the weld nugget decreases. This leads to the decrease of the failure load. The competition of the influences of the weld diameter and the upper sheet thickness near the weld nugget leads to a maximum failure load as the processing time increases. As shown in Figure 3.7, the maximum failure load of the 5754/7075 welds is 4.04 kN at 3.8 sec. Also, the maximum failure load of the 7075/5754 welds is 5.65 kN at 6.5 sec. These processing times are considered as the optimal processing times to maximize the failure loads of the 5754/7075 and 7075/5754 welds under lap-shear loading conditions for this particular set of processing parameters. As indicated in Figure 3.7, the maximum failure load of the 7075/5754 welds is about 40% larger than that of the 5754/7075 welds.

3.5. Failure modes of 5754/7075 spot friction welds

Based on the experimental observations, the failed 5754/7075 spot friction welds at the processing time ranging from 1.6 sec to 2.4 sec (short processing time) show one failure mode. The failed 5754/7075 spot friction welds at the processing time ranging from 2.6 sec to 3.4 sec (medium processing time) shows a different failure mode. The failed 5754/7075 spot friction welds at the processing time ranging from 3.6 sec to 4.0 sec (long processing time) show another failure mode. Note that the ranges of short, medium and long processing times have been defined only for convenient presentation of this paper.

Figures 3.8(a), 3.8(b) and 3.8(c) show optical micrographs of the cross sections along the symmetry planes of the failed 5754/7075 spot friction welds at the processing times of 1.8 sec, 2.8 sec and 3.8 sec, respectively. The bold arrows in the figures schematically show the direction of the applied load. Due to the large deformation in the final stage of the specimen failure, the weld nugget rotated clockwise. Therefore, the sheets near the nugget are slightly bent. The applied load stretches the upper right 5754 sheet and the lower left 7075 sheet. Based on the optical micrographs, there are three types of cracks or fracture surfaces which occurred during the tests of the spot friction welds made at different processing times. Letters I, U, and L are used to denote for cracks or fracture surfaces which occurred along the interfacial surface between the two deformed sheet materials, in the deformed upper sheet material and in the deformed lower sheet material, respectively. These notations are valid for the rest of the paper.

As shown in Figure 3.8(a), at the processing time of 1.8 sec, two cracks, marked as I1a and I1b, appear to emanate from the original crack tips of the weld and propagate along the interfacial surface between the two deformed sheet materials toward the central hole. When the load continues to increase, the upper and lower sheets are separated through the fracture surface in the deformed upper sheet material near the central hole, marked by U1a and U1b in Figure 3.8(a). Note that two small cracks, marked as I1c and I1d in Figure 3.8(a), grow just a bit along the interfacial surface between the two deformed sheet materials in the downward direction possibly due to the weak strength of the interfacial surface. In summary, the 5754/7075 welds at the short processing time mainly fail from the nearly flat fracture surface through the deformed upper 5754 sheet material.

As shown in Figure 3.8(b), at the processing time of 2.8 sec, two cracks, marked as I2a and I2b, appear to emanate from the original crack tips of the weld and propagate along the interfacial surface between the two deformed sheet materials toward the central hole. Crack I2b becomes crack L1 that propagates through the deformed lower sheet material (see Figure 3.4(b)) in the downward direction toward the central hole. Crack L1 then becomes crack I2c that propagates along the interfacial surface toward the central hole. Crack I2c then propagates along the nugget circumference to cause a partially curved interfacial fracture surface as shown later in Figure 3.9. When the load continues to increase, the upper and lower sheets are finally separated through the fracture surfaces in the deformed upper sheet material near the central hole, marked by U2a and U2b in Figure 3.8(b). Note that a small crack, marked as I2d in Figure 3.8(b), appears to propagate along the interfacial

surface between the two deformed sheet materials (see Figure 3.4(b)). Note also that this crack was generated possibly due to the weak strength of the interfacial surface between the two deformed sheet materials and continued to propagate into the upper sheet material. In summary, the 5754/7075 welds at the medium processing time mainly fail from the partially curved interfacial fracture surface through the interfacial surface between the two deformed sheet materials and the fracture surfaces in the deformed upper 5754 sheet material.

As shown in Figure 3.8(c), at the processing time of 3.8 sec, two cracks, marked as I3a and I3b, appear to emanate from the original crack tips of the weld and propagate along the interfacial surface between the two deformed sheet materials toward the central hole. Crack I3a then becomes crack U3 that propagates through the deformed upper 5754 sheet (with a reduced thickness). As shown in the figure, crack U3 appears to be caused by a necking failure due to shear localization. Note that this necking failure of the 5754/7075 weld at 3.8 sec is quite similar to that of the aluminum 6111 spot friction weld made by the concave tool under lap-shear loading conditions as reported in Lin et al. [8,14]. The failure then propagates along the nugget circumference. When the load continues to increase, the upper and lower sheets are finally separated through a curved fracture surface marked as L3a and L3b in Figure 3.8(c) in the deformed lower sheet material near the central hole. Based on the experimental observation, crack U3 appears to be the dominant crack to cause the failure of the specimen. In summary, the 5754/7075 welds at the long processing time mainly fail from the fracture surface in the deformed upper 5754 sheet material and the curved fracture surface through the deformed lower 7075 sheet material.

Figure 3.9 shows close-up top views of the lower sheets and close-up top and bottom views of the upper sheets of the failed 5754/7075 spot friction welds at the processing times of 1.8 sec, 2.8 sec and 3.8 sec. As shown in the figure, different failure modes can be seen for the failed 5754/7075 welds made at different processing times. The marked outer rough surfaces near the outer circumferences of the welds between the marked large circles and small ellipses for the failed welds at the processing times of 1.8 sec, 2.8 sec and 3.8 sec in Figure 3.9 represent the unwelded surfaces. The marked interfacial fracture surfaces in the ring regions between the marked ellipses and the marked fracture surfaces for the failed welds at the processing times of 1.8 sec, 2.8 sec and 3.8 sec in Figure 3.9 represent the interfacial fracture surfaces caused by cracks I1a and I1b in Figure 3.8(a), by cracks I2a and I2b in Figure 3.8(b), and by cracks I3a and I3b in Figure 3.8(c), respectively. The marked fracture surfaces outside the nearly circular smooth central areas (due to the tool probe pin indentation) or the central holes for the failed welds at the processing times of 1.8 sec and 2.8 sec in Figure 3.9 represent the fracture surfaces marked as U1a and U1b in Figure 3.8(a), and as U2a and U2b in Figure 3.8(b), respectively. The marked small ellipses with the major axis in the vertical direction for the failed weld at the processing time of 2.8 sec in Figure 3.9 correspond to the partially curved interfacial fracture surface marked as I2c in Figure 3.8(b). The marked curved fracture surfaces for the failed weld at the processing time of 3.8 sec in Figure 3.9 correspond to the curved fracture surface marked as L3a and L3b in Figure 3.8(c). The marked circumferential cracks for the failed weld at the processing time of 3.8 sec in Figure 3.9 correspond to crack U3 in Figure 3.8(c) that propagates along the nugget

circumference. Note that the central holes due to the tool probe pin indentation on the upper sheets of the failed welds in Figure 3.9 were bent and distorted.

Scanning electron micrographs obtained from another failed 5754/7075 spot friction weld made at 3.8 sec are presented in Figures 3.10(a) and 3.10(b) to examine the fracture surfaces in details. Figure 3.10(a) shows a scanning electron micrograph of the fracture surface on the lower sheet. The large arrow in Figure 3.10(a) schematically shows the direction of the applied load. Figure 3.10(b) shows scanning electron micrographs of the fracture surfaces at ten different locations along the symmetry plane of the weld marked as A, B, C, D, E, F, G, H, I and J in Figure 3.10(a). The scanning electron micrographs of these locations are correlated to various types of fracture surfaces on the top view of the lower sheet of the failed weld in Figure 3.9. In Figure 3.10(a), the fracture surface of A corresponds to the outer rough surface on the lower sheet (as marked in Figure 3.9). The fracture surfaces of B, C, D, E and J in Figure 3.10(a) correspond to the interfacial fracture surface on the lower sheet (as marked in Figure 3.9). As shown in Fig 10(b), the micrographs of these fracture surfaces appear to be quite different. Note that the dimples were observed on the right portion of the fracture surface of B and on the fracture surface of C. In Figure 3.10(a), the fracture surfaces of F, G, H and I correspond to the curve fracture surface on the lower sheet (as marked in Figure 3.9). As shown in Figure 3.10(b), the micrographs of these fracture surfaces appear to be quite different. As shown in Figure 3.10(b), the scanning electron micrographs of the fracture surfaces of the same type of the fracture surface according to the optical micrographs at different locations are different.

Since it is difficult to take a scanning electron micrograph of the fracture surface of crack U3 as marked in Figure 3.8(c), another failed specimen was used to obtain a scanning electron micrograph which is presented in Figure 3.10(c). Note that a small arrow in Figure 3.8(c) is used to mark the approximate location of the fracture surface shown in Figure 3.10(c). Figure 3.10(c) shows elongated dimples on the fracture surface. Note that the dimples represent the ductile fracture process of the necking failure due to shear localization. As shown in Figure 3.10, the fracture mechanisms of the failed 5754/7075 weld made at 3.8 sec are quite complex. It appears that various types of the fracture surfaces shown in Figure 3.10 can only be explained by a further detailed investigation of the spot friction welding process and the failure mechanisms of the welds under lap-shear loading conditions. It should be noted that only the scanning electron micrographs of the fracture surfaces of the failed 5754/7075 weld made at 3.8 sec are presented here.

3.6. Failure modes of 7075/5754 spot friction welds

Based on the experimental observations, the failed 7075/5754 spot friction weld at the processing time of 1.0 sec (short processing time) shows one failure mode. The failed 7075/5754 spot friction welds at the processing time ranging from 1.5 sec to 5.5 sec (medium processing time) show a different failure mode. The failed 7075/5754 spot friction welds at the processing time ranging from 6.0 sec to 8.0 sec (long processing time) show another failure mode. Note that the ranges of short, medium and long processing times have been defined only for convenient presentation of this paper.

Figures 3.11(a), 3.11(b) and 3.11(c) show optical micrographs of the cross sections along the symmetry planes of the failed 7075/5754 spot friction welds at the processing times of 1.0 sec, 3.5 sec and 6.5 sec, respectively. The bold arrows in the figures schematically show the direction of the applied load. Due to the large deformation in the final stage of the specimen failure, the weld nugget rotated clockwise. Therefore, the sheets near the nugget are slightly bent. The applied load stretches the upper right 7075 sheet and the lower left 5754 sheet.

As shown in Figure 3.11(a), at the processing time of 1.0 sec, two cracks, marked as I1a and I1b, appear to emanate from the original crack tips of the weld and grow a bit along the interfacial surface between the two deformed sheet materials toward the central hole. When the load continues to increase, the upper and lower sheets are eventually separated through the fracture surface in the deformed upper sheet material, marked by U1a and U1b in Figure 3.11(a). Note that two small cracks, marked as I1c and I1d in Figure 3.11(a), grow just a bit along the interfacial surface between the two deformed sheet materials in the upward direction possibly due to the weak strength of the interfacial surface. In summary, the 7075/5754 weld at the short processing time mainly fails from the nearly flat fracture surface through the deformed upper 7075 sheet material. Note that the 5754/7075 welds at the short processing time also fail from the nearly flat fracture surface through the deformed upper 5754 sheet material.

As shown in Figure 3.11(b), at the processing time of 3.5 sec, two cracks, marked as I2a and I2b, appear to emanate from the original crack tips of the weld and propagate along the interfacial surface between the two deformed sheet materials toward the central hole. Note that the interfacial surface between the two deformed

sheet materials for the 7075/5754 weld made at 3.5 sec can be seen in Figure 3.5. Then, possibly, crack I2a propagates along the nugget circumference. When the load continues to increase, the upper and lower sheets are separated first through the interfacial surface between the two deformed sheet materials, caused by the propagation of crack I2b along the interfacial surface, and then through the fracture surfaces in the deformed upper sheet material, marked as U2a and U2b in Figure 3.11(b). Note that a small crack, marked as I2c in Figure 3.11(b), grows a bit along the interfacial surface between the two deformed sheet materials in the upward direction possibly due to the weak strength of the interfacial surface. In summary, the 7075/5754 welds at the medium processing time mainly fail from the fracture surfaces through the interfacial surface between the two deformed sheet materials and in the deformed upper 7075 sheet material.

As shown in Figure 3.11(c), at the processing time of 6.5 sec, two cracks, marked as I3a and I3b, appear to emanate from the original crack tips of the weld and propagate along the interfacial surface between the two deformed sheet materials toward the central hole. Crack I3a then becomes crack U3a that propagates through the upper 7075 sheet (with a reduced thickness). Crack U3a then propagates along the nugget circumference. When the load continues to increase, the upper and lower sheets are separated first through the interfacial surface between the two deformed sheet materials caused by the propagation of crack I3b in Figure 3.11(c), and then through the fracture surface in the deformed upper sheet marked as U3b in Figure 3.11(c). Note that a thin layer of the upper sheet material was remained on the upper sheet of the failed weld as shown in Figure 3.11(c). Based on the experimental

observation, crack U3a appears to be the dominant crack to cause the failure of the specimen. Another large crack, marked as U3c in Figure 3.11(c), is likely a defect of this particular specimen since no similar crack was found in the other specimen made at this processing time as shown in Figure 3.5. Note also that crack U3c should not significantly affect the failure load of the weld since the upper left portion of the weld is not the main load-carrying region. In summary, the 7075/5754 welds at the long processing time mainly fail from the fracture surfaces in the deformed upper 7075 sheet material and along the interfacial surface between the two deformed sheet materials.

Figure 3.12 shows close-up top views of the lower sheets and close-up top and bottom views of the upper sheets of the failed 7075/5754 spot friction welds at the processing times of 1.0 sec, 3.5 sec and 6.5 sec. As shown in the figure, different failure modes can be seen for the failed 7075/5754 welds made at different processing times. The marked outer rough surfaces near the outer circumferences of the welds between the marked large circles and small ellipses for the failed welds at the processing times of 1.0 sec, 3.5 sec and 6.5 sec in Figure 3.12 represent the unwelded surfaces. The marked interfacial fracture surfaces in the ring regions between the marked ellipses and the marked fracture surfaces for the failed welds at the processing times of 1.0 sec, 3.5 sec and 6.5 sec in Figure 3.12 represent the interfacial fracture surfaces caused by cracks I1a and I1b in Figure 3.11(a), by cracks I2a and I2b in Figure 3.11(b), and by cracks I3a and I3b in Figure 3.11(c), respectively. The marked fracture surfaces outside the nearly circular smooth central areas (due to the tool probe pin indentation) or the central holes for the failed welds at the processing

times of 1.0 sec, 3.5 sec and 6.5 sec in Figure 3.12 represent the fracture surfaces marked as U1a and U1b in Figure 3.11(a), as U2a and U2b in Figure 3.11(b), and as U3b in Figure 3.11(c), respectively. The marked circumferential cracks for the failed weld at the processing time of 6.5 sec in Figure 3.12 correspond to crack U3a in Figure 3.11(c) that propagates along the nugget circumference. Note that the central holes due to the tool probe pin indentation on the upper sheets of the failed welds as shown in Figure 3.12 were bent and distorted.

Scanning electron micrographs obtained from another failed 7075/5754 spot friction weld made at 6.5 sec are presented here to examine the fracture surfaces in details. Figure 3.13(a) shows a scanning electron micrograph of the fracture surface on the lower sheet. The large arrow in Figure 3.13(a) schematically shows the direction of the applied load. Figure 3.13(b) shows scanning electron micrographs of the fracture surfaces at fourteen different locations along the symmetry plane of the weld marked as A, B, C, D, E, F, G, H, I, J, K, L, M and N in Figure 3.13(a). The scanning electron micrographs of these locations are correlated to various types of fracture surfaces on the top view of the lower sheet of the failed specimen in Figure 3.12. In Figure 3.13(a), the fracture surfaces of A and N correspond to the outer rough surface on the lower sheet (as marked in Figure 3.12). The fracture surfaces of B, C, D, E, F, K, L and M in Figure 3.13(a) correspond to the interfacial fracture surface on the lower sheet (as marked in Figure 3.12). As shown in Figure 3.13(b), the micrographs of these fracture surfaces appear to be quite different. Note that the dimples were observed on the right portion of the fracture surface of E and on the fracture surfaces of K and L. In Figure 3.13(a), the fracture surfaces of G, H, I and J

correspond to the fracture surface on the lower sheet (as marked in Figure 3.12). As shown Figure 3.13(b), the micrographs of these fracture surfaces appear to be quite different. As shown in Figure 3.13(b), the scanning electron micrographs of the fracture surfaces of the same type of the fracture surface according to the optical micrographs at different locations are different.

Figure 3.13(c) shows a scanning electron micrograph of the fracture surface of crack U3a as marked in Figure 3.11(c) obtained from the upper sheet of the same failed weld shown in Figures 3.13(a) and 3.13(b). Note that a small arrow in Figure 3.11(c) is used to mark the approximate location of the fracture surface shown in Figure 3.13(c). As shown in Figure 3.13, the fracture mechanisms of the failed 7075/7075 weld made at 6.5 sec are quite complex. It appears that various types of the fracture surfaces shown in Figure 3.13 can only be explained by a further detailed investigation of the spot friction welding process and the failure mechanisms of the welds under lap-shear loading conditions. It should be noted that only the scanning electron micrographs of the fracture surfaces of the failed 7075/7075 weld made at 6.5 sec are presented here.

3.7. Discussions

The volumes of the deformed lower and upper sheet materials after welding as observed in Figures 3.4(a) and 3.5(a) can be estimated by using the SolidWorks 2007 software. First, a half of the cross-sectional area of the deformed upper and lower sheet materials based on the optical micrograph, limited by the observed interfacial surface and the center line of the central hole, is manually sketched. The sketched

surface is then spun around the center line to generate a three-dimensional weld made of the deformed sheet materials. The volumes of the deformed sheet materials of the weld are then automatically estimated by SolidWorks 2007. The details of this procedure are straightforward and are not reported here. For both types of welds, the estimated volumes of the deformed upper and lower sheet materials after welding are nearly the same as those of the upper and lower sheet materials before welding.

As shown in Figures 3.8(a) and 3.11(a), cracking occurred along the interfacial surfaces between the two deformed sheet materials and in the deformed upper sheet materials near the central holes for both types of welds at the short processing time. As shown in Figure 3.8(b) and 3.11(b), cracking mainly occurred along the interfacial surfaces between the two deformed sheet materials and in the deformed upper sheet materials near the central holes for both types of welds at the medium processing time. As shown in Figure 3.8(c), cracking occurred along the interfacial surface between the two deformed sheet materials, and in the deformed upper and lower sheet materials for the 5754/7075 welds at the long processing time. As shown in Figure 3.11(c), cracking occurred along the interfacial surface between the two deformed sheet materials and in the deformed upper 7075 sheet material for the 7075/5754 welds at the long processing time. As shown in Figures 3.8 and 3.11, cracking in both types welds made at different processing times was initiated at the original crack tips and grew along the interfacial surface between the two deformed sheet materials. However, these cracks did not continue to grow along the interfacial surfaces but propagate through the deformed sheet materials near the central holes at the final stage of the specimen failure. It is possible that the strength of the interfacial surface

is weaker than that of the sheet materials near the original crack tips of the welds. Another possible reason is that the material at the interfacial surfaces near the central hole is subjected to unfavorable stress conditions during the tests. Based on the experimental observations, the failure modes of the 5754/7075 and 7075/5754 spot friction welds at the short, medium and long processing times under quasi-static loading conditions are quite complex and appear to strongly depend on the geometry and strength of the interfacial surface between the two deformed sheet materials.

As shown in Figure 3.7, the optimal processing times to maximize the failure loads of the 5754/7075 and 7075/5754 spot friction welds under lap-shear loading conditions for this particular set of welding processing parameters are 3.8 sec and 6.5 sec, respectively. Figure 3.14 shows the typical load-displacement curves of the 5754/7075 and 7075/5754 spot friction welds at the optimal processing times under lap-shear loading conditions. Note that the slackness in the test setup has been removed in the load-displacement curves. The average failure loads of three tested 5754/7075 and 7075/5754 welds in lap-shear specimens are 4.03 kN and 5.65 kN, respectively. As discussed earlier, the failures of both 5754/7075 and 7075/5754 welds at the optimal processing times are mainly due to the cracks, marked as U3 in Figure 3.8(c) and as U3a in Figure 3.11(c), respectively, that propagate in the deformed upper sheets (with reduced thicknesses). Therefore, for nearly the same weld diameters and reduced thicknesses of the upper sheets, the weld made of the upper sheet with a stronger material will eventually sustain a larger failure load. Note that the weld diameters (indicated by Figure 3.6) and the reduced thicknesses of the deformed upper sheets (indicated by Figures 3.8(c) and 3.11(c)) for both 5754/7075

and 7075/5754 welds at the optimal processing times are nearly the same. Therefore, the stronger material of the upper 7075 sheet of the 7075/5754 welds will consequently result in a larger failure load compared to that of the 5754/7075 welds at the optimal processing times. This observation can partially explain why the failure load of the 7075/5754 welds at the optimal processing time is about 40% larger than that of the 5754/7075 welds at the optimal processing time as indicated in Figures 3.7 and 3.14.

As shown in Figure 3.14, the load-displacement curve for the 5754/7075 specimen is quite different from that for the 7075/5754 lap-shear specimen. As shown in Figure 3.14, the load of the 7075/5754 specimen increases with one small load drop before reaching the maximum and then drops to zero as the displacement increases. However, for the 5754/7075 specimen, the load increases with one small load drop before reaching the maximum and the load then experiences three load drops before decreasing to zero as the displacement increases. The locations of the load drops in the load-displacement curves for both 5754/7075 and 7075/5754 specimens possibly correspond to different stages of the crack initiation and propagation occurred in these specimens during the tests as discussed earlier. Further investigation should be conducted to fully investigate this phenomenon.

Note that the initial part of the load-displacement curve for the 5754/7075 specimen is slightly higher than that for the 7075/5754 specimen. As shown in Figure 3.14, the displacement at the final separation (when the load drops to zero) of the 7075/5754 specimen is slightly larger than that of the 5754/7075 specimen. However, the displacement at the failure load (when the load reaches the maximum)

of the 7075/5754 specimen is much larger than that of the 5754/7075 specimen. As shown in Figure 3.14, the energy dissipation to separate the specimen with the 7075/5754 weld, indicated by the area under the load-displacement curve, is larger than that with the 5754/7075 weld at the optimal processing times.

Based on this investigation, the 7075/5754 welds at the optimal processing time have both advantages and disadvantages as compared to the 5754/7075 welds at the optimal processing time. As discussed earlier, the failure load, the displacement at the failure load and the energy dissipation to separate the specimen for the 7075/5754 weld at the optimal processing time are higher than those for the 5754/7075 weld at the optimal processing time. Therefore, from the mechanics viewpoint, the performance of the 7075/5754 welds at the optimal processing time is better than that of the 5754/7075 welds at the optimal processing time. However, the 7075/5754 welds require larger optimal processing time than that of the 5754/7075 welds do. Also, when making the 7075/5754 welds, the tool wears more due to the high strength of the 7075 upper sheet material. Therefore, from the manufacturing viewpoint, the performance of the 5754/7075 welds at the optimal processing time is better than that of the 7075/5754 welds at the optimal processing time.

3.8. Conclusions

The effects of the processing time on the strengths and failure modes of two types of dissimilar spot friction welds between aluminum 5754-O and 7075-T6 sheets are investigated by experiments. Dissimilar 5754/7075 and 7075/5754 spot friction welds made at different processing conditions were tested under lap-shear loading

conditions. The experimental results indicate that the failure loads of both types of welds in lap-shear specimens increase when the processing time increases for the given ranges of the processing time. The optimal processing times to maximize the failure loads of the 5754/7075 and 7075/5754 welds under lap-shear loading conditions are identified. The maximum failure load of the 7075/5754 welds is about 40% larger than that of the 5754/7075 welds. Selected optical and scanning electron micrographs of both types of welds made at different processing times before and after failure are examined. The micrographs show different weld geometries and different failure modes of the welds made at different processing times. The failure modes of the dissimilar 5754/7075 and 7075/5754 spot friction welds are quite complex and appear to strongly depend on the geometry and strength of the interfacial surface between the two deformed sheet materials. More investigations of the effects of the processing time on the strengths and failure modes of the dissimilar 5754/7075 and 7075/5754 spot friction welds in other types of specimens such as cross-tension specimens and under other loading conditions such as cyclic loading conditions should also be carried out.

Table 3.1 The mechanical properties of the aluminum 5754-O and 7075-T6 sheets.

	Young Modulus (GPa)	Yield Strength (MPa)	Tensile Strength (MPa)	Elongation (%)
Al 5754-O	69	97	207	26
Al 7075-T6	71	469	578	11

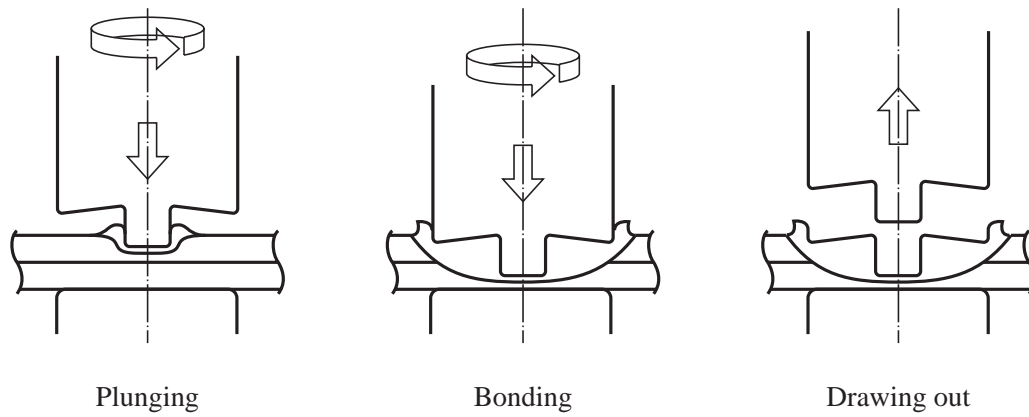


Figure 3.1 A schematic illustration of the spot friction welding process.

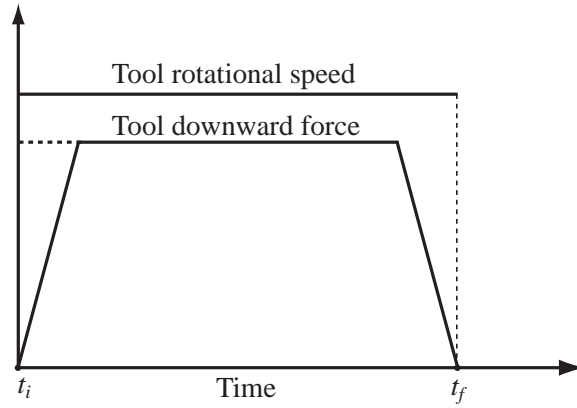


(a)

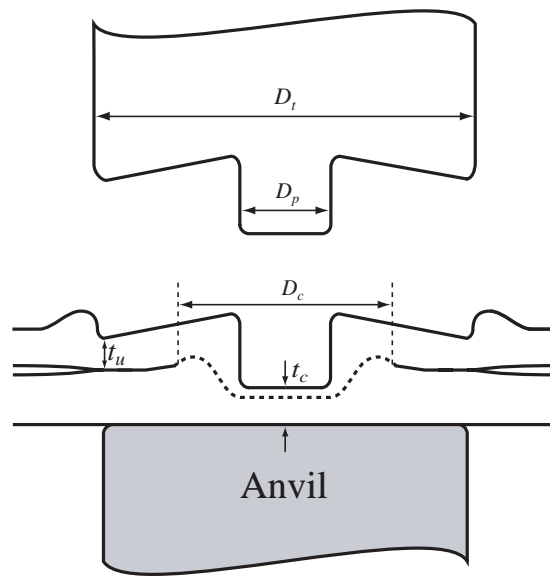


(b)

Figure 3.2 (a) A lap-shear specimen with a 5754/7075 spot friction weld, (b) a lap-shear specimen with a 7075/5754 spot friction weld.

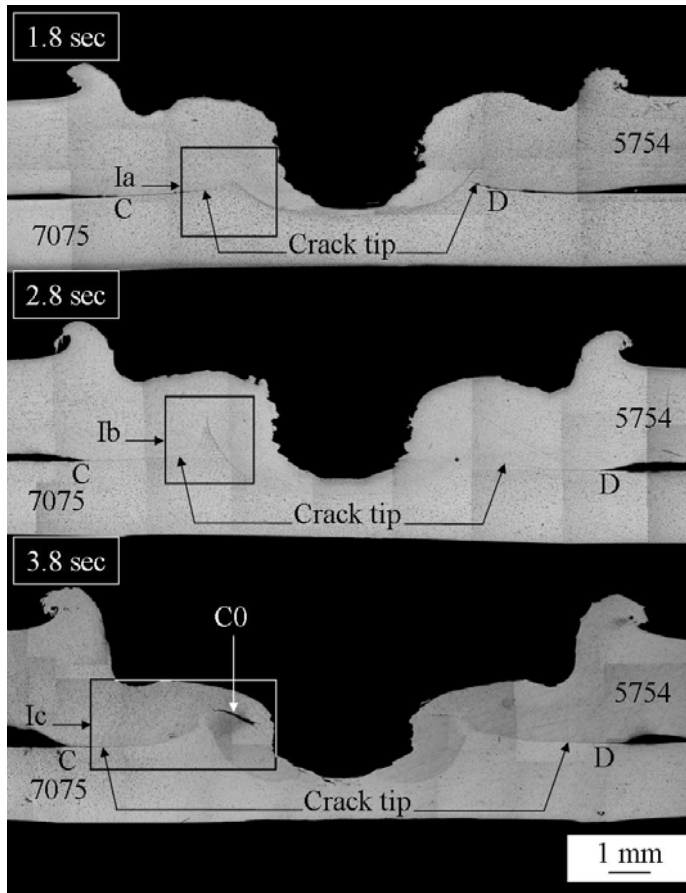


(a)

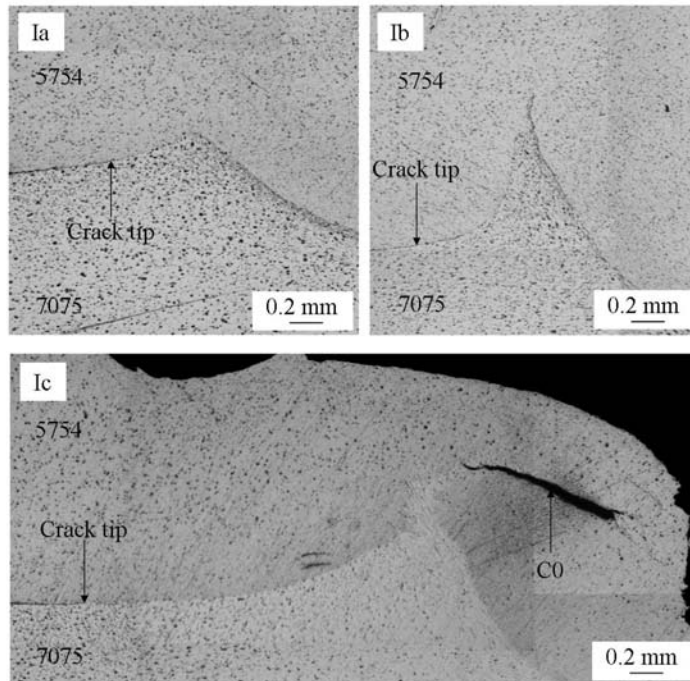


(b)

Figure 3.3 (a) A schematic plot of the tool rotational speed and the tool downward force as functions of the time, (b) a schematic plot of an extracted tool and two welded sheets after spot friction welding.



(a)



(b)

(to be continued on the next page)

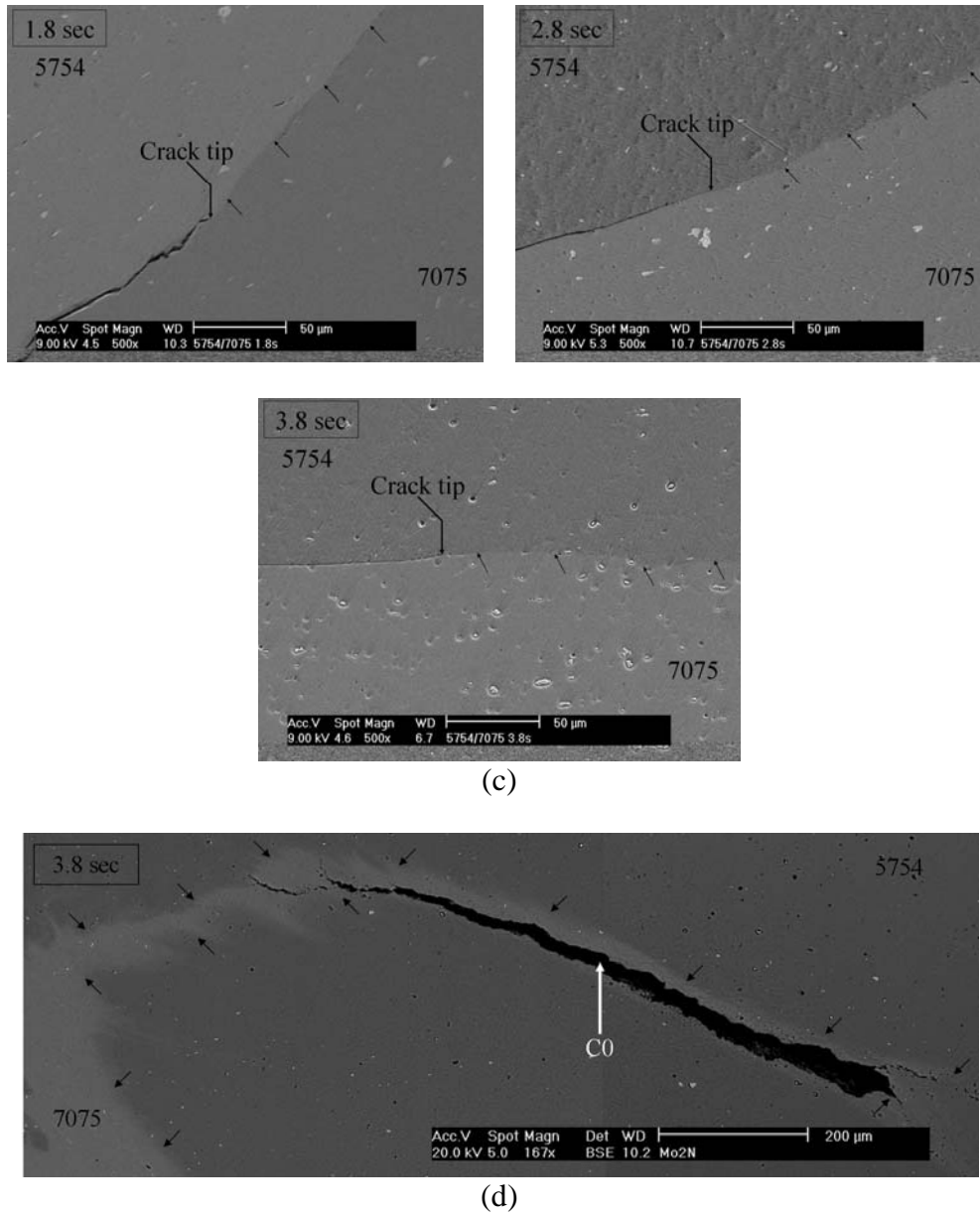
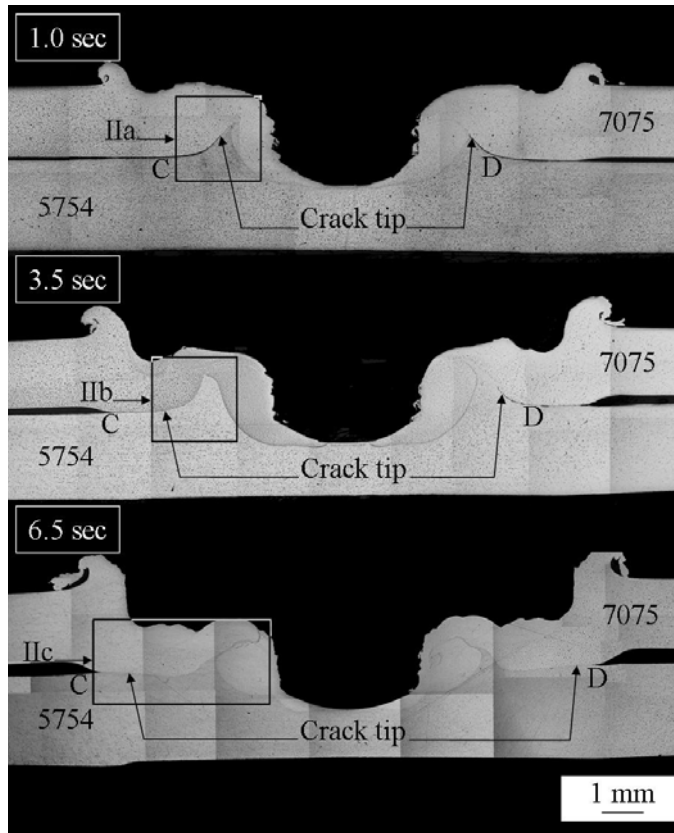
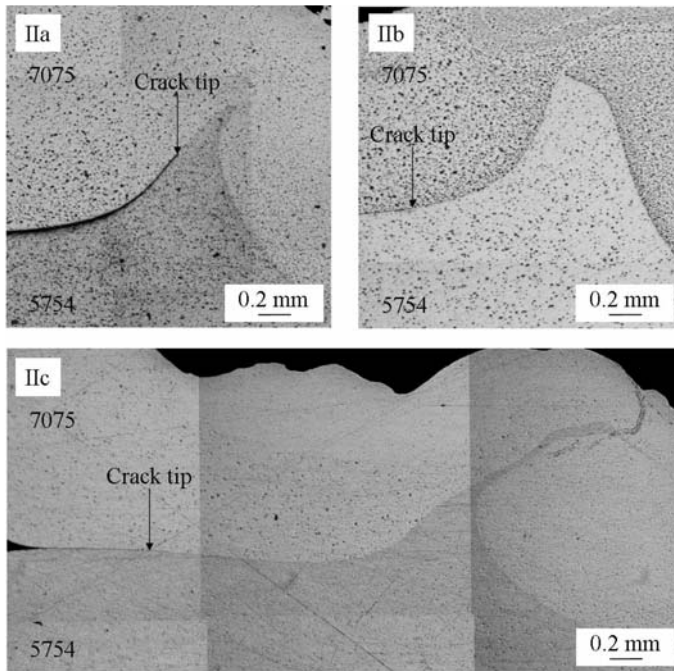


Figure 3.4 (a) Optical micrographs of the cross sections along the symmetry planes of the 5754/7075 spot friction welds at the processing times of 1.8 sec, 2.8 sec and 3.8 sec before testing, (b) close-up optical micrographs of regions Ia, Ib and Ic, (c) scanning electron micrographs of the crack tip regions as marked in (b), (d) a scanning electron micrograph of crack C0 as marked in (a) and (b).



(a)



(b)

(to be continued on the next page)

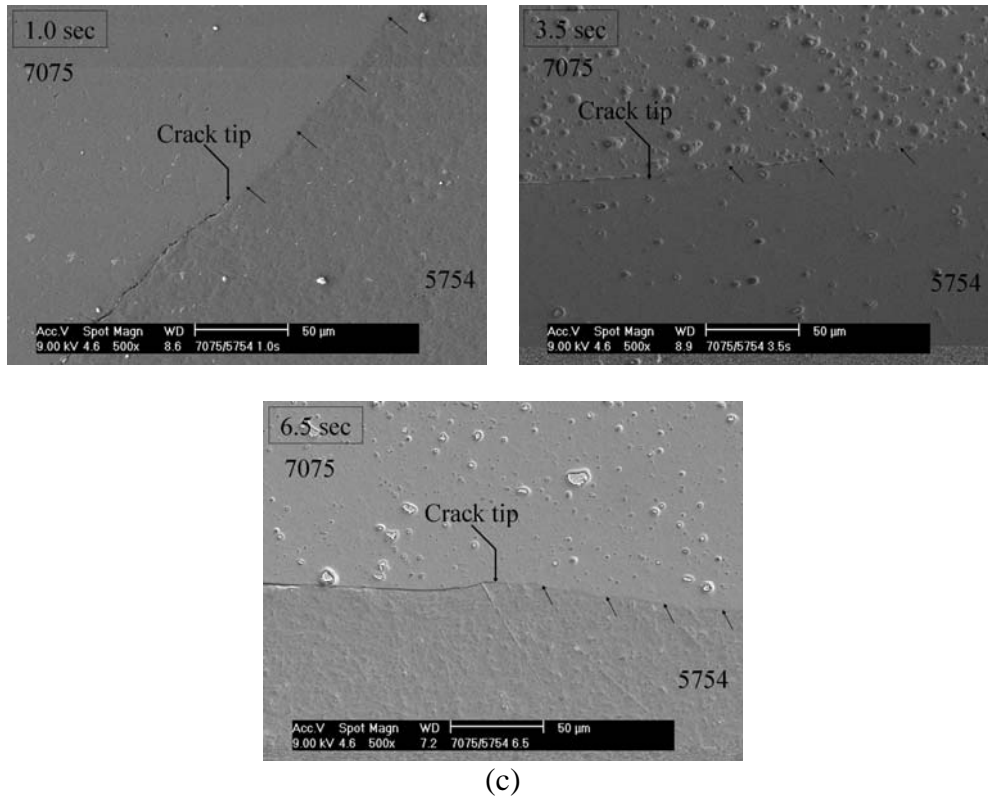


Figure 3.5 (a) Optical micrographs of the cross sections along the symmetry planes of the 7075/5754 spot friction welds at the processing times of 1.0 sec, 3.5 sec and 6.5 sec before testing, (b) close-up optical micrographs of regions IIa, IIb and IIc, (c) scanning electron micrographs of the crack tip regions as marked in (b).

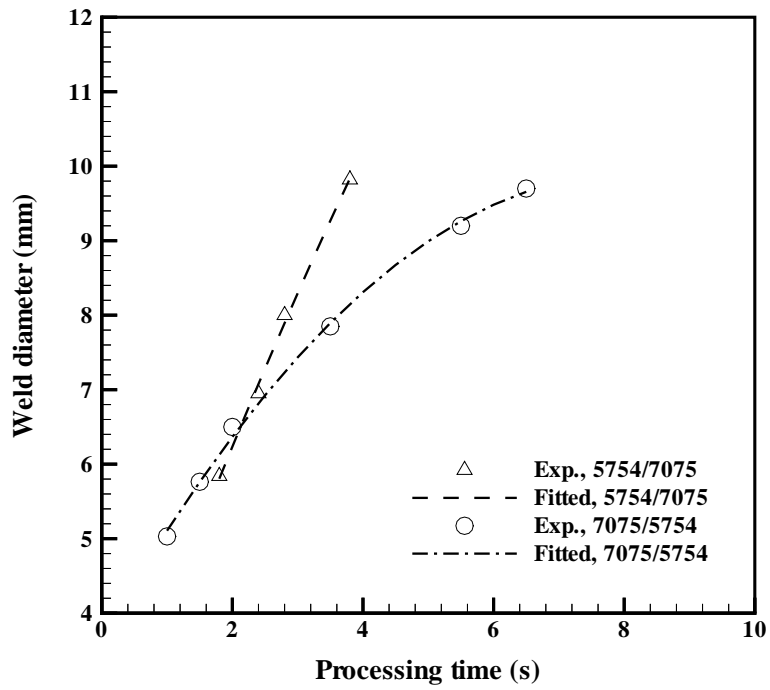


Figure 3.6 The weld diameters as functions of the processing time for the 5754/7075 and 7075/5754 spot friction welds in lap-shear specimens.

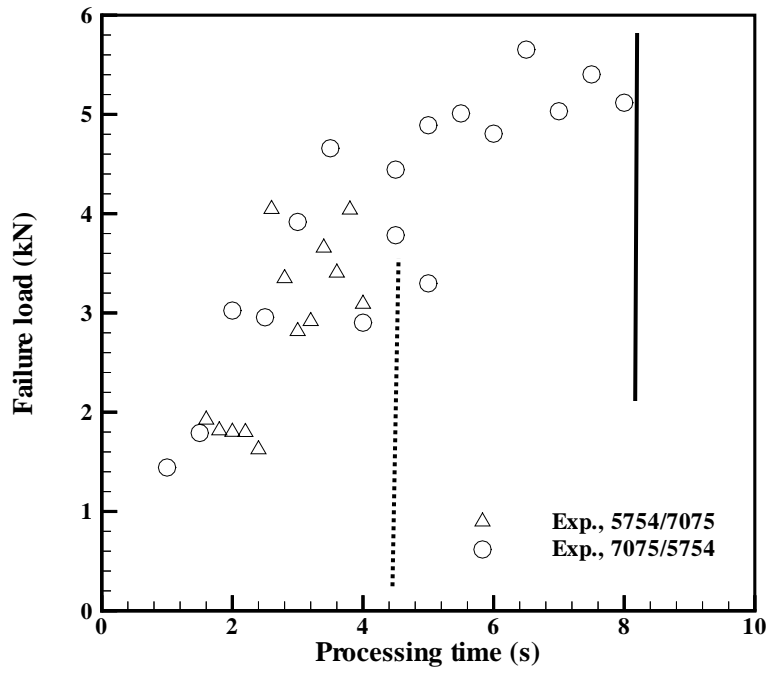
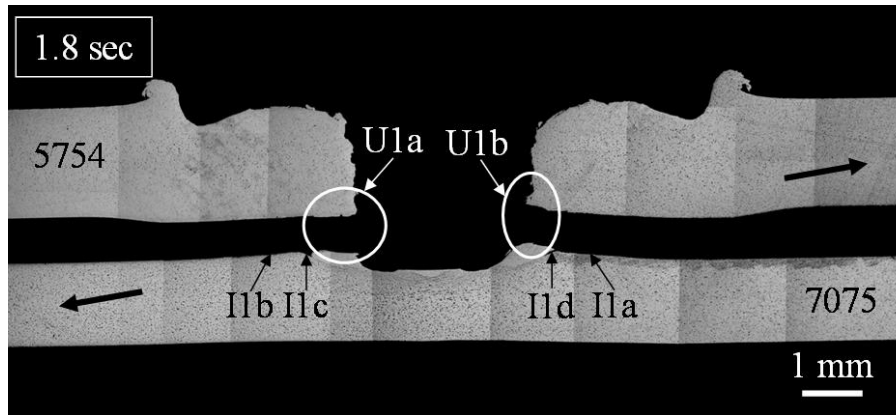
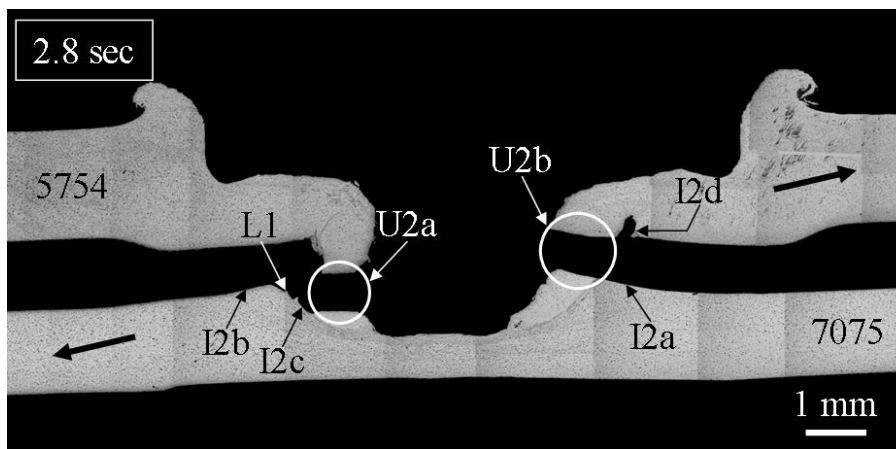


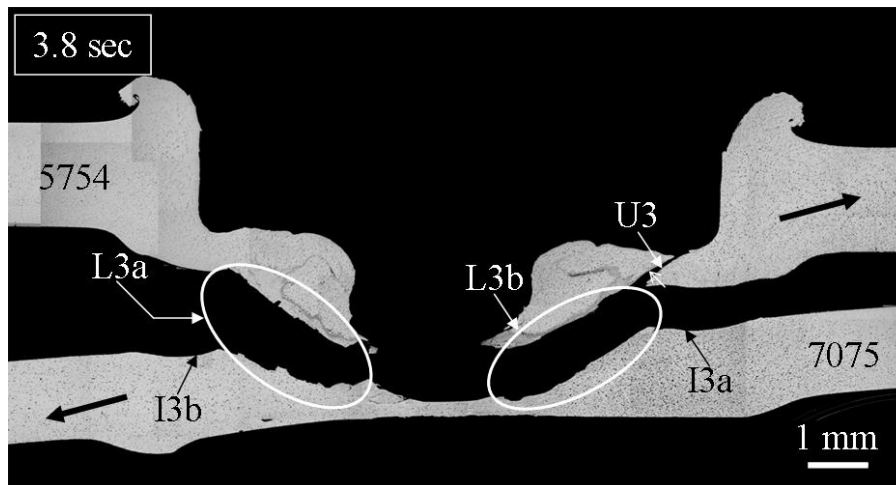
Figure 3.7 The failure loads as functions of the processing time for both 5754/7075 and 7075/5754 spot friction welds in lap-shear specimens under quasi-static loading conditions.



(a)



(b)



(c)

Figure 3.8 Optical micrographs of the cross sections along the symmetry planes of the failed 5754/7075 spot friction welds at the processing times of (a) 1.8 sec, (b) 2.8 sec, (c) 3.8 sec.

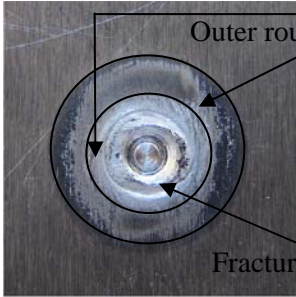
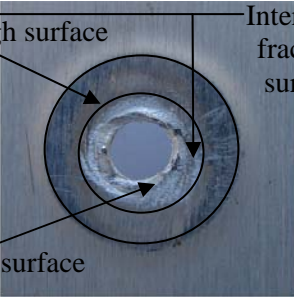
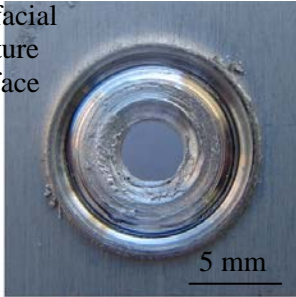
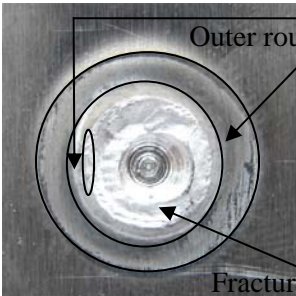
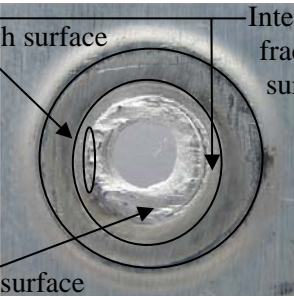
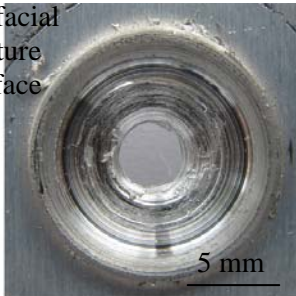
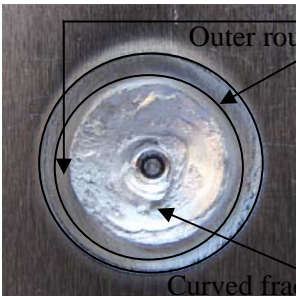
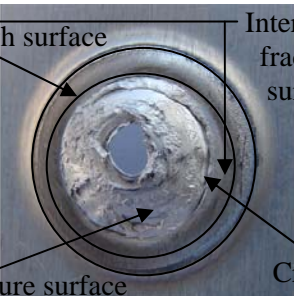
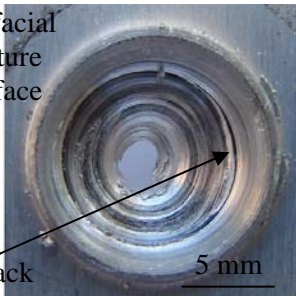
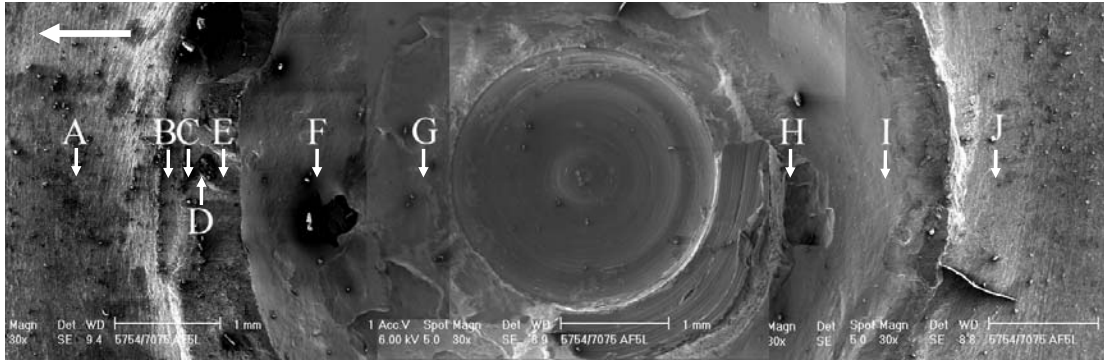
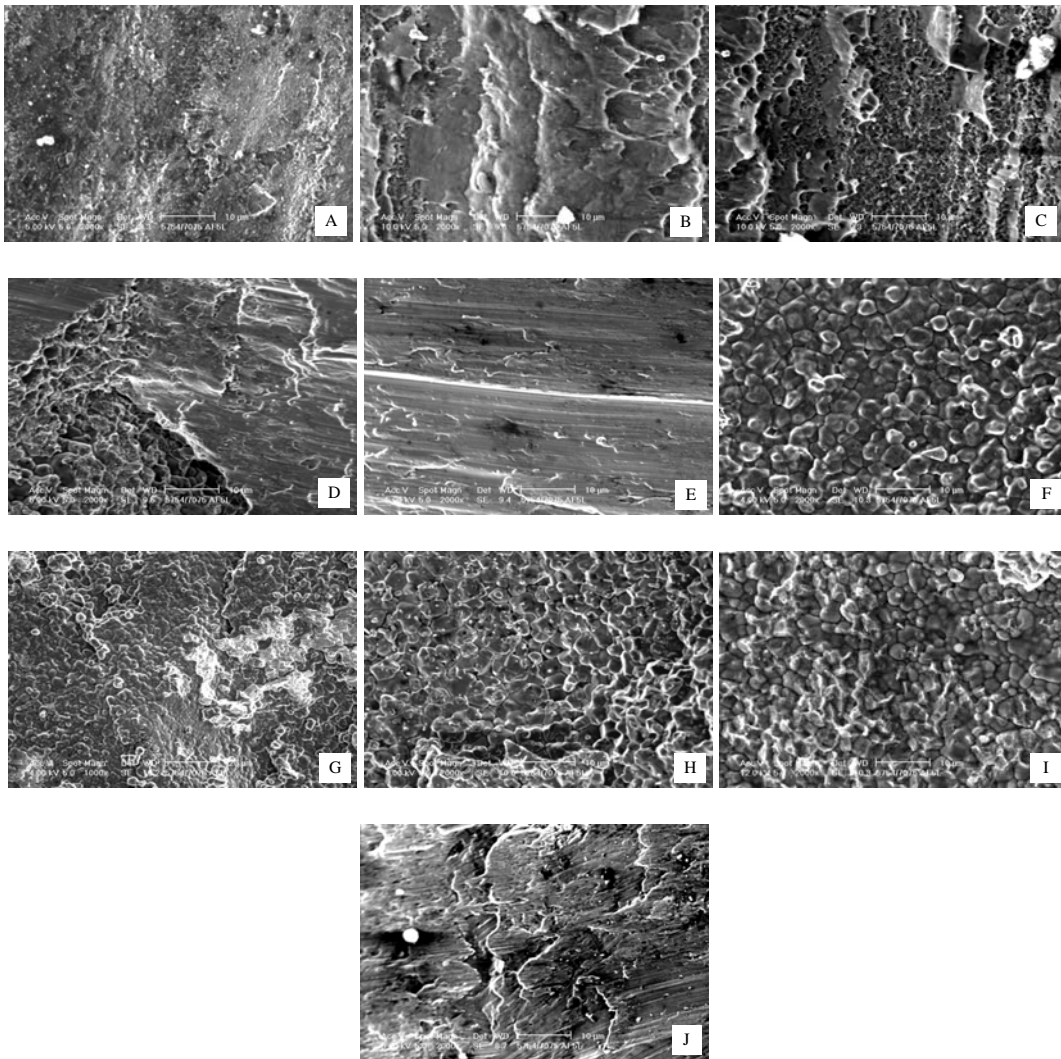
Time (s)	Lower Sheet Top View (Al 7075-T6)	Upper Sheet Bottom View (Al 5754-O)	Upper Sheet Top View (Al 5754-O)
1.8 sec	 <p>Outer rough surface</p> <p>Fracture surface</p>	 <p>Interfacial fracture surface</p>	 <p>5 mm</p>
2.8 sec	 <p>Outer rough surface</p> <p>Fracture surface</p>	 <p>Interfacial fracture surface</p>	 <p>5 mm</p>
3.8 sec	 <p>Outer rough surface</p> <p>Curved fracture surface</p>	 <p>Interfacial fracture surface</p>	 <p>Crack</p> <p>5 mm</p>

Figure 3.9 Close-up top views of the lower sheets and close-up top and bottom views of the upper sheets of the failed 5754/7075 spot friction welds at the processing times of 1.8 sec, 2.8 sec and 3.8 sec.

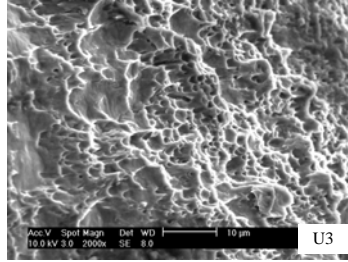


(a)



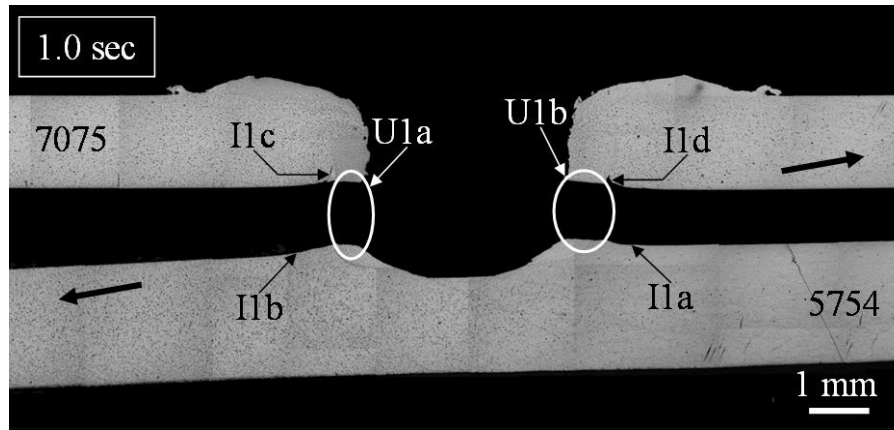
(b)

(to be continued on the next page)

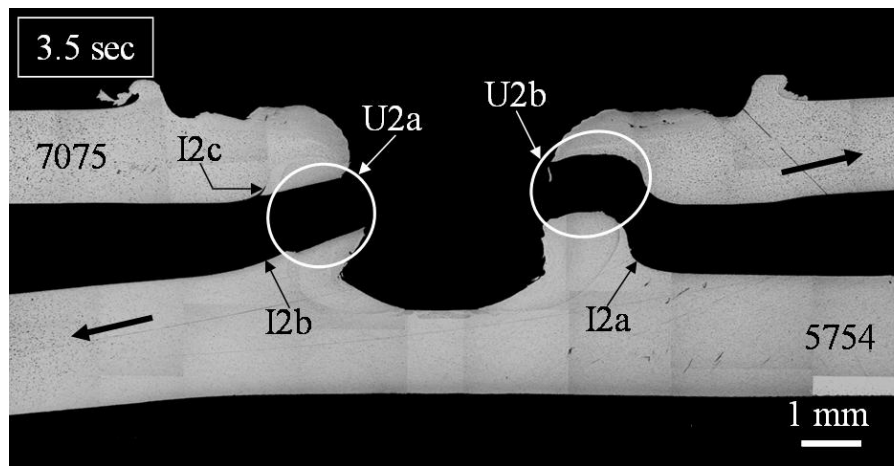


(c)

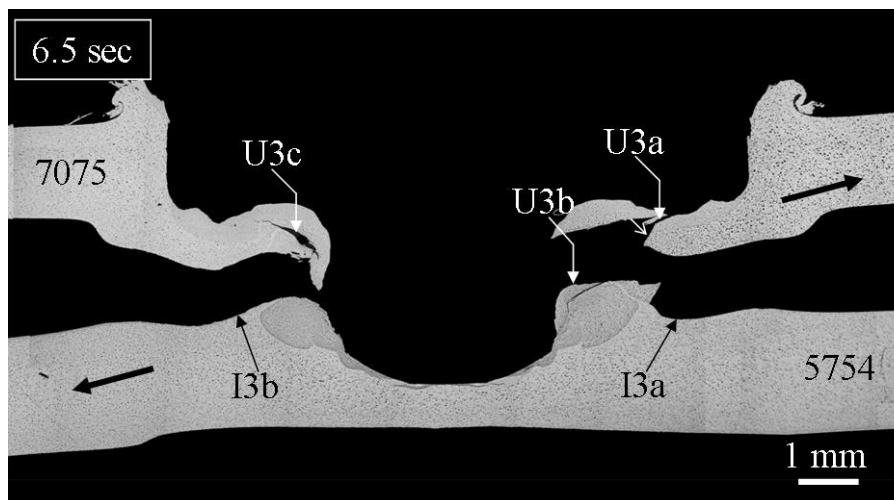
Figure 3.10 Scanning electron micrographs of (a) a fracture surface on the lower sheet obtained from another failed 5754/7075 spot friction weld made at 3.8 sec, (b) fracture surfaces of A, B, C, D, E, F, G, H, I and J, (c) a fracture surface of crack U3 as marked in Figure 3.8(c).



(a)



(b)



(c)

Figure 3.11 Optical micrographs of the cross sections along the symmetry planes of the failed 7075/5754 spot friction welds at the processing times of (a) 1.0 sec, (b) 3.5 sec, (c) 6.5 sec.

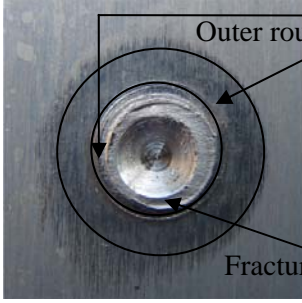
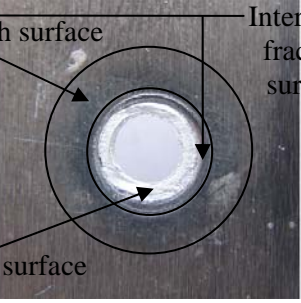
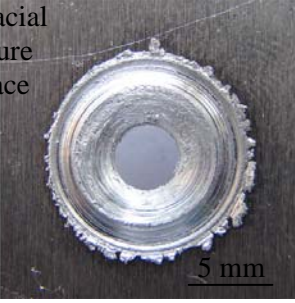
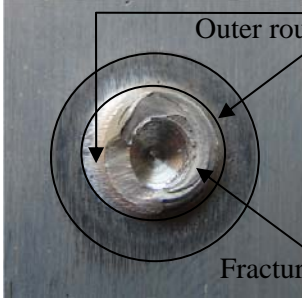
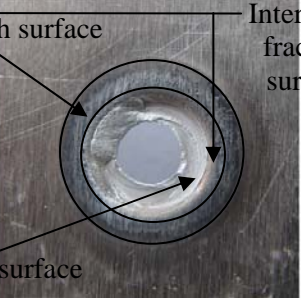
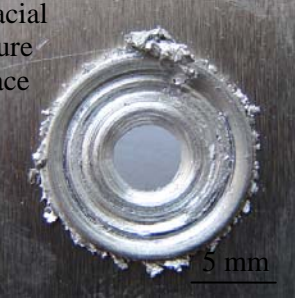
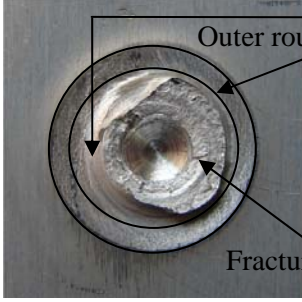
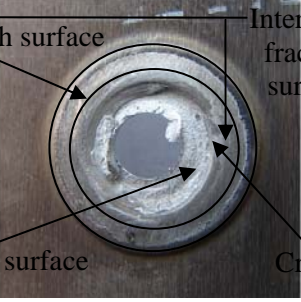
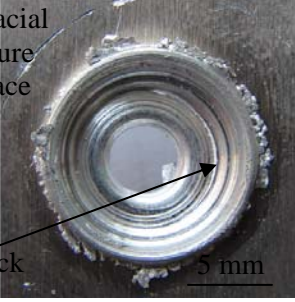
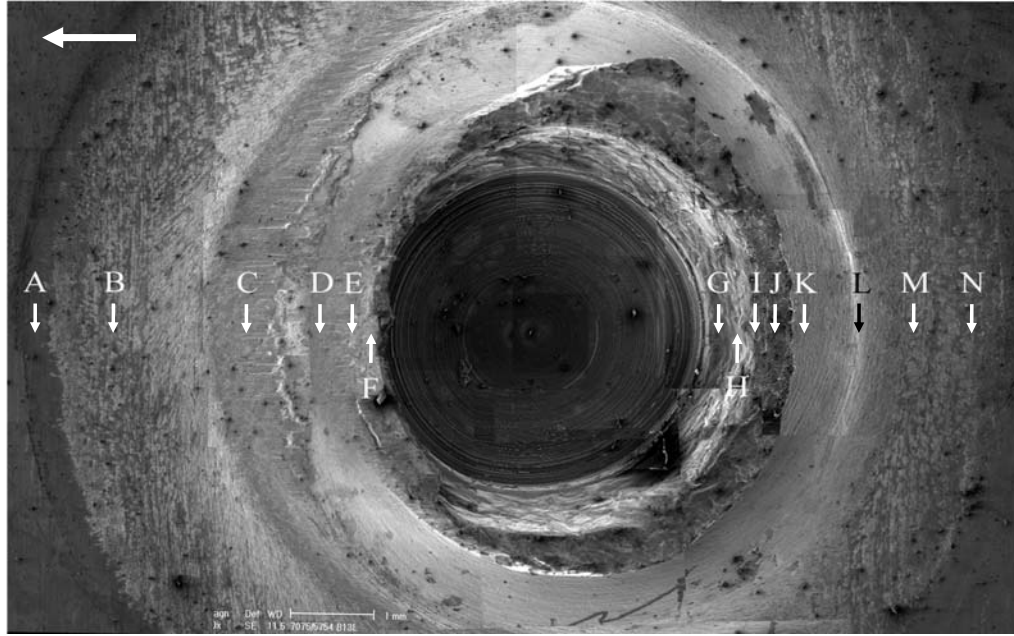
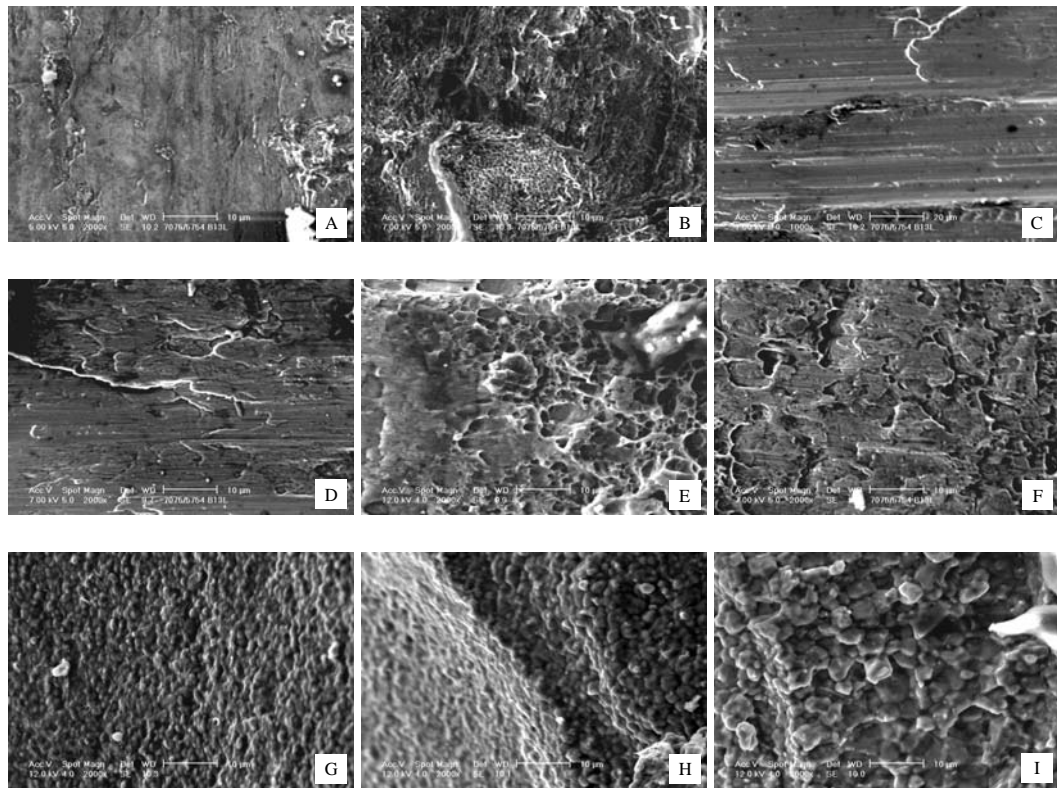
Time (s)	Lower Sheet Top View (Al 5754-O)	Upper Sheet Bottom View (Al 7075-T6)	Upper Sheet Top View (Al 7075-T6)
1.0 sec	 <p>Outer rough surface</p> <p>Fracture surface</p>	 <p>Interfacial fracture surface</p>	 <p>5 mm</p>
3.5 sec	 <p>Outer rough surface</p> <p>Fracture surface</p>	 <p>Interfacial fracture surface</p>	 <p>5 mm</p>
6.5 sec	 <p>Outer rough surface</p> <p>Fracture surface</p>	 <p>Interfacial fracture surface</p>	 <p>Crack</p> <p>5 mm</p>

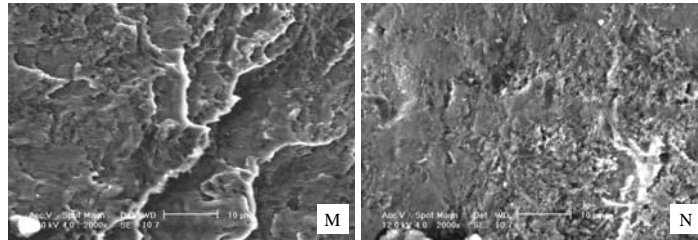
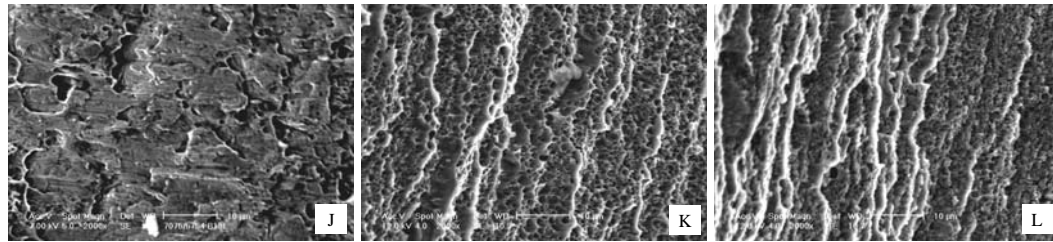
Figure 3.12 Close-up top views of the lower sheets and close-up top and bottom views of the upper sheets of the failed 7075/5754 spot friction welds at the processing times of 1.0 sec, 3.5 sec and 6.5 sec.



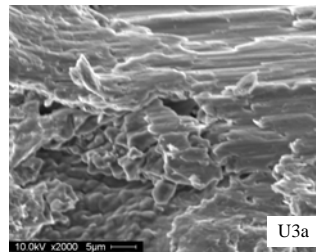
(a)



(to be continued on the next page)



(b)



(c)

Figure 3.13 Scanning electron micrographs of (a) a fracture surface on the lower sheet obtained from another failed 7075/5754 spot friction weld made at 6.5 sec, (b) fracture surfaces of A, B, C, D, E, F, G, H, I, J, K, L, M and N, (c) a fracture surface of crack U3a as marked in Figure 3.11(c).

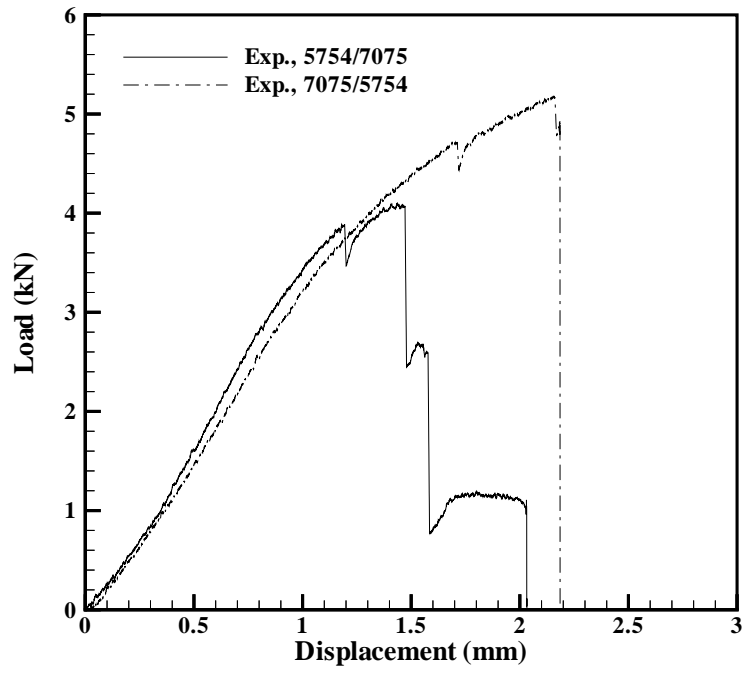


Figure 3.14 Typical load-displacement curves of the 5754/7075 and 7075/5754 spot friction welds at the optimal processing times under lap-shear loading conditions.

References

- [1] Thornton PH, Krause, AR, Davies, R G. The aluminum spot weld. *Welding J* 1996;75:101s-108s.
- [2] Gean A, Westgate SA, Kucza JC, Ehrstrom JC. Static and fatigue behavior of spot-welded 5182-O aluminum alloy sheet. *Welding J* 1999;78:80s-86s.
- [3] Sakano R, Murakami K, Yamashita K, Hyoe T, Fujimoto M, Inuzuka M, Nagao Y, Kashiki H. Development of spot FSW robot system for automobile body members. In: *Proceedings of the 3rd international symposium of friction stir welding*, Kobe, Japan, September 27-28, 2001.
- [4] Iwashita T. Method and apparatus for joining. US Patent 6601751 B2, August 5, 2003.
- [5] Fujimoto M, Inuzuka M, Nishio M, Nakashima Y. Development of friction spot joining (Report 1) - Cross sectional structures of friction spot joints. The National Meeting of Japan Welding Society, No. 74, 2004, pp. 4-5.
- [6] Fujimoto M, Inuzuka M, Nishio M, Nakashima Y. Development of friction spot joining (Report 2) - Mechanical properties of friction spot joints. The National Meeting of Japan Welding Society, No. 74, 2004, pp. 6-7.
- [7] Hinrichs JF, Smith CB, Orsini BF, DeGeorge RJ, Smale BJ, Ruehl PC. Friction stir welding for the 21st century automotive industry. In: *Proceedings of the 5th international symposium of friction stir welding*, Metz, France, September 14-16, 2004.
- [8] Lin P-C, Lin S-H, Pan J, Pan T, Nicholson JM, Garman, MA. Microstructures and failure modes of spot friction welds in lap-shear specimens of aluminum 6111-T4 sheets. SAE Technical Paper No. 2004-01-1330, Society of Automotive Engineers, Warrendale, PA: 2004.
- [9] Pan T, Joaquin A, Wilkosz DE, Reatherford L, Nicholson JM. Spot friction welding for sheet aluminum joining. In: *Proceedings of the 5th international symposium of friction stir welding*, Metz, France, September 14-16, 2004.
- [10] Mitlin D, Radmilovic V, Pan T, Chen J, Feng Z, Santella ML. Structure-properties relations in spot friction welded (also known as friction stir spot welded) 6111 aluminum. *Mater Sci Eng A* 2006;441:79-96.
- [11] Tran V-X, Lin P-C, Pan J, Pan T, Tyan T. Failure loads of aluminum 6111 spot friction welds under quasi-static and dynamic loading conditions. SAE Technical Paper No. 2007-01-0983, Society of Automotive Engineers, Warrendale, PA:2007.

- [12] Lin P-C, Pan J, Pan T. Fracture and fatigue mechanisms of spot friction welds in lap-shear specimens of aluminum 6111 sheets. SAE Technical Paper No. 2005-01-1247, Society of Automotive Engineers, Warrendale, PA:2005.
- [13] Lin P-C, Pan J, Pan T. Fatigue failures of aluminum 6111 spot friction welds under cyclic loading conditions. SAE Technical Paper No. 2006-01-1207, Society of Automotive Engineers, Warrendale, PA:2006.
- [14] Lin P-C, Pan J, Pan T. Failure modes and fatigue life estimations of spot friction welds in lap-shear specimens of aluminum 6111-T4 sheets, Part 1: Welds made by a concave tool. *Int J Fatigue* 2008;30:74-89.
- [15] Lin P-C, Pan J, Pan T. Failure modes and fatigue life estimations of spot friction welds in lap-shear specimens of aluminum 6111-T4 sheets, Part 2: Welds made by a flat tool. *Int J Fatigue* 2008;30:90-105.
- [16] Tran V-X, Pan J, Pan T. Fatigue behaviors of aluminum 5754-O spot friction welds in lap-shear Specimen. SAE Technical Paper No. 2008-01-1139, Society of Automotive Engineers, Warrendale, PA:2008.
- [17] Tran V-X, Pan J, Pan T. Fatigue behavior of aluminum 5754-O and 6111-T4 spot friction welds in lap-shear specimens. *Int J Fatigue*, 2008;3:2175-2190.
- [18] Pan T. Friction stir spot welding (FSSW) - A literature review. SAE Technical Paper No. 2007-01-1702, Society of Automotive Engineers, Warrendale, PA:2007.
- [19] Tozaki Y, Uematsu Y, Tokaji K. Effect of welding condition on tensile strength of dissimilar friction stir spot welds between different aluminum alloys. In: Proceedings of 6th international symposium on friction stir welding, Saint-Sauveur, Nr Montreal, Canada, October 10 - 13, 2006.
- [20] Su P, Gerlich A, North TH, Bendzsak GJ. Intermixing in dissimilar friction stir spot welds. *Metall Mater Trans A* 2007;38A:584-595.
- [20] Kaufman J-G. Introduction to Aluminum Alloys and Tempers. The Materials Information Society - ASM International, Materials Park, OH:2000.
- [21] Auto Steel Partnership, 1997. <http://www.a-sp.org/database/default.asp?doc=34>

CHAPTER IV

INVESTIGATION OF FATIGUE BEHAVIORS OF SPOT FRICTION WELDS BETWEEN DISSIMILAR SHEET MATERIALS IN LAP-SHEAR AND CROSS-TENSION SPECIMENS PART 1: WELDS BETWEEN ALUMINUM 5754-O AND 7075-T6 SHEETS

Abstract

Fatigue behavior of dissimilar 5754/7075 and 7075/5754 spot friction welds between aluminum 5754-O and 7075-T6 sheets in lap-shear and cross-tension specimens is investigated based on experimental observations and three fatigue life estimation models. Optical micrographs of the 5754/7075 and 7075/5754 welds before and after failure under quasi-static and cyclic loading conditions are examined to understand the fracture and failure mechanisms of the welds. The micrographs show that the 5754/7075 welds in lap-shear specimens mainly fail from the kinked crack through the lower sheet thickness under cyclic loading conditions. Also, the 7075/5754 welds in lap-shear specimens mainly fail from the kinked crack through the lower sheet thickness and from the fracture surface through the upper sheet thickness under cyclic loading conditions. The micrographs show that the 5754/7075 and 7075/5754 welds in cross-tension specimens mainly fail from the fracture surfaces along the interfacial surface between the two deformed sheet materials and in the deformed upper sheet material under cyclic loading conditions. A kinked fatigue crack growth model based on the stress intensity factor solutions for finite kinked cracks, a structural stress model based on the closed-form structural stress solutions at

the critical locations of the welds and a through-nugget fatigue crack growth model based on the closed-form stress intensity factor solutions for the through-nugget cracks are adopted and developed to estimate the fatigue lives of the 5754/7075 and 7075/5754 welds in lap-shear and cross-tension specimens. The fatigue life estimations based on the kinked fatigue crack growth model, the structural stress model and the through-nugget fatigue crack growth model agree well with the experimental results. Finally, the effective stress intensity factor and J integral solutions at the critical locations of the welds obtained from three-dimensional finite element analyses appear to be good fracture mechanics parameters to correlate the experimental fatigue data for the 5754/7075 and 7075/5754 welds in lap-shear and cross-tension specimens.

Keywords: Spot friction weld; Friction stir spot weld; Failure mode; Fatigue life; Kinked crack; Through-nugget crack; Structural stress; Life estimation; Correlation

4.1. Introduction

Resistance spot welding is the most commonly used joining method for body-in-white parts made of steel sheets. However, resistance spot welding of aluminum sheets is likely to produce poor welds as reported by Thornton et al. [1] and Gean et al. [2]. Recently, a spot friction welding technology to join aluminum sheets was developed by Mazda Motor Corporation and Kawasaki Heavy Industry [3,4]. The most significant advantage of the spot friction welding process comparing to the conventional welding processes is that the joint can be made without melting the base

metal. A schematic illustration of the spot friction welding process used to join two aluminum sheets was presented, for example, in Lin et al. [5].

The mechanical behavior of aluminum spot friction welds under quasi-static loading conditions was studied, for example, see Fujimoto et al. [6,7], Hinrichs et al. [8], Lin et al. [5] and Pan et al. [9]. The metallurgical aspects of aluminum 6111-T4 spot friction welds were investigated by Mitlin et al. [10]. Tran et al. [11] investigated the failure loads of spot friction welds in aluminum 6111-T4 lap-shear specimens under quasi-static and dynamic loading conditions. Recently, Lin et al. [12-15] and Tran et al. [16,17] investigated the fatigue behaviors of spot friction welds in aluminum 6111-T4 and 5754-O sheets based on experimental observations, fracture mechanics, and the structural stress approach. A comprehensive literature review for spot friction welds can be found in Pan [18]. Note that most of the literature is for spot friction welds between similar aluminum sheets.

It should be noted that many types of aluminum alloys are currently used to make different components of vehicles in the automotive industry. For example, aluminum 5754 alloys are widely employed to produce different parts such as internal door stiffeners, entire body-in-white, and inner body panels as reported in Kaufman [19]. Therefore, dissimilar spot friction welds between different aluminum sheets have been studied by many researchers. For example, dissimilar spot friction welds between aluminum 2017-T6 and 5052 sheets, and between aluminum 7075-T6 and 2024-T3 sheets were investigated by Tozaki et al. [20] and Tweedy et al. [21], respectively. Also, Su et al. [22] investigated the intermixing of dissimilar spot friction welds between aluminum 5754 and 6111 sheets by experiments and

numerical simulations. Recently, Tran et al. [23,24] investigated the effects of the processing time on the strengths and failure modes of two types of dissimilar spot friction welds between aluminum 5754-O and 7075-T6 sheets in lap-shear specimens by experiments. With the increasing use of aluminum alloys in vehicles, an efficient joining method is also needed to join different components made of aluminum and steel sheets. Therefore, the spot friction welding between aluminum and steel sheets needs to be explored.

Accurate models for the static, dynamic and fatigue strengths of spot friction welds between dissimilar materials are critical to enhance the product development for the crashworthiness, structural integrity and durability of the automotive components. However, the fracture and failure mechanisms of spot friction welds between dissimilar materials under cyclic loading conditions have not been investigated. Note that lap-shear and cross-tension specimens were commonly used to investigate the mechanical behaviors of spot welds under shear and tensile dominant loading conditions, respectively. However, most of the current literature is for spot friction welds in lap-shear specimens. Therefore, spot friction welds in lap-shear and cross-tension specimens are tested under quasi-static and cyclic loading conditions in this investigation. Research results for dissimilar spot friction welds between aluminum 5754-O and 7075-T6 sheets are reported in Part 1 and those for dissimilar spot friction welds between aluminum 6000 series alloy and coated steel sheets are reported in Part 2.

In this paper, fatigue behavior of dissimilar spot friction welds between aluminum 5754-O and 7075-T6 sheets in lap-shear and cross-tension specimens is investigated

based on experimental observations and three fatigue life estimation models. As in Tran et al. [23,24], the dissimilar spot friction welds are denoted as 5754/7075 when aluminum alloys 5754-O and 7075-T6 were used as the upper and lower sheets, respectively. The dissimilar spot friction welds are denoted as 7075/5754 when aluminum alloys 7075-T6 and 5754-O were used as the upper and lower sheets, respectively. The 5754/7075 and 7075/5754 spot friction welds between aluminum 5754-O and 7075-T6 sheets in lap-shear and cross-tension specimens are first tested under quasi-static and cyclic loading conditions. Optical micrographs of the welds before and after failure under quasi-static and cyclic loading conditions are examined to understand the fracture and failure mechanisms of the welds under different loading conditions. Based on the experimental observations of the paths of the dominant fatigue cracks, three estimation fatigue life models are adopted and developed to estimate the fatigue lives of the welds. A kinked fatigue crack growth model based on the stress intensity factor solutions for finite kinked cracks and a structural stress model based on the closed-form structural stress solutions at the critical locations of the welds as reported in Tran et al. [17] are adopted to estimate the fatigue lives of the 5754/7075 and 7075/5754 welds in lap-shear specimens. A through-nugget fatigue crack growth model based on the closed-form stress intensity factor solutions for the through-nugget cracks and the Paris law for the fatigue crack propagation is developed to estimate the fatigue lives of the 5754/7075 and 7075/5754 welds in cross-tension specimens. The fatigue life estimations based on the kinked fatigue crack growth model, the structural stress model and the through-nugget fatigue crack growth model are compared with the experimental results.

Finally, the effective stress intensity factor and J integral solutions at the critical locations of the welds obtained from three-dimensional finite element analyses are used to correlate the experimental fatigue data for the 5754/7075 and 7075/5754 spot friction welds in lap-shear and cross-tension specimens.

4.2. Micrographs of 5754/7075 and 7075/5754 spot friction welds

Aluminum 5754-O and 7075-T6 sheets with the thicknesses of 2.0 mm and 1.6 mm, respectively, are used to make the spot friction welds tested in this investigation. The sheet materials used in this investigation are identical to those used in Tran et al. [23,24]. The mechanical properties of the aluminum 5754-O and 7075-T6 sheets can be found in Tran et al. [23,24]. The welds were made by using a spot friction welding gun manufactured by Kawasaki Robotics, USA. For the spot friction welding process under load-controlled conditions, the important welding processing parameters are the tool geometry, the tool rotational speed, the tool downward force and the processing time. In this investigation, a tool with a concave shoulder and a threaded probe pin was used to make the dissimilar 5754/7075 and 7075/5754 spot friction welds in lap-shear and cross-tension specimens. A tool rotational speed of 3000 rpm and a tool downward force of 5.88 kN were specified to make both types of welds. The 5754/7075 and 7075/5754 welds in lap-shear specimens were first made under different processing times and tested under quasi-static loading conditions. The optimal processing times for the maximum failure loads of the spot friction welds under this particular set of the welding processing parameters in lap-shear specimens were identified as 3.8 sec and 6.5 sec for the 5754/7075 and 7075/5754 spot friction

welds, respectively (Tran et al. [23,24]). These optimal processing times and the welding processing parameters specified above were then used to make the 5754/7075 and 7075/5754 spot friction welds in lap-shear and cross-tension specimens tested in this investigation.

Figures 4.1(a) and 4.2(a) show optical micrographs of the cross sections along the symmetry planes of the 5754/7075 and 7075/5754 spot friction welds before testing. Note that the aluminum 5754-O and 7075-T6 polished surfaces have different gray levels due to different chemical compositions as shown in the figures. In Figures 4.1(a) and 4.2(a), the indentation profile reflects the general shape of the threaded probe pin and the concave shoulder of the tool. The bottom surfaces of the lower sheets are slightly dented as shown in Figures 4.1(a) and 4.2(a).

As shown in Figures 4.1(a) and 4.2(a), a layer of the upper sheet material, pushed and deformed by the threaded probe pin, can be seen near the outer area of the central hole. The interfacial surface between the two deformed sheet materials can be seen near the outer area of the central hole. Due to the rotating pin penetration, the heated and softened upper sheet material was pushed down near the probe pin. Also, the heated and softened lower sheet material rose upward and outward and then toward the central hole as shown in Figures 4.1(a) and 4.2(a). The notch tips are marked by points C and D in Figures 4.1(a) and 4.2(a). The notches extend into the welds and become cracks. The locations of the crack tips are marked in the figures. Note that the concave tool shoulder squeezed out some upper sheet material but maintained some upper sheet material near the central hole. The tool shoulder indentation resulted in a radial expansion of the upper sheet material along the outer

circumference of the tool shoulder indentation. However, due to the constraint of the neighboring material, the sheet was therefore bent along the outer circumference of the tool shoulder indentation. The bends are marked as B1 and B2 as shown in Figures 4.1(a) and 4.2(a).

Figure 4.1(b) shows a close-up optical micrograph of region I as marked in Figure 4.1(a). Figure 4.2(b) shows a close-up optical micrograph of region II as marked in Figure 4.2(a). The locations of the crack tips are also marked in the figures. As shown in Figure 4.1(b), the lower sheet material extends significantly into the upper sheet material. As shown in Figure 4.2(b), the lower sheet material extends significantly into the upper sheet material and reaches the rim of the central hole. Note that the interfacial surfaces between the two deformed sheet materials near the central holes appear to be well bonded possibly due to high pressure and large plastic deformation.

Figure 4.1(c) shows a scanning electron micrograph of the crack tip region of the 5754/7075 spot friction weld as marked in Figure 4.1(b). Figure 4.2(c) shows a scanning electron micrograph of the crack tip region of the 7075/5754 spot friction weld as marked in Figure 4.2(b). The small arrows are used to mark the interfacial surfaces between the two deformed sheet materials. The locations of the crack tips can be identified by the scanning electron micrographs of the crack tip regions as shown in the figures. As shown in the figures, some part of the crack surfaces near the tips become vague and may be bonded by the welding process. A large crack, marked as C0 in Figures 4.1(a) and 4.1(b), is shown near the central hole in the

deformed upper sheet. Crack C0 was likely formed during the welding process (Tran et al. [23,24]).

4.3. Specimens and experiments

Lap-shear specimens were made by using two 25.4 mm × 101.6 mm aluminum sheets with a 38.1 mm × 25.4 mm overlap area. Figures 4.3(a) and 4.3(b) show a lap-shear specimen with a 5754/7075 spot friction weld and a lap-shear specimen with a 7075/5754 spot friction weld, respectively. Note that one doubler made of the upper sheet and another doubler made of the lower sheet with a dimension of 25.4 mm × 25.4 mm are attached to the ends of the upper and lower sheets, respectively, of the lap-shear specimen during testing. The doublers are used to align the applied load to avoid the initial realignment of the specimen under lap-shear loading conditions. The cross-tension specimens were made by using two 25.4 mm × 101.6 mm aluminum sheets with a 25.4 mm × 25.4 mm overlap area. Figures 4.3(c) and 4.3(d) show a cross-tension specimen with a 5754/7075 spot friction weld and a cross-tension specimen with a 7075/5754 spot friction weld, respectively. Note that four steel pieces with a cross sectional area of 25.4 mm × 25.4 mm are used to clamp the upper and lower sheets, except the overlap area, to the cross-tension testing fixture. Therefore, the tolerance width between the overlap area and the clamped area is 12.7 mm. Also, the effective length of the cross-tension specimen, measured as the length of the sheets without clamped parts is 50.8 mm. Due to the load-controlled welding process, the actual plunge depths of the tool penetration and the geometries of the spot friction welds may not be controlled precisely under the same welding

processing parameters. In order to minimize the effects of the weld geometry on the experimental results, we selected the lap-shear and cross-tension specimens with the 5754/7075 and 7075/5754 spot friction welds that have nearly the same actual plunge depths of the tool penetration for the quasi-static and fatigue tests.

Lap-shear and cross-tension specimens with 5754/7075 and 7075/5754 spot friction welds were first tested under quasi-static loading conditions by using an Instron testing machine at a monotonic displacement rate of 1.0 mm per minute. The tests were terminated when specimens were separated. The load and displacement histories were simultaneously recorded during each test. Figures 4.4(a) and 4.4(b) show typical load-displacement curves for the 5754/7075 and 7075/5754 spot friction welds, respectively, in lap-shear and cross-tension specimens under quasi-static loading conditions. Note that the slackness in the test set up has been removed in the load-displacement curves. The average failure loads, defined as the maximum load of the load-displacement curve, obtained from three tested lap-shear specimens and three tested cross-tension specimens with the 5754/7075 welds are 4.03 kN and 1.48 kN, respectively. The average failure loads obtained from three tested lap-shear specimens and three tested cross-tension specimens with the 7075/5754 welds are 5.65 kN and 1.55 kN, respectively.

The failure loads of the lap-shear and cross-tension specimens with spot friction welds under quasi-static loading conditions were used as reference loads to determine the loads applied in the fatigue tests. The lap-shear and cross-tension specimens were then tested under cyclic loading conditions by using an Instron servo-hydraulic fatigue testing machine. The test frequency was 10 Hz and the load ratio R was 0.2.

The tests were terminated when the specimens were separated, or nearly separated when the displacement of the two grips of the lap-shear and cross-tension specimens exceeded 5 mm and 10 mm, respectively. Some tests were stopped before the final failures of the specimens to examine the fatigue crack growth patterns. Figures 4.4(c) and 4.4(d) show the experimental results for the 5754/7075 and 7075/5754 spot friction welds, respectively, in lap-shear and cross-tension specimens under cyclic loading conditions.

4.4. Failure modes of spot friction welds in lap-shear specimens

4.4.1. Failure modes of 5754/7075 welds in lap-shear specimens

We conducted experiments for the 5754/7075 spot friction welds in lap-shear specimens under quasi-static and cyclic loading conditions. Based on the experimental observations, the failed 5754/7075 welds in lap-shear specimens under quasi-static loading conditions show one failure mode. The failed 5754/7075 welds in lap-shear specimens under cyclic loading conditions show another failure mode. Figure 4.5(a) shows a schematic plot of a lap-shear specimen with a 5754/7075 spot friction weld with the upper sheet thickness $t_u = 2.0$ mm and the lower sheet thickness $t_l = 1.6$ mm under applied resultant loads (shown as the bold arrows). Figure 4.5(b) shows a schematic plot of the cross section along the symmetry plane of the 5754/7075 spot friction weld in a lap-shear specimen. In this figure, the thick dashed lines represent the interfacial surfaces between the two deformed sheet materials and the thin solid lines represent either the fracture surfaces or cracks. It should be noted that the interfacial surface between the two deformed sheet materials

was well bonded as discussed earlier. Figure 4.5(c) summarizes the failure modes of the 5754/7075 spot friction welds in lap-shear specimens under quasi-static and cyclic loading conditions.

As shown in Figure 4.5(b) and as summarized in Figure 4.5(c), under quasi-static loading conditions, cracks A and B appear to emanate from the original crack tips of the weld and propagate a bit along the interfacial surface. Crack A then becomes crack C that propagates into the upper sheet thickness. After propagating through the upper sheet thickness, crack C becomes a circumferential crack that propagates along the nugget circumference. When the load continues to increase, the upper and lower sheets are eventually separated by fracture surfaces D and E mostly in the lower sheet material. Under cyclic loading conditions, cracks A and B appear to emanate from the original crack tips of the weld and propagate a bit along the interfacial surface. Crack B then becomes fatigue crack D that propagates into the lower sheet material in the downward direction toward the central hole. Near the final stage of the specimen failure, crack D becomes crack F that propagates through the remaining lower sheet thickness. Finally, crack F becomes a transverse through crack that propagates in the width direction of the specimen and the left part of the lower sheet is eventually separated. It should be noted that the micrographs to show the failure mode of the 5754/7075 spot friction welds in lap-shear specimens under quasi-static loading conditions were presented in Tran et al. [23,24] and are not reported here.

Figures 4.6(a) and 4.6(b) show optical micrographs of the cross sections along the symmetry planes of a partially failed 5754/7075 spot friction weld in a lap-shear specimen at the fatigue life of 3.7×10^4 cycles and a failed 5754/7075 spot friction

weld in a lap-shear specimen at the fatigue life of 4.3×10^4 cycles under a load range of 1.17 kN, respectively. Note that the lap-shear specimen with the partially failed spot friction weld was subjected to the same load range as the lap-shear specimen with the failed spot friction weld. However, we stopped the test for the partially failed spot friction weld at about 85% of the fatigue life of the failed spot friction weld under the same load range to examine the fatigue crack growth pattern before the final failure. Therefore, the spot friction weld in Figure 4.6(a), marked with $0.85N_f$, was partially failed and not separated while the spot friction weld in Figure 4.6(b), marked with N_f , was failed and separated. We will follow the same notation for other figures presented later in the paper. The bold arrows in the figures schematically show the direction of the applied load. Due to the large deformation in the final stage of the specimen failure, the weld nugget rotated clockwise. Therefore, the sheets near the nugget are slightly bent. The applied load stretches the upper right 5754 sheet and the lower left 7075 sheet as shown. Based on the optical micrographs, there are three types of cracks or fracture surfaces which occurred during the tests of the dissimilar spot friction welds under different loading conditions. Letters I, U, and L are used to denote for cracks or fracture surfaces which occurred along the interfacial surface between the two deformed sheet materials, in the deformed upper sheet material and in the deformed lower sheet material, respectively. In this investigation, letter C is used to denote for cracks that were likely formed during the welding process. The notations of letters I, U, L and C are valid for the rest of the paper.

As shown in Figures 4.6(a) and 4.6(b), two cracks, marked as I2a and I2b in each of the figures, appear to emanate from the original crack tips of the welds and propagate a bit along the interfacial surfaces. As shown in Figures 4.6(a) and 4.6(b), cracks I2b becomes fatigue cracks L2a that propagate partially into the lower sheet material toward the central hole due to the favorable stress condition. Note that crack L2a shown in Figure 4.6(a) appears not to coalesce with crack C2b that was likely formed during the welding process. As shown in Figure 4.6(b), near the final stage of the specimen failure, crack L2a then becomes crack L2b that propagates through the remaining lower sheet thickness. After propagating through the remaining lower sheet thickness, crack L2b becomes a transverse through crack that propagates in the width direction of the specimen. Finally, the left part of the lower sheet is separated. Note that cracks C2a, C2b in Figure 4.6(a) and crack C2c in Figure 4.6(b) were likely formed during the welding process. Note also that no noticeable cracking occurred on the right portions of the upper sheets as shown in Figures 4.6(a) and 4.6(b). As shown in Figures 4.6(a) and 4.6(b), cracks L2a can be considered as kinked cracks emanating from the original crack tips on the left side of the welds. Based on the experimental observations, cracks L2a can be considered as the dominant kinked fatigue cracks that cause the final failure of the specimen. In summary, the 5754/7075 spot friction welds in lap-shear specimens mainly fail from the kinked crack through the lower 7075 sheet thickness under cyclic loading conditions.

4.4.2. Failure modes of 7075/7075 welds in lap-shear specimens

We conducted experiments for the 7075/5754 spot friction welds in lap-shear specimens under quasi-static and cyclic loading conditions. Based on the experimental observations, the failed 7075/5754 welds in lap-shear specimens under quasi-static loading conditions show one failure mode. The failed 7075/5754 welds in lap-shear specimens under cyclic loading conditions show another failure mode. Figure 4.7(a) shows a schematic plot of a lap-shear specimen with a 7075/5754 spot friction weld with the upper sheet thickness $t_u = 1.6$ mm and the lower sheet thickness $t_l = 2$ mm under applied resultant loads (shown as the bold arrows). Figure 4.7(b) shows a schematic plot of the cross section along the symmetry plane of the 7075/5754 spot friction weld in a lap-shear specimen. In this figure, the thick dashed lines represent the interfacial surfaces between the two deformed sheet materials and the thin solid lines represent either the fracture surfaces or cracks. It should be noted that the interfacial surface between the two deformed sheet materials was well bonded as discussed earlier. Figure 4.7(c) summarizes the failure modes of the 7075/5754 spot friction welds in lap-shear specimens under quasi-static and cyclic loading conditions.

As shown in Figure 4.7(b) and as summarized in Figure 4.7(c), under quasi-static loading conditions, cracks A and B appear to emanate from the original crack tips of the weld and propagate a bit along the interfacial surface. Crack A then becomes crack C that propagates into the upper 7075 sheet thickness. After propagating through the upper sheet with a reduced thickness, crack C becomes a circumferential crack that propagates along the nugget circumference. When the load continues to

increase, the upper and lower sheets are eventually separated by fracture surfaces D and E mostly along the interfacial surface and in the upper sheet material, respectively. Under cyclic loading conditions, cracks A and B appear to emanate from the original crack tips of the weld and propagate a bit along the interfacial surface. Crack B then becomes fatigue crack F that propagates into the lower sheet thickness. Another fatigue crack, marked as G, appears to be initiated near the bend surface outside the nugget on the right portion of the upper sheet and propagates into the upper sheet thickness. After propagating through the lower and upper sheet thicknesses, fatigue crack F becomes a circumferential crack that propagates along the nugget circumference while fatigue crack G becomes first a circumferential crack that propagates partially along the circumference of the bend and then becomes a transverse through crack that propagates in the width direction of the specimen. The right portion of the upper sheet is finally separated. It should be noted that the micrographs to show the failure mode of the 7075/5754 spot friction welds in lap-shear specimens under quasi-static loading conditions were presented in Tran et al. [23,24] and are not reported here.

Figures 4.8(a) and 4.8(c) show optical micrographs of the cross sections along the symmetry planes of a partially failed 7075/5754 spot friction weld in a lap-shear specimen at the fatigue life of 3.4×10^3 cycles and a failed 7075/5754 spot friction weld in a lap-shear specimen at the fatigue life of 4.0×10^3 cycles under a load range of 3.24 kN, respectively. Figure 4.8(b) shows close-up optical micrographs of regions I and II as marked in Figure 4.8(a) in order to examine in more details fatigue cracks L2 and U2 at the fatigue life of 3.4×10^3 cycles. The bold arrows in Figures

4.8(a) and 4.8(c) schematically show the direction of the applied load. As shown in Figures 4.8(a) and 4.8(c), two cracks, marked as I2a and I2b in each of the figures, appear to emanate from the original crack tips of the welds and propagate a bit along the interfacial surfaces. As shown in Figures 4.8(a), 4.8(b) and 4.8(c), cracks I2b become fatigue cracks, marked as L2 in each of the figures, that propagate into the lower sheet thickness. Another cracks, marked as cracks U2 in each of the figures, appear to be initiated near the bend surface outside the nugget on the right portion of the upper 7075 sheet possibly due to high stress concentration of the bend surface and propagate into the upper sheet thickness. As shown in Figures 4.8(a) and 4.8(b), fatigue cracks L2 and U2 propagate partially into the lower and upper sheet thicknesses, respectively, at the fatigue life of 3.4×10^3 cycles. Note that the length for fatigue crack U2 is smaller than that for fatigue crack L2 at the fatigue life of 3.4×10^3 cycles as indicated in Figure 4.8(b). As shown in Figure 4.8(c), fatigue cracks L2 and U2 propagate through the lower and upper sheet thicknesses, respectively, at the fatigue life of 4.0×10^3 cycles. After propagating through the lower and upper sheet thicknesses, fatigue crack L2 becomes a circumferential crack that propagates along the nugget circumference while fatigue crack U2 first becomes a circumferential crack that propagates partially along the circumference of the bend and then becomes a transverse through crack that propagates in the width direction of the specimen. The right portion of the upper sheet is finally separated.

As shown in Figures 4.8(a) and 4.8(c), fatigue cracks L2 can be considered as kinked cracks emanating from the original crack tips on the left side of the welds. Fatigue cracks L2 can be considered as the dominant fatigue cracks that control the

fatigue behavior of the 7075/5754 spot friction welds in lap-shear specimens under cyclic loading conditions as shown in Figures 4.8(a) and 4.8(b). However, near the final stage of the specimen failure, crack U2 in Figure 4.8(c) appears to become more dominant and finally causes the failure of the specimen. In summary, the 7075/5754 welds in lap-shear specimens mainly fail from the kinked crack through the lower 5754 sheet thickness and the fracture surface through the upper 7075 sheet thickness under cyclic loading conditions. Note that similar failure modes were also observed for aluminum 6111 spot friction welds made by the concave and flat tools in lap-shear specimens under cyclic loading conditions as reported in Lin et al. [12-15].

4.5. Failure modes of spot friction welds in cross-tension specimens

4.5.1. Failure modes of 5754/7075 welds in cross-tension specimens

We conducted experiments for the 5754/7075 spot friction welds in cross-tension specimens under quasi-static and cyclic loading conditions. Based on the experimental observations, the failed 5754/7075 welds in cross-tension specimens under quasi-static loading conditions show one failure mode. The failed 5754/7075 welds in cross-tension specimens under cyclic loading conditions show another failure mode. A schematic plot of a cross-tension specimen with a spot weld under resultant applied loads is shown in Figure 4.9(a). In Figure 4.9(a), the shaded parts represent the parts where the specimen is clamped to the testing fixture and the large bold arrows schematically show the loads applied to the specimen. In the figure, the half width b , the tolerance width e between the overlap area and the clamped area, and the upper and lower sheet thicknesses, t_u and t_l , represent the dimensions of the

cross-tension specimen. Note that $2a$ represents the diameter of the spot weld. The critical locations of the weld are marked as A, B, A' and B' in the figure. Two cross sections along the symmetry planes of the spot weld cross-tension specimen marked as cross section A-B and cross section A'-B' are shown in the Figure 4.9(a). A Cartesian coordinate system is also shown in the figure. The failed 5754/7075 welds in cross-tension specimens were sectioned along cross sections A-B and A'-B' as marked in Figure 4.9(a) to examine in details the cracking patterns.

Figure 4.9(b) shows schematic plots of cross sections A-B and A'-B' of the 5754/7075 spot friction weld in a cross-tension specimen. In this figure, the thick dashed lines represent the interfacial surfaces between the two deformed sheet materials and the thin solid lines represent either the fracture surfaces or cracks. It should be noted that the interfacial surface between the two deformed sheet materials was well bonded as discussed earlier. The Cartesian coordinate systems are also shown in the figure. Figure 4.9(c) summarizes the failure modes of the 5754/7075 spot friction welds in cross-tension specimens under quasi-static and cyclic loading conditions. In Figure 4.9(c) (and also in Figure 4.10 as shown later), cracks or fracture surfaces labeled with prime indicate cracks or fracture surfaces which are observed on cross section A'-B' while cracks or fracture surfaces labeled without prime indicate cracks or fracture surfaces which are observed on cross section A-B.

As shown in Figure 4.9(b) and as summarized in Figure 4.9(c), under quasi-static loading conditions, cracks A and B on cross section A-B and cracks A' and B' on cross section A'-B' appear to emanate from the original crack tips of the weld and propagate along the interfacial surface in the upward direction toward the central hole.

Cracks A' and B' become cracks C' and D', respectively, that propagate through the upper sheet thickness. These cracks then become circumferential cracks that propagate along the nugget circumference. Most likely, the circumferential cracks that grew from cracks C' and D' on cross section A'-B' then become cracks C and D on cross section A-B. When the load continues to increase, the upper and lower sheets are eventually separated.

Under cyclic loading conditions, cracks A and B on cross section A-B and cracks A' and B' on cross section A'-B' appear to emanate from the original crack tips of the weld and propagate along the interfacial surface in the upward direction toward the central hole. Cracks A' and B' then become cracks E' and F', respectively, that propagate along the interfacial surface in the downward direction toward the central hole. Near the final stage of the specimen failure, crack F' becomes crack I' that propagates through the remaining lower sheet thickness near the central hole. Then, cracks E', F' and I' become circumferential cracks that propagate along the nugget circumference. Most likely, the circumferential cracks that grew from cracks E' and F' on cross section A'-B' then become cracks E and F on cross section A-B based on the micrographs of another partially failed weld at a different orientation. Eventually, the upper and lower sheets are separated by fracture surfaces G and H on cross section A-B and fracture surfaces G' and H' on cross section A'-B' mostly in the upper sheet material near the central hole. Since we focus on the fatigue behavior of the 5754/7075 spot friction weld, only the micrographs to show the failure mode of the welds under cyclic loading conditions are reported here.

Figures 4.10(a) and 4.10(b) show optical micrographs of the cross sections along symmetry planes A-B and A'-B' of failed 5754/7075 spot friction welds in cross-tension specimens at the fatigue life of 2.7×10^3 cycles under a load range of 0.83 kN. Note that the micrographs shown in Figures 4.10(a) and 4.10(b) were obtained from two different failed welds sectioned along cross sections A-B and A'-B', respectively, as marked in Figure 4.9(a). In these figures, the bold arrows schematically represent the loading directions. As shown in the figures, four fatigue cracks, marked as I2a and I2b in Figure 4.10(a) and as I2a' and I2b' in Figure 4.10(b), appear to emanate from the original crack tips of the welds on cross sections A-B and A'-B', respectively, and propagate along the interfacial surfaces in the upward direction toward the central hole. Cracks I2a' and I2b' then become fatigue cracks I2c' and I2d', respectively, that propagate along the interfacial surfaces in the downward direction toward the central hole as shown in Figure 4.10(b). Near the final stage of the specimen failure, fatigue crack I2d' on cross section A'-B' becomes crack L2b' that propagates through the remaining lower sheet thickness as shown in Figure 4.10(b). Then, fatigue cracks I2c' and I2d' (and also crack L2b') become circumferential cracks that propagate along the nugget circumference. Most likely, the circumferential cracks that grew from cracks I2c' and I2d' on cross section A'-B' then become cracks I2c and I2d on cross section A-B based on the micrographs of another partially failed weld at a different orientation. Eventually, the upper and lower sheets are separated through the fracture surfaces in the upper sheet material near the central hole marked as U2a, U2b, U2a' and U2b' in Figures 4.10(a) and 4.10(b). Note that small cracks, marked as L2a' and U2c' in Figure 4.10(b), appear to

emanate from crack I2b' and propagate a bit into the lower sheet thickness toward the central hole and into the upper sheet material in the upward direction, respectively, possibly due to the favorable stress condition or weak interface strength. It should be noted that the cracking patterns on cross sections A-B and A'-B' appear to be quite symmetric with respect to the center line of the central hole as shown in Figures 4.10(a) and 4.10(b). Based on the micrographs of the partially failed welds, fatigue cracks I2a', I2b, I2c' and I2d' on cross section A'-B' appear to be dominant fatigue cracks that cause the final failure of the specimen. In summary, the 5754/7075 spot friction welds in cross-tension specimens mainly fail from the fracture surfaces along the interfacial surface between the two deformed sheet materials and in the deformed upper 5754 sheet material under cyclic loading conditions.

4.5.2. Failure modes of 7075/7075 welds in cross-tension specimens

We conducted experiments for the 7075/5754 spot friction welds in cross-tension specimens under quasi-static and cyclic loading conditions. Based on the experimental observations, the failed 7075/5754 welds in cross-tension specimens under quasi-static loading conditions show one failure mode. The failed 7075/5754 welds in cross-tension specimens under cyclic loading conditions show another failure mode. A schematic plot of a cross-tension specimen with a spot weld is shown in Figure 4.11(a). In Figure 4.11(a), the shaded parts represent the parts where the specimen is clamped to the testing fixture, and the large bold arrows schematically show the loads applied to the specimen. In the figure, the half width b , the tolerance width e between the overlap area and the clamped area, and the upper

and lower sheet thicknesses, t_u and t_l , represent the dimensions of the cross-tension specimen. Note that $2a$ represents the diameter of the spot weld. The critical locations of the weld are marked as C, D, C' and D' in the figure. A Cartesian coordinate system is also shown in the figure. Two cross sections along the symmetry planes of the spot weld cross-tension specimen marked as cross section C-D and cross section C'-D' are also shown in the Figure 4.11(a). The failed 7075/5754 welds in cross-tension specimens were sectioned along cross sections C-D and C'-D' as marked in Figure 4.11(a) to examine the cracking patterns in details.

Figure 4.11(b) shows schematic plots of cross sections C-D and C'-D' of the 7075/5754 spot friction weld in a cross-tension specimen. In this figure, the thick dashed lines represent the interfacial surfaces between the two deformed sheet materials and the thin solid lines represent either the fracture surfaces or cracks. It should be noted that the interfacial surface between the two deformed sheet materials was well bonded as discussed earlier. The Cartesian coordinate systems are also shown in the figure. Figure 4.11(c) summarizes the failure modes of the 7075/5754 spot friction welds in cross-tension specimens under quasi-static and cyclic loading conditions. In Figure 4.11(c) (and also in Figure 4.12 as shown later), cracks or fracture surfaces labeled with prime indicate the cracks or fracture surfaces which are observed on cross section C'-D' while cracks or fracture surfaces labeled without prime indicate the cracks or fracture surfaces which are observed on cross section C-D.

As shown in Figure 4.11(b) and as summarized in Figure 4.11(c), under quasi-static loading conditions, cracks C and D on cross section C-D and cracks C' and D'

on cross section C'-D' appear to emanate from the original crack tips of the weld and propagate along the interfacial surface. Cracks C and D become cracks E and F, respectively, that propagate through the upper sheet thickness. These cracks then become circumferential cracks that propagate along the nugget circumference. Most likely, the circumferential cracks that grew from cracks E and F on cross section C-D then become cracks E' and F' on cross section C'-D'. When the load continues to increase, the upper and lower sheets are eventually separated. Under cyclic loading conditions, cracks C and D on cross section C-D and cracks C' and D' on cross section C'-D' appear to emanate from the original crack tips of the weld and propagate along the interfacial surface toward the central hole. After propagating along the interfacial surface just before reaching the rim of the central hole near the final stage of the specimen failure, cracks C, D, C' and D' become circumferential cracks that propagate along the nugget circumference. The upper and lower sheets are eventually separated through fracture surfaces G, H, E' and F' in the upper sheet material. Since we focus on the fatigue behavior of the 7075/5754 spot friction weld, only the micrographs to show the failure mode of the welds under cyclic loading conditions are reported here.

Figures 4.12(a) and 4.12(b) show optical micrographs of the cross sections along symmetry planes C-D and C'-D', respectively, of failed 7075/5754 spot friction welds in cross-tension specimens at the fatigue life of 1.7×10^4 cycles under a load range of 0.55 kN. Note that the micrographs shown in Figures 4.12(a) and 4.12(b) were obtained from two different failed specimens sectioned along cross sections C-D and C'-D', respectively, as marked in Figure 4.11(a). In these figures, the bold

arrows schematically represent the loading directions. As shown in the figures, four cracks, marked as I2a and I2b in Figure 4.12(a) and as I2a' and I2b' in Figure 4.12(b), appear to emanate from the original crack tips of the welds on cross sections C-D and C'-D', respectively, and propagate along the interfacial surfaces toward the central hole. Near the final stage of the specimen failure, after propagating almost through the interfacial surface before reaching to the rim of the central hole, cracks I2a, I2b, I2a' and I2b' become circumferential cracks that propagate along the nugget circumference. The upper and lower sheets are eventually separated through the fracture surfaces in the upper sheet material marked as U2a and U2b in Figure 4.12(a), and as U2a' and U2b' in Figure 4.12(b). Note that cracks marked as L2a and L2b in Figure 4.12(a) appear to emanate from cracks I2a and I2b, respectively, and propagate a bit into the lower sheet thickness possibly due to the favorable stress condition. Note also that the crack marked as L2' in Figure 4.12(b) appears to emanate from crack I2a' and propagates partially into the lower sheet thickness possibly due to the favorable stress condition. As shown in Figures 4.12(a) and 4.12(b), the lengths for fatigue cracks I2a and I2b on cross section C-D are larger than those for fatigue cracks I2a' and I2b' on cross section C'-D', respectively. Also, based on the micrographs of the partially failed welds, cracks I2a and I2b on cross section C-D appear to be dominant fatigue cracks that cause the final failure of the specimen. It should be noted that the cracking patterns on cross sections C-D and C'-D' appear to be quite symmetric with respect to the center line of the central hole as shown in Figures 4.12(a) and 4.12(b). In summary, the 7075/5754 spot friction welds in cross-tension specimens mainly fail from the fracture surfaces along the interfacial

surface between the two deformed sheet materials and in the deformed upper 7075 sheet material under cyclic loading conditions.

4.6. Fatigue life estimations for 5754/7075 and 7075/5754 welds in lap-shear specimens

In order to develop engineering fatigue life estimation models, we idealize the three-dimensional spot friction weld problem as a two-dimensional crack problem as in Newman and Dowling [22], Lin et al. [12-15,23] and Tran et al. [16,17]. Figures 4.13(a) and 4.13(b) show schematic plots of the cross sections along the symmetry planes of the 5754/7075 and 7075/5754 spot friction welds in lap-shear specimens, respectively, under a statically equivalent combined tensile and bending load shown as the bold arrows in the figures. In these figures, the thick dashed lines represent the interfacial surfaces between the two deformed sheet materials and the thin solid lines represent either the fracture surfaces or cracks. According to Lin et al. [23], the global stress intensity factors solutions K_I and K_{II} are maximum at the original crack tips on the cross section along the symmetry plane of the spot weld in the lap-shear specimen. These critical locations are marked as a and b in Figures 4.13(a) and 4.13(b) (and also in Figures 4.5(a) and 4.7(a)).

4.6.1. A kinked fatigue crack growth model

As schematically shown in Figure 4.13(a) for the cross section along the symmetry plane of the failed 5754/7075 weld in a lap-shear specimen under cyclic loading conditions, a kinked fatigue crack, marked as crack 1, is initiated near the original crack tip on the left side of the weld with the kink angle α . Based on the

experimental observations, the failure of the 5754/7075 welds in lap-shear specimens under cyclic loading conditions appears to be dominated by kinked fatigue crack 1 that propagates through the lower sheet thickness. Note that the kink angle α of kinked crack 1 is estimated to be 23° from Figure 4.6(b). As schematically shown in Figure 4.13(b) for the cross section along the symmetry plane of the failed 7075/5754 weld in a lap-shear specimen under cyclic loading conditions, a kinked fatigue crack, marked as crack 1, is initiated from the original crack tip on the left side of the weld with the kink angle α . Another crack, marked as crack 2, appears to be initiated near the bend surface outside the weld nugget on the right portion of the upper 7075 sheet. Based on the experimental observations, the failure of the 7075/5754 welds in lap-shear specimens under cyclic loading conditions appears to be dominated by kinked crack 1 that propagates through the lower sheet thickness. Note that the kink angle α of kinked crack 1 is estimated to be 68° from Figures 4.8(a) and 4.8(c).

Here, we adopt the kinked fatigue crack growth model with consideration of the local stress intensity factor solutions for finite kinked cracks as discussed in details in Lin et al. [12-15] and in Tran et al. [16,17]. Due to the complex weld geometries of the 5754/7075 and 7075/5754 spot friction welds, three-dimensional finite element analyses based on the micrographs shown in Figures 4.1(a) and 4.2(a), respectively, were employed to obtain accurate global stress intensity factors for the crack fronts along the nugget circumferences of the welds. Note that both upper and lower sheet materials were assumed to be homogeneous and linear elastic in the finite element models. The global stress intensity factors K_I and K_{II} solutions at the critical locations of the welds obtained from the finite element analyses are then used to

estimate the fatigue lives of the 5754/7075 and 7075/5754 spot friction welds in lap-shear specimens. The local stress intensity factor solutions k_I and k_{II} for the finite kinked cracks in this investigation are determined as in Lin et al. [12-15] and Tran et al. [16,17] with consideration of the finite kink length.

4.6.2. A structural stress model

Recently, Tran et al. [17] presented a structural stress model based on the closed-form structural stress solutions at the critical locations of the welds and the experimental stress-life fatigue data to estimate the fatigue lives of aluminum 5754 and 6111 spot friction welds in lap-shear specimens. This structural stress model is adopted here to estimate the fatigue lives of dissimilar 5754/7075 and 7075/5754 spot friction welds in lap-shear specimens. As summarized in Tran et al. [17], the total structural stress σ_{total} at the critical locations of a spot weld in a lap-shear specimen under a resultant lap-shear load F is presented here as a function of the radius a of the spot weld (idealized as a rigid inclusion), the relevant sheet thickness t , the half width b of the lap-shear specimen and the Poisson's ratio ν as

$$\sigma_{total} = \frac{-3F}{8btXY} [2b^2X + 4Y(a^4b^4 + b^8)] + \frac{3F}{2\pi at} + \frac{F}{2\pi at} + \frac{F}{4bt} \left[\frac{1}{1+\nu} - \frac{2}{\nu-3} \right] \quad (4.1)$$

where X and Y are defined as

$$X = (-1+\nu)(a^4 + b^4)^2 - 4a^2b^6(1+\nu) \quad (4.2)$$

$$Y = a^2(-1+\nu) - b^2(1+\nu) \quad (4.3)$$

As discussed earlier, the dominant kinked fatigue cracks for the 5754/7075 and 7075/5754 spot friction welds in lap-shear specimens under cyclic-loading conditions

were initiated at the critical locations b as schematically shown in Figures 4.13(a) and 4.13(b). Therefore, Equation (4.1) can be adopted to estimate the structural stress range at the critical locations b of the spot friction welds for a given load range. By using Equation (4.1) for the structural stress range at the critical location b for the two-dimensional crack model and the experimental stress-life fatigue data of the aluminum 5754-O and 7075-T6 sheets, we can estimate the fatigue lives of the 5754/7075 and 7075/5754 spot friction welds in lap-shear specimens.

4.6.3. Fatigue life estimations

As discussed in Tran et al. [17], the spot weld radius a , the relevant sheet thickness t , the half width b of the lap-shear specimen, the Poisson's ratio ν and the kinked angle α are used to determine the global and local stress intensity factor solutions for the dominant kinked fatigue crack, and the material constants C and m in the Paris law are needed to estimate the fatigue lives of the spot friction welds in lap-shear specimens based on the kinked fatigue crack growth model. However, due to the complex geometries of the 5754/7075 and 7075/5754 spot friction welds, three-dimensional finite element analyses are used to determine the global stress intensity factors K_I and K_{II} solutions at the critical locations of the welds. As indicated in Equation (4.1), the spot weld radius a , the relevant sheet thickness t , the half width b of the lap-shear specimen, the Poisson's ratio ν and the stress-life fatigue data are needed to estimate the fatigue lives of the spot friction welds in lap-shear specimens based on the structural stress model. It should be emphasized that the relevant sheet

thickness t is the thickness of the sheet through which the dominant kinked fatigue crack propagates.

Figure 4.14(a) shows the experimental results and fatigue life estimations based on the kinked fatigue crack growth model and the structural stress model for the 5754/7075 spot friction welds in lap-shear specimens under cyclic loading conditions. The fatigue life estimations shown in Figure 4.14(a) were obtained from the weld nugget radius $a = 4.75$ mm based on the micrograph shown in Figure 4.1(a), the half width $b = 12.7$ mm of the lap-shear specimen and the Poisson's ratio $\nu = 0.33$. For the kinked fatigue crack growth model, the kink angle $\alpha = 23^\circ$, estimated from the micrographs shown in Figures 4.6(a) and 4.6(b), was used to estimate the fatigue lives of the 5754/7075 welds in lap-shear specimens. The relevant sheet thickness $t = 0.95$ mm, measured at the end of fatigue crack L2a as shown in Figure 4.6(a), is used in the kinked fatigue crack growth model. The material constants $C = 4.31 \times 10^{-8}$

$$\frac{\text{mm/cycle}}{(\text{MPa} \sqrt{\text{m}})^m} \text{ and } m = 3.56 \text{ for aluminum 7075-T6 sheets (Bergner and Zouhar [28])}$$

were used to estimate the fatigue lives of the 5754/7075 spot friction welds in lap-shear specimens. For the structural stress model, the stress-life fatigue data of aluminum 7075-T6 sheets were obtained from Dowling [29] and the relevant lower sheet thickness $t = 1.65$ mm are used in the structural stress model. As shown in Figure 4.14(a), the estimated fatigue lives of the 5754/7075 spot friction welds in lap-shear specimens under cyclic loading conditions based on the kinked fatigue crack growth model and the structural stress model agree well with the experimental results.

Figure 4.14(b) shows the experimental results and fatigue life estimations based on the kinked fatigue crack growth model and the structural stress model for the

7075/5754 spot friction welds in lap-shear specimens. The fatigue life estimations shown in Figure 4.14(b) were obtained from the weld nugget radius $a = 4.85$ mm based on the micrograph shown in Figure 4.2(a), the half width $b = 12.7$ mm of the lap-shear specimen and the Poisson's ratio $\nu = 0.33$. For the 7075/5754 welds in lap-shear specimens, the dominant kinked fatigue crack propagates through the lower sheet thickness under cyclic loading conditions as discussed earlier. The thickness of the lower sheet $t = 1.95$ mm (due to the denting after welding) was used as the relevant sheet thickness in both fatigue life estimation models for the 7075/5754 welds under cyclic loading conditions. For the kinked fatigue crack growth model, the kink angle $\alpha = 68^\circ$, estimated from the micrographs shown in Figure 4.8, was used to estimate the fatigue lives of the welds. Since the material constants for the Paris law for aluminum 5754-O sheets are not available, the material constants $C = 2.0244 \times 10^{-9} \frac{\text{mm/cycle}}{(\text{MPa}\sqrt{\text{m}})^m}$ and $m = 4.64$ for aluminum 5083-O sheets obtained from Campell et al. [30] were used to estimate the fatigue lives of the 7075/5754 welds. For the structural stress model, the experimental stress-life fatigue data of aluminum 5754-O sheets supplied by Friedman [31] were used. As shown in Figure 4.14(b), the estimated fatigue lives of the 7075/5754 spot friction welds in lap-shear specimens under cyclic loading conditions based on the kinked fatigue crack growth model and the structural stress model agree well with the experimental results.

4.7. Fatigue life estimations for 5754/7075 and 7075/5754 welds in cross-tension specimens

Figures 4.15(a) and 4.15(b) show schematic plots of cross section A'-B' of a 5754/7075 spot friction weld and cross section C-D of a 7075/5754 spot friction weld, respectively, in cross-tension specimens under cyclic loading conditions. In these figures, the thick dashed lines represent the interfacial surfaces between the two deformed sheet materials and the thin solid lines represent either the fracture surfaces or cracks. The critical locations are marked as a' and b' in Figure 4.15(a) and marked as c and d in Figure 4.15(b) represent the locations where the dominant fatigue cracks are initiated.

4.7.1. A through-nugget fatigue crack growth model

It should be noted that within the context of the linear elastic fracture mechanics, interface cracks between two different aluminum alloys can be treated as cracks in a homogeneous aluminum when the elastic moduli of the two aluminum alloys are assumed to be equal. From this viewpoint, cracks 1a' and 1b' in Figure 4.15(a), and cracks 1 and 2 in Figure 4.15(b) can be considered as cracks that propagate through the weld nugget made of homogeneous aluminum when calculating the stress intensity factor and J integral solutions based on linear elastic analyses. As schematically shown in Figure 4.15(a) for cross section A'-B' of the failed 5754/7075 weld in a cross-tension specimen under cyclic loading conditions, two fatigue cracks, marked as cracks 1a' and 1b', are initiated near the original crack tips of the weld and propagate through the weld nugget toward the central hole. Cracks 1a' and 1b' then become kinked cracks, marked as cracks 2a' and 2b' that propagate into the lower

sheet thickness with a the kink angle α . Based on the experimental observations, the failure of the 5754/7075 welds in cross-tension specimens under cyclic loading conditions appears to be dominated by cracks 1a', 2a', 1a' and 1b' . As schematically shown in Figure 4.15(b) for cross section C-D of the failed 7075/5754 weld in a cross-tension specimen under cyclic loading conditions, two fatigue cracks, marked as cracks 1 and 2, are initiated near the original crack tips of the weld and propagate through the weld nugget toward the central hole. Based on the experimental observations, the failure of the 7075/5754 welds in cross-tension specimens under cyclic loading conditions appears to be dominated by fatigue cracks 1 and 2.

As shown in Figures 4.10 and 12, the patterns of the through-nugget fatigue cracks appear to be quite symmetric with respect to the center line of the welds. The available analytical stress intensity factor solutions for spot welds (idealized as rigid inclusions) in cross-tension specimens developed in Lin and Pan [27] can be therefore used to estimate the stress intensity factor solutions K_I and K_{II} for each increment of the crack through the weld nugget. The stress intensity factor solutions K_I and K_{II} can be rewritten as functions of the radius of the remaining weld nugget a as

$$K_I = K_I(a) \quad (4.4)$$

$$K_{II} = K_{II}(a) \quad (4.5)$$

The detailed expressions for the K_I and K_{II} solutions as functions of other geometric parameters of the cross-tension specimen are listed in the Appendix A.

Since the through-nugget fatigue crack growth is under combined mode I and mode II loading conditions, an effective stress intensity factor, K_e , can be defined as (Broek [32])

$$K_e(a) = \sqrt{K_I(a)^2 + \beta K_{II}(a)^2} \quad (4.6)$$

where β is an empirical constant to account for the sensitivity of materials to mode II loading conditions. For lack of any further information, we take β as 1 in this paper.

Now we adopt the Paris law to describe the fatigue crack propagation

$$\frac{da}{dN} = C(\Delta K_e(a))^m \quad (4.7)$$

where N is the life or number of cycles, C and m are material constants, and ΔK_e is the range of the effective stress intensity factor. It should be noted that the “crack length” a in Equation (4.7) is the radius of the remaining weld nugget after N cycles. Finally, the fatigue life N_f of the spot welds due to the through-nugget fatigue crack growth can be obtained by integrating Equation (4.7) as

$$N_f = \frac{1}{C} \int_{a_0}^{a_f} \frac{1}{(\Delta K_{eq}(a))^m} da \quad (4.8)$$

where a_0 and a_f are the original and final spot weld radii, respectively.

4.7.2. Fatigue life estimations

As indicated in Appendix A, the original spot weld radius a_0 , the final spot weld radius a_f , the half width b of the overlap area, the half effective length L of the cross-tension specimen, the thicknesses t_u and t_l , the elastic modulus E , the Poisson’s ratio ν , and the material constants C and m of the Paris law for the materials in the weld nugget are needed to estimate the fatigue lives of the 5754/7075 and 7075/5754 spot friction welds in cross-tension specimens based on the through-

nugget fatigue crack growth model. Figures 4.16(a) and 4.16(b) show the experimental results and fatigue life estimations based on the through-nugget fatigue crack growth model for the 5754/7075 and 7075/5754 spot friction welds in cross-tension specimens, respectively. The fatigue life estimations shown in Figures 4.16(a) and 4.16(b) were obtained from the half width $b = 12.7$ mm, the half effective length $L = 25.4$ mm, the elastic modulus $E = 68.9$ GPa and the Poisson's ratio $\nu = 0.33$. Note that the close-up optical micrographs of the failed welds in cross-tension specimens show that the through-nugget cracks schematically shown in Figures 4.15(a) and 4.15(b) appear to occur in the deformed aluminum 7075-T6 sheets just near the interfacial surfaces between the two deformed sheets. The material constants $C = 4.31 \times 10^{-8} \frac{\text{mm/cycle}}{(\text{MPa} \sqrt{\text{m}})^m}$ and $m = 3.56$ for aluminum 7075-T6 sheets (Bergner and Zouhar [28]) were approximately used to estimate the fatigue lives of the 5754/7075 and 7075/5754 spot friction welds in cross-tension specimens. Due to the tool indentation, the nominal thicknesses, denoted as t_u and t_l , of the upper and lower sheets used to make the welds are different from the effective upper and lower sheet thicknesses, denoted as t'_u and t'_l , measured at the crack tips of the welds. Therefore, both nominal thicknesses, t_u and t_l , and effective thicknesses, t'_u and t'_l are employed in the through-nugget fatigue crack growth model. The estimated fatigue lives shown in Figures 4.16(a) and 4.16(b) were presented in the solid and dashed lines which represent the fatigue life estimations based on the through-nugget fatigue crack growth model with the nominal and effective sheet thicknesses, respectively. The shaded regions in Figures 4.16(a) and 4.16(b)

represent the differences between the estimated fatigue lives obtained from the through-nugget fatigue crack growth model with the nominal thicknesses and the effective thicknesses.

As schematically shown in Figure 4.15(a), the 5754/7075 welds in cross-tension specimens mainly fail by through-nugget fatigue cracks 1a' and 1b', and kinked fatigue cracks 2a' and 2b'. Therefore, the through-nugget fatigue crack growth model is used to estimate the fatigue lives corresponding to the propagation of cracks 1a' and 1b' and the kinked fatigue crack growth model is employed to estimate the fatigue lives corresponding to the propagation of cracks 2a' and 2b'. The total estimated fatigue lives are reported in Figure 4.16(a). The fatigue life estimations based on the through-nugget fatigue crack growth were obtained from the original weld nugget radius $a_0 = 4.75$ mm based on the micrograph shown in Figure 4.1(a) and the remaining radius $a_f = 3.85$ mm measured at the end of the through-nugget fatigue cracks 1a' and 1b'. The fatigue life estimations based on the kinked fatigue crack growth were obtained from the kink angle $\alpha = 45^\circ$ estimated from Figure 4.10(b). For the 5754/7075 welds, the nominal sheet thicknesses $t_u = 2.0$ mm, $t_l = 1.6$ mm and the effective sheet thicknesses $t'_u = 1.53$ mm, $t'_l = 1.65$ mm are used to estimate the fatigue lives of the welds. As shown in Figure 4.16(a), the estimated fatigue lives for the 5754/7075 spot friction welds in cross-tension specimens based on combined through-nugget fatigue crack growth model and kinked fatigue crack growth model agree well with the experimental results.

The fatigue life estimations shown in Figure 4.16(b) were obtained from the original weld nugget radius $a_0 = 4.75$ mm based on the micrographs shown in Figure

4.2(a) and the remaining radius $a_f = 1.25$ mm which is the radius of the central hole due to tool probe pin indentation. For the 7075/5754 welds, the nominal sheet thicknesses $t_u = 1.6$ mm, $t_l = 2.0$ mm and the effective sheet thicknesses $t'_u = 1.15$ mm, $t'_l = 1.95$ mm are used to estimate the fatigue lives of the welds. As shown in Figure 4.16(b), the estimated fatigue lives for the 7075/5754 spot friction welds in cross-tension specimens based on the through-nugget fatigue crack growth model agree well with the experimental results.

4.8. Correlations of the experimental fatigue data

Figure 4.17(a) shows the load range as a function of the fatigue life for the 5754/7075 and 7075/5754 spot friction welds in lap-shear and cross-tension specimens under cyclic loading conditions. As shown in Figure 4.17(a), the experimental fatigue results for the 5754/7075 and 7075/5754 welds in lap-shear and cross-tension specimens in terms of the applied load range are quite different. Therefore, it is difficult to assess the experimental fatigue results and to compare the fatigue strengths of the 5754/7075 and 7075/5754 welds in lap-shear and cross-tension specimens in terms of the applied load range. In the following, we attempt to employ the fracture mechanics parameters such as the effective stress intensity factor and J integral to correlate the experimental fatigue data for the 5754/7075 and 7075/5754 spot friction welds in lap-shear and cross-tension specimens. Three-dimensional finite element analyses based on the micrographs of the welds shown in Figures 4.1(a) and 4.2(a) are used to obtain accurate global stress intensity factor and J integral solutions for the crack fronts along the nugget circumferences of the welds.

The details of the finite element models for the 5754/7075 and 7075/5754 spot friction welds in lap-shear and cross-tension specimens are similar to those for the Al/Fe spot friction welds in lap-shear and cross-tension specimens which will be reported in details in Part 2.

For the 5754/7075 and 7075/5754 welds in lap-shear specimens, based on the experimental observations, the kinked fatigue cracks initiating at the original crack tips on the left side of the welds (marked as b in Figures 4.13(a) and 4.13(b)) propagating through the lower sheet thickness appear to be dominant fatigue cracks that cause the failures of the specimens. The results obtained from the finite element computations indicate that the maximum values of the effective stress intensity factor and J integral solutions are located at the crack tips marked as b in Figures 4.13(a) and 4.13(b). For the 5754/7075 welds in cross-tension specimens, based on the experimental observations, the fatigue cracks initiating at the original crack tips on cross section A'-B' of the weld (marked as a' and b' in Figure 4.13(a)) and propagating along the interfacial surface appear to be dominant fatigue cracks that cause the failure of the specimen. The results obtained from the finite element computation indicate that the maximum values of the effective stress intensity factor and J integral solutions are located at the crack tips marked as a' and b' in Figure 4.15(a). For the 7075/5754 welds in cross-tension specimens, the fatigue cracks initiating at the original crack tips on cross section C-D of the weld (marked as c and d in Figure 4.15(b)) and propagating along the interfacial surface appear to be dominant fatigue cracks that cause the failure of the specimen. The results obtained from the finite element computation indicate that the maximum values of the effective

stress intensity factor and J integral solutions are located at the crack tips marked as c and d in Figure 4.15(a). The agreement between the results obtained from the finite element computations and experimental observations suggests that the effective stress intensity factor and J integral solutions at the critical locations of the welds obtained from three-dimensional finite element analyses may be appropriate parameters to correlate the experimental fatigue data for the 5754/7075 and 7075/5754 welds in lap-shear and cross-tension specimens.

Figures 4.17(b) and 4.17(c) show the effective stress intensity range ΔK_e and J integral range ΔJ , respectively, as a function of the fatigue life for the 5754/7075 and 7075/5754 spot friction welds in lap-shear and cross-tension specimens under cyclic loading conditions. Since the K_{III} solutions for the cracks on the symmetry planes of the lap-shear and cross-tension specimens are zero, the effective stress intensity factor range ΔK_e at the critical locations of the maximum effective stress intensity factor (also the J integral solution) is obtained from Equation (4.6). As shown in Figures 4.17(b) and 4.17(c), the experimental fatigue data for the 5754/7075 and 7075/5754 welds in lap-shear and cross-tension specimens in terms of the effective stress intensity range ΔK_e and the J integral range ΔJ become very close together when compared to those in terms of the applied load range shown in Figure 4.17(a). Note that the fatigue lives for the 5754/7075 welds in lap-shear specimens under cyclic loading conditions with higher applied load ranges appear to be slightly smaller than the remaining data under the same ΔK_e and ΔJ possibly due to the effects of the cracks that were likely formed during the welding process in the 5754/7075 welds in lap-shear specimens as discussed later. As shown in Figure 4.17(b) and 4.17(c), the

effective stress intensity factor K_e and J integral solutions at the critical locations of the welds obtained from three-dimensional finite element analyses appear to be good fracture mechanics parameters to correlate the experimental fatigue data for the 5754/7075 and 7075/5754 spot friction welds in lap-shear and cross-tension specimens under the given applied load ranges.

4.9. Discussions

As shown in Figures 4.4(a) and 4.4(b), the failure load of the 7075/5754 weld in the lap-shear specimen under quasi-static loading conditions is about 40% larger than that of the 5754/7075 weld in the lap-shear specimen as indicated in the figure. As expected, the 7075/5754 welds in lap-shear specimens have longer fatigue lives than the 5754/7075 welds in lap-shear specimens for a given applied load range. Based on the trends of the experimental fatigue data as indicated in Figure 4.17(a), the performance of the 5754/7075 welds in lap-shear specimens under cyclic loading conditions with lower applied load ranges in terms of the fatigue life is quite similar to that of the 7075/5754 welds in lap-shear specimens. However, under cyclic loading conditions with higher applied load ranges, the performance of the 7075/5754 welds in lap-shear specimens in terms of the fatigue life is much better than that of the 5754/7075 welds. It should be noted that some particular 5754/7075 welds in lap-shear specimens contain cracks that were likely formed during the welding process as shown in Figures 4.6(a) and 4.6(b). These cracks possibly coalesced with the dominant fatigue cracks during the tests, accelerated the fatigue crack growth and consequently reduced the fatigue lives of the 5754/7075 welds in lap-shear specimens.

As shown in Figures 4.4(a) and 4.4(b), the failure loads of the 5754/7075 and 7075/5754 welds in cross-tension specimens under quasi-static loading conditions are nearly the same. As expected, the 5754/7075 and 7075/5754 welds in cross-tension specimens have nearly the same fatigue lives for a given load range. The performance of the 7075/5754 welds in cross-tension specimens in terms of fatigue life is then quite similar to that of the 5754/7075 welds in cross-tension specimens as indicated in Figure 4.17(a).

As shown in Figures 4.6(a) and 4.6(b), the 5754/7075 spot friction welds in lap-shear specimens contain cracks that were likely formed during the welding process. Note that the welding processing parameters such as the tool geometry, the tool rotational speed and the tool downward force were first specified and the optimal processing times were then determined for the maximum failure loads of the spot friction welds under lap-shear loading conditions based on the work of Tran et al. [24]. As discussed in Tran et al. [24], cracks that were likely formed during the welding process may not significantly affect the loading carrying capacity of the specimen under lap-shear loading conditions and therefore were not detected after quasi-static tests. For this reason, the optimal processing time of 3.8 sec were used to make the 5754/7075 welds tested in this investigation. In general, the specimens with the welds that contain cracks that were likely formed during the welding process should be rejected from the manufacturing viewpoint. However, the specimens with defective welds can be only detected after sectioning the failed welds due to the lack of available equipment. For the completeness of this research study and also for the contribution to the studies of the defects for spot friction welds in the future, the

results for the 5754/7075 spot friction welds in lap-shear specimens are presented in this paper. As shown in Figure 4.17, the cracks that were likely formed during the welding process may affect the fatigue lives of the 5754/7075 welds in lap-shear specimens.

It should be noted that for the kinked fatigue crack growth model, we used the global stress intensity factor solutions obtained from the finite element analyses for the 5754/7075 and 7075/5754 welds based on the micrographs shown in Figures 4.1(a) and 4.2(a), respectively. In general, finite element computations are also needed to determine the accurate local stress intensity factor solutions for the kinked cracks emanating from the original crack tips of the welds with the exact weld geometries and loading conditions. However, the computational effort is quite extensive since the computations are three-dimensional in nature and the number of the cases for the weld geometries and the loading conditions are quite large. Therefore, the local stress intensity factor solutions k_I and k_{II} for finite kinked cracks in this investigation were determined as in Lin et al. [12-15] with consideration of the finite kink length. This model is therefore approximate in nature by considering that the geometry of the spot friction welds is different from that of the resistance spot welds.

As discussed in Tran et al. [17], it should be emphasized that the closed-form structural stress solutions used in the structural stress model were obtained from a linear elastic analysis. For the 5754/7075 welds in lap-shear specimens under cyclic loading conditions, the estimated structural stress ranges based on Equation (4.1) are smaller than $2\sigma'_0$ where σ'_0 represents the initial cyclic yield strength of the lower

7075-T6 sheet. The cyclic behavior of materials at the critical location marked as b in Figure 4.13(a) for the 5754/7075 welds in lap-shear specimens can be therefore considered as linear elastic under high-cycle loading conditions. For 7075/5754 welds in lap-shear specimens, under cyclic loading conditions with lower applied load ranges, the estimated structural stress ranges based on Equation (4.1) are smaller than $2\sigma'_0$ where σ'_0 represents the initial cyclic yield strength of the lower 5754-O sheet. The cyclic behavior of materials at the critical location at the critical location marked as b in Figure 4.15(a) for the 7075/5754 welds in lap-shear specimens can be therefore considered as linear elastic under cyclic loading conditions with lower applied load ranges. Under cyclic loading conditions with higher applied load ranges, the estimated structural stress ranges based on Equation (4.1) can be as high as $2.8\sigma'_0$ for the 7075/5754 welds. Neuber's type of life estimation methods can be used to improve the life estimations since the life estimations are based on the experimental stress-life fatigue data here. As shown in Figures 4.14(a) and 4.14(b), the structural stress model appears to give good estimations of the fatigue lives of the 5754/7075 and 7075/5754 welds in lap-shear specimens without detailed information on the initiation and propagation of the kinked cracks emanating from the original crack tips of the welds under cyclic loading conditions.

It should be noted that the through-nugget fatigue crack growth model developed earlier is based on the closed-form stress intensity factor solutions and the Paris law for the fatigue crack propagation through the weld nugget. The closed-form stress intensity factor solutions listed in Appendix A are obtained from Lin and Pan [27] for a spot weld (idealized as a rigid inclusion) in a cross-tension specimen with a

geometry that is different from that of the cross-tension specimens tested in this investigation. Also, the geometry of the spot friction welds during fatigue testing may deviate from the assumption of a rigid inclusion. The closed-form stress intensity factor solutions employed in the through-nugget fatigue crack growth model are therefore approximate in nature. As discussed in Tran et al. [23,24], it seems that the intermixing of the upper and lower sheet materials did not occur for the 5754/7075 and 7075/5754 spot friction welds. Therefore, the chemical compositions of the upper and lower sheet materials in the weld nugget will be likely as similar as those of the base metals before welding. However, the material constants C and m in the Paris law for the materials in the weld nugget may be different from those for the base metals due to the change of the microstructure for the materials in the weld nugget after spot friction welding. The use of the material constants C and m in the Paris law for the base metals in the through-nugget fatigue crack growth model may partially explain the difference between the experimental results and the estimated fatigue lives as shown in Figures 4.16(a) and 4.16(b).

As shown in Figures 4.17(b) and 4.17(c), the experimental fatigue data for the 5754/7075 and 7075/5754 welds in terms of the effective stress intensity factor range and the J integral range become very close to each other. As discussed earlier, the weld geometries and failure modes of the 5754/7075 and 7075/5754 welds in lap-shear and cross-tension specimens under cyclic loading conditions are quite different. The results shown in Figures 4.17(b) and 4.17(c) indicate that the effective stress intensity factor and J integral solutions at the critical locations of the welds can be used to correlate the experimental fatigue data of the 5754/7075 and 7075/5754 spot

friction welds for two types of specimens. Note that the maximum size of the plastic zone near the crack tips of the 5754/7075 and 7075/5754 spot friction welds under the maximum loads applied in the fatigue tests is estimated about 0.07 mm. The small plastic zone size as compared to the geometric dimensions of the lap-shear and cross-tension specimens can explain why the fracture mechanics parameters based on the linear elastic analyses can correlate very well the experimental fatigue data for the 5754/7075 and 7075/5754 welds in lap-shear and cross-tension specimens.

4.10. Conclusions

Fatigue behavior of dissimilar 5754/7075 and 7075/5754 spot friction welds between aluminum 5754-O and 7075-T6 sheets in lap-shear and cross-tension specimens is investigated based on experimental observations and three fatigue life estimation models. Optical micrographs of the 5754/7075 and 7075/5754 welds before and after failure under quasi-static and cyclic loading conditions are examined to understand the fracture and failure mechanisms of the welds. The micrographs show that the 5754/7075 welds in lap-shear specimens mainly fail from the kinked crack through the lower sheet thickness under cyclic loading conditions. Also, the 7075/5754 welds in lap-shear specimens mainly fail from the kinked crack through the lower sheet thickness and from the fracture surface through the upper sheet thickness under cyclic loading conditions. The micrographs show that the 5754/7075 and 7075/5754 welds in cross-tension specimens mainly fail from the fracture surfaces along the interfacial surface between the two deformed sheet materials and in the deformed upper sheet material under cyclic loading conditions. A kinked fatigue

crack growth model based on the stress intensity factor solutions for finite kinked cracks, a structural stress model based on the closed-form structural stress solutions at the critical locations of the welds and a through-nugget fatigue crack growth model based on the closed-form stress intensity factor solutions for the through-nugget cracks are adopted and developed to estimate the fatigue lives of the 5754/7075 and 7075/5754 welds in lap-shear and cross-tension specimens. The fatigue life estimations based on the kinked fatigue crack growth model, the structural stress model and the through-nugget fatigue crack growth model agree well with the experimental results. Finally, the effective stress intensity factor and J integral solutions at the critical locations of the welds obtained from three-dimensional finite element analyses appear to be good fracture mechanics parameters to correlate the experimental fatigue data for the 5754/7075 and 7075/5754 welds in lap-shear and cross-tension specimens.

Appendix A

Figure 4.18(a) shows the front and side views of the left half of the strip model near the crack tip with linearly distributed stresses based on the classical Kirchhoff plate theory as shown in Tran and Pan [33]. In Figure 4.18(a), the normal stresses σ_{ui} , σ_{uo} , σ_{li} and σ_{lo} represent the normal stresses for line \overline{FG} and line \overline{AB} , the normal stresses σ_{ui}^* , σ_{uo}^* , σ_{li}^* and σ_{lo}^* represent the normal stresses for line \overline{DE} and line \overline{CD} at the inner (*i*) and outer (*o*) surfaces of the upper (*u*) and lower (*l*) strips, respectively. As discussed in details in Tran and Pan [33], for spot welds joining two sheets of identical material $E_u = E_l = E$, in reference to Figure 4.18(a), the in-plane stress intensity factor solutions K_I and K_{II} can be written as (Zhang [34])

$$\begin{aligned}
 K_I = & \frac{\sqrt{t_u}}{2\sqrt{2(1+\delta)(1+3\delta+3\delta^2)(1+\tan^2\omega)}} \left\{ \left[\frac{1+3\delta+6\delta^2}{\sqrt{3}(1+\delta)} \tan\omega - 1 \right] \sigma_{ui} \right. \\
 & - \left[\frac{1+3\delta}{\sqrt{3}(1+\delta)} \tan\omega + 1 \right] \sigma_{uo} + \left[\frac{\delta(1-3\delta)}{\sqrt{3}(1+\delta)} \tan\omega + 2 + \delta \right] \sigma_{li} \\
 & \left. - \delta \left[\frac{1+3\delta}{\sqrt{3}(1+\delta)} \tan\omega + 1 \right] \sigma_{lo} \right\} \quad (A.1)
 \end{aligned}$$

$$\begin{aligned}
 K_{II} = & \frac{\sqrt{t_u}}{2\sqrt{2(1+\delta)(1+3\delta+3\delta^2)(1+\tan^2\omega)}} \left\{ \left[\frac{1+3\delta+6\delta^2}{\sqrt{3}(1+\delta)} + \tan\omega \right] \sigma_{ui} \right. \\
 & - \left[\frac{1+3\delta}{\sqrt{3}(1+\delta)} - \tan\omega \right] \sigma_{uo} + \left[\frac{\delta(1-3\delta)}{\sqrt{3}(1+\delta)} - (2+\delta)\tan\omega \right] \sigma_{li} \\
 & \left. - \delta \left[\frac{1+3\delta}{\sqrt{3}(1+\delta)} - \tan\omega \right] \sigma_{lo} \right\} \quad (A.2)
 \end{aligned}$$

where $\delta = t_u/t_l$ and the angular function ω obtained from the numerical calculations and is tabulated in the Appendices of Zhang [34] and Suo and Hutchinson [35].

Based on the recent publication of Lin and Pan [27], the normal stresses σ_{ui} , σ_{uo} , σ_{li}

and σ_{lo} along the nugget circumference at $r = a$ of a spot weld in a cross-tension specimen under a resultant load F are presented here as functions of the radius a of the spot weld (idealized as a rigid inclusion), the sheet thicknesses t_u and t_l , the half width b of the sheet, the half effective length L , the Poisson's ratio ν and the angular location θ defined in Figure 4.18(b) as (Lin and Pan [27])

$$\begin{aligned} \sigma_{ui} = & \frac{-3F[(a^2 - b^2)(-1 + \nu_u) + 2b^2(1 + \nu_u)\ln(b'/a)]}{2\pi t_u^2[a^2(-1 + \nu) - b^2(1 + \nu_u)]} \\ & - \frac{3(\tilde{M}_b - \tilde{M}_c)}{t_u^2 X_u Y_u} [2b^2 X_u + 4Y_u(a^4 b^4 + b^8)\cos 2\theta] \\ & - \frac{24\tilde{M}_{x'y'}}{t_u^2 X_u'} [a^4(b/\sqrt{2})^4 + (b/\sqrt{2})^8]\cos 2\theta \end{aligned} \quad (\text{A.3})$$

$$\sigma_{uo} = -\sigma_{ui} \quad (\text{A.4})$$

$$\begin{aligned} \sigma_{li} = & \frac{-3F[(a^2 - b^2)(-1 + \nu_l) + 2b^2(1 + \nu_l)\ln(b'/a)]}{2\pi t_l^2[a^2(-1 + \nu) - b^2(1 + \nu_l)]} \\ & - \frac{3(\tilde{M}_b - \tilde{M}_c)}{t_l^2 X_l Y_l} \left[2b^2 X_l + 4Y_l(a^4 b^4 + b^8)\cos 2(\theta + \frac{\pi}{2}) \right] \\ & - \frac{24\tilde{M}_{x'y'}}{t_l^2 X_l'} [a^4(b/\sqrt{2})^4 + (b/\sqrt{2})^8]\cos 2(\theta + \frac{\pi}{2}) \end{aligned} \quad (\text{A.5})$$

$$\sigma_{lo} = -\sigma_{li} \quad (\text{A.6})$$

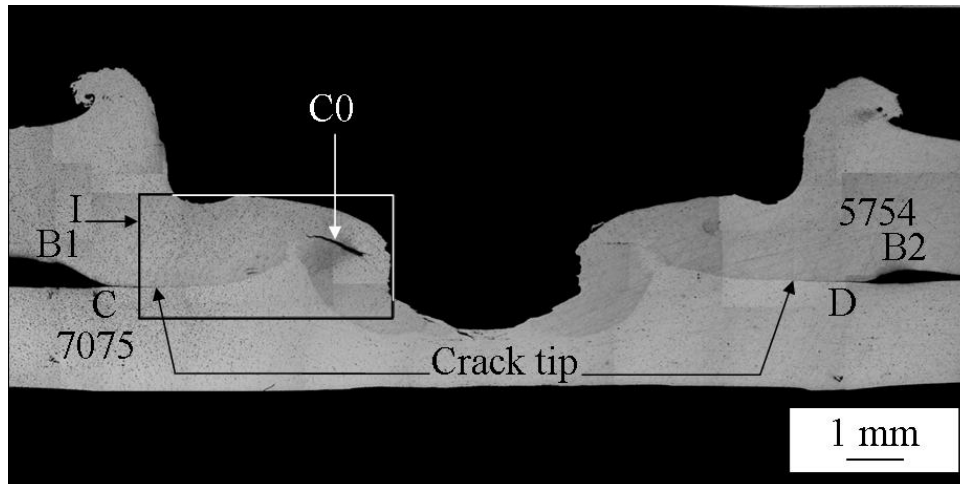
where $b' = 2b/\sqrt{\pi}$, $\tilde{M}_b = F(L - b)/4b$, $\tilde{M}_{x'y'} = F/16$ and

$$\tilde{M}_c = \frac{F[a^2 - b^2 + 2a^2 \ln(b'/a)]}{4\pi(a^2 - b^2)} \quad (\text{A.7})$$

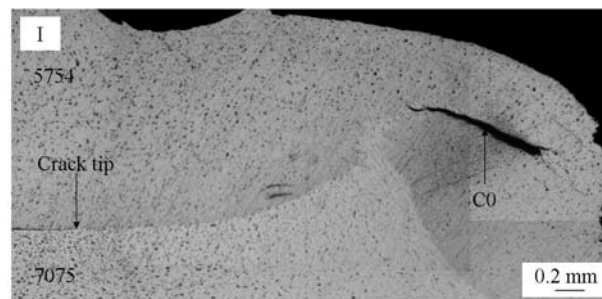
$$X_k = (-1 + \nu)(a^4 + b^4)^2 - 4a^2 b^6(1 + \nu_k) \quad (k = u, l) \quad (\text{A.8})$$

$$Y_k = a^2(-1 + \nu_k) - b^2(1 + \nu_k) \quad (k = u, l) \quad (\text{A.9})$$

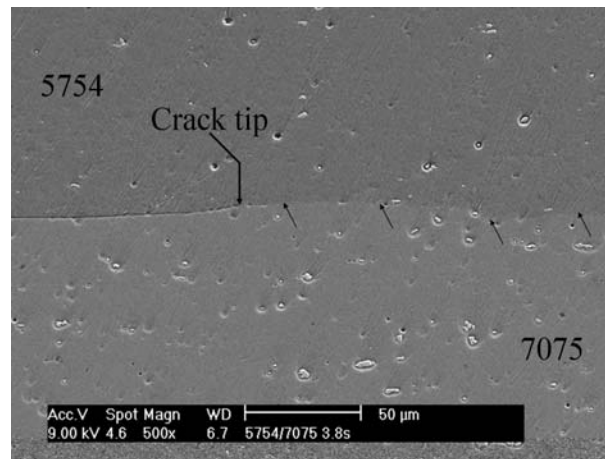
$$X_k' = -[a^4 + (b/\sqrt{2})^4]^2(1 - \nu_k) - 4a^2(b/\sqrt{2})^6(1 + \nu_k) \quad (k = u, l) \quad (\text{A.10})$$



(a)

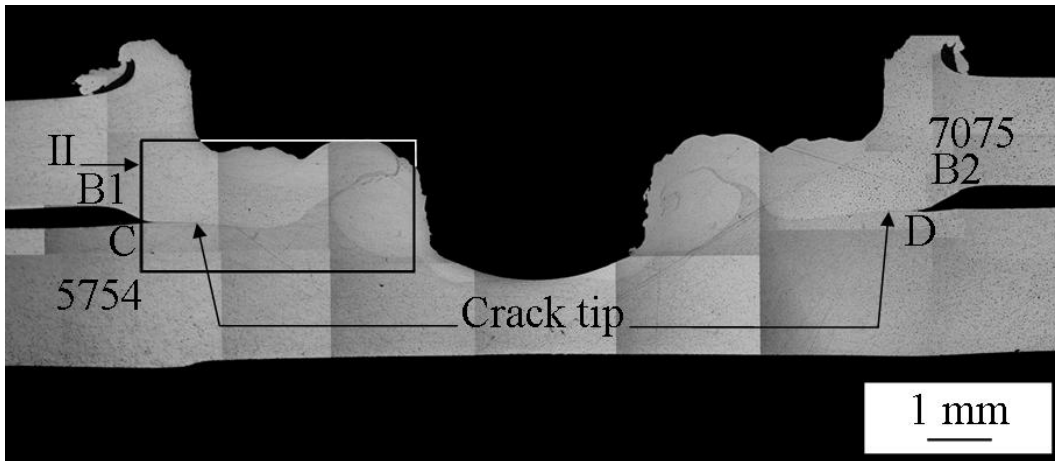


(b)

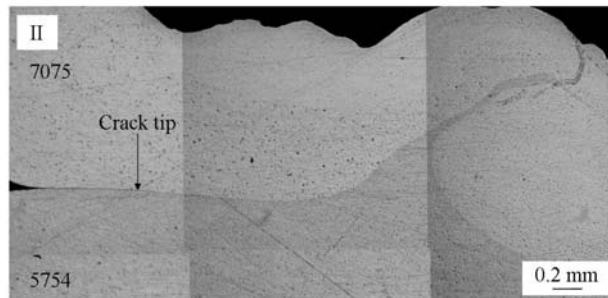


(c)

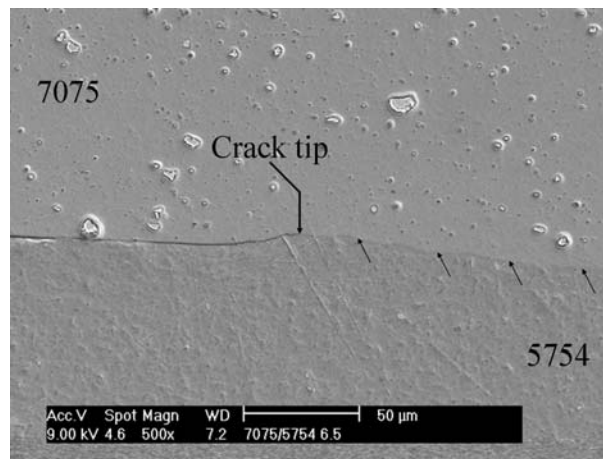
Figure 4.1 (a) An optical micrograph of the cross section along the symmetry plane of a 5754/5754 spot friction weld before testing, (b) a close-up optical micrograph of region I, (c) a scanning electron micrograph of the crack tip region as marked in (b).



(a)



(b)



(c)

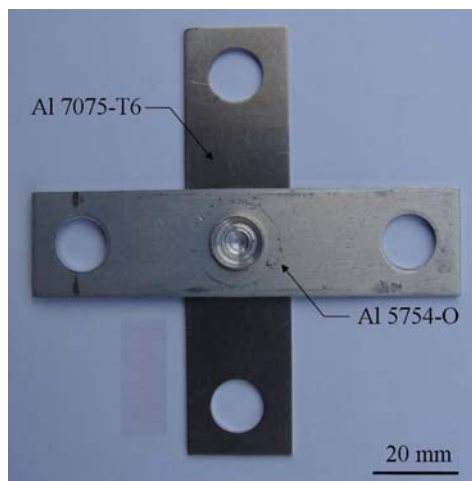
Figure 4.2 (a) An optical micrograph of the cross section along the symmetry plane of a 7075/5754 spot friction weld before testing, (b) a close-up optical micrograph of region II, (c) a scanning electron micrograph of the crack tip region as marked in (b).



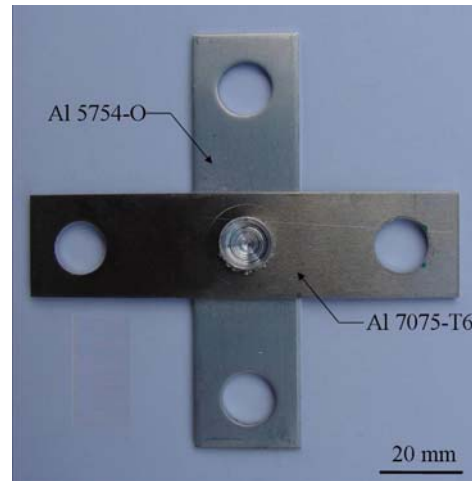
(a)



(b)

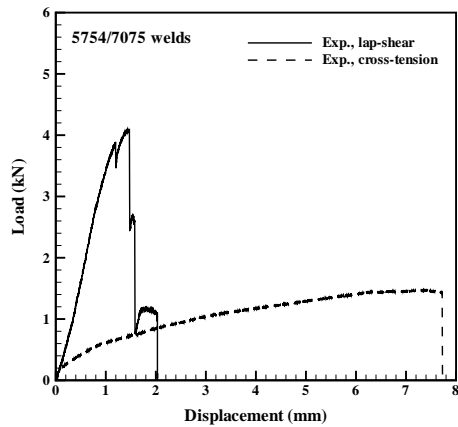


(c)

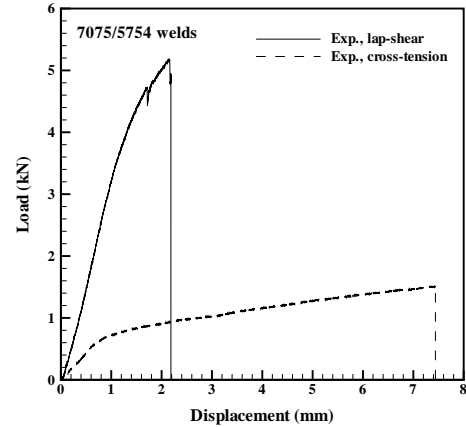


(d)

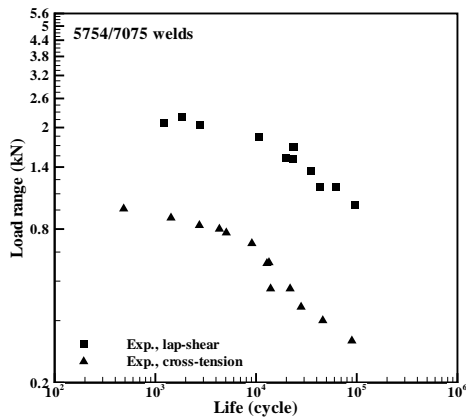
Figure 4.3 (a) A lap-shear specimen with a 5754/7075 spot friction weld, (b) a lap-shear specimen with a 7075/5754 spot friction weld, (c) a cross-tension specimen with a 5754/7075 spot friction weld, (d) a cross-tension specimen with a 7075/5754 spot friction weld.



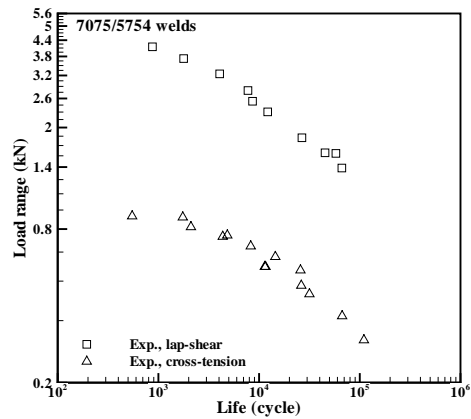
(a)



(b)



(c)



(d)

Figure 4.4 (a) Typical load-displacement curves for the 5754/7075 spot friction welds in lap-shear and cross-tension specimens under quasi-static loading conditions, (b) typical load-displacement curves for the 7075/5754 spot friction welds in lap-shear and cross-tension specimens under quasi-static loading conditions, (c) experimental results for the 5754/7075 spot friction welds in lap-shear and cross-tension specimens under cyclic loading conditions, (d) experimental results for the 7075/5754 spot friction welds in lap-shear and cross-tension specimens under cyclic loading conditions.

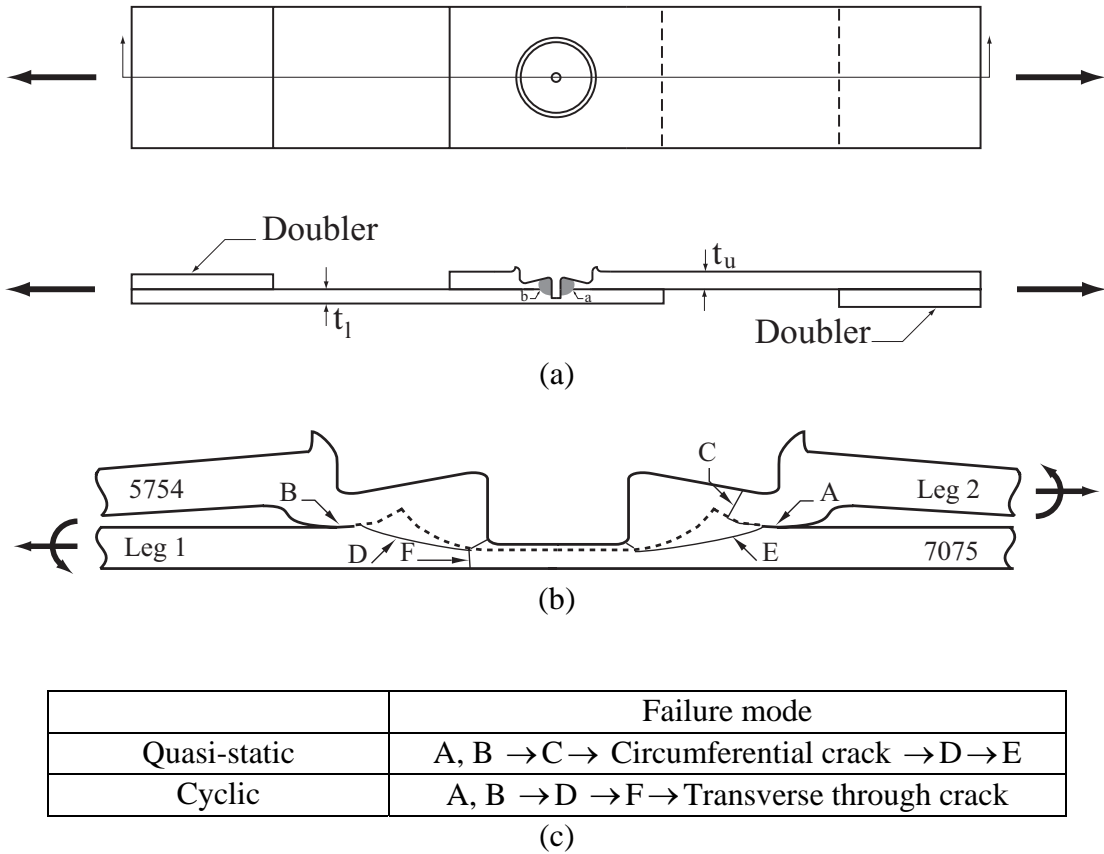
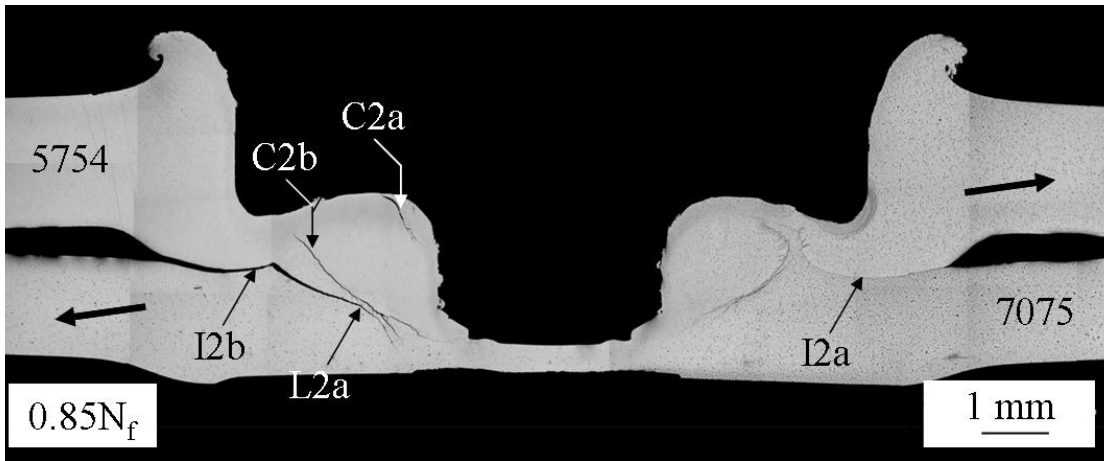
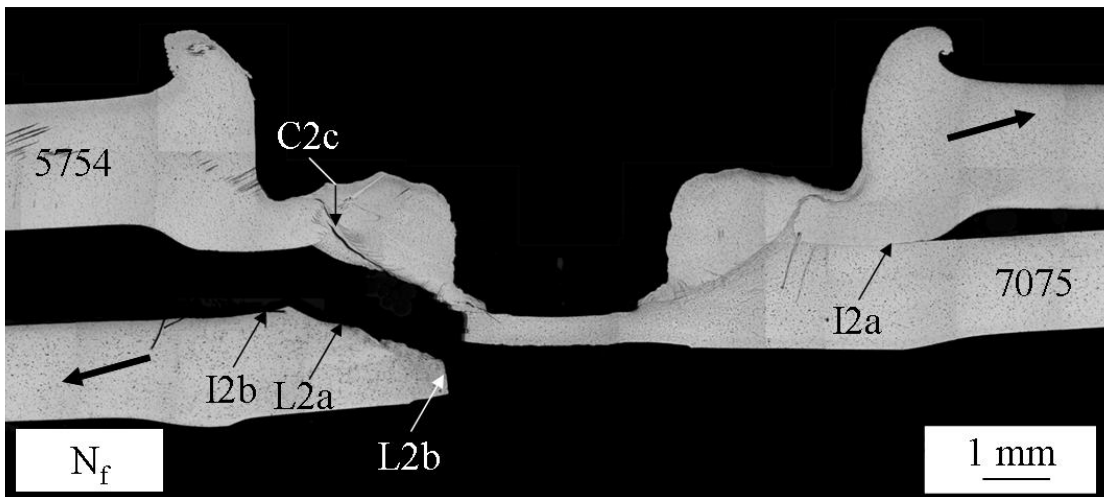


Figure 4.5 (a) A schematic plot of a lap-shear specimen with a 5754/7075 spot friction weld with the upper sheet thickness $t_u = 2.0$ mm and the lower sheet thickness $t_l = 1.6$ mm under applied resultant loads (shown as the bold arrows), (b) a schematic plot of the cross section along the symmetry plane of the 5754/7075 spot friction weld in a lap-shear specimen, (c) failure modes of the 5754/7075 spot friction welds in lap-shear specimens under quasi-static and cyclic loading conditions.

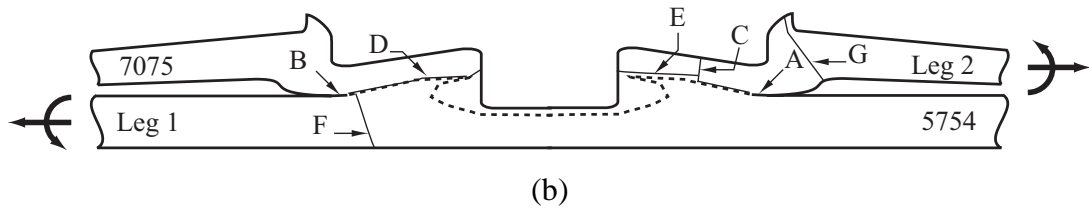
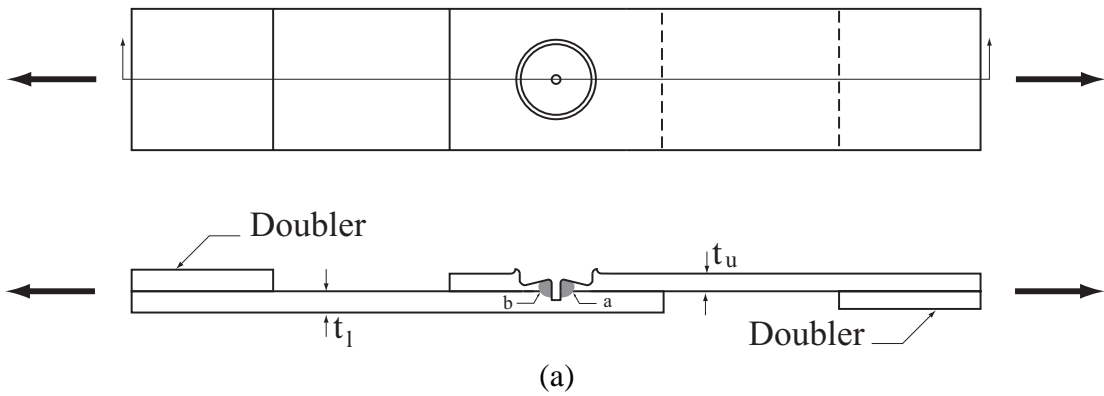


(a)



(b)

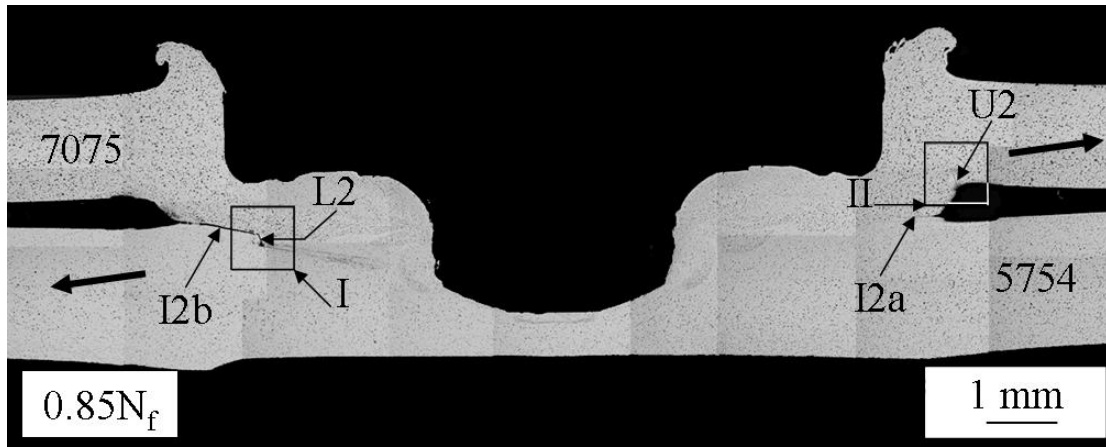
Figure 4.6 Optical micrographs of the cross sections along the symmetry planes of (a) a partially failed 5754/7075 spot friction weld in a lap-shear specimen at the fatigue life of 3.7×10^4 cycles, (b) a failed 5754/7075 spot friction weld in a lap-shear specimen at the fatigue life of 4.3×10^4 cycles under a load range of 1.17 kN.



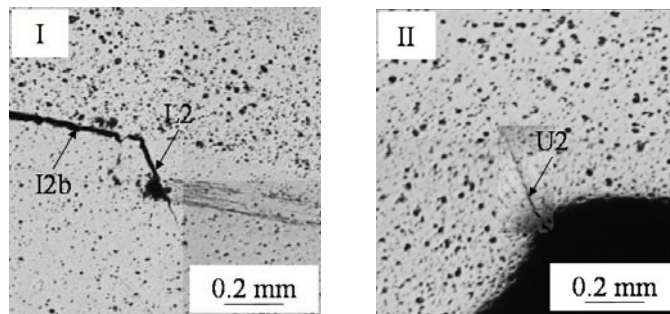
	Failure mode
Quasi-static	A, B → C → Circumferential crack → D → E
Cyclic	A, B → F → Circumferential crack G → Circumferential crack → Transverse through crack

(c)

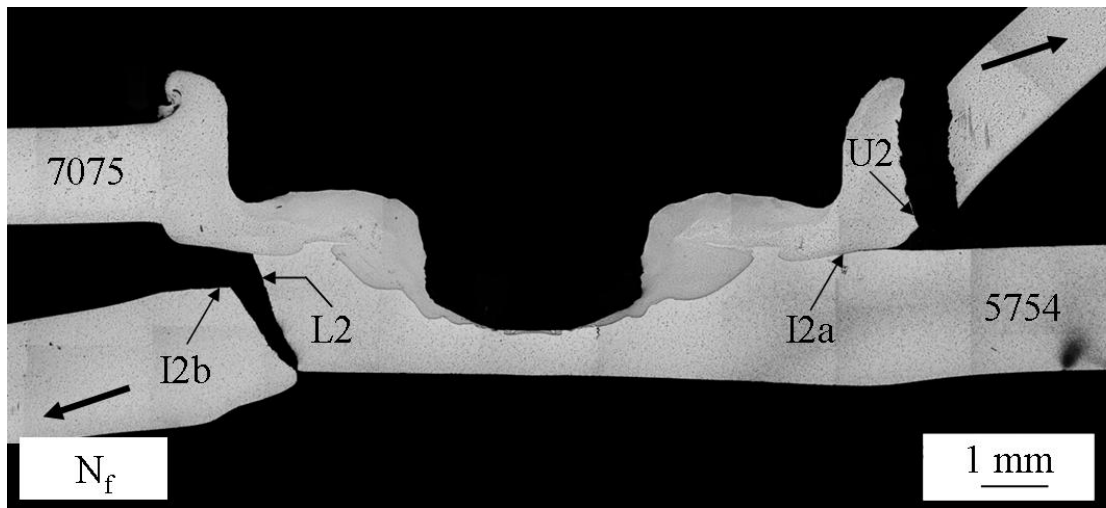
Figure 4.7 (a) A schematic plot of a lap-shear specimen with a 7075/5754 spot friction weld with the upper sheet thickness $t_u = 1.6$ mm and the lower sheet thickness $t_l = 2$ mm under applied resultant loads (shown as the bold arrows), (b) a schematic plot of the cross section along the symmetry plane of the 7075/5754 spot friction weld in a lap-shear specimen, (c) failure modes of the 7075/5754 spot friction welds in lap-shear specimens under quasi-static and cyclic loading conditions.



(a)

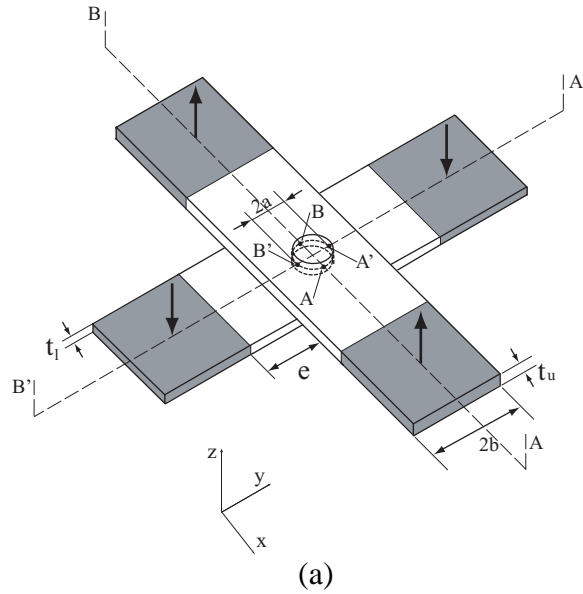


(b)

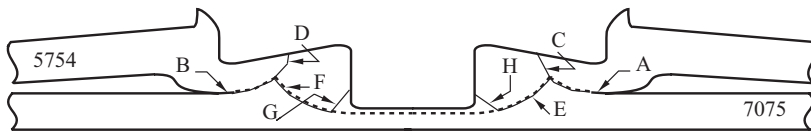


(c)

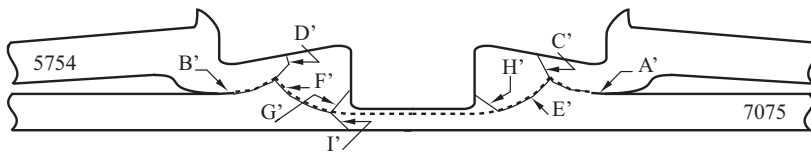
Figure 4.8 (a) An optical micrograph of the cross section along the symmetry plane of a partially failed 7075/5754 spot friction weld in a lap-shear specimen at the fatigue life of 3.4×10^3 cycles, (b) close-up optical micrographs of regions I and II as marked in (a), (c) an optical micrograph of the cross section along the symmetry plane of a failed 7075/5754 spot friction weld in a lap-shear specimen at the fatigue life of 4.0×10^3 cycles under a load range of 3.24 kN.



Cross section A-B



Cross section A'-B'

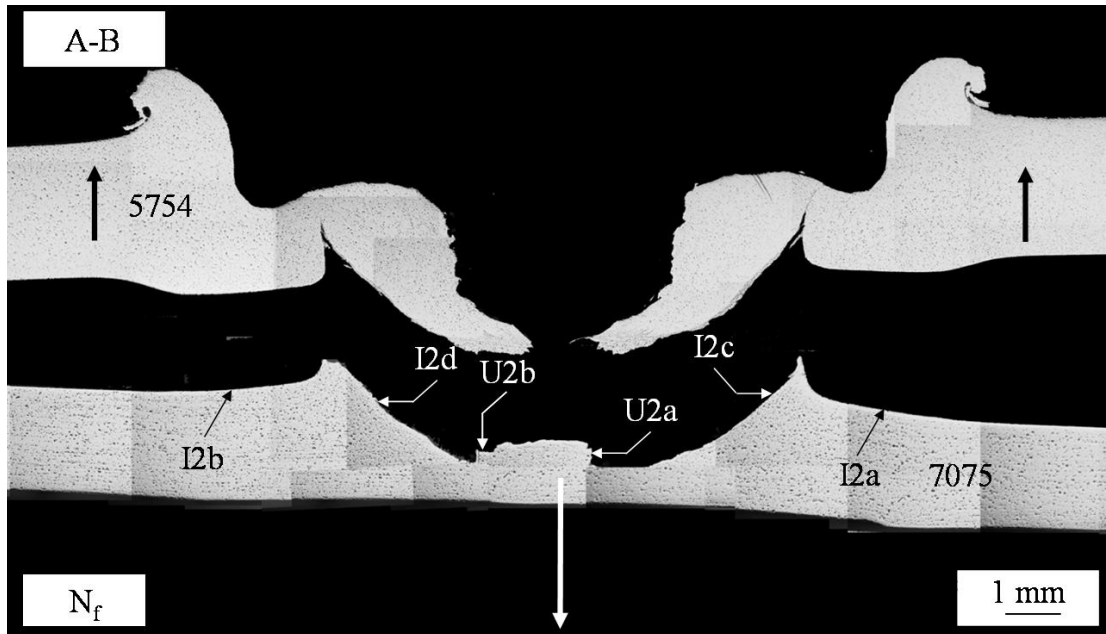


(b)

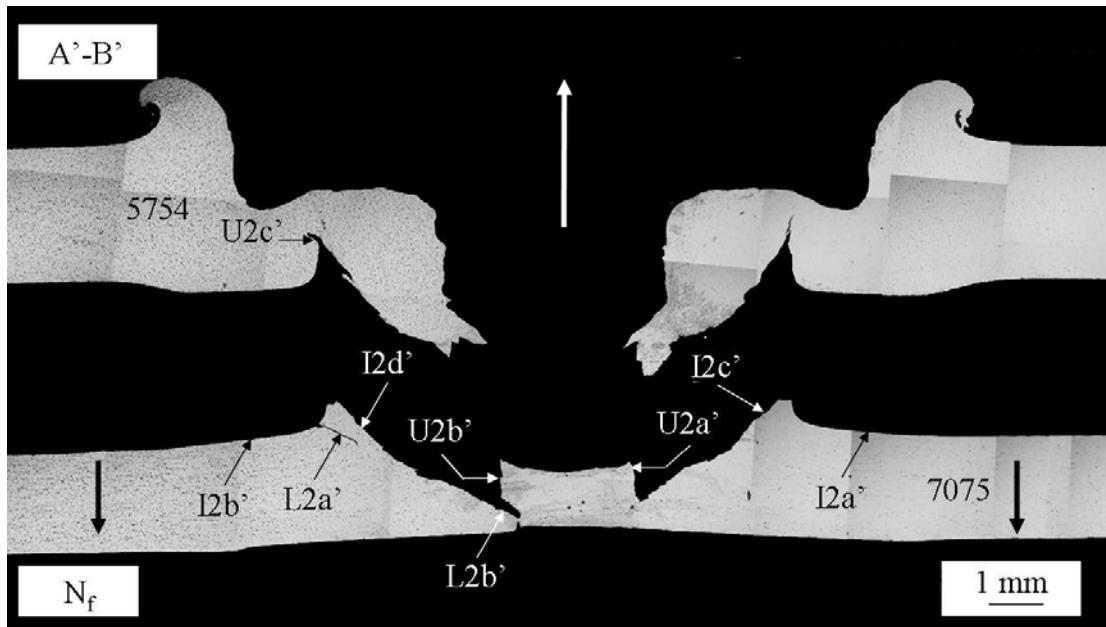
	Failure mode
Quasi-static	A, B, A', B' → C', D' → Circumferential cracks → C, D
Cyclic	A, B, A', B' → E', F' → I' → Circumferential cracks → E, F → G, H, G', H'

(c)

Figure 4.9 (a) A schematic plot of a cross-tension specimen with a spot weld under applied resultant loads (shown as the bold arrows), (b) schematic plots of cross sections A-B and A'-B' for the 5754/7075 spot friction weld in a cross-tension specimen, (c) failure modes of the 5754/7075 spot friction welds in cross-tension specimens under quasi-static and cyclic loading conditions.

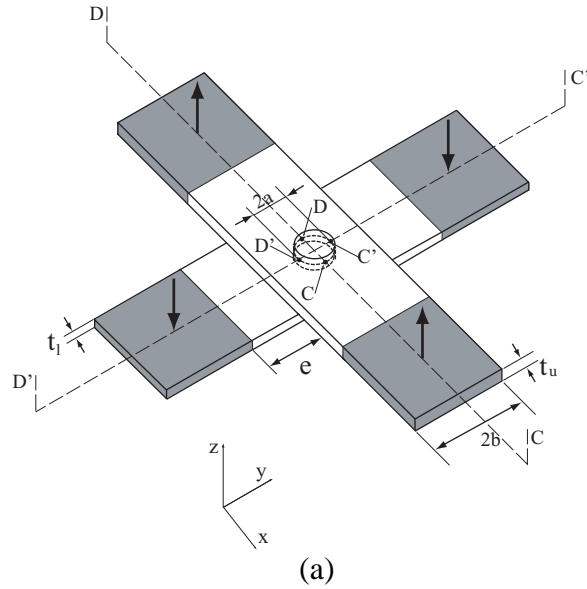


(a)

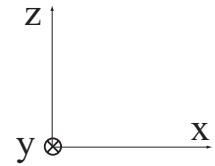
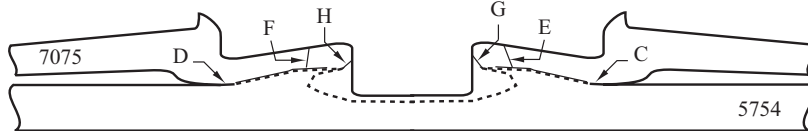


(b)

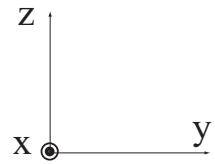
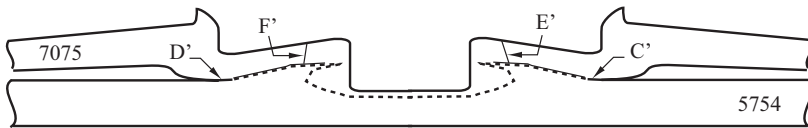
Figure 4.10 Optical micrographs of the cross sections along symmetry planes (a) A-B, (b) A'-B' of failed 5754/7075 spot friction welds in cross-tension specimens at the fatigue life of 2.7×10^3 cycles under a load range of 0.83 kN. The cross sections A-B and A'-B' are schematically marked in Figure 4.11(a).



Cross section C-D



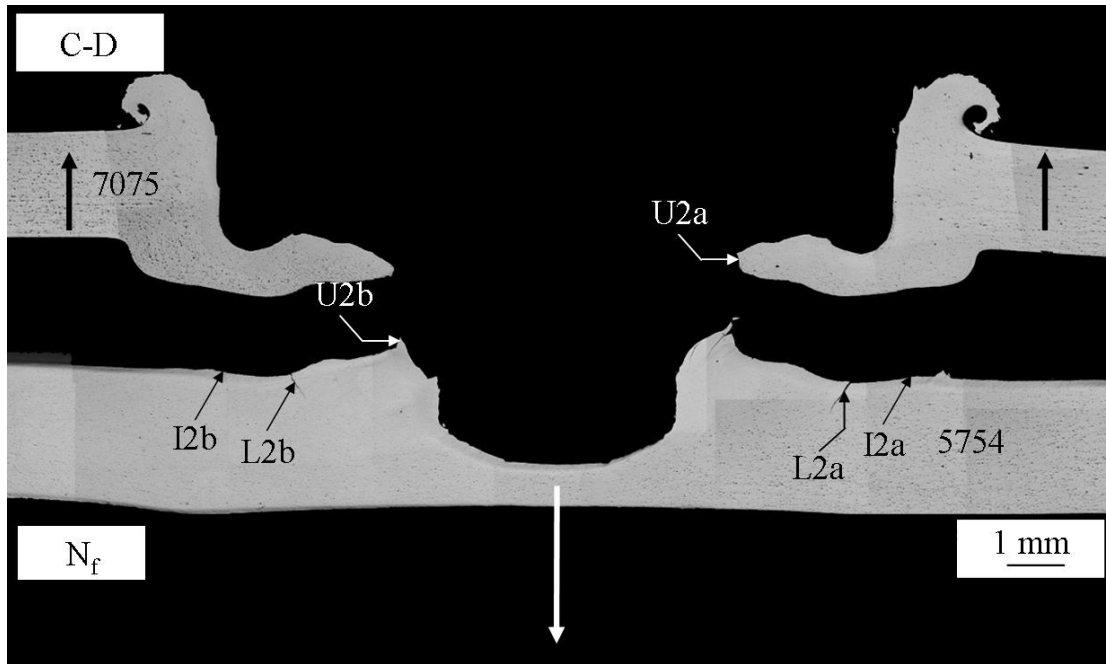
Cross section C'-D'



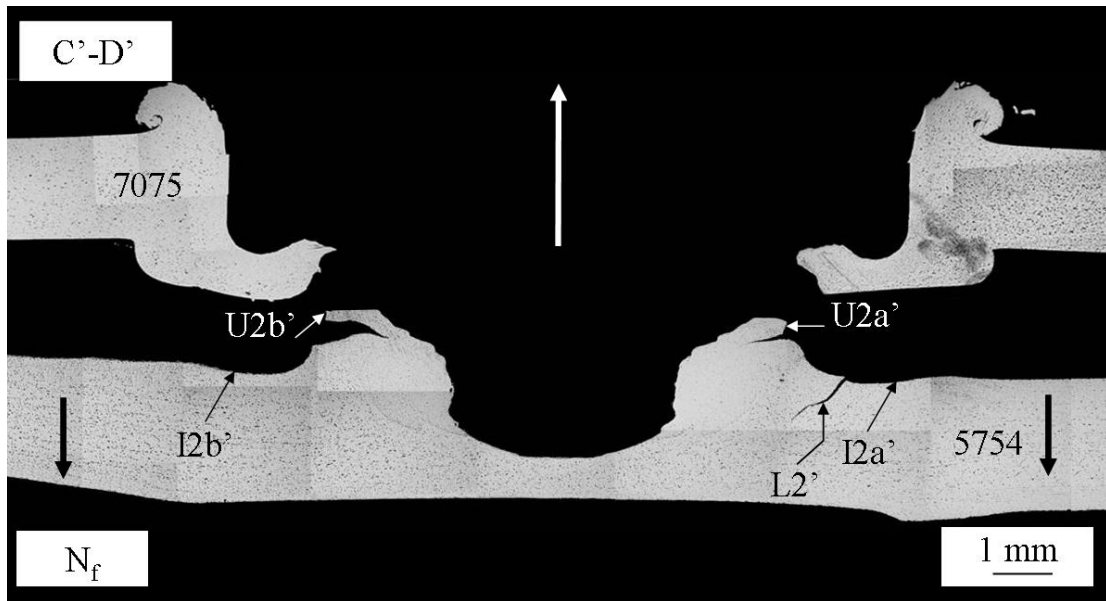
	Failure mode
Quasi-static	C, D, C', D' → E, F → Circumferential cracks → E', F'
Cyclic	C, D, C', D' → Circumferential cracks → G, H, E', F'

(c)

Figure 4.11 (a) A schematic plot of a cross-tension specimen with a spot weld under applied resultant loads (shown as the bold arrows), (b) schematic plots of cross sections C-D and C'-D' for the 7075/5754 spot friction weld in a cross-tension specimen, (c) failure modes of the 7075/5754 spot friction welds in cross-tension specimens under quasi-static and cyclic loading conditions.



(a)



(b)

Figure 4.12 Optical micrographs of the cross sections along symmetry planes (a) C-D, (b) C'-D' of failed 7075/5754 spot friction welds in cross-tension specimens at the fatigue life of 1.7×10^4 cycles under a load range of 0.55 kN. The cross sections C-D and C'-D' are schematically marked in Figure 4.11(a).

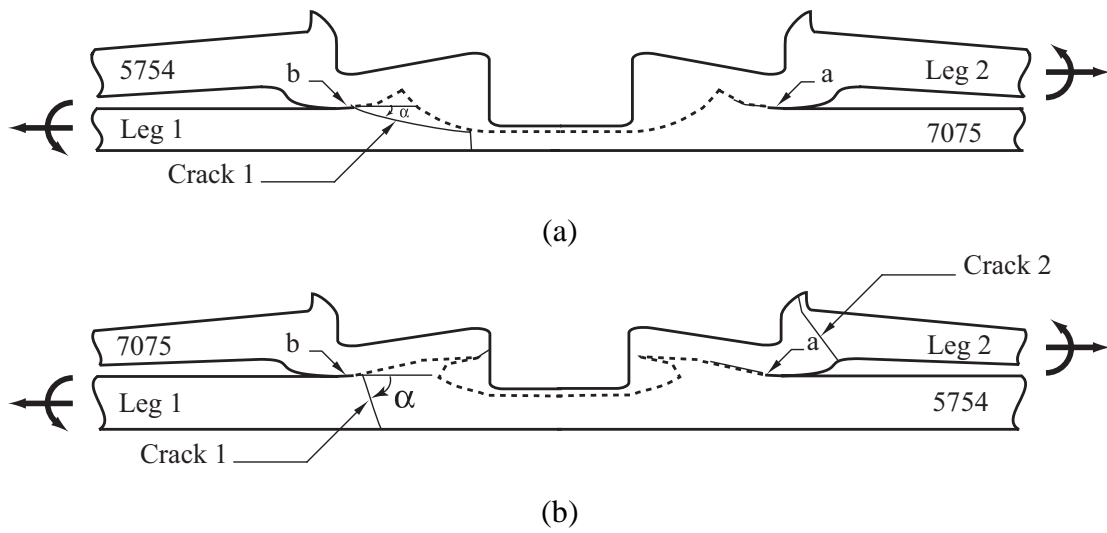
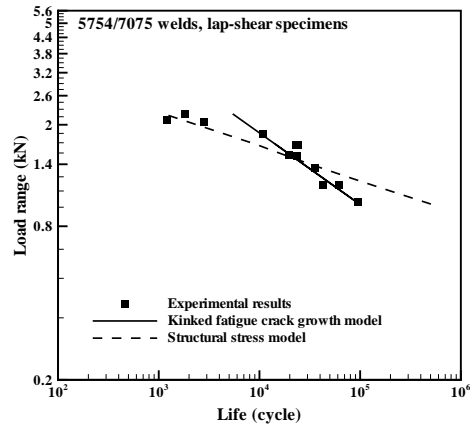
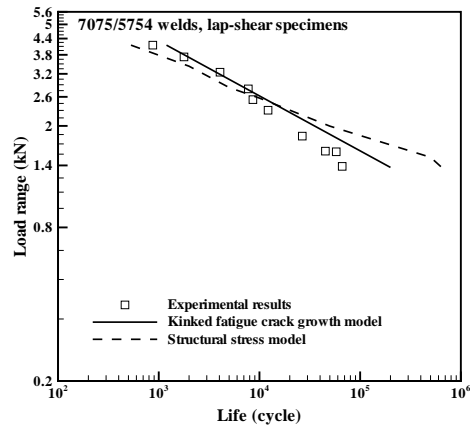


Figure 4.13 (a) A schematic plot of the cross section along the symmetry plane of a 5754/7075 spot friction weld in a lap-shear specimen under cyclic loading conditions, (b) a schematic plot of the cross section along the symmetry plane of a 7075/5754 spot friction weld in a lap-shear specimen under cyclic loading conditions.



(a)



(b)

Figure 4.14 (a) Experimental results and fatigue life estimations for the 5754/7075 spot friction welds in lap-shear specimens, (b) experimental results and fatigue life estimations for the 7075/5754 spot friction welds in lap-shear specimens. The symbols represent the experimental results. The solid and dash lines represent the fatigue life estimations based on the kinked fatigue crack growth model and the structural stress model, respectively.

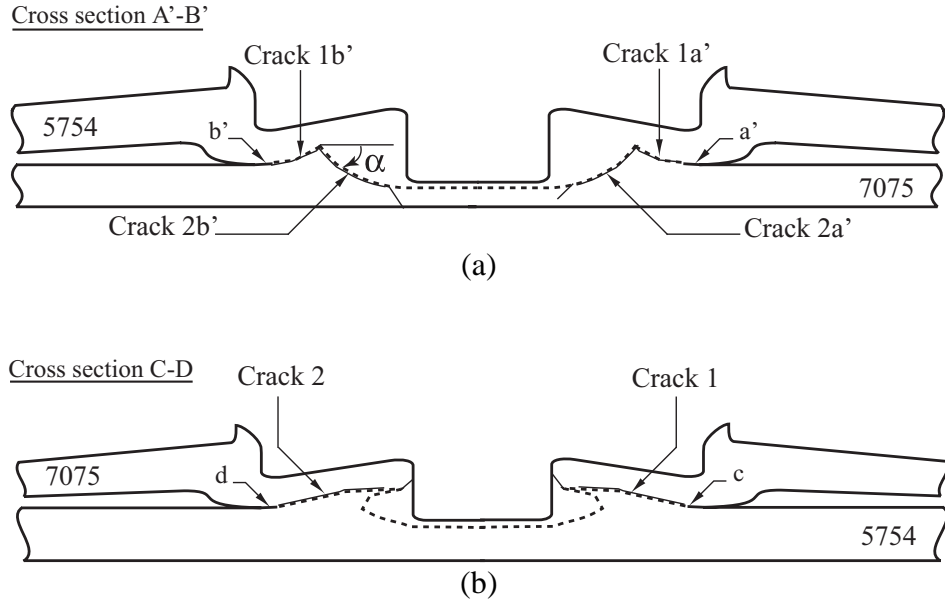
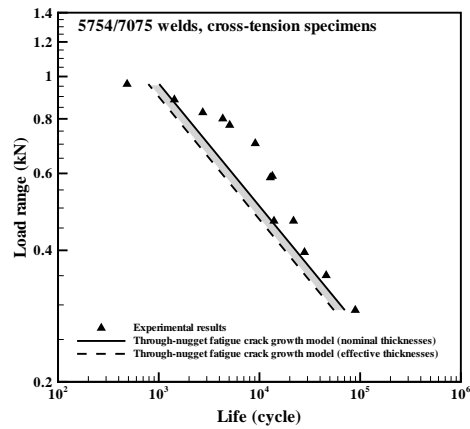
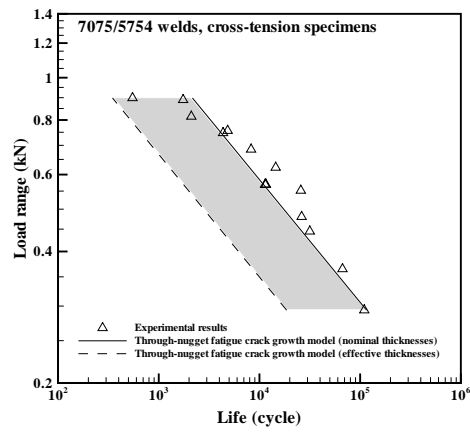


Figure 4.15 (a) A schematic plot of cross section A'-B' of a 5754/7075 spot friction weld in a cross-tension specimen under cyclic loading conditions, (b) a schematic plot of cross section C-D of a 7075/5754 spot friction weld in a cross-tension specimen under cyclic loading conditions.

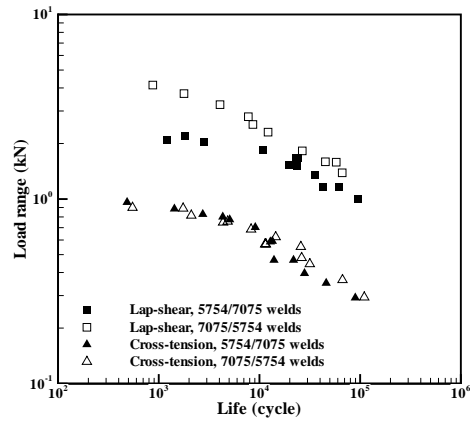


(a)

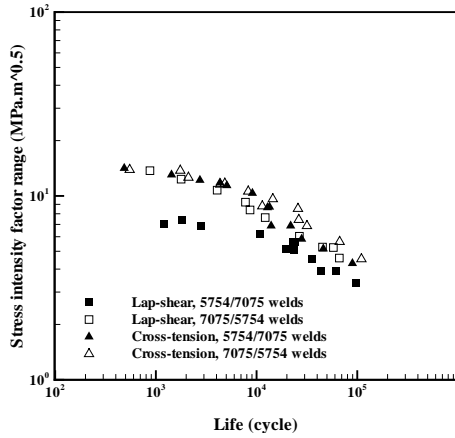


(b)

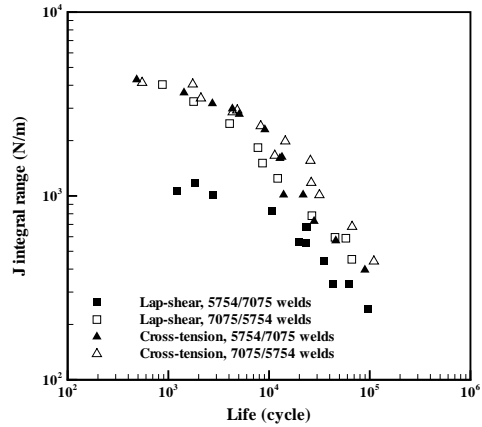
Figure 4.16 (a) Experimental results and fatigue life estimations for the 5754/7075 spot friction welds in cross-tension specimens, (b) experimental results and fatigue life estimations for the 7075/5754 spot friction welds in cross-tension specimens. The symbols represent the experimental results. The solid and dash lines represent the fatigue life estimations based on the through-nugget fatigue crack growth model with the nominal thicknesses and effective thicknesses, respectively.



(a)



(b)



(c)

Figure 4.17 (a) The load range as a function of the fatigue life for the 5754/7075 and 7075/5754 spot friction welds in lap-shear and cross-tension specimens under cyclic loading conditions, (b) the effective stress intensity range as a function of the fatigue life for the 5754/7075 and 7075/5754 spot friction welds in lap-shear and cross-tension specimens under cyclic loading conditions, (c) the J integral range as a function of the fatigue life for the 5754/7075 and 7075/5754 spot friction welds in lap-shear and cross-tension specimens under cyclic loading conditions.

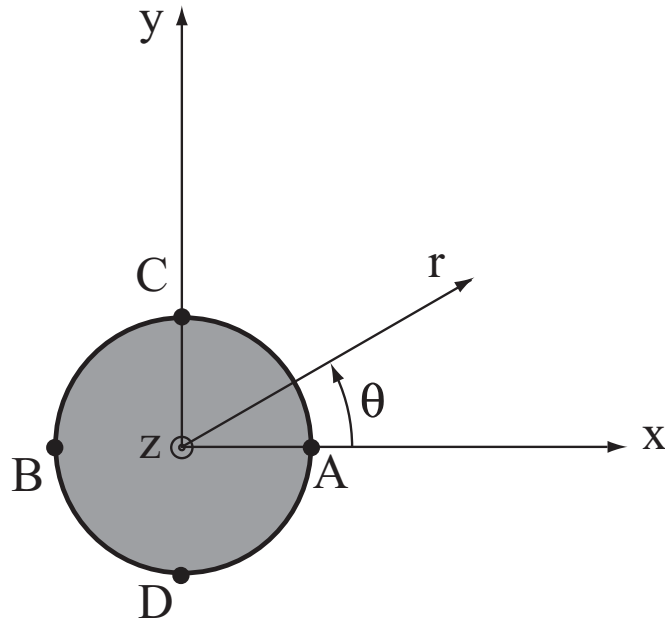
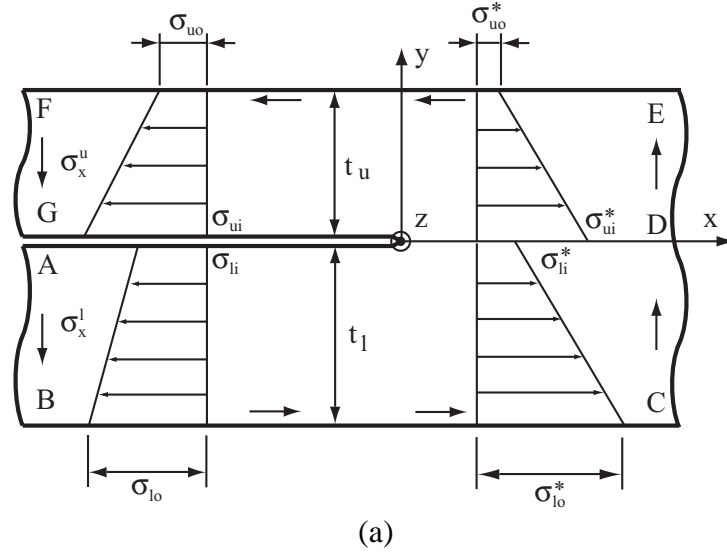


Figure 4.18 (a) The front and side views of the left half of the strip model. The normal stresses σ_{ui} , σ_{uo} , σ_{li} and σ_{lo} represent the normal stresses for line \overline{FG} and line \overline{AB} , the normal stresses σ_{ui}^* , σ_{uo}^* , σ_{li}^* and σ_{lo}^* represent the normal stresses for line \overline{DE} and line \overline{CD} at the inner (*i*) and outer (*o*) surfaces of the upper (*u*) and lower (*l*) strips, respectively, (b) a schematic plot of a top view of the weld nugget (idealized as a rigid inclusion) in the upper sheet of the spot weld specimen with the cylindrical and Cartesian coordinate systems centered at the center of the upper half of the weld nugget.

References

- [1] Thornton PH, Krause, AR, Davies, R G. The aluminum spot weld. *Welding J* 1996;75:101s-108s.
- [2] Gean A, Westgate SA, Kucza JC, Ehrstrom JC. Static and fatigue behavior of spot-welded 5182-O aluminum alloy sheet. *Welding J* 1999;78:80s-86s.
- [3] Sakano R, Murakami K, Yamashita K, Hyoe T, Fujimoto M, Inuzuka M, Nagao Y, Kashiki H. Development of spot FSW robot system for automobile body members. In: *Proceedings of the 3rd international symposium of friction stir welding*, Kobe, Japan, September 27-28, 2001.
- [4] Iwashita T. Method and apparatus for joining. US Patent 6601751 B2, August 5, 2003.
- [5] Lin P-C, Lin S-H, Pan J, Pan T, Nicholson JM, Garman, MA. Microstructures and failure modes of spot friction welds in lap-shear specimens of aluminum 6111-T4 sheets. SAE Technical Paper No. 2004-01-1330, Society of Automotive Engineers, Warrendale, PA: 2004.
- [6] Fujimoto M, Inuzuka M, Nishio M, Nakashima Y. Development of friction spot joining (Report 1) - Cross sectional structures of friction spot joints. The National Meeting of Japan Welding Society, No. 74, 2004, pp. 4-5.
- [7] Fujimoto M, Inuzuka M, Nishio M, Nakashima Y. Development of friction spot joining (Report 2) - Mechanical properties of friction spot joints. The National Meeting of Japan Welding Society, No. 74, 2004, pp. 6-7.
- [8] Hinrichs JF, Smith CB, Orsini BF, DeGeorge RJ, Smale BJ, Ruehl PC. Friction stir welding for the 21st century automotive industry. In: *Proceedings of the 5th international symposium of friction stir welding*, Metz, France, September 14-16, 2004.
- [9] Pan T, Joaquin A, Wilkosz DE, Reatherford L, Nicholson JM. Spot friction welding for sheet aluminum joining. In: *Proceedings of the 5th international symposium of friction stir welding*, Metz, France, September 14-16, 2004.
- [10] Mitlin D, Radmilovic V, Pan T, Chen J, Feng Z, Santella ML. Structure-properties relations in spot friction welded (also known as friction stir spot welded) 6111 aluminum. *Mater Sci Eng A* 2006;441:79-96.
- [11] Tran V-X, Lin P-C, Pan J, Pan T, Tyan T. Failure loads of 6111 spot friction welds under quasi-static and dynamic loading conditions. SAE Technical Paper No. 2007-01-0983, Society of Automotive Engineers, Warrendale, PA:2007.

- [12] Lin P-C, Pan J, Pan T. Fracture and fatigue mechanisms of spot friction welds in lap-shear specimens of aluminum 6111 sheets. SAE Technical Paper No. 2005-01-1247, Society of Automotive Engineers, Warrendale, PA:2005.
- [13] Lin P-C, Pan J, Pan T. Fatigue failures of 6111 spot friction welds under cyclic loading conditions. SAE Technical Paper No. 2006-01-1207, Society of Automotive Engineers, Warrendale, PA:2006.
- [14] Lin P-C, Pan J, Pan T. Failure modes and fatigue life estimations of spot friction welds in lap-shear specimens of aluminum 6111-T4 sheets, Part 1: Welds made by a concave tool. *Int J Fatigue* 2008;30:74-89.
- [15] Lin P-C, Pan J, Pan T. Failure modes and fatigue life estimations of spot friction welds in lap-shear specimens of aluminum 6111-T4 sheets, Part 2: Welds made by a flat tool. *Int J Fatigue* 2008;30:90-105.
- [16] Tran V-X, Pan J, Pan T. Fatigue behaviors of aluminum 5754-O spot friction welds in lap-shear Specimen. SAE Technical Paper No. 2008-01-1139, Society of Automotive Engineers, Warrendale, PA:2008.
- [17] Tran V-X, Pan J, Pan T. Fatigue behavior of aluminum 5754-O and 6111-T4 spot friction welds in lap-shear specimens. *Int J Fatigue*, 2008;3:2175-2190.
- [18] Pan T. Friction stir spot welding (FSSW) - A literature review. SAE Technical Paper No. 2007-01-1702, Society of Automotive Engineers, Warrendale, PA:2007.
- [19] Kaufman J-G. Introduction to Aluminum Alloys and Tempers. The Materials Information Society - ASM International, Materials Park, OH:2000.
- [20] Tozaki Y, Uematsu Y, Tokaji K. Effect of welding condition on tensile strength of dissimilar friction stir spot welds between different aluminum alloys. In: Proceedings of 6th international symposium on friction stir welding, Saint-Sauveur, Nr Montreal, Canada, October 10 - 13, 2006.
- [21] Tweedy BM, Widener CA, Merry JD, Brown JM, Burford DA. Factors affecting the properties of swept friction stir spot welds. SAE Technical Paper No. 2008-01-1135, Society of Automotive Engineers, Warrendale, PA:2008.
- [22] Su P, Gerlich A, North TH, Bendzsak GJ. Intermixing in dissimilar friction stir spot welds. *Metall Mater Trans A* 2007;38A:584-595.
- [23] Tran V-X, Pan J, Pan T. Effects of processing time on strengths and failure modes of dissimilar spot friction welds between aluminum 5754-O and 7075-T6 sheets. SAE Technical Paper No. 2008-01-1138, Society of Automotive Engineers, Warrendale, PA:2008.

- [24] Tran V-X, Pan J, Pan T. Effects of processing time on strengths and failure modes of dissimilar spot friction welds between aluminum 5754-O and 7075-T6 sheets. *J Mater Process Technol* 2009; 209:3724-3739.
- [25] Newman JA, Dowling NE. A crack growth approach to life estimation of spot-welded lap joints. *Fatigue Fract Eng Mater Struct* 1998;21:1123-1132.
- [26] Lin S-H, Pan J, Wung P, Chiang J. A fatigue crack growth model for spot welds in various types of specimens under cyclic loading conditions. *Int J Fatigue* 2006;28:792-803.
- [27] Lin P-C, Pan J. Closed-form structural stresses and stress intensity factor solutions for spot welds in commonly used specimens. *Eng Fract Mech* 2008;75:5187-5206.
- [28] Bergner F, Zouhar G. A new approach to the correlation between the coefficient and the exponent in the power law equation of fatigue crack growth. *Int J Fatigue* 2000;22:229-239.
- [29] Dowling NE. *Mechanical behavior of materials: Engineering methods for deformation, fracture and fatigue*, second ed. Prentice-Hall, Inc, NJ:1999.
- [30] Campbell EJ, Gerberich WW, Underwood JH. *Application of fracture mechanics for selection of metallic structural materials*. American Society for Metals, Metals Parks, OH:1982.
- [31] Friedman P. Private communication, 2007.
- [32] Broek D. *Elementary engineering fracture mechanics*, fourth ed. Martinus Nijhoff Publisher: 1986.
- [33] Tran V-X, Pan J. Effects of weld geometry on fracture mechanics parameters for resistance spot welds and spot friction welds between similar and dissimilar materials in lap-shear specimens, to be submitted for publication.
- [34] Zhang S. Stress intensity factors for spot welds joining sheets of unequal thickness. *Int J Fract* 2003;122:L119-124.
- [35] Suo Z, Hutchinson JW. Interface crack between two elastic layers. *Int J Fract* 1990;43:1-18.

CHAPTER V

INVESTIGATION OF FATIGUE BEHAVIORS OF SPOT FRICTION WELDS BETWEEN DISSIMILAR SHEET MATERIALS IN LAP-SHEAR AND CROSS-TENSION SPECIMENS PART 2: WELDS BETWEEN ALUMINUM AND STEEL SHEETS

Abstract

Fatigue behavior of dissimilar Al/Fe spot friction welds between aluminum 6000 series alloy and coated mild steel sheets in lap-shear and cross-tension specimens is investigated based on experiments and three-dimensional finite element analyses. The Al/Fe welds in lap-shear and cross-tension specimens were tested under quasi-static and cyclic loading conditions. Optical micrographs of the welds after failure under quasi-static and cyclic loading conditions show that the Al/Fe welds in lap-shear and cross-tension specimens mainly fail along the interfacial surface between the aluminum and steel sheets. Three-dimensional finite element analyses based on the micrograph of the cross section along the symmetry plane of the weld before testing were conducted to obtain accurate stress intensity factor and J integral solutions for the crack fronts along the nugget circumferences of the welds under lap-shear and cross-tension loading conditions. The results obtained from the finite element computations correlate well with those obtained from the experimental observations. The numerical results suggest that the in-plane effective stress intensity

factor and J integral solutions at the critical locations of the welds obtained from three-dimensional finite element analyses may be used as fracture mechanics parameters to correlate the experimental fatigue data for the Al/Fe spot friction welds in lap-shear and cross-tension specimens.

Keywords: Spot friction weld; Friction stir spot weld; Dissimilar Al/Fe weld; Stress intensity factor; J integral; Finite element analysis; Fatigue; Correlation; Interfacial surface

5.1. Introduction

Aluminum alloys are becoming to be widely used in the automotive industry. Recently, a spot friction welding technology to join aluminum sheets was developed by Mazda Motor Corporation and Kawasaki Heavy Industry [1,2]. A schematic illustration of the spot friction welding process used to join two aluminum sheets was presented; for example, in Lin et al. [3] and Tran et al. [4]. As summarized in Part 1, most of the current literature is for spot friction welds joining two aluminum sheets.

Material substitution from steels to aluminum alloys is one of the approaches to reduce vehicle weight. Recently, vehicles made of hybrid body structures which combine steel and aluminum parts have been produced in the automotive companies [5,6]. Therefore, an efficient joining method is needed to join different components made of aluminum and steel sheets. Recently, Mazda Motor Corporation [7] has modified the conventional spot friction welding technology to join aluminum to steel sheets. A schematic illustration of the spot friction welding process used to join an

aluminum sheet to a coated steel sheet is shown in Figure 5.1. As shown in the figure, a rotating tool with a probe pin is first plunged into the upper aluminum sheet until a pre-set plunge depth smaller than the thickness of the upper sheet is achieved. An anvil beneath the lower steel sheet is used to support the tool downward force induced by the tool penetration. The tool rotational speed is then maintained at the pre-set plunge depth for an appropriate time to generate frictional heat. Then, heated and softened material adjacent to the tool deforms plastically, and the interfacial oxide films on the surfaces of the aluminum and coated steel sheets are destroyed. The coating layer of the steel sheet is also removed at the same time due to the plastic flow of the aluminum sheet. As a result, the fresh surfaces of aluminum and steel sheets come in contact directly and a solid-state bond is made between the surfaces of the aluminum and steel sheets. Finally, the tool is drawn out of the upper aluminum sheet.

It should be noted that the microstructures and failure modes of dissimilar spot friction welds between aluminum and steel sheets under quasi-static loading conditions have been studied by many researchers based on experimental observations (Tanaka et al. [8,9]; Gendo et al. [10]). However, the fracture and failure mechanisms of dissimilar spot friction welds between aluminum and coated steel sheets under cyclic loading conditions have not been investigated. In this part of the paper, the fatigue behavior of dissimilar spot friction welds between aluminum and coated steel sheets in lap-shear and cross-tension specimens is investigated based on experimental observations and three-dimensional finite element analyses. Since the spot friction welding process used to join an aluminum sheet to a coated steel

sheet is different from that used to join two aluminum sheets, a separate presentation of the fatigue behavior of dissimilar spot friction welds between aluminum and coated steel sheets in this part appears to be warranted.

As schematically shown in Figure 5.1, during the spot friction welding process, the tool contacts the upper aluminum sheet and penetrates the upper sheet to weld together the upper and lower sheets. The dissimilar spot friction weld between aluminum and coated steel sheets is therefore denoted as the Al/Fe weld in this paper. The Al/Fe welds in lap-shear and cross-tension specimens were tested under quasi-static and cyclic loading conditions. Optical micrographs of the welds after failure were examined to understand the fracture and failure mechanisms of the welds. Three-dimensional finite element analyses based on the micrograph of the cross section along the symmetry plane of the weld before testing were conducted to obtain accurate stress intensity factor and J integral solutions for the crack fronts along the nugget circumferences of the welds under lap-shear and cross-tension loading conditions. The results obtained from the finite element computations are correlated with those obtained from the experimental observations. Finally, the in-plane effective stress intensity factor and J integral solutions at the critical locations of the welds obtained from three-dimensional finite element analyses are used to correlate the experimental fatigue data for the Al/Fe spot friction welds in lap-shear and cross-tension specimens.

5.2. Micrographs of Al/Fe spot friction weld before testing

Aluminum 6000 series alloy and coated steel sheets with the thicknesses of 1.3 mm and 0.8 mm, respectively, are used in this investigation. The coated steel sheet is made by coating the mild steel sheets with coating material consisting of Zn-11%Al-3%Mg with a mass of 90 g/m^2 for one side [10]. Dissimilar Al/Fe spot friction welds were made by using a spot friction welding gun at Mazda Motor Corporation, Japan. For the spot friction welding process under displacement-controlled conditions, the important welding processing parameters are the tool geometry, the tool rotational speed, the tool plunge depth and the processing time. In this investigation, a tool with a concave shoulder and a smooth probe pin was used to make the Al/Fe welds. The diameters of the tool shoulder and the tool probe pin are 10 mm and 2 mm, respectively. A tool rotational speed of 1500 rpm and a tool holding time of 5 sec were specified. The optimal plunge depth of 0.85 mm for the maximum failure load of the Al/Fe welds in lap-shear specimens under this particular set of the welding processing parameters was identified by experiments. This optimal plunge depth and the welding processing parameters specified above were then used to make the Al/Fe spot friction welds in lap-shear and cross-tension specimens tested in this investigation.

Figure 5.2(a) shows an optical micrograph of the cross section along the symmetry plane of an Al/Fe spot friction weld before testing. As shown in the figure, the indentation profile reflects the general shape of the smooth probe pin and the concave shoulder of the tool. Note that the tool probe pin penetrated partially into the upper aluminum sheet. The bottom surface of the lower steel sheet appears to be

slightly bent. Two notches, marked as N1 and N2, can be seen in the figure. The locations of the crack tips are also marked in the figure. The locations of the crack tips can be identified by, for example, a scanning electron micrograph of the crack tip region as shown in Figure 5.2(b). Note that the aluminum 6000 series alloy and mild steel surfaces have different gray levels under the scanning electron microscopy due to different chemical compositions as shown in the figure. Note also that the microstructure of the materials in the interface layer between the aluminum and steel sheets in the Al/Fe spot friction weld was discussed in details in Gendo et al. [10].

As shown in Figure 5.2(a), the thickness of the weld nugget near the central hole is larger than that near the outer circumference of the tool shoulder indentation due to the concave geometry of the tool shoulder. The concave tool shoulder squeezed out some upper sheet material but maintained some upper sheet material near the central hole. As suggested in Figure 5.2(a), the material under the tool shoulder indentation flowed outward and resulted in a radial expansion of the upper sheet material along the outer circumference of the tool shoulder indentation. However, due to the constraint of the neighboring material, the sheet was therefore bent along the outer circumference of the tool shoulder indentation. The bends are marked as B1 and B2 as shown in Figure 5.2(a). Note that a small gap between the upper and lower sheets is observed for the Al/Fe weld shown in Figure 5.2(a). Note also that the flashes on the top surface of the upper sheet near the outer boundary of the tool shoulder indentation were also observed in Figure 5.2(a).

5.3. Specimens and experiments

Lap-shear specimens were made by using a 30 mm × 100 mm aluminum sheet and a 30 mm × 100 mm coated steel sheet with a 30 mm × 30 mm overlap area. Figure 5.3(a) shows a lap-shear specimen with an Al/Fe spot friction weld. Note that one doubler made of the upper sheet and another doubler made of the lower sheet with a dimension of 30 mm × 30 mm are attached to the ends of the upper and lower sheets, respectively, of the lap-shear specimen during testing to align the applied load to minimize the initial realignment of the specimen during testing. Figure 5.3(b) shows a cross-tension specimen with an Al/Fe spot friction weld. Cross-tension specimens were made by using a 30 mm × 100 mm aluminum sheet and a 30 mm × 100 mm coated steel sheet with a 30 mm × 30 mm overlap area. Note that four steel pieces with a cross-sectional area of 33 mm × 30 mm are used to clamp the upper and lower sheets, except the overlap area, to the cross-tension testing fixture. Therefore, the tolerance width between the overlap area and the clamped area is 2 mm. Due to the finite compliance of the welding machine and welding fixture, the actual plunge depths of the tool penetration and weld geometries were not precisely the same under the same welding processing parameters. As discussed in Tran and Pan [11], the complex weld geometry of the Al/Fe spot friction weld appears to strongly affect the stress intensity factor and J integral solutions for the crack front along the nugget circumference of the weld in the lap-shear specimen. In order to minimize the effects of the weld geometry on the experimental results, we selected the lap-shear and cross-tension specimens with the Al/Fe spot friction welds that have nearly the same actual plunge depths of the tool penetration for quasi-static and fatigue tests.

Lap-shear and cross-tension specimens with Al/Fe spot friction welds were first tested under quasi-static loading conditions by using an Instron testing machine at a monotonic displacement rate of 1.0 mm per minute. The tests were terminated when specimens were separated. The load and displacement histories were simultaneously recorded during each test. Figure 5.4(a) shows typical load-displacement curves for the Al/Fe spot friction welds in lap-shear and cross-tension specimens under quasi-static loading conditions. Note that the slackness in the test set up has been removed in the load-displacement curves. The average failure loads, defined as the maximum load of the load-displacement curve, obtained from five tested lap-shear specimens and five tested cross-tension specimens are 3.1 kN and 0.44 kN, respectively. The failure loads were used as the reference loads to determine the loads applied for the fatigue tests. The lap-shear and cross-tension specimens were then tested under cyclic loading conditions by using an Instron servo-hydraulic fatigue testing machine with the load ratio R of 0.2. The test frequency was 10 Hz. The tests were terminated when the specimens were separated, or nearly separated when the displacement of the two grips of specimens exceeded 5 mm. Some tests were stopped before the final failures of the specimens to examine the fatigue crack growth patterns. Figure 5.4(b) shows the load range as a function of the fatigue life for the Al/Fe spot friction welds in lap-shear and cross-tension specimens under cyclic loading conditions. As shown in Figure 5.4(b), the number of available specimens for fatigue testing is limited.

5.4. Failure modes of Al/Fe spot friction welds under cyclic loading conditions

5.4.1. Failure modes of Al/Fe welds in lap-shear specimens

We conducted experiments for the Al/Fe spot friction welds in lap-shear specimens under quasi-static and cyclic loading conditions. Based on the experimental observations, the failed Al/Fe spot friction welds in lap-shear specimens under quasi-static loading conditions show the interfacial failure mode. The failed Al/Fe spot friction welds in lap-shear specimens under cyclic loading conditions also show the interfacial failure mode but with fatigue crack growth near the bend. Figure 5.5(a) shows a schematic plot of a lap-shear specimen with an Al/Fe spot friction weld and with the upper sheet thickness $t_u = 1.3$ mm and the lower sheet thickness $t_l = 0.8$ mm under applied resultant loads (shown as the bold arrows). Figure 5.5(b) shows a schematic plot of the cross section along the symmetry plane of the Al/Fe spot friction weld in a lap-shear specimen. In this figure, the thick dashed line represents the interfacial surface between the aluminum and steel sheets and the thin solid lines represent either the fracture surfaces or cracks. It should be noted that the interfacial surface appears to be well bonded as discussed earlier. Figure 5.5(c) summarizes the failure modes of the Al/Fe spot friction welds in lap-shear specimens under quasi-static and cyclic loading conditions.

As shown in Figure 5.5(b) and as summarized in Figure 5.5(c), under quasi-static loading conditions, cracks A and B appear to emanate from the original crack tips of the weld and propagate a bit along the interfacial surface. Crack B then becomes crack I that continues to grow along the interfacial surface. When the load continues to increase, the upper and lower sheets are eventually separated by a fracture surface

along the interfacial surface. Under cyclic loading conditions, cracks A and B appear to emanate from the original crack tips of the weld and propagate a bit along the interfacial surface. Crack B then becomes crack I that continues to grow along the interfacial surface. Another fatigue crack, marked as D, appears to emanate from the bend surface outside the nugget on the right portion of the upper aluminum sheet and propagates into the upper sheet thickness. Finally, the upper and lower sheets are eventually separated by a fracture surface along the interfacial surface. Since we focus on the fatigue behavior of the Al/Fe spot friction weld, only the micrographs to show the failure mode of the welds under cyclic loading conditions are reported here.

Figure 5.6(a) shows an optical micrograph of the cross sections along the symmetry plane of a partially failed Al/Fe spot friction weld in a lap-shear specimen at the fatigue life of 6.5×10^3 cycles under a load range of 2.08 kN. The bold arrows in the figure schematically show the direction of the applied load. Due to the large deformation in the final stage of the specimen failure, the weld nugget rotated clockwise slightly. Therefore, the sheets near the nugget are slightly bent. The applied loads stretch the upper right aluminum sheet and the lower left steel sheet as shown. The location of the crack tip as marked in Figure 5.6(a) due to the propagation of crack I2b along the interfacial surface at the fatigue life of 6.5×10^3 cycles can be identified by a scanning electron micrograph of the crack tip region as shown in Figure 5.6(b).

As shown in Figure 5.6(a), two fatigue cracks, marked as I2a and I2b, appear to emanate from the original crack tips of the weld and propagate a bit along the interfacial surface. Crack I2b then continues to grow along the interfacial surface.

Another fatigue crack, marked as crack U2, appears to be initiated near the bend surface outside the nugget on the right portion of the upper aluminum sheet. As shown in Figure 5.6(a), fatigue crack U2 propagates partially into the upper sheet thickness at the fatigue live of 6.5×10^3 cycles. Near the final stage of the specimen failure, after fatigue crack U2 propagates almost through the upper sheet thickness, without enough support of the upper sheet near the stretching side of the nugget, the nugget is rotated clockwise and the sheets near the nugget are therefore bent. The upper and lower sheets are eventually separated through a fracture surface along the interfacial surface. Based on the micrograph shown in Figure 5.6(a), fatigue crack I2b appears to be the dominant fatigue crack that causes the final failure of the lap-shear specimen.

Figure 5.6(c) shows a close-up top view of the lower sheet and a close-up bottom view of the upper sheet of a failed lap-shear specimen under cyclic loading conditions. The interfacial failure mode can be seen from the Al/Fe weld produced by this particular set of welding parameters on the lower and upper sheets of the failed lap-shear specimen. The marked outer rough surfaces near the outer circumferences of the welds between the marked large circles and small ellipses in Figure 5.6(c) represent the unwelded surfaces. The rough surfaces in the smaller marked ellipses outside the central smooth circular area represent the interfacial fracture surfaces due to the propagation of fatigue crack I2b along the interfacial surface as marked in Figure 5.6(a) on the upper and lower sheets. In summary, the Al/Fe spot friction welds in lap-shear specimens mainly fail along the interfacial surface between

aluminum and steel sheets and from the crack in the upper aluminum sheet under cyclic loading conditions.

5.4.2. Failure modes of Al/Fe welds in cross-tension specimens

We conducted experiments for the Al/Fe spot friction welds in cross-tension specimens under quasi-static and cyclic loading conditions. Based on the experimental observations, the failure modes of the Al/Fe spot friction welds in cross-tension specimens under quasi-static and cyclic loading conditions are quite similar. A schematic plot of a cross-tension specimen with a spot weld is shown in Figure 5.7(a). In Figure 5.7(a), the shaded parts represent the parts where the specimen is clamped to the testing fixture and the large bold arrows schematically show the loads applied to the specimen. In the figure, the half width b , the tolerance width e between the overlap area and the clamped area, and the upper and lower sheet thicknesses t_u and t_l represent the dimensions of the cross-tension specimen. Note that $2a$ represents the diameter of the spot weld. The critical locations of the weld are marked as A, B, C and D in the figure. Two cross sections along the symmetry planes of the cross-tension specimen marked as cross section A-B and cross section C-D are shown in the Figure 5.7(a). A Cartesian coordinate system is also shown in the figure. The failed Al/Fe spot friction welds in cross-tension specimens were sectioned along cross sections A-B and C-D as marked in Figure 5.7(a) to examine in details the cracking patterns.

Figure 5.7(b) shows schematic plots of cross sections A-B and C-D of the Al/Fe spot friction weld in a cross-tension specimen. In this figure, the thick dashed lines

represent the interfacial surfaces between the aluminum and steel sheets and the thin solid lines represent either the fracture surfaces or cracks. It should be noted that the interfacial surface appears to be well bonded as discussed earlier. The Cartesian coordinate systems are also shown in the figure. Figure 5.7(c) summarizes the failure modes of the Al/Fe spot friction welds in cross-tension specimens under quasi-static and cyclic loading conditions. As shown in Figure 5.7(b) and as summarized in Figure 5.7(c), under quasi-static and cyclic loading conditions, cracks A and B on cross section A-B and cracks C and D on cross section C-D appear to emanate from the original crack tips of the weld. Cracks A, B, C and D then become cracks I1, I2, I3 and I4, respectively, that propagate along the interfacial surface. Eventually, the upper and lower sheets are separated by a fracture surface along the interfacial surface. Since the failure modes of the Al/Fe welds in cross-tension specimens under quasi-static and cyclic loading conditions are quite similar, only the micrographs to show the failure mode of the Al/Fe welds under cyclic loading conditions are reported here.

Figures 5.8(a) and 5.8(b) show the optical micrographs of cross sections A-B and C-D of partially failed Al/Fe spot friction welds in cross-tension specimens at the fatigue life of 10^4 cycles under a load range of 0.16 kN. Note that the micrographs shown in Figures 5.8(a) and 5.8(b) were obtained from two different partially failed welds sectioned along cross sections A-B and C-D, respectively, as marked in Figure 5.7(a). In these figures, the bold arrows schematically represent the loading directions. As shown in the figures, four fatigue cracks, marked as I2a and I2b in Figure 5.8(a) and as I2c and I2d in Figure 5.8(b), appear to emanate from the original

crack tips of the welds on cross sections A-B and C-D, respectively, and propagate along the interfacial surfaces toward the central hole. The locations of the crack tips due to the propagation of cracks I2a, I2b, I2c and I2d along the interfacial surfaces at the fatigue life of 10^4 cycles are also marked in the figures. As shown in Figures 5.8(a) and 5.8(b), the crack lengths for fatigue cracks I2c and I2d are larger than those for fatigue cracks I2a and I2b. Fatigue cracks I2c and I2d appear to be dominant fatigue cracks that caused the final failure of the cross-tension specimen. Finally, the upper and lower sheets are separated through a fracture surface along the interface.

Figure 5.8(c) shows a close-up top view of the lower sheet and a close-up bottom view of the upper sheet of a failed cross-tension specimen under-cyclic loading conditions. The interfacial failure mode can be seen from the Al/Fe weld produced by this particular set of welding parameters on the lower and upper sheets of the failed cross-tension specimen. The marked outer rough surfaces near the outer circumferences of the welds between the marked large circles and small ellipses in Figure 5.8(c) represent the unwelded surfaces. The rough surfaces in the smaller marked ellipses outside the central smooth circular area represent the interfacial fracture surfaces due to the propagation of fatigue cracks I2a, I2b, I2c and I2d as shown in Figures 5.8(a) and 5.8(b) along the interfacial surface on the upper and lower sheets. In summary, the Al/Fe spot friction welds in cross-tension specimens mainly fail along the interfacial surface between aluminum and steel sheets under cyclic loading conditions.

5.5. Three-dimensional finite element analyses

As shown in Figure 5.4, the experimental fatigue results for the Al/Fe spot friction welds in lap-shear and cross-tension specimens in terms of the applied load range are quite different. Therefore, it is difficult to assess the experimental fatigue results and to compare the fatigue strengths of the Al/Fe welds in different types of specimens in terms of the applied load range. In this investigation, we attempt to employ the fracture mechanics parameters such as the in-plane effective stress intensity factor and J integral solutions at the critical locations of the welds to correlate the experimental fatigue data for the Al/Fe spot friction welds in lap-shear and cross-tension specimens. First, the stress intensity factors and J integral for an interface crack between two dissimilar elastic materials are summarized here.

As presented in Tran and Pan [11], the asymptotic in-plane stress field around the interface crack tip is an oscillatory field scaled by a complex stress intensity factor $\mathbf{K} = K_1 + iK_2$ ($i = \sqrt{-1}$) (Rice and Sih [14]). The stresses (σ_y, τ_{xy}) at a small distance r ahead of an interface crack tip and the displacements (δ_x, δ_y) at a small distance r behind the interface crack tip are characterized by \mathbf{K} as

$$\sigma_y + i\tau_{xy} = \frac{K_1 + iK_2}{\sqrt{2\pi r}} \left(\frac{r}{t} \right)^{i\varepsilon} \quad (5.1)$$

$$\delta_y + i\delta_x = \frac{(1 + \kappa_u)/G_u + (1 + \kappa_l)/G_l}{2\sqrt{2\pi}(1 + 2i\varepsilon)\cosh(\pi\varepsilon)} (K_1 + iK_2) \sqrt{r} \left(\frac{r}{t} \right)^{i\varepsilon} \quad (5.2)$$

where the parameters $\kappa_j = 3 - 4\nu_j$ and $\kappa_j = (3 - \nu_j)/(1 + \nu_j)$ ($j = u, l$) are in terms of

the Poisson's ratios ν_j for the plane strain and plane stress conditions, respectively, and G_j ($j = u, l$) denote the shear moduli. The bimaterial constant ε is defined as

$$\varepsilon = \frac{1}{2\pi} \ln \frac{\kappa_u / G_u + 1 / G_l}{\kappa_l / G_l + 1 / G_u} \quad (5.3)$$

In Equations (5.1) and (5.2), t represents a characteristic length (Rice [15]; Suo and Hutchinson [16]; Zhang [17]). In this investigation, t is taken as the smaller value of the upper and lower sheet thicknesses as in Suo and Hutchinson [16] and Zhang [17]. It should be noted that when the two materials are identical, $\varepsilon = 0$, the definitions of the K_1 and K_2 solutions as in Equations (5.1) and (5.2) for the interface crack become identical to the conventional stress intensity factor solutions K_I and K_{II} for the crack in a homogenous material, respectively. Note also that the out-of-plane shear stress field near the interface crack tip is similar to that near the crack in a homogenous material. However, the mode III stress intensity factor solution for the interface crack is denoted as K_3 in this paper in order to be consistent with the definitions of K_1 and K_2 .

Under plane strain conditions, for an interface crack between two dissimilar linear elastic materials, the J integral is related to the K_1 , K_2 and K_3 stress intensity factor solutions as

$$J = \frac{K_1^2 + K_2^2}{\cosh^2(\pi\varepsilon)E^*} + \frac{K_3^2}{2G^*} \quad (5.4)$$

$$\text{with } \frac{1}{E^*} = \frac{1}{2} \left(\frac{1}{E'_u} + \frac{1}{E'_l} \right) \text{ and } \frac{1}{G^*} = \frac{1}{2} \left(\frac{1}{G_u} + \frac{1}{G_l} \right).$$

As discussed in Tran and Pan [11], the complex weld geometry of the Al/Fe spot friction weld appears to strongly affect the fracture mechanics parameters for the crack front along the nugget circumference of the weld in the lap-shear specimen. Therefore, three-dimensional finite element analyses are employed in this investigation to obtain accurate stress intensity factor and J integral solutions for the crack fronts along the nugget circumferences of the welds in lap-shear and cross-tension specimens. In the finite element analyses, the weld nugget and base metals are assumed to be linear elastic isotropic materials. The Young's moduli of the aluminum and coated steel sheets are taken as 68.9 GPa and 207 GPa, respectively. The Poisson's ratios of the aluminum and coated steel sheets are taken as 0.33 and 0.30, respectively. The commercial finite element program ABAQUS [12] is employed to perform the computations. Second-order quarter point crack-tip elements with collapsed nodes traditionally used to model the $1/\sqrt{r}$ singularity near the crack front are adopted. Here r represents the radial distance to the crack front. The stress intensity factor and J integral solutions are directly computed by ABAQUS. The computational stress intensity factor solutions are obtained based on the interaction integral method for cracks under mixed-mode loading conditions (Shih and Asaro [13]).

It should be noted that the components K_1^A and K_2^A of the complex stress intensity factor solution $\mathbf{K}^A = K_1^A + iK_2^A$ obtained directly from ABAQUS are defined such that the stresses (σ_y, τ_{xy}) at a small distance r ahead of an interface crack tip are characterized by \mathbf{K}^A as

$$\sigma_y + i\tau_{xy} = \frac{K_1^A + iK_2^A}{\sqrt{2\pi r}} r^{i\varepsilon} \quad (5.5)$$

The K_1 and K_2 solutions as defined in Equation (5.1) are related to the K_1^A and K_2^A solutions as defined in Equation (5.5) as

$$K_1 = K_1^A \cos(\varepsilon \ln t) - K_2^A \sin(\varepsilon \ln t) \quad (5.6)$$

$$K_2 = K_1^A \sin(\varepsilon \ln t) + K_2^A \cos(\varepsilon \ln t) \quad (5.7)$$

Therefore, the K_1 and K_2 solutions for the Al/Fe spot friction welds reported in this investigation can be obtained from Equations (5.6) and (5.7) with the K_1^A and K_2^A solutions directly computed by ABAQUS. Finally, the in-plane effective stress intensity factor solution K_e is defined as

$$K_e = \sqrt{K_1^2 + K_2^2} \quad (5.8)$$

Note that K_e is the magnitude of the complex stress intensity factor \mathbf{K} . Note also that K_e does not depend on the choice of a characteristic length.

Figure 5.9(a) shows a schematic plot of a half of a lap-shear specimen with a spot weld and the boundary conditions of the finite element analysis. In Figure 5.9(a), the length L (= 100 mm), the overlap length V (= 30 mm), the half width b (= 15 mm), and the upper and lower sheet thicknesses t_u (= 1.3 mm) and t_l (= 0.8 mm) are based on the dimensions of the specimen and testing fixture. Note that $2a$ (= 9.7 mm) represents the diameter of the spot weld. The critical locations of the weld are marked as A, B and C in the figure. As shown in Figure 5.9(a), a uniform displacement in the $+x$ direction is applied along the interfacial surface between the upper sheet and the doubler on the right edge surface of the specimen. Also, the

displacements in the x , y and z directions for the interfacial surface between the doubler and the lower sheet on the left edge surface of the specimen are fixed. Due to symmetry, only a half of the lap-shear specimen is modeled. The displacement in the y direction of the symmetry plane, the xz plane, of the specimen is constrained to represent the symmetry conditions due to the loading conditions.

A three-dimensional finite element mesh and a close-up view of the mesh near the weld for a half of a lap-shear specimen are shown in Figures 5.9(b) and 5.9(c), respectively. Note that the three-dimensional finite element mesh near the weld shown in Figure 5.9(c) is based on the optical micrograph shown in Figure 5.2. As shown in Figure 5.9(c), the mesh near the crack front along the circumference of the weld is refined to assure reasonable aspect ratios of the three-dimensional solid elements. The three-dimensional finite element model for the half lap-shear specimen has 18,077 second-order solid elements. Two crack tips, marked as A and B, are also shown in Figure 5.9(c). The resultant reaction forces F_x , F_y and F_z in the x , y and z directions, respectively, for the interfacial surface between the doubler and the lower sheet on the left edge of the lap-shear specimen are directly calculated by ABAQUS. The numerical results indicate that F_y and F_z are small when compared to F_x . The force F_x is then used as the applied load F for the lap-shear specimen.

A schematic plot of a cross-tension specimen with a spot weld is shown in Figure 5.10(a). In Figure 5.10(a), the shaded parts represent the parts where the specimen is clamped to the testing fixture, and the large bold arrows schematically show the loads applied to the specimen. In the figure, the half width b ($= 15$ mm), the tolerance width e ($= 2.0$ mm) between the overlap area and the clamped area, and the upper

and lower sheet thicknesses t_u (= 1.3 mm) and t_l (= 0.8 mm) are based on the dimensions of the specimen and testing fixture. Note that $2a$ (= 9.7 mm) represents the diameter of the spot weld. The critical locations of the weld are marked as A, B, C and D in the figure.

In the finite element analysis, the shaded parts of the cross-tension specimen in Figure 5.10(a) were not modeled. The finite element analysis was based on an equivalent specimen geometry without the clamped parts shown in Figure 5.10(b). As shown in Figure 5.10(b), a uniform displacement in the $+z$ direction is applied to the outer edge surfaces of the tolerance areas of the upper sheet and the displacements in the x and y directions for the outer edge surfaces of the tolerance areas of the upper sheet are constrained. Also, the displacements in the x , y and z directions for the outer edge surfaces of the tolerance areas of the lower sheet are fixed. Due to symmetry, only a quarter of the equivalent cross-tension specimen shown in Figure 5.10(b) is modeled. The displacement in the y direction of the symmetry xz plane, and the displacement in the x direction of the symmetry yz plane of the cross-tension specimen are constrained to represent the symmetry conditions due to the loading conditions.

A three-dimensional finite element mesh and a close-up view of the mesh near the weld for a quarter of an equivalent cross-tension specimen are shown in Figures 5.10(c) and 5.10(d), respectively. Note that the three-dimensional finite element mesh near the weld shown in Figure 5.10(d) is based on the optical micrograph shown in Figure 5.2. As shown in Figure 5.10(d), the mesh near the crack front along the circumference of the weld is refined to assure reasonable aspect ratios of the

three-dimensional solid elements. The three-dimensional finite element model for the quarter equivalent cross-tension specimen has 8,469 second-order solid elements. Two crack tips, marked as A and C, are also shown in Figure 5.10(d). The resultant reaction forces F_x , F_y and F_z in the x , y and z directions, respectively, for the outer edge surface of the tolerance area of the lower sheet of the equivalent cross-tension specimen are directly calculated by ABAQUS. The force F_y is then used as the applied load F for the cross-tension specimen.

Figure 5.11(a) shows a schematic plot of a top view of the weld nugget (idealized as a rigid inclusion) in the upper sheet of the spot weld specimen with the cylindrical and Cartesian coordinate systems centered at the center of the upper half of the weld nugget. The critical locations of points A, B, C and D are 0° , 180° , 90° and 270° with respect to the x axis, respectively. The locations of points A, B, C and D can also be seen in the Figures 5.7(a), 5.9(a) and 5.10(a). The orientation angle θ represents the angular location along the nugget circumference of the spot weld. Note that the angle θ is measured counterclockwise from the critical location of point A.

Figures 5.11(b) and 5.11(c) show the stress intensity factor K_1 , K_2 , K_3 and K_e solutions as functions of θ for the crack fronts along the nugget circumferences of the Al/Fe spot friction welds in a lap-shear specimen and a cross-tension specimen, respectively, based on our three-dimensional finite element computations. It should be noted that the order of θ is reversed the figures reported in this paper to be consistent with the definition of the angular location θ and the geometry/loading as shown in Figures 5.9 and 5.10. Note also that the K_1 and K_2 solutions shown in Figures 5.11(b) and 5.11(c) are obtained from Equations (5.6) and (5.7), and the in-

plane effective stress intensity factor solution K_e is obtained from Equation (5.8). The results presented in Figures 5.11(b) and 5.11(c) are obtained under the applied resultant lap-shear and cross-tension loads of 1 N, respectively.

As shown in Figure 5.11(b) for the Al/Fe spot friction weld in the lap-shear specimen, based on the finite element computation, the maximum value of the K_1 solution is located at point B ($\theta = 180^\circ$) and the maximum values of the K_2 solution are located at point A ($\theta = 0^\circ$) and point B ($\theta = 180^\circ$), respectively. As shown in Figure 5.11(b), the maximum value of the in-plane effective stress intensity factor solution K_e is located at point B ($\theta = 180^\circ$). At point B ($\theta = 180^\circ$), the K_1 solution is about 2.5 times of the K_2 solution. The results in Figure 5.11(b) also indicate that K_1 solution is the dominant stress intensity factor for the Al/Fe weld spot friction weld at point B ($\theta = 180^\circ$) under lap-shear loading conditions. Note that the distribution of the J integral solution for the Al/Fe spot friction weld in the lap-shear specimen is similar to that of the in-plane K_e solution shown in Figure 5.10(b) and is not reported here.

As shown in Figure 5.11(c) for the Al/Fe spot friction weld in the cross-tension specimen, based on the finite element computation, the maximum value of the K_1 solution is located at point C ($\theta = 90^\circ$), the maximum value of the K_2 solution is located at point A ($\theta = 0^\circ$) and the maximum value of the K_3 solution is located at $\theta = 45^\circ$. As shown in Figure 5.11(c), the maximum value of the in-plane effective stress intensity factor solution K_e is located at point C ($\theta = 90^\circ$). At point C ($\theta = 90^\circ$), the K_1 solution is about 7 times of the K_2 solution. Note also that the

distributions of the K_1 and K_e solutions along the nugget circumference of the weld as shown in Figure 5.11(c) are nearly the same. The results in Figure 5.11(c) also indicate that K_1 solution is the dominant stress intensity factor for the Al/Fe spot friction weld at point C ($\theta = 90^\circ$) under cross-tension loading conditions. Note that the distribution of the J integral solution for the Al/Fe spot friction weld in the cross-tension specimen is similar to that of the K_e solution shown in Figure 5.10(c) and is not reported here.

5.6. Correlations of the experimental fatigue data

Based on the optical micrographs of the partially failed Al/Fe welds, the fatigue crack that is initiated at the original crack tip on the left side of the weld, as schematically marked as B in Figure 5.9(a), appears to be the dominant fatigue crack that caused the final failure of the lap-shear specimens under cyclic loading conditions. Also, fatigue cracks that are initiated at the original crack tips on cross section C-D, as schematically marked as C and D in Figure 5.10(a), appear to be the dominant fatigue cracks that caused the final failure of the cross-tension specimens under cyclic loading conditions. Based on the finite element analyses, the maximum values of the in-plane effective stress intensity factor and J integral solutions are located at the crack tip marked as B in Figure 5.9(a) for the lap-shear specimen and at the crack tips marked as C and D in Figure 5.10(a) for the cross-tension specimen. At these critical locations, the out-of-plane shear K_3 solutions are zero. The results obtained from the finite element analyses are therefore correlate well with those obtained from the experimental observations. The agreement between the numerical

results and the experimental observations suggests that the in-plane effective stress intensity factor and J integral solutions at the critical locations of the spot friction welds, defined as the location where the in-plane effective stress intensity factor and J integral solutions are maximum, may be used as appropriate fracture mechanics parameters to correlate the experimental fatigue data for the Al/Fe spot friction welds in lap-shear and cross-tension specimens.

Figure 5.12(a) shows the J integral range as a function of the fatigue life for the Al/Fe spot friction welds in lap-shear and cross-tension specimens under cyclic loading conditions. As shown in Figures 5.4(b) and 5.12(a), the experimental results for the Al/Fe welds in lap-shear and cross-tension specimens in terms of the J integral range become closer to each other when compared to those in terms of the applied load range. As shown in Figure 5.12(a), the J integral solution at the critical locations of the welds obtained from three-dimensional finite analyses may be a good fracture mechanics parameter to correlate the experimental fatigue data for the Al/Fe spot friction welds in lap-shear and cross-tension specimens for the given applied load ranges.

Figure 5.12(b) shows the in-plane effective stress intensity factor range as a function of the fatigue life for the Al/Fe spot friction welds in lap-shear and cross-tension specimens under cyclic loading conditions. As shown in Figures 5.4(b) and 5.12(b), the experimental results for the Al/Fe welds in lap-shear and cross-tension specimens in terms of the in-plane effective stress intensity factor range become closer to each other when compared to those in terms of the applied load range. As shown in Figure 5.12(b), the in-plane effective stress intensity factor solution at the

critical locations of the welds obtained from three-dimensional finite analyses may be a good fracture mechanics parameter to correlate the experimental fatigue data for the Al/Fe spot friction welds in lap-shear and cross-tension specimens for the given applied load ranges.

5.7. Discussions

As discussed in Rice [14], the oscillatory fields for the interface crack based on the elastic solutions cause the overlapping of crack faces or the contact zone near the crack tip. The ratio of the contact zone size r_c to the characteristic geometric length t can be estimated as (Rice [14])

$$\frac{r_c}{t} = \exp\left(-\frac{\pi/2 + \psi}{\varepsilon}\right) \quad (5.9)$$

where the mode mixity is defined as

$$\psi = \tan^{-1}(K_2 / K_1) \quad (5.10)$$

and ε is the bimaterial constant as defined in Equation (5.3). Note that Equation (5.9) is only valid for the case of $\varepsilon > 0$. For the case of $\varepsilon < 0$, one should replace ψ by $-\psi$, and ε by $-\varepsilon$ to describe the same physical problem but with $\varepsilon > 0$. Also, Rice [14] recommended that the ratio r_c/t should be smaller than 0.01 so that the effects of the contact zone can be neglected. For the Al/Fe welds tested in this investigation, the maximum ratio r_c/t under the loads applied in the fatigue tests obtained from Equation (5.9) is 8.3×10^{-18} . Note that the maximum size of the plastic zone near the crack tips of the Al/Fe spot friction welds under the maximum loads applied in the fatigue tests is estimated about 0.06 mm. Since the contact zone size

and plastic zone size are very small when compared to the other geometric parameters of the lap-shear and cross-tension specimens with the Al/Fe welds, the use of the fracture mechanics parameters based on the linear elastic analyses to correlate the experimental fatigue data for the Al/Fe spot friction welds in lap-shear and cross-tension specimens appears to be plausible.

As shown in Figures 5.11(b) and 5.11(c), the numerical results obtained from the finite element analyses indicate that the Al/Fe spot friction welds in lap-shear and cross-tension specimens are both under mode I dominant loading conditions at the critical locations of the welds. It should be noted that the lap-shear specimen is commonly used to investigate the mechanical behavior of the spot weld under shear dominant loading conditions. The mode I dominant loading condition for the Al/Fe spot friction weld in the lap-shear specimen as indicated in Figure 5.11(b) is due to the effects of the complex weld geometry of the Al/Fe spot friction weld as discussed in details in Tran and Pan [11]. Note also that the cross-tension specimen is commonly used to investigate the mechanical behavior of the spot weld under tensile dominant loading conditions. The mode I dominant loading condition for the Al/Fe spot friction weld in the cross-tension specimen as indicated in Figure 5.11(c) is therefore expected. The mode I dominant loading conditions at the critical locations of the Al/Fe spot friction welds in the lap-shear and cross-tension specimens can partially explain why the in-plane effective stress intensity factor solution at the critical locations of the welds may be used as an appropriate parameter to correlate the experimental fatigue data for the Al/Fe spot friction welds in lap-shear and cross-tension specimens.

As shown in Figure 5.11(b), the ratio $(K_e)_{180^\circ}/(K_e)_{0^\circ}$ of the in-plane effective stress intensity factor solution at point B ($\theta = 180^\circ$) to that at point A ($\theta = 0^\circ$) for the Al/Fe weld in the lap-shear specimen is about 2. The larger value of the in-plane effective stress intensity factor solution at point B ($\theta = 180^\circ$) can explain why fatigue crack I2b shown in Figure 5.6(a) propagated more along the interfacial surface while fatigue crack I2a just grew a bit along the interfacial surface. As shown in Figure 5.11(c), the ratio $(K_e)_{90^\circ}/(K_e)_{0^\circ}$ of the in-plane effective stress intensity factor solution at point C ($\theta = 90^\circ$) to that at point A ($\theta = 0^\circ$) for the Al/Fe weld in the cross-tension specimen is about 1.33. The larger value of the in-plane effective stress intensity factor solution at point C ($\theta = 90^\circ$) can explain why fatigue cracks I2c and I2d on cross section C-D shown in Figure 5.8(b) propagated more along the interfacial surface with larger crack growth rates than fatigue cracks I2a and I2b on cross section A-B shown in Figure 5.8(a).

As shown in Figures 4.17(b) and 4.17(c) in Part 1, the experimental fatigue data for the 5754/7075 and 7075/5754 spot friction welds in lap-shear and cross-tension specimens in terms of the in-plane effective stress intensity factor range and the J integral range at the critical locations of the welds obtained from the three-dimensional finite element analyses are quite similar. As shown in Figures 5.12(a) and 5.12(b), though the experimental fatigue data for the Al/Fe spot friction welds in lap-shear and cross-tension specimens in terms of the in-plane effective stress intensity factor range and the J integral range became closer to each other when compared to those in terms of the applied load range as shown in Figure 5.4(b), the differences between the experimental fatigue data for the lap-shear and cross-tension

specimens as shown in Figures 5.12(a) and 5.12(b) are still relatively significant. As discussed in Hutchinson and Suo [18], the fracture toughness of the interface between two dissimilar elastic materials under mixed mode loading conditions is a function of the mode mixity ψ , as defined in Equation (5.10). Hence, the fatigue crack growth properties of the interface between two dissimilar elastic materials are also likely functions of ψ . Note that the mode mixity ψ at the critical locations of the Al/Fe spot friction welds in the lap-shear and cross-tension specimens are about -25° and -10° , respectively, as indicated in Figures 5.11(b) and 5.11(c). Therefore, the fatigue crack growth properties for the interfacial surface between aluminum and steel sheets in the lap-shear specimen under the applied loads schematically shown as the bold arrows in Figure 5.5(a) may not be the same as those for the Al/Fe interface in the cross-tension specimen under the applied loads schematically shown as the bold arrows in Figure 5.7(a). This remark may partially explain the difference between the experimental fatigue data for the Al/Fe spot friction welds in lap-shear and cross-tension specimens in terms of the in-plane effective stress intensity factor range as shown in Figure 5.12(b).

As shown in Figure 5.6(a), dominant fatigue crack I2b propagated from the left side to the right side of the weld in the lap-shear specimen. As shown in Figure 5.8(a), dominant fatigue cracks I2c and I2d propagated from the left side and the right side of the weld toward the central hole in the cross-tension specimen. The crack growth path for the dominant fatigue crack in lap-shear specimen is longer than that for the dominant fatigue cracks in the cross-tension specimen. The longer crack growth path and the larger mode mixity at the critical locations for the dominant

fatigue crack in the lap-shear specimen when compared to those in the cross-tension specimen can explain why the fatigue life of the weld in the lap-shear specimen is higher than that in the cross-tension specimen under the same given applied in-plane effective stress intensity factor range as shown in Figure 5.12(b).

It should be emphasized that the microstructure of the interface layer between aluminum and steel in the Al/Fe spot friction weld is quite complicated and may consist of Al-Zn oxide with an amorphous structure and small intermetallics in an aluminum base matrix as discussed in Gendo et al. [10]. Note that the interface layer was not modeled in the finite element analyses since the thickness of the interface layer is very small when compared to the aluminum and steel sheet thicknesses. As discussed in Hutchinson and Suo [18], the details of the cracking morphology in the interface layer of a third phase can also affect the mixed mode toughness. Close-up optical micrographs of the failed Al/Fe welds tested in this investigation indicate that the Al/Fe welds in lap-shear specimens seem to fail along the interface between the upper aluminum sheet and the interface layer, whereas the Al/Fe welds in cross-tension specimens seem to fail through the interface layer. Different cracking morphologies observed for the Al/Fe welds in the lap-shear and cross-tension specimens are likely due to the different mode mixity at the critical locations of the welds in lap-shear and cross-tension specimens as discussed earlier. This remark may also partially explain the difference between the experimental fatigue data for the Al/Fe spot friction welds in lap-shear and cross-tension specimens in terms of the in-plane effective stress intensity factor range as shown in Figure 5.12(b). A further detailed investigation of the cracking morphologies along the interface layer is

therefore needed to correlate better the experimental fatigue data for the Al/Fe spot friction welds in lap-shear and cross-tension specimens.

5.8. Conclusions

Fatigue behavior of dissimilar Al/Fe spot friction welds between aluminum 6000 series alloy and coated mild steel sheets in lap-shear and cross-tension specimens is investigated based on experiments and three-dimensional finite element analyses. The Al/Fe welds in lap-shear and cross-tension specimens were tested under quasi-static and cyclic loading conditions. Optical micrographs of the welds after failure under quasi-static and cyclic loading conditions show that the Al/Fe welds in lap-shear and cross-tension specimens mainly fail along the interfacial surface between the aluminum and steel sheets. Three-dimensional finite element analyses based on the micrograph of the cross section along the symmetry plane of the weld before testing were conducted to obtain accurate stress intensity factor and J integral solutions for the crack fronts along the nugget circumferences of the welds under lap-shear and cross-tension loading conditions. The results obtained from the finite element computations correlate well with those obtained from the experimental observations. The numerical results suggest that the in-plane effective stress intensity factor and J integral solutions at the critical locations of the welds obtained from three-dimensional finite element analyses may be used as fracture mechanics parameters to correlate the experimental fatigue data for the Al/Fe spot friction welds in lap-shear and cross-tension specimens.

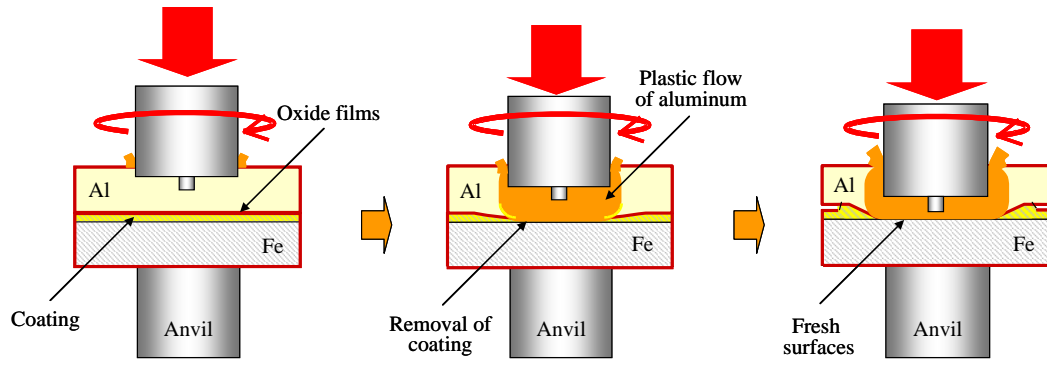
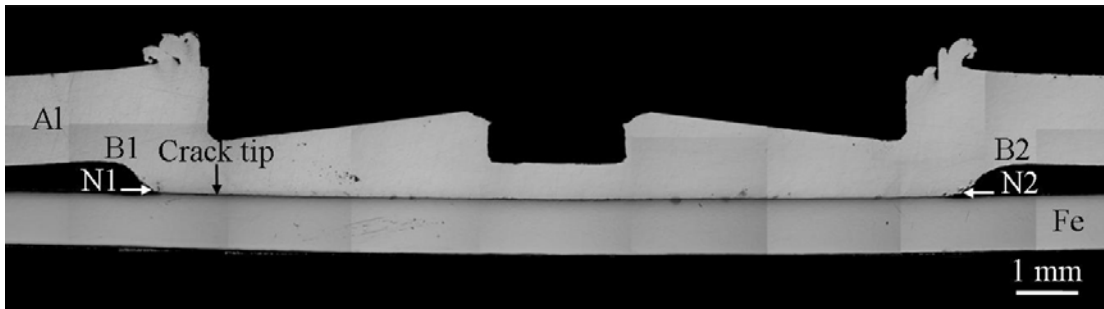
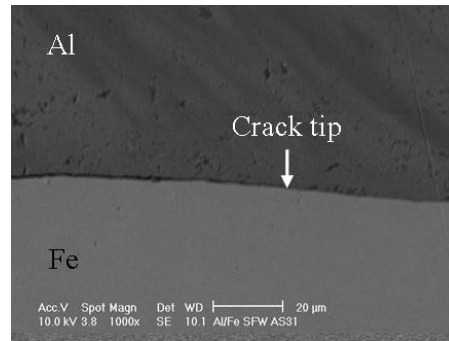


Figure 5.1 A schematic illustration of the spot friction welding process used to join an aluminum sheet to a coated steel sheet.



(a)

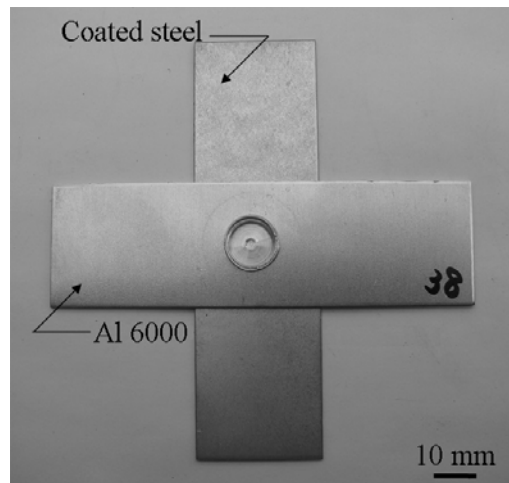


(b)

Figure 5.2 (a) An optical micrograph of the cross section along the symmetry plane of an Al/Fe spot friction weld before testing, (b) a scanning electron micrograph of the crack tip region as marked in (a).

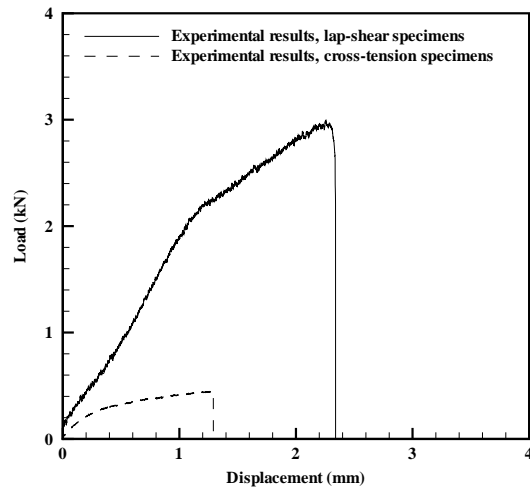


(a)

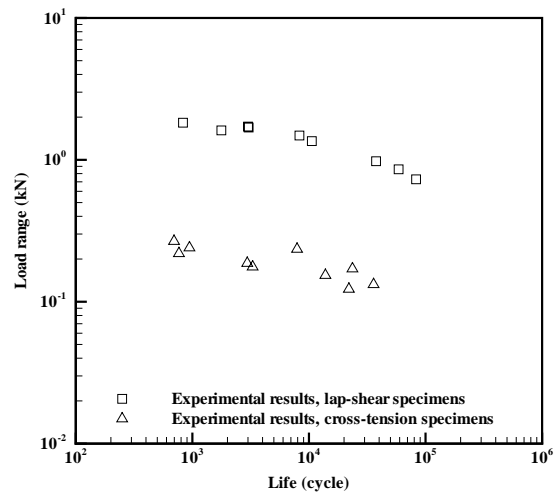


(b)

Figure 5.3 (a) A lap-shear specimen with an Al/Fe spot friction weld, (b) a cross-tension specimen with an Al/Fe spot friction weld.



(a)



(b)

Figure 5.4 (a) Typical load-displacement curves for the Al/Fe spot friction welds in lap-shear and cross-tension specimens under quasi-static loading conditions, (b) the load range as a function of the fatigue life for the Al/Fe spot friction welds in lap-shear and cross-tension specimens under cyclic loading conditions.

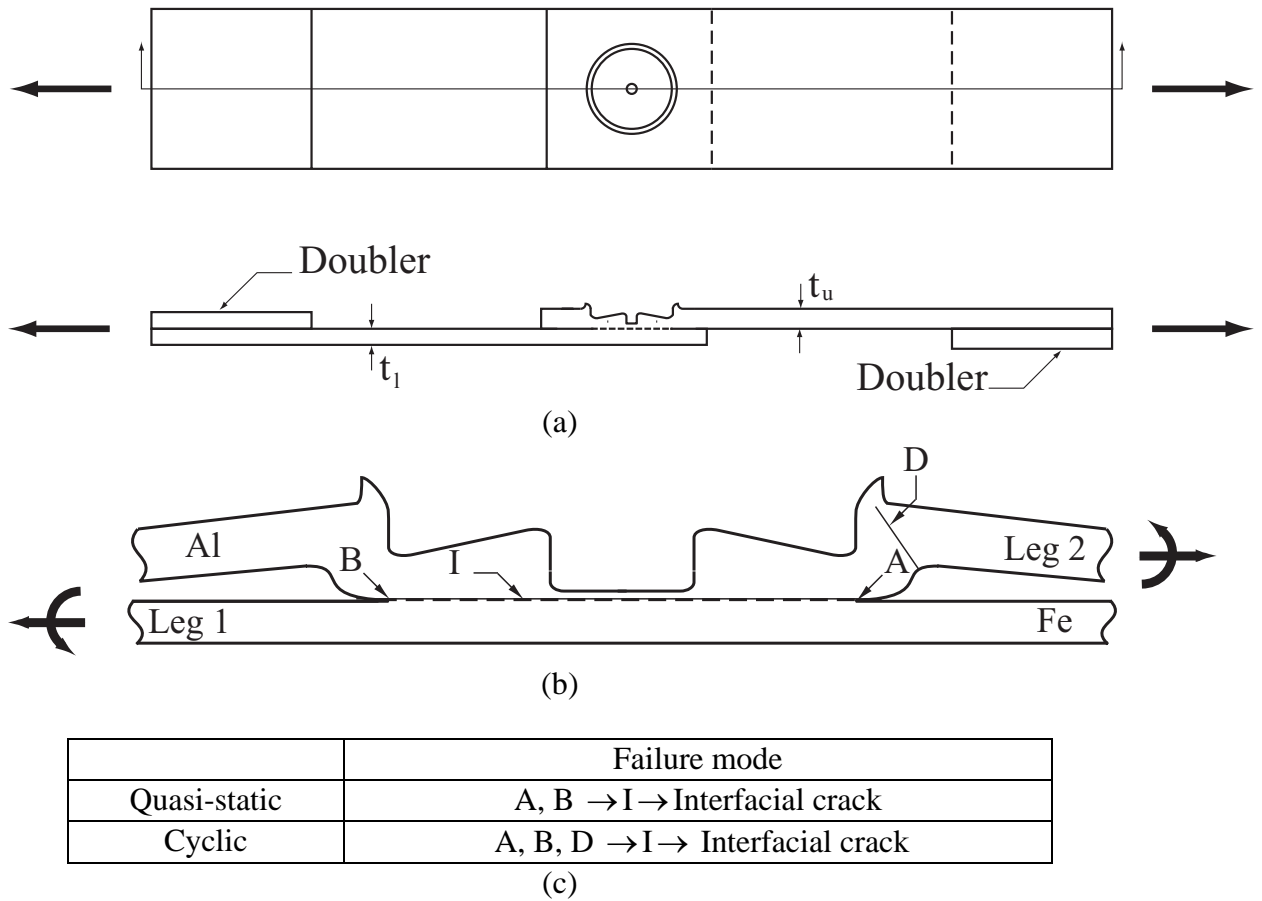
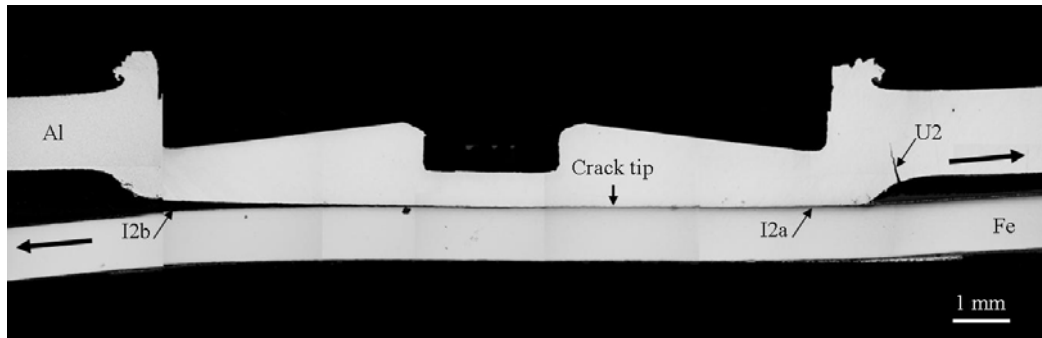
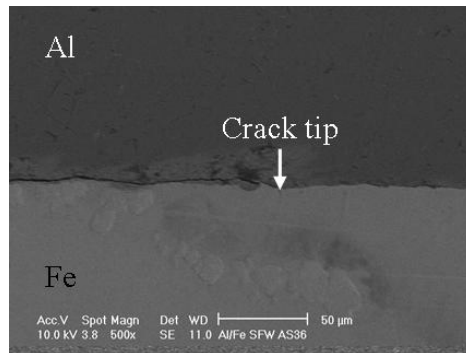


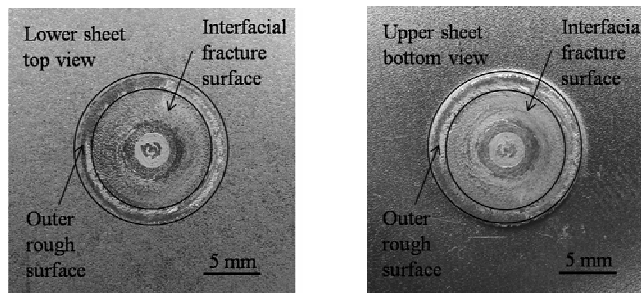
Figure 5.5 (a) A schematic plot of a lap-shear specimen with an Al/Fe spot friction weld and with the upper sheet thickness $t_u = 1.3$ mm and the lower sheet thickness $t_l = 0.8$ mm under applied resultant loads (shown as the bold arrows), (b) a schematic plot of the cross section along the symmetry plane of the Al/Fe spot friction weld in a lap-shear specimen, (c) failure modes of the Al/Fe spot friction welds in lap-shear specimens under quasi-static and cyclic loading conditions.



(a)

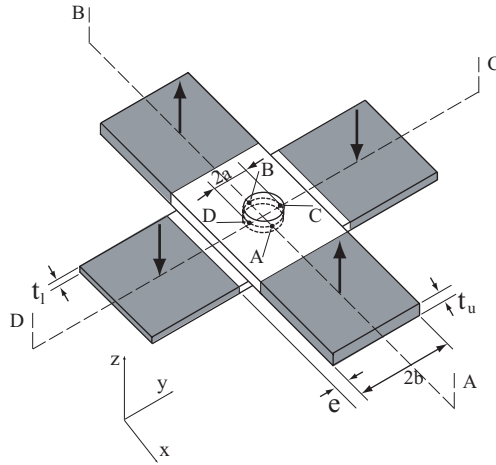


(b)



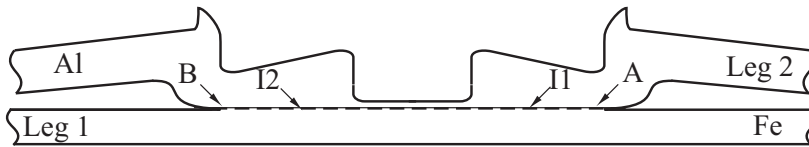
(c)

Figure 5.6 (a) An optical micrograph of the cross section along the symmetry plane of a partially failed Al/Fe spot friction weld in a lap-shear specimen at the fatigue life of 6.5×10^3 cycles under a load range of 2.08 kN, (b) a scanning electron micrograph of the crack tip region as marked in (a), (c) a close-up top view of the lower sheet and a close-up bottom view of the upper sheet of a failed lap-shear specimen under cyclic loading conditions.

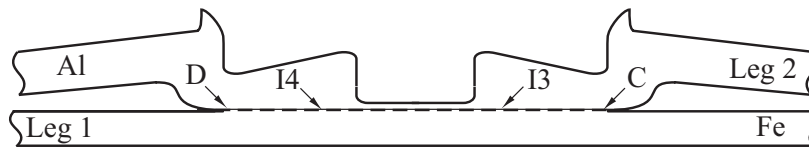


(a)

Cross section A-B



Cross section C-D

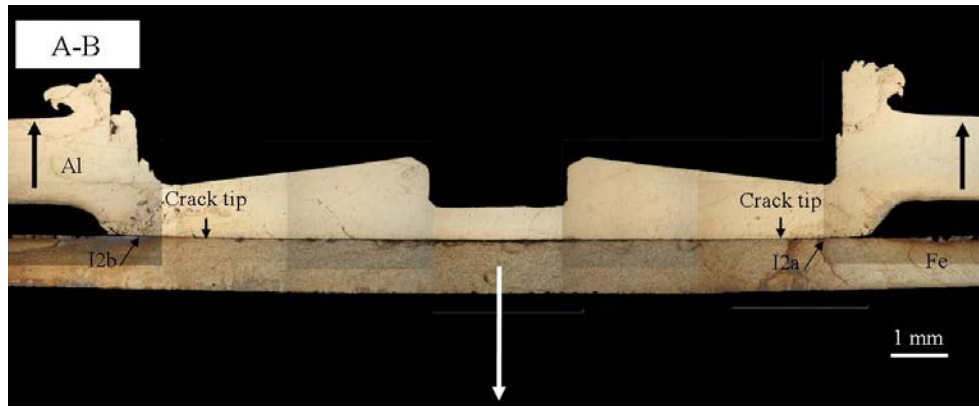


(b)

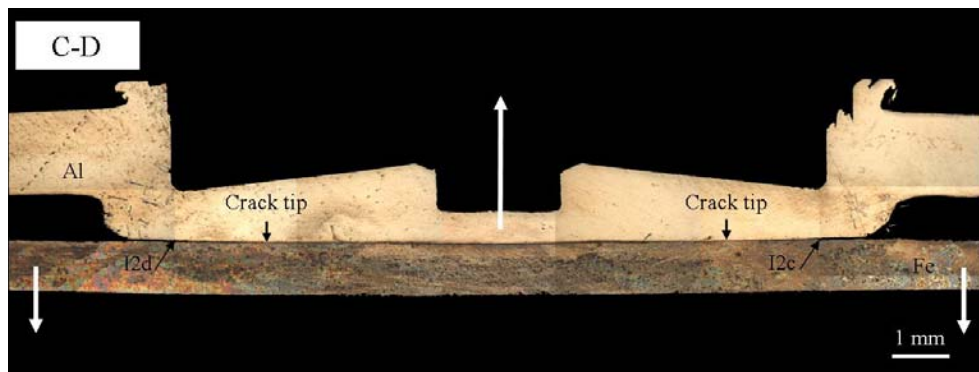
	Failure mode
Quasi-static	A, B → I1, I2 → Interfacial crack C, D → I3, I4 → Interfacial crack
Cyclic fatigue	A, B → I1, I2 → Interfacial crack C, D → I3, I4 → Interfacial crack

(c)

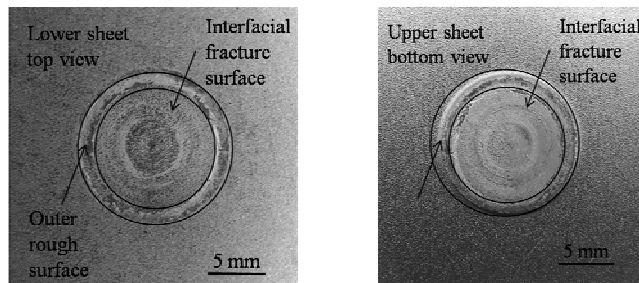
Figure 5.7 (a) A schematic plot of a top view of a cross-tension specimen with a spot weld under applied resultant loads (shown as the bold arrows), (b) schematic plots of cross sections A-B and C-D for the Al/Fe spot friction weld in a cross-tension specimen, (c) failure modes of the Al/Fe spot friction welds in cross-tension specimens under quasi-static and cyclic loading conditions.



(a)

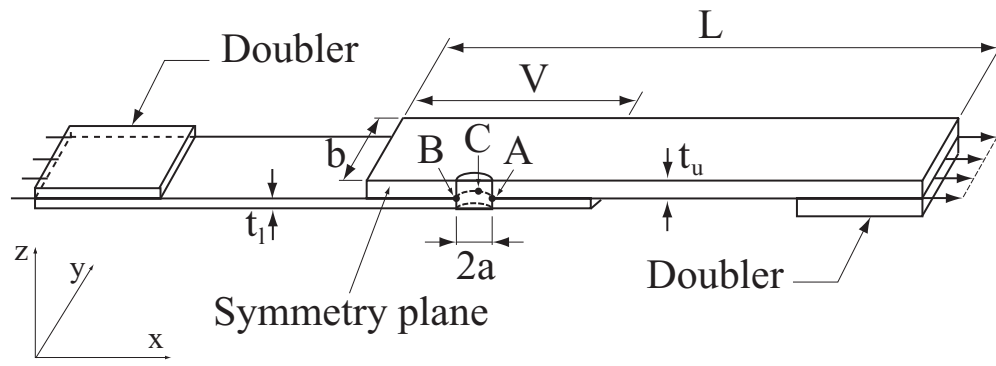


(b)

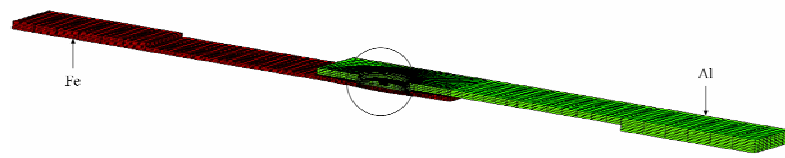


(c)

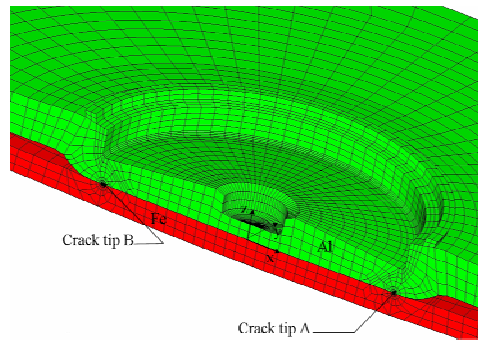
Figure 5.8 Optical micrographs of cross sections (a) A-B, (b) C-D of failed Al/Fe spot friction welds in cross-tension specimens at the fatigue life of 10^4 cycles under a load range of 0.16 kN, (c) a close-up top view of the lower sheet and a close-up bottom view of the upper sheet of a failed cross-tension specimen under cyclic loading conditions.



(a)

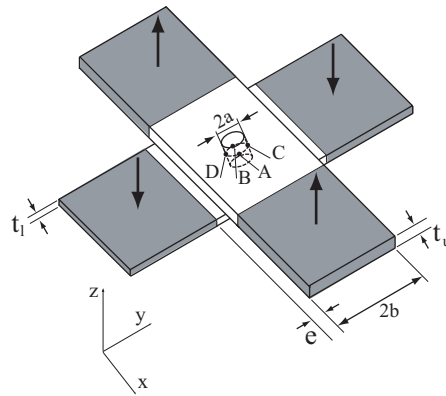


(b)

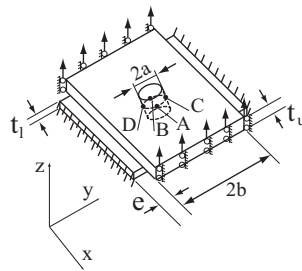


(c)

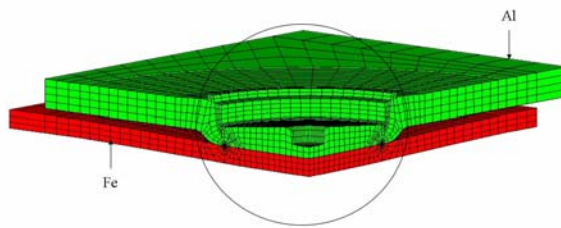
Figure 5.9 (a) A schematic plot of a half of a lap-shear specimen with a spot weld and the boundary conditions of a finite element analysis, (b) a three-dimensional finite element mesh for a half of a lap-shear specimen, (c) a close-up view of the mesh near the weld.



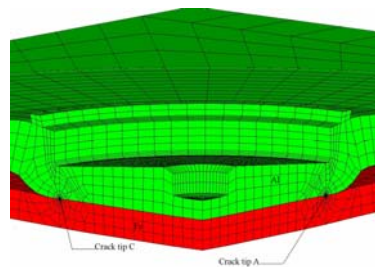
(a)



(b)

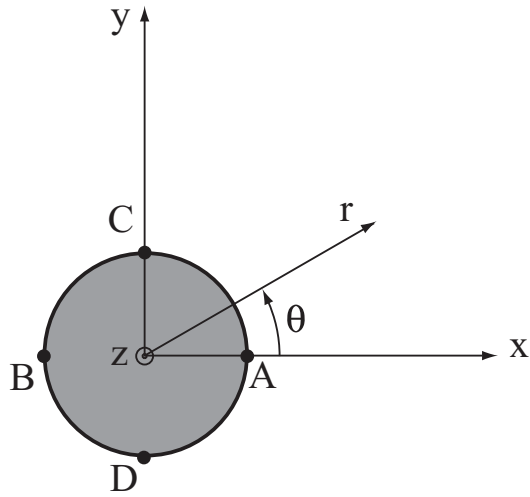


(c)

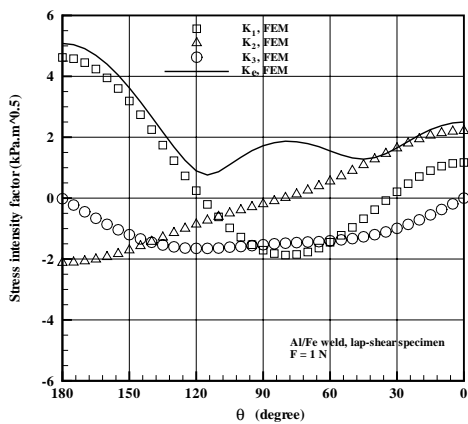


(d)

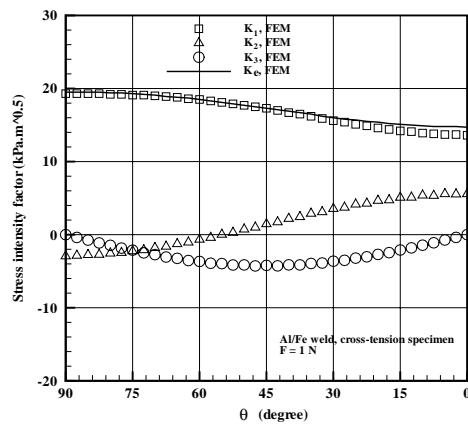
Figure 5.10 (a) A schematic plot of a cross-tension specimen with a spot weld under applied loads shown as the bold arrows and clamped parts shaded, (b) a schematic plot of an equivalent cross-tension specimen without the clamped parts and the boundary conditions of a finite element analysis, (c) a three-dimensional finite element mesh for a quarter of an equivalent cross-tension specimen, (d) a close-up view of the mesh near the weld.



(a)

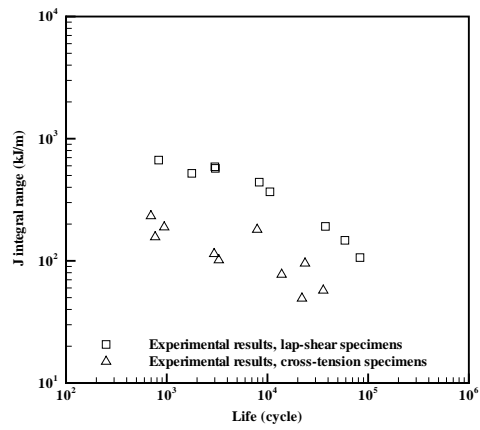


(b)

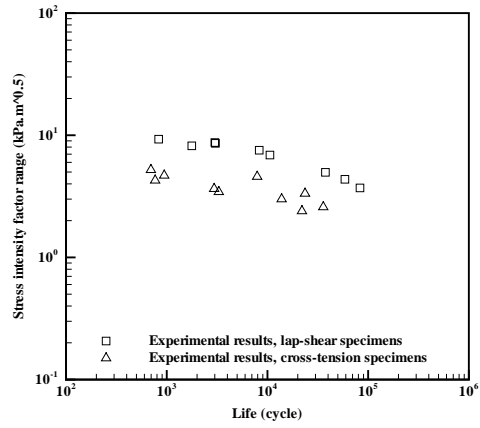


(c)

Figure 5.11 (a) A schematic plot of a top view of the weld nugget (idealized as a rigid inclusion) in the upper sheet of the spot weld specimen with the cylindrical and Cartesian coordinate systems centered at the center of the upper half of the weld nugget, (b) the K_1 , K_2 , K_3 and K_e stress intensity factor solutions as functions of θ for the crack front along the nugget circumference of the Al/Fe spot friction weld in a lap-shear specimen, (c) the K_1 , K_2 , K_3 and K_e stress intensity factor solutions as functions of θ for the crack front along the nugget circumference of the Al/Fe spot friction weld in a cross-tension specimen.



(a)



(b)

Figure 5.12 (a) The J integral range as a function of the fatigue life for the Al/Fe spot friction welds in lap-shear and cross-tension specimens under cyclic loading conditions, (b) the effective stress intensity factor range as a function of the fatigue life for the Al/Fe spot friction welds in lap-shear and cross-tension specimens under cyclic loading conditions.

References

- [1] Sakano R, Murakami K, Yamashita K, Hyoe T, Fujimoto M, Inuzuka M, Nagao Y, Kashiki H. Development of spot FSW robot system for automobile body members. In: Proceedings of the 3rd international symposium of friction stir welding, Kobe, Japan, September 27-28, 2001.
- [2] Iwashita T. Method and apparatus for joining. US Patent 6601751 B2, August 5, 2003.
- [3] Lin P-C, Lin S-H, Pan J, Pan T, Nicholson JM, Garman MA. Microstructures and failure modes of spot friction welds in lap-shear specimens of aluminum 6111-T4 sheets. SAE Technical Paper No. 2004-01-1330, Society of Automotive Engineers, Warrendale, PA: 2004.
- [4] Tran V-X, Pan J, Pan T. Effects of processing time on strengths and failure modes of dissimilar spot friction welds between aluminum 5754-O and 7075-T6 sheets. J Mater Process Technol 2009; 209:3724-3739.
- [5] Carle D, Blount G. The suitability of aluminium as an alternative material for car bodies. Mater Design 1999;20:267-272.
- [6] Sakurai T. The latest trends in aluminum alloy sheets for automotive body panels. Kobelco Technology Review, No. 28, October, 2008. http://www.kobelco.co.jp/english/ktr/pdf/ktr_28/022-028.pdf
- [7] Mazda Motor Corporation. Mazda develops world's first steel and aluminum joining technology using friction heat. Mazda Press Release, June 2, 2005.
- [8] Tanaka K, Kumagai M. Dissimilar joining of aluminum alloy and steel sheets by friction stir spot welding (in Japanese with English summary). Proceedings of International Symposium on Joining Technologies in Advanced Automobile Assembly, pp. 181-189, 2005.
- [9] Tanaka K, Kumagai M, Yoshida H. Dissimilar joining of aluminum alloy and steel sheets by friction stir spot welding (in Japanese with English summary). J Japan Institute of Light Metals 2006;56:317-322.
- [10] Gendo T, Nishiguchi K, Asakawa M, Tanioka S. Spot friction welding of aluminum to steel. SAE Technical Paper No. 2007-01-1703, Society of Automotive Engineers, Warrendale, PA: 2007.
- [11] Tran V-X, Pan J. Effects of weld geometry on fracture mechanics parameters for resistance spot welds and spot friction welds between similar and dissimilar materials in lap-shear specimens, to be submitted for publication.
- [12] Hibbitt HD, Karlsson B, Sorensen EP. ABAQUS User Manual. Version 6-2

2001.

- [13] Shih, CF, Asaro RJ. Elastic-plastic analysis of cracks on bimaterial interfaces: Part I – small scale yielding. *J Appl Mech* 1988;55:299-316.
- [14] Rice JR, Shih GC. Plane problems of cracks in dissimilar media. *J Appl Mech* 1965;32:418-423.
- [15] Rice JR. Elastic fracture mechanics concepts for interfacial cracks. *J Appl Mech* 1988;55:98-103.
- [16] Suo Z, Hutchinson JW. Interface crack between two elastic layers. *Int J Fract* 1999;43:1-18.
- [17] Zhang S. Stress intensities derived from stresses around a spot weld. *Int J Fract* 1999;99:239-257.
- [18] Hutchinson JW, Suo Z. Mixed mode cracking in layered materials. *Advances in Applied Mechanics*, edited by John W. Hutchinson and Theodore Y. Wu, Academic Press, Inc., CA 1992;29:64-187.

CHAPTER VI

EFFECTS OF WELD GEOMETRY AND SHEET THICKNESS ON FRACTURE MECHANICS PARAMETERS FOR RESISTANCE SPOT WELDS AND SPOT FRICTION WELDS BETWEEN SIMILAR AND DISSIMILAR SHEET MATERIALS IN LAP-SHEAR SPECIMENS

Abstract

In this paper, the effects of weld geometry and sheet thickness on the fracture mechanics parameters for the crack fronts along the nugget circumferences of resistance spot welds and spot friction welds between similar and dissimilar sheet materials in lap-shear specimens are investigated based on a combined theoretical and numerical approach. The analytical stress intensity factor and J integral solutions for spot welds with ideal geometry, gap and bend joining two sheets of different materials and thicknesses in lap-shear specimens are first developed based on the strip model and the new structural stress solutions for a rigid inclusion in a finite square plate subjected to a lap-shear load and a coach-peel load (Lin and Pan [18]). The numerical results obtained from the three-dimensional finite element analyses for spot welds with ideal geometry in lap-shear specimens are then used to validate the accuracy of the analytical solutions. Three-dimensional finite element models based on the micrographs of the cross sections along the symmetry planes of an aluminum 6111 resistance spot weld, an aluminum 5754 spot friction weld, and a dissimilar Al/Fe spot friction weld are conducted to obtain accurate stress intensity factor and J integral solutions for the crack fronts along the nugget circumferences of these welds

under lap-shear loading conditions. The numerical results indicate that the complex weld geometries of the aluminum 6111 resistance spot weld and aluminum 5754 spot friction weld appear not to affect the stress intensity factor and J integral solutions when compared to the analytical solutions for the welds with ideal geometry. However, the complex weld geometry of the Al/Fe spot friction weld appears to strongly affect the stress intensity factor and J integral solutions when compared to the analytical solutions for the weld with ideal geometry. The numerical results indicate that the gap between the upper and lower sheets and the bend near the weld are the important geometric parameters that strongly affect the fracture mechanics parameters for the Al/Fe spot friction weld in the lap-shear specimen. The analytical stress intensity factor and J integral solutions for spot welds with the gap and bend agree with the results obtained from the three-dimensional finite element computation for the Al/Fe spot friction weld under lap-shear loading conditions. Finally, the results obtained from the theoretical and numerical analyses and the experimental observations are correlated.

Keywords: Resistance spot weld; Spot friction weld; Friction stir spot weld; Weld geometry; Gap; Bend; Lap-shear specimen; Stress intensity factor; J integral; Fracture; Fatigue

6.1. Introduction

Resistance spot welding is widely used to join sheet metals in the automotive industry. These resistance spot welds are subjected to complex multiaxial loads

under service or crash conditions. The fatigue lives of resistance spot welds in various types of specimens have been investigated by many researchers, for example, see Zhang [1]. Since a resistance spot weld provides a natural crack or notch along the nugget circumference, fracture mechanics has been adopted to investigate the stress intensity factors at the critical locations of the welds in order to investigate the fatigue lives of spot welds in various types of specimens [1-15]. A comprehensive review for fatigue behaviors of resistance spot welds in various types of specimens based on the fracture mechanics approach can be found in Lin et al. [16] and Lin and Pan [17,18].

Aluminum alloys are becoming to be widely used in the automotive industry. However, resistance spot welding of aluminum sheets is likely to produce poor welds as reported by Thornton et al. [19] and Gean et al. [20]. In 2001, a spot friction welding technology for joining aluminum sheets was developed by Mazda Motor Corporation and Kawasaki Heavy Industry [21,22]. The most significant advantage of the spot friction welding process comparing to the conventional welding processes is that the joint can be made without melting the base metals. A schematic illustration of the spot friction welding process used to join two aluminum sheets was presented, for example, in Lin et al. [23]. Note that Lin et al. [24-27], Tran et al. [28,29] and Tran and Pan [30] investigated the fatigue behaviors of aluminum 6111 and 5754 spot friction welds in lap-shear specimens and dissimilar 5754/7075 and 7075/5754 spot friction welds between aluminum 5754-O and 7075-T6 sheets in lap-shear and cross-tension specimens based on experiments, fracture mechanics and the structural stress approach.

Material substitution from steels to aluminum alloys is one of the current approaches to reduce vehicle weight. Vehicles made of hybrid body structures which combine steel and aluminum parts have been produced in the automotive companies [31,32]. Mazda Motor Corporation [33] has modified the conventional spot friction welding technology to join aluminum to steel sheets. A schematic illustration of the spot friction welding process used to join an aluminum sheet and a coated steel sheet can be found in Gendo et al. [34] and Tran and Pan [35]. The fatigue behavior of dissimilar Al/Fe spot friction welds between aluminum 6000 series alloy and coated steel sheets in lap-shear and cross-tension specimens was investigated by Tran and Pan [35] based on experiments and three-dimensional finite element analyses.

It should be noted that most of the current literature is for resistance spot welds with ideal geometry. The spot welds can be therefore idealized as rigid inclusions. In the derivations of the stress intensity factor solutions for various types of specimens, the structural stress solutions along the circumference of a rigid inclusion in a thin plate need to be derived first. Zhang [1,11,12] obtained the structural stress solutions at the critical locations of spot welds in various types of specimens and automotive structures, where spot welds were assumed as rigid inclusions in the analytical or numerical solution procedures. Recently, Lin et al. [16] developed a new analytical solution for a rigid inclusion in a finite square plate under counter bending conditions. The new analytical solution was used to obtain the mode I stress intensity factor solutions which are compared well with the computational results of Wang et al. [14]. Subsequently, Lin and Pan [17] derived and presented relevant closed-form structural stress and stress intensity factor solutions for spot welds under various types of

loading conditions based on the stress function approach. Later, Lin and Pan [18] developed new closed-form structural stress and stress intensity factor solutions for spot welds in commonly used specimens.

From the fracture mechanics viewpoint, the structural stresses are local stress parameters that can be used to obtain the stress intensity factor and J integral solutions. Also, the crack initiation and growth near the nugget circumference of the weld are controlled by the stress intensity factor and/or J integral solutions for the main cracks or kinked cracks near the weld nuggets. Therefore, the structural stresses are possible candidates to characterize the fatigue lives of spot welds. It should be noted that the analytical stress intensity factor solutions developed in Lin et al. [16] and Lin and Pan [18], and the finite element analyses conducted by Wang et al. [14] are for spot welds with ideal geometry joining two sheets of identical material and equal thickness. A further investigation is therefore needed to develop new analytical stress intensity factor and J integral solutions for spot welds with ideal geometry joining two sheets of different materials and thicknesses based on the new closed-form structural stress solutions developed in Lin and Pan [18].

Note that Lin et al. [15] attempted to correlate the experimental fatigue data for resistance spot welds in lap-shear, square-cup and coach-peel specimens of low-carbon, high strength and dual phase steels based on a fracture mechanics crack growth model with consideration of kinked fatigue crack growth. Based on this approach, Lin et al. [24-27], Tran et al. [28,29] and Tran and Pan [30] developed the kinked fatigue crack growth models that predicted very well the fatigue lives of aluminum 5754 and 6111 spot friction welds and dissimilar 5754/7075 and

7075/5754 spot friction welds in lap-shear specimens. It should be emphasized that the analytical solutions for the global stress intensity factors K_I and K_{II} for the main cracks used in Lin et al. [24-27] are based on the works of Lin et al. [16] and Zhang [11] for the equivalent spot welds with ideal geometry (idealized as rigid inclusions) joining two sheets of identical material and equal thickness in lap-shear specimens, respectively. These K_I and K_{II} solutions are therefore approximate in nature due to the complex geometry of the spot friction weld as shown later. Hence, three-dimensional finite element analyses based on the micrographs of the cross sections along the symmetry planes of spot friction welds before testing were employed to obtain accurate global stress intensity factors at the crack tips of the welds as shown in Tran et al. [28,29] and Tran and Pan [30]. Note that the numerical results obtained in Tran and Pan [35] suggest that the J integral solutions at the critical locations of the welds obtained from three-dimensional finite element analyses may be used as a fracture mechanics parameter to correlate the experimental fatigue data of the Al/Fe spot friction welds in lap-shear and cross-tension specimens. However, the computational results reported in Tran et al. [28,29] and Tran and Pan [30, 35] are for their specimens of specific geometries and these results can not be used for general applications to specimens of different designs.

Figure 6.1 shows schematic plots of spot welds with different geometries under lap-shear loading conditions. The bold arrows in Figure 6.1 schematically show the applied loads. Figure 6.1(a) shows a schematic plot of a spot weld with ideal geometry. Figure 6.1(b) shows a schematic plot of a resistance spot weld with electrode indentation, gap and bend. Figure 6.1(c) shows a schematic plot of an

aluminum spot friction weld with complex geometry, gap and bend. Figure 6.1(d) shows a schematic plot of a dissimilar Al/Fe spot friction weld with complex geometry, gap and bend. In Figures 6.1(a), 6.1(b), 6.1(c) and 6.1(d), the nominal thicknesses of the upper and lower sheets used to make the welds are denoted as t_u and t_l , respectively. Due to the welding processes, the upper and lower sheet materials near the welds were deformed plastically. Therefore, the effective thicknesses of the upper and lower sheets, denoted as t'_u and t'_l in Figures 6.1(b), 6.1(c) and 6.1(d), measured at the crack tips of the weld, are different from the nominal thicknesses t_u and t_l , respectively. As shown in the figures, the actual bonding diameter for the weld or the weld diameter is denoted as D_c . The weld diameter D_c is determined as the distance between the locations of the two crack tips identified by the optical and/or scanning electron micrographs of the cross sections along the symmetry planes of the welds before testing. As schematically shown in Figure 6.1(d), during the spot friction welding process, the tool contacts the upper sheet and penetrates the upper sheet to weld together the upper and lower sheets. The dissimilar spot friction welds are denoted as the Al/Fe weld when an aluminum 6000 series alloy and coated steel were used as the upper and lower sheets, respectively.

For resistance spot welds, the electrode indentation may exist due to large electrode force, and the gap and bend may exist due to poor fit-up. For spot friction welds, during the welding process, the tool shoulder indentation resulted in a radial expansion of the upper sheet material along the outer circumference of the tool shoulder indentation. However, due to the constraint of the neighboring material, the sheets were therefore bent along the outer circumferences of the tool shoulder

indentation and result in a gap. Note that the gap g as shown in Figures 6.1(b), 6.1(c) and 6.1(d) is defined as the distance between the bottom surface of the upper sheet and the top surface of the lower sheet where the lap-shear loads applied. Also, due to the bend near the weld, the offset distance between the bond line connecting the two crack tips and the top surface of the lower sheet where the lap-shear load applied is marked as e in each of the figures. These parameters g and e are important geometric parameters for resistance spot welds and spot friction welds under lap-shear loading conditions as discussed later. In Figures 6.1(c) and 6.1(d) for spot friction welds, the thick dashed lines represent the interfacial surfaces between the two deformed sheet materials. It should be noted that the interfacial surfaces for the spot friction welds reported in this investigation were well bonded as shown later.

The analytical stress intensity factor and J integral solutions for spot welds with ideal geometry developed in the first part of this investigation can be approximately used for the resistance spot welds and spot friction welds with small values of g and e . However, the weld geometries of the resistance spot welds and spot friction welds observed from the micrographs of the welds can deviate significantly from the ideal geometry. As schematically shown in Figures 6.1(b), 6.1(c) and 6.1(d), the geometric parameters g and e appear to be relatively large when compared to the nominal thicknesses of the upper and lower sheets t_u and t_l . Therefore, comprehensive investigation on the effects of the weld geometry and sheet thickness on the fracture mechanics parameters such as the stress intensity factors and J integral for the crack fronts along the nugget circumferences of resistance spot welds and spot friction welds is therefore needed in order to develop the fatigue life estimation models and to

correlate the experimental fatigue data of the welds with different weld geometries in different types of specimens.

In this paper, the effects of the weld geometry and sheet thickness on the fracture mechanics parameters for the crack fronts along the nugget circumferences of resistance spot welds and spot friction welds between similar and dissimilar sheet materials in lap-shear specimens are investigated based on a combined theoretical and numerical approach. The analytical stress intensity factor and J integral solutions for spot welds with ideal geometry, gap and bend joining two sheets of different materials and thicknesses in lap-shear specimens are first developed based on the new closed-form structural stress solutions for a rigid inclusion in a finite square plate subjected to a lap-shear load and a coach-peel load (Lin and Pan [18]). Three-dimensional finite element analyses for spot welds with ideal geometry in lap-shear specimens are then developed to validate the analytical solutions. Three-dimensional finite element models based on the micrographs of the cross sections along the symmetry planes of an aluminum 6111 resistance spot weld, an aluminum 5754 spot friction weld, and a dissimilar Al/Fe spot friction weld before testing are conducted to obtain accurate stress intensity factor and J integral solutions for the crack fronts along the nugget circumferences of the welds under lap-shear loading conditions. Different three-dimensional finite element models based on the meshes that represent different features of the weld geometry are also conducted to identify important geometric parameters that strongly affect the fracture mechanics parameters for the Al/Fe spot friction weld. The analytical stress intensity factor and J integral solutions for the spot welds with the gap and bend in lap-shear specimens are used to

correlate with the results obtained from the finite element analyses for the Al/Fe spot friction weld. Finally, the results obtained from the analytical and finite element models and the experimental observations are correlated.

6.2. Analytical stress intensity factor and J integral solutions for spot welds in lap-shear specimens

Lap-shear specimens are commonly used to investigate the mechanical behavior of spot welds under shear dominant loading conditions. Figure 6.2 shows a schematic plot of a lap-shear specimen with a spot weld idealized as a circular cylinder under the applied forces shown as the bold arrows. The upper and lower sheets used to make the specimen have the nominal thicknesses t_u and t_l , respectively. As shown in Figure 6.2, the lap-shear specimen has the specimen width $2b$ and the nugget diameter $2a$. Here, L represents the length of the upper and lower sheets of the specimen, and V represents the overlap length. In Figure 6.2, a set of doublers is used to align the loads to avoid the initial realignment of the specimen under lap-shear loading conditions. The critical locations of the spot weld are marked as A, B, C and D in Figure 6.2.

Lin and Pan [18] treated the spot weld in the lap-shear specimen as a rigid inclusion and assumed that the inclusion is perfectly bonded to the neighboring sheet materials in the derivations of the closed-form structural stress solutions employed later in this investigation. Figure 6.3 shows a schematic plot of a top view of the weld nugget (idealized as a rigid inclusion) in the upper sheet of the spot weld specimen with the cylindrical and Cartesian coordinate systems centered at the center of the upper half of the weld nugget. The critical locations of points A, B, C and D

are 0° , 180° , 90° and 270° with respect to the x axis, respectively. The locations of points A, B, C and D can also be seen in the Figure 6.2. The orientation angle θ represents the angular location along the nugget circumference of the spot weld. Note that the angle θ is measured counterclockwise from the critical location of point A.

6.2.1. J integral solutions for a strip model

First, the strip model of Radaj and Zhang [6-8] is adopted here to derive stress intensity factor solutions for spot welds under various types of loading conditions as in Lin et al. [16] and Lin and Pan [17]. Figure 6.4 shows a two-dimensional model of two infinite strips made of different materials and thicknesses with the connection under plane strain loading conditions. The strip model can be used to represent the cross section perpendicular to the crack front along the weld nugget circumference. In Figure 6.4, the Young's moduli and Poisson's ratios for the upper (u) and lower (l) sheet materials are denoted as E_u , ν_u and E_l , ν_l , respectively. As schematically shown in Figure 6.4, the radial stress σ_{rr} and the shear stress $\sigma_{r\theta}$ along the rigid inclusion circumference obtained from a plate with a rigid inclusion under various types of loading conditions are used to represent the normal structural stresses, σ_x^u and σ_x^l , and the shear structural stresses, τ_{zx}^u and τ_{zx}^l , for the strip model with respect to the Cartesian coordinate system as shown in the figure (Lin et al. [16]; Lin and Pan [18]). Note that the effects of the transverse shear stresses are neglected (Radaj [4]; Radaj and Zhang [6]; Lin et al. [16]; Lin and Pan [18]).

For linear elastic materials, the J integral (Rice [36]) represents the energy release rate.

Figure 6.5(a) shows a crack and a Cartesian coordinate system centered at the crack tip. In reference to Figure 6.5(a), the J integral is defined as

$$J = \int_{\Gamma} (Wn_x - T_i \frac{\partial u_i}{\partial x}) ds, \quad i = x, y, z \quad (6.1)$$

where Γ represents a contour counterclockwise from the lower crack face to the upper crack face, ds represents the differential arc length of the contour Γ , n_x represents the x component of the unit outward normal \mathbf{n} to the differential arc length ds , $T_i (= \sigma_{ij}n_j)$ represent the components of the traction vector \mathbf{T} on the differential arc length ds , and u_i represent the components of the displacement vector \mathbf{u} . In Equation (6.1), the strain energy density W is defined as

$$W = \int_0^{\varepsilon_{ij}} \sigma_{ij} d\varepsilon_{ij} \quad (i, j = x, y, z) \quad (6.2)$$

As shown in Figure 6.5(b), the line $\overline{ABCDEFG}$ is considered as the contour Γ for the J integral. The J integral is written for the contour lines \overline{AB} , \overline{BC} , \overline{CD} , \overline{DE} , \overline{EF} and \overline{FG} as

$$J = \left(\int_{\overline{AB}} + \int_{\overline{BC}} + \int_{\overline{CD}} + \int_{\overline{DE}} + \int_{\overline{EF}} + \int_{\overline{FG}} \right) (Wn_x - T_i \frac{\partial u_i}{\partial x}) ds \quad (6.3)$$

where the integrals along line \overline{BC} and line \overline{EF} are zero because n_x is zero and T_i are zeros. For the integrals along line \overline{AB} , line \overline{CD} , line \overline{DE} and line \overline{FG} , the contributions of the shear stress τ_{xy} are taken to be zero as in Radaj and Zhang [6], Lin et al. [16] and Lin and Pan [18]. Therefore, the J integral can be written as in

$$J = - \left(\int_{\overline{AB}} W dy + \int_{\overline{CD}} W dy + \int_{\overline{DE}} W dy + \int_{\overline{FG}} W dy \right) \quad (6.4)$$

where the strain energy density W is

$$W = \frac{1-\nu^2}{2E} \sigma_x^2 + \frac{\tau_{zx}^2}{2G} \quad (6.5)$$

Under plane strain conditions, for a crack in a homogeneous linear elastic material, the J integral is related to the K_I , K_{II} and K_{III} stress intensity factor solutions as

$$J = \frac{1-\nu^2}{E} (K_I^2 + K_{II}^2) + \frac{K_{III}^2}{2G} \quad (6.6)$$

where G denotes the shear modulus.

Rice [36] showed that the J integral is a path-independent line integral for the crack in a homogeneous linear elastic material. For the interface crack between two dissimilar linear elastic materials, Smelser [37] showed that the J integral is also a path-independent line integral provided the bond line is straight. Note that the bond line is idealized as a straight line in the strip model and in this investigation. Since the integrals along line \overline{BC} and line \overline{EF} are zero, line \overline{AB} , line \overline{CD} , line \overline{DE} and line \overline{FG} can be taken near the crack tip or at the far ends of the two infinite strips by the path-independence of the J integral.

Figure 6.5(b) shows the front and side views of the left half of the strip model near the crack tip with linearly distributed structural stresses based on the classical Kirchhoff plate theory. As shown in Figure 6.5(b), the normal stresses, σ_x^u and σ_x^l , and the shear stresses, τ_{zx}^u and τ_{zx}^l , represent the structural stresses for the upper (u) and lower (l) strips. The normal stresses σ_{ui} , σ_{uo} , σ_{li} and σ_{lo} represent the normal stresses σ_x^u and σ_x^l for line \overline{FG} and line \overline{AB} at the inner (i) and outer (o) surfaces of the upper (u) and lower (l) strips, respectively. The shear stresses τ_u and τ_l represent the shear stresses τ_{zx}^u and τ_{zx}^l of the upper (u) and lower (l) strips,

respectively, for line \overline{FG} and line \overline{AB} . Since the spot weld is modeled as a rigid inclusion with a perfect bonding to the neighboring sheet materials, the twisting moment along the nugget circumference is zero. Therefore, τ_{zx}^u and τ_{zx}^l are uniformly distributed through the thickness as shown in Figure 6.5(b).

It should be noted that the normal structural stresses for line \overline{DE} and line \overline{CD} in the weld nugget are required to balance the resultant force and moment induced by the distributions of the stresses for line \overline{FG} and line \overline{AB} . Note that the continuity conditions of the strain ε_x and the strain gradient $d\varepsilon_x/dy$ at the bond line are also required according to the plate theory for the perfect bonding of the interfacial surface between the upper and lower sheets. In Figure 6.5(b), the normal stresses σ_{ui}^* , σ_{uo}^* , σ_{li}^* and σ_{lo}^* represent the required normal stresses for line \overline{DE} and line \overline{CD} at the inner (*i*) and outer (*o*) surfaces of the upper (*u*) and lower (*l*) strips, respectively.

In reference to Figure 6.5(b), the normal stresses σ_{ui}^* , σ_{uo}^* , σ_{li}^* and σ_{lo}^* can be obtained from the normal stresses σ_{ui} , σ_{uo} , σ_{li} and σ_{lo} , and the ratios $\delta = t_u/t_l$ and $\eta = E'_u/E'_l$ with $E' = E/(1-\nu^2)$ for the plane strain condition and $E' = E$ for the plane stress condition from the four following equations after manipulations:

1. The equilibrium of the resultant force in the x direction requires

$$\delta(\sigma_{ui}^* + \sigma_{uo}^*) + (\sigma_{li}^* + \sigma_{lo}^*) = \delta(\sigma_{ui} + \sigma_{uo}) + (\sigma_{li} + \sigma_{lo}) \quad (6.7)$$

2. The equilibrium of the resultant moment in the z direction requires

$$\delta^2(\sigma_{ui}^* + 2\sigma_{uo}^*) - (\sigma_{li}^* + 2\sigma_{lo}^*) = \delta(\sigma_{ui} + 2\sigma_{uo}) - (\sigma_{li} + 2\sigma_{lo}) \quad (6.8)$$

3. The continuity of the strain ε_x at the bond line requires

$$\sigma_{ui}^* = \eta \sigma_{li}^* \quad (6.9)$$

4. The continuity of the strain gradient $d\varepsilon_x/dy$ at the bond line requires

$$(1 + \delta)\sigma_{ui}^* = \sigma_{uo}^* + \eta\delta\sigma_{lo}^* \quad (6.10)$$

The normal structural stresses σ_{ui}^* , σ_{uo}^* , σ_{li}^* and σ_{lo}^* can be then solved from Equations (6.7)-(6.10) as

$$\begin{Bmatrix} \sigma_{ui}^* \\ \sigma_{uo}^* \\ \sigma_{li}^* \\ \sigma_{lo}^* \end{Bmatrix} = \begin{bmatrix} \delta & \delta & 1 & 1 \\ \delta^2 & 2\delta^2 & -1 & -2 \\ 1 & 0 & -\eta & 0 \\ 1+\delta & -1 & 0 & -\eta\delta \end{bmatrix}^{-1} \begin{bmatrix} \delta & \delta & 1 & 1 \\ \delta^2 & 2\delta^2 & -1 & -2 \\ 0 & 0 & 0 & 0 \\ 0 & 0 & 0 & 0 \end{bmatrix} \begin{Bmatrix} \sigma_{ui} \\ \sigma_{uo} \\ \sigma_{li} \\ \sigma_{lo} \end{Bmatrix} \quad (6.11)$$

First, the in-plane part of the J integral solution, J_{xy} , related to the in-plane stresses is calculated. Based on the classical Kirchhoff plate theory, the distributions of the normal structural stress along line \overline{AB} , line \overline{CD} , line \overline{DE} and line \overline{FG} can be calculated. Then, J_{xy} can be explicitly calculated from Equations (6.4) and (6.5). The procedure for calculating J_{xy} for the strip model shown in Figure 6.5(b) is straightforward and only the final result is reported here as

$$\begin{aligned} J_{xy} = & \frac{(1-\nu_u^2)t_u}{6E_u} (\sigma_{uo}^2 + \sigma_{uo}\sigma_{ui} + \sigma_{ui}^2) + \frac{(1-\nu_l^2)t_l}{6E_l} (\sigma_{lo}^2 + \sigma_{lo}\sigma_{li} + \sigma_{li}^2) \\ & - \frac{(1-\nu_u^2)t_u}{6E_u} (\sigma_{uo}^{*2} + \sigma_{uo}^*\sigma_{ui}^* + \sigma_{ui}^{*2}) - \frac{(1-\nu_l^2)t_l}{6E_l} (\sigma_{lo}^{*2} + \sigma_{lo}^*\sigma_{li}^* + \sigma_{li}^{*2}) \end{aligned} \quad (6.12)$$

Now, the out-of-plane shear part of the J integral solution, J_{III} or J_3 , related to the out-of-plane shear stresses is derived. Figure 6.6 shows the decomposition process of the distributions of the out-of-plane shear stresses τ_u and τ_l in model A into the two loading conditions shown in models G and H. Model G represents a strip

model subjected to a uniform out-of-plane shear strain γ with a crack on the xz plane. The shear strain γ is the uniform strain on the right end of the strips of model A. Equilibrium condition in the z direction gives

$$\gamma = \frac{t_u \tau_u + t_l \tau_l}{G_u t_u + G_l t_l} \quad (6.13)$$

The uniform shear stresses τ_U and τ_L on the left end of the upper and lower strips, respectively, of strip model H are

$$\tau_U = \tau_u - G_u \gamma \quad (6.14)$$

$$\tau_L = G_l \gamma - \tau_l \quad (6.15)$$

Note that the J integral solution for strip model G based on Equations (6.4) and (6.5) is zero. The J_{III} or J_3 solution for strip model H based on Equations (6.4) and (6.5) leads to

$$J_{III} = J_3 = \frac{t_u (\tau_u - \beta \tau_l)^2}{2G_u (1 + \beta \delta)} \quad (6.16)$$

where $\beta = G_u/G_l$ is the shear modulus ratio.

Finally, the total J integral solution for the strip model shown in Figure 6.5(b) is obtained from Equations (6.12) and (6.16) as

$$J = J_{xy} + J_{III} = J_{xy} + J_3 \quad (6.17)$$

It should be noted that the J integral solutions in Equations (6.12), (6.16) and (6.17) are developed for a strip model connecting two infinite strips made of different materials and thicknesses under plane strain loading conditions. The solutions in Equations (6.12), (6.16) and (6.17) can be used to determine the J integral solutions

for the crack fronts along the nugget circumferences of spot welds joining two sheets of different materials and thicknesses.

6.2.2. Stress intensity factor solutions for spot welds between joining two sheets of different materials and thicknesses in lap-shear specimens

The asymptotic in-plane stress field around an interface crack tip is an oscillatory field scaled by a complex stress intensity factor $\mathbf{K} = K_1 + iK_2$ ($i = \sqrt{-1}$) (Rice and Sih [38]). As summarized in Zhang [39], the stresses (σ_y, τ_{xy}) at a small distance r ahead of the interface crack tip and the displacements (δ_x, δ_y) at a small distance r behind the interface crack tip are characterized by \mathbf{K} as

$$\sigma_y + i\tau_{xy} = \frac{K_1 + iK_2}{\sqrt{2\pi r}} \left(\frac{r}{t} \right)^{i\varepsilon} \quad (6.18)$$

$$\delta_y + i\delta_x = \frac{(1 + \kappa_u)/G_u + (1 + \kappa_l)/G_l}{2\sqrt{2\pi}(1 + 2i\varepsilon)\cosh(\pi\varepsilon)} (K_1 + iK_2)\sqrt{r} \left(\frac{r}{t} \right)^{i\varepsilon} \quad (6.19)$$

where the parameters $\kappa_j = 3 - 4\nu_j$ and $\kappa_j = (3 - \nu_j)/(1 + \nu_j)$ ($j = u, l$) are in terms of the Poisson's ratios ν_j for the plane strain and plane stress conditions, respectively.

The bimaterial constant ε is defined as

$$\varepsilon = \frac{1}{2\pi} \ln \frac{\kappa_u/G_u + 1/G_l}{\kappa_l/G_l + 1/G_u} \quad (6.20)$$

In Equations (6.18) and (6.19), t represents a characteristic length (Rice [36]; Suo and Hutchinson [40]; Zhang [39]). In this investigation, t is taken as the smaller value of the upper and lower sheet thicknesses as in Suo and Hutchinson [40] and Zhang [39]. It should be noted that when the two materials are identical, $\varepsilon = 0$, the

definitions of the K_1 and K_2 solutions as in Equations (6.18) and (6.19) for the interface crack become identical to the conventional stress intensity factor solutions K_I and K_{II} for the crack in a homogenous material, respectively. Note also that the out-of-plane shear stress field near the interface crack tip is similar to that near the crack in a homogenous material. However, the mode III stress intensity factor solution for the interface crack is denoted as K_3 in this paper in order to be consistent with the definitions of K_1 and K_2 .

Under plane strain conditions, for an interface crack between two dissimilar linear elastic materials, the J integral is related to the K_1 , K_2 and K_3 stress intensity factor solutions as

$$J = \frac{K_1^2 + K_2^2}{\cosh^2(\pi\varepsilon)E^*} + \frac{K_3^2}{2G^*} \quad (6.21)$$

$$\text{with } \frac{1}{E^*} = \frac{1}{2} \left(\frac{1}{E'_u} + \frac{1}{E'_l} \right) \text{ and } \frac{1}{G^*} = \frac{1}{2} \left(\frac{1}{G_u} + \frac{1}{G_l} \right).$$

Zhang [12] derived the general approximate stress intensity factor solutions K_1 and K_2 of the complex stress intensity factor $\mathbf{K} = K_1 + iK_2$ (as defined in Equations (6.18) and (6.19)) for spot welds joining two sheets of different materials and thicknesses from the structural stress distributions in the upper and lower sheets of a strip model (represented by σ_{ui} , σ_{uo} , σ_{li} and σ_{lo} as defined in Figure 6.5(b)) based on the in-plane part of the J integral solution, J_{xy} , of the strip model and the analytic separation of the mixed mode stress intensity factors (Suo and Hutchinson [40]). In

reference to Figure 6.5(b), the stress intensity factor solutions K_1 and K_2 can be rewritten as

$$K_1 = a_1\sigma_{ui} + a_2\sigma_{uo} + a_3\sigma_{li} + a_4\sigma_{lo} \quad (6.22)$$

$$K_2 = b_1\sigma_{ui} + b_2\sigma_{uo} + b_3\sigma_{li} + b_4\sigma_{lo} \quad (6.23)$$

where a_j and b_j ($j=1,2,3,4$) are the factors which depend on the ratios η and δ .

The complete expressions for a_j and b_j ($j=1,2,3,4$) are given in the Appendix B.

Based on the out-of-plane shear part of the J integral solution, J_3 , the K_3 solution can be obtained as

$$K_3 = \sqrt{\frac{2}{(1+\beta)(1+\beta\delta)}}(\tau_u - \beta\tau_l)\sqrt{t_u} \quad (6.24)$$

Note also that with the introduction of the thickness t as a characteristic length in Equations (6.18) and (6.19), the phase angle ω of the in-plane loading condition can be defined as

$$\omega = \tan^{-1}\left(\frac{K_2}{K_1}\right) \quad (6.25)$$

For spot welds joining two sheets of identical material with different thicknesses ($\eta = \beta = 1$), Equations (6.22)-(6.24) can be rewritten as

$$K_I = \frac{\sqrt{t_u}}{2\sqrt{2(1+\delta)(1+3\delta+3\delta^2)(1+\tan^2\omega)}} \left\{ \left[\frac{1+3\delta+6\delta^2}{\sqrt{3}(1+\delta)} \tan\omega - 1 \right] \sigma_{ui} \right. \\ \left. - \left[\frac{1+3\delta}{\sqrt{3}(1+\delta)} \tan\omega + 1 \right] \sigma_{uo} + \left[\frac{\delta(1-3\delta)}{\sqrt{3}(1+\delta)} \tan\omega + 2 + \delta \right] \sigma_{li} \right. \\ \left. - \delta \left[\frac{1+3\delta}{\sqrt{3}(1+\delta)} \tan\omega + 1 \right] \sigma_{lo} \right\} \quad (6.26)$$

$$\begin{aligned}
K_{II} = & \frac{\sqrt{t_u}}{2\sqrt{2(1+\delta)(1+3\delta+3\delta^2)(1+\tan^2\omega)}} \left\{ \left[\frac{1+3\delta+6\delta^2}{\sqrt{3}(1+\delta)} + \tan\omega \right] \sigma_{ui} \right. \\
& - \left[\frac{1+3\delta}{\sqrt{3}(1+\delta)} - \tan\omega \right] \sigma_{uo} + \left[\frac{\delta(1-3\delta)}{\sqrt{3}(1+\delta)} - (2+\delta)\tan\omega \right] \sigma_{li} \\
& \left. - \delta \left[\frac{1+3\delta}{\sqrt{3}(1+\delta)} - \tan\omega \right] \sigma_{lo} \right\} \quad (6.27)
\end{aligned}$$

$$K_{III} = \sqrt{\frac{1}{1+\delta}} (\tau_u - \tau_l) \sqrt{t_u} \quad (6.28)$$

where the angular function ω is obtained from the numerical calculations and is tabulated in the Appendices of Suo and Hutchinson [40] and Zhang [39].

For spot welds joining two sheets of identical material and equal thickness ($\eta = \delta = \beta = 1$), Equations (6.26)-(6.28) can be simplified as

$$K_I = \frac{\sqrt{3}}{12} (\sigma_{ui} - \sigma_{uo} + \sigma_{li} - \sigma_{lo}) \sqrt{t} \quad (6.29)$$

$$K_{II} = \frac{1}{4} (\sigma_{ui} - \sigma_{uo}) \sqrt{t} \quad (6.30)$$

$$K_{III} = \frac{\sqrt{2}}{2} (\tau_u - \tau_l) \sqrt{t} \quad (6.31)$$

6.3. Closed-form structural stress solutions along nugget circumferences of spot welds in lap-shear specimens

As discussed earlier, the normal structural stresses, σ_{ui} , σ_{uo} , σ_{li} and σ_{lo} , and the shear structural stresses, τ_u and τ_l , are needed to obtain the stress intensity factor and J integral solutions. As schematically shown in Figures 6.1(b), 6.1(c) and 6.1(d), the geometries of the resistance spot welds and spot friction welds appear to be quite different and complex. Therefore, the new closed-form structural stress solutions for

spot welds with ideal geometry and with the gap and bend under lap-shear loading conditions will be reported in this section.

6.3.1. For spot welds with ideal geometry in lap-shear specimens

For the spot welds with ideal geometry in lap-shear specimens, the decompositions of the resultant lap-shear load and the general structural stress distributions of a strip model based on the approach presented in Radaj and Zhang [6,8] are adopted here as in Lin et al. [16] and Lin and Pan [18]. Figure 6.7(a) schematically shows the decomposition of the lap-shear loads applied at the overlap part of a lap-shear specimen (as schematically shown in Figure 6.2). Figure 6.7(b) schematically shows the decomposition process of the general normal structural stress distributions of a strip model. In each of these schematics, two strips of thicknesses t_u and t_l represent the upper (u) and lower (l) sheets, respectively, of the lap-shear specimen. Also, the gray-shaded areas (with a size of $2a$ as marked in model A) in Figure 6.7(a) represent the spot weld. Note that $2a$ represents the diameter of the spot weld.

As shown in Figure 6.7(a), model A represents a spot weld with ideal geometry under lap-shear loading conditions. The lap-shear forces F represent the resultant forces applied to the ends of the sheets on the bottom surface of the upper sheet and on the top surface of the bottom sheet. Note that the action line of the lap-shear forces F passes through the interfacial surface between the upper and lower sheets or the bond line connecting the two crack tips. Model B represents a spot weld under an equivalent loading condition of model A. As shown in the figure, the shear forces F

are shifted from the bottom surface of the upper sheet and the top surface of the bottom sheet to the middle surfaces of the upper and lower sheets, respectively. Two additional bending moments $Ft_u/2$ and $Ft_l/2$ are required for equilibrium. Finally, the forces and moments of model B are decomposed into four types of simple loads: counter bending (model C), central bending (model D), shear (model E) and tension/compression (model F). Note that the bending moments in models C and D have magnitudes of $Ft_u/4$ and $Ft_l/4$ for the upper and lower sheets, respectively, and the forces in models E and F all have a magnitude of $F/2$.

The general distributions of the normal structural stress for line \overline{FG} and line \overline{AB} in the lower and upper sheets for the spot weld under lap-shear loading conditions are represented by σ_{ui} , σ_{uo} , σ_{li} and σ_{lo} as shown in model B in Figure 6.7(b). The general distributions of the normal structural stress of model B can be then decomposed into four types of simple distributions: counter bending (model C), central bending (model D), shear (model E) and tension/compression (model F), corresponding to the loading conditions shown in models C, D, E and F in Figure 6.7(a), respectively. The maximum normal stresses σ_{CB}^k , σ_{CIB}^k , σ_S^k and σ_T^k ($k = u, l$) in the upper (u) and lower (l) sheets for models C, D, E and F, respectively, are also presented in Figure 6.7(b). Based on the superposition principle of the linear elasticity theory, the normal structural stresses σ_{ui} , σ_{uo} , σ_{li} and σ_{lo} for the spot weld under lap-shear loading conditions can be written as functions of σ_{CB}^k , σ_{CIB}^k , σ_S^k and σ_T^k ($k = u, l$) as

$$\sigma_{uo} = -\sigma_{CB}^u - \sigma_{CIB}^u + \sigma_S^u + \sigma_T^u \quad (6.32)$$

$$\sigma_{ui} = \sigma_{CB}^u + \sigma_{CiB}^u + \sigma_S^u + \sigma_T^u \quad (6.33)$$

$$\sigma_{li} = \sigma_{CB}^l - \sigma_{CiB}^l - \sigma_S^l + \sigma_T^l \quad (6.34)$$

$$\sigma_{lo} = -\sigma_{CB}^l + \sigma_{CiB}^l - \sigma_S^l + \sigma_T^l \quad (6.35)$$

Recently, Lin and Pan [18] derived new closed-form structural stress solutions for a rigid inclusion in a finite square plate subjected to a lap-shear load based on the stress function approach and the Kirchoff plate theory for linear elastic materials. The maximum stresses σ_{CB}^k , σ_{CiB}^k , σ_S^k and σ_T^k ($k = u, l$) as shown in Figure 6.7(b) along the nugget circumference $r = a$ under counter bending, central bending, shear and tension/compression loading conditions, respectively, are presented here as functions of the radius a of the spot weld (idealized as a rigid inclusion), the thicknesses t_k and the Poisson's ratios ν_k ($k = u, l$) of the upper (u) and lower (l) sheets, the half width b of the lap-shear specimen and the angular location θ as defined in Figure 6.3 as

$$\sigma_{CB}^k = \frac{-3F}{8bt_k X_k Y_k} [2b^2 X_k + 4Y_k (a^4 b^4 + b^8) \cos 2\theta] \quad (6.36)$$

$$\sigma_{CiB}^k = \frac{3F \cos \theta}{2\pi a t_k} \quad (6.37)$$

$$\sigma_S^k = \frac{F \cos \theta}{2\pi a t_k} \quad (6.38)$$

$$\sigma_T^k = \frac{F [3 - \nu_k + 2(1 + \nu_k) \cos \theta]}{4bt_k (3 + 2\nu_k - \nu_k^2)} \quad (6.39)$$

where X and Y are defined as

$$X_k = (-1 + \nu_k)(a^4 + b^4)^2 - 4a^2 b^6 (1 + \nu_k) \quad (6.40)$$

$$Y_k = a^2(-1 + \nu_k) - b^2(1 + \nu_k) \quad (6.41)$$

Note that the four closed-form structural stress solutions shown in Equations (6.36)-(6.39) were developed from the analytical structural stress solutions for a rigid inclusion in a finite square plate subjected to the corresponding loading conditions shown in Figures 6.7(a) and 6.7(b) for models C, D, E and F, respectively.

The shear stresses τ_u and τ_l shown in model A in Figure 6.6 can be obtained from the out-of-plane shear structural stress solutions for model E in Figure 6.7(a) as

$$\tau_u = -\frac{F \sin \theta}{2\pi a t_u} \quad (6.42)$$

$$\tau_l = \frac{F \sin \theta}{2\pi a t_l} \quad (6.43)$$

The K_1 , K_2 and K_3 for spot welds joining two sheets of different materials and thicknesses can be then obtained from Equations (6.22)-(6.24) based on the structural stress solutions in Equations (6.32)-(6.43). The K_I , K_{II} and K_{III} for spot welds joining two sheets of identical material with different thicknesses can be then obtained from Equations (6.26)-(6.28) based on the structural stress solutions in Equations (6.32)-(6.43). For the special case of $E_u = E_l = E$ and $t_u = t_l = t$, by using the structural stress solutions in Equations (6.32)-(6.43), Equations (6.29)-(6.31) can be rewritten as (Lin and Pan [18])

$$K_I = \frac{\sqrt{3}F}{8b\sqrt{t}XY} \left[-2b^2X - 4Y(a^4b^4 + b^8) \cos 2\theta \right] \quad (6.44)$$

$$K_{II} = \frac{F \cos \theta}{\pi a \sqrt{t}} \quad (6.45)$$

$$K_{III} = -\frac{F \sin \theta}{\sqrt{2\pi a}\sqrt{t}} \quad (6.46)$$

where X and Y are given in Equations (6.40) and (6.41), respectively.

6.3.2. For spot welds with gaps and bends in lap-shear specimens

In general, the geometries of spot friction welds appear to be quite complex as shown in Lin et al. [23-27], Tran et al. [28,29] and Tran and Pan [30]. As discussed later, based on the finite element computations, the gaps between the upper and lower sheets and the bends near the spot friction welds appear to strongly affect the stress intensity factor and J integral solutions for the crack fronts along the nugget circumferences of spot friction welds. In this section, the analytical structural stress solutions along the nugget circumferences of spot welds with the gaps and bends in the lap-shear specimens are presented.

Figure 6.8(a) shows a schematic plot of a spot weld with a gap and a bend in a lap-shear specimen under the resultant applied forces F marked as the bold arrows. The spot weld is idealized as a circular cylinder in the figure. The nominal upper and lower sheet thicknesses t_u and t_l , the nugget diameter $2a$, the length L and the overlap length V are similar to those shown in Figure 6.2. As shown in Figure 6.8(a), the gap and bend are represented by g and e , respectively. Note that the resultant forces F are applied to the ends of the sheets on the bottom surface of the upper sheet and on the top surface of the lower sheet. Due to the presence of the gap between the upper and lower sheets, the specimen is a two-force member when mounted in the lap-shear testing fixture. The action line of the two resultant applied forces F is therefore realigned as shown in Figure 6.8(a). Figure 6.8(b) shows a

schematic plot of the loading condition near the right edge surface of the specimen. In Figure 6.8(b), the angle $\phi (= g/(2L-V))$ represents the inclined angle of the force F with respect to the horizontal axis. As shown in Figure 6.8(b), the inclined force F is resolved into a horizontal force F_1 and a vertical force F_2 .

It should be noted that the structural stress solutions developed in Section 6.3.1 are for the lap-shear forces that act along the bond line connecting the two crack tips. Therefore, the forces F_1 applied for the spot weld with a gap and a bend in a lap-shear specimen should be resolved along the bond line in order to employ the results developed in the previous section. Figure 6.8(c) shows the decomposition process of the loading conditions of the spot weld with the gap and bend in a lap-shear specimen. Model R* represents a spot weld with the gap and bend in a lap-shear specimen under the applied forces of F_1 and F_2 . The forces in model R* are decomposed into two simple loading conditions as shown in models S* and T* in Figure 6.8(c). As shown in Figure 6.8(c), two additional moments $M_u (= eF_1 + gF_1)$ and $M_l (= eF_1)$ are introduced in model S* due to the shift of the action line of the horizontal forces F_1 from the bottom surface of the upper sheet and the top surface of the lower sheet, where the forces F_1 applied, to the bond line connecting the two crack tips. Note the parameter e is assigned as a positive value if the top surface of the lower sheet, where the force F applied, is above the bond line and vice versa. Model T* represents a spot weld with the gap and bend under two coach-peel forces of F_2 (Lin and Pan [18]).

Figure 6.8(d) shows the decomposition process of the loading condition shown in model S*. The forces and moments in model S* are decomposed into three simple

loading conditions: lap-shear loading, counter bending and central bending, marked as models A*, C* and D*, respectively. Note that the loading conditions for the models marked as A*, C* and D* in Figure 6.8(b) are similar to those marked as A, C and D, respectively, in Figure 6.7(b).

In general, the inclined angle ϕ is quite small due the large value of $2L - V$ when compared to g . Therefore, the forces F_1 and F_2 can be approximated as F and $F\phi$, respectively. The additional moments M_u and M_l can be rewritten as

$$M_u = (g + e)F \quad (6.47)$$

$$M_l = eF \quad (6.48)$$

As shown in Figure 6.7(a), two bending moments $Ft_u/2$ and $Ft_l/2$ are applied on the upper left leg and the lower right leg of the lap-shear specimen, respectively.

Here, we define two dimensionless geometric factors f_u and f_l as

$$f_u = \frac{M_u}{Ft_u/2} = \frac{2(g + e)}{t_u} \quad (6.49)$$

$$f_l = \frac{M_l}{Ft_l/2} = \frac{2e}{t_l} \quad (6.50)$$

The factors f_u and f_l represent the relative significance of the contributions of the additional bending moments due to the gap and bend when compared to the bending moments induced by the lap-shear load.

Similar to Section 6.3.1, in reference to Figure 6.5(b), the structural stresses σ_{ui} , σ_{uo} , σ_{li} and σ_{lo} for a spot weld with a gap and a bend in a lap-shear specimen are derived here. For model S*, as shown in Figure 6.8(d), based on the structural stress solutions for spot welds with ideal geometry and the stress distributions under counter

and central bending conditions as developed in Section 6.3.1, the normal structural stresses $(\sigma_{ui})_{S^*}$, $(\sigma_{uo})_{S^*}$, $(\sigma_{li})_{S^*}$ and $(\sigma_{lo})_{S^*}$ at the inner (*i*) and outer (*o*) surfaces of the upper (*u*) and lower (*l*) strips of model S^* can be written as

$$(\sigma_{uo})_{S^*} = -\sigma_{CB}^u - \sigma_{CtB}^u + \sigma_S^u + \sigma_T^u + f_u(\sigma_{CB}^u + \sigma_{CtB}^u) \quad (6.51)$$

$$(\sigma_{ui})_{S^*} = \sigma_{CB}^u + \sigma_{CtB}^u + \sigma_S^u + \sigma_T^u - f_u(\sigma_{CB}^u + \sigma_{CtB}^u) \quad (6.52)$$

$$(\sigma_{li})_{S^*} = \sigma_{CB}^l - \sigma_{CtB}^l - \sigma_S^l + \sigma_T^l + f_l(\sigma_{CB}^l - \sigma_{CtB}^l) \quad (6.53)$$

$$(\sigma_{lo})_{S^*} = -\sigma_{CB}^l + \sigma_{CtB}^l - \sigma_S^l + \sigma_T^l - f_l(\sigma_{CB}^l - \sigma_{CtB}^l) \quad (6.54)$$

Note that σ_{CB}^k , σ_{CtB}^k , σ_S^k and σ_T^k ($k = u, l$) are determined from Equations (6.36)-(6.41).

For model T^* , based on the recent publication of Lin and Pan [18], the normal structural stresses $(\sigma_{ui})_{T^*}$, $(\sigma_{uo})_{T^*}$, $(\sigma_{li})_{T^*}$ and $(\sigma_{lo})_{T^*}$ at the inner (*i*) and outer (*o*) surfaces of the upper (*u*) and lower (*l*) strips of model T^* are

$$\begin{aligned} (\sigma_{ui})_{T^*} = & \frac{3F_2 b(a^2 - b'^2) \left[a^2(-1 + \nu_u) - b'^2(3 + \nu_u) \right] \cos(\theta + \pi)}{\pi a t_u^2 \left[a^4(-1 + \nu_u) - b'^4(3 + \nu_u) \right]} \\ & - \frac{3F_2 \left[(a^2 - b'^2)(-1 + \nu_u) + 2b'^2(1 + \nu_u) \ln(b'/a) \right]}{2\pi a^2 \left[a^2(-1 + \nu_u) - b'^2(1 + \nu_u) \right]} \\ & - \frac{24\tilde{M}_{x'y'}}{t_u^2 X_u'} \left[a^4(b/\sqrt{2})^4 + (b/\sqrt{2})^8 \right] \cos 2(\theta + \pi) \\ & + \frac{3\tilde{M}_b}{2t_u^2 X_u Y_u} \left[-2b^2 X_u - 4Y_u(a^4 b^4 + b^8) \cos 2(\theta + \pi) \right] + \frac{6b\tilde{M}_b(a^2 - b'^2) \cos(\theta + \pi)}{\pi a t_u^2 (a^2 + b'^2)} \quad (6.55) \end{aligned}$$

$$(\sigma_{uo})_{T^*} = -(\sigma_{ui})_{T^*} \quad (6.56)$$

$$\begin{aligned}
(\sigma_{li})_{T^*} = & \frac{3F_2 b(a^2 - b'^2) [a^2(-1 + \nu_l) - b'^2(3 + \nu_l)] \cos \theta}{\pi a t_l^2 [a^4(-1 + \nu_l) - b'^4(3 + \nu_l)]} \\
& - \frac{3F_2 [(a^2 - b'^2)(-1 + \nu_l) + 2b'^2(1 + \nu_l) \ln(b'/a)]}{2\pi t_l^2 [a^2(-1 + \nu_l) - b'^2(1 + \nu_l)]} \\
& - \frac{24\tilde{M}_{x'y'}}{t_l^2 X_l'} [a^4(b/\sqrt{2})^4 + (b/\sqrt{2})^8] \cos 2\theta \\
& + \frac{3\tilde{M}_b}{2t_l^2 X_l Y_l} [-2b^2 X_l - 4Y_l(a^4 b^4 + b^8) \cos 2\theta] + \frac{6b\tilde{M}_b(a^2 - b'^2) \cos \theta}{\pi a t_l^2 (a^2 + b'^2)} \quad (6.57)
\end{aligned}$$

$$(\sigma_{lo})_{T^*} = -(\sigma_{li})_{T^*} \quad (6.58)$$

where $b' = 2b/\sqrt{\pi}$, $\tilde{M}_b = F_2(L - V/2 - b)/2b$, $\tilde{M}_{x'y'} = F_2/16$, X_k and Y_k ($k = u, l$) are given in Equations (6.40) and (6.41), respectively, and

$$\tilde{M}_c = \frac{F_2 [a^2 - b'^2 + 2a^2 \ln(b'/a)]}{4\pi(a^2 - b'^2)} \quad (6.59)$$

$$X_k' = -[a^4 + (b/\sqrt{2})^4]^2 (1 - \nu_k) - 4a^2 (b/\sqrt{2})^6 (1 + \nu_k) \quad (k = u, l) \quad (6.60)$$

Finally, the normal structural stresses σ_{ui} , σ_{uo} , σ_{li} , σ_{lo} at the inner (i) and outer (o) surfaces of the upper (u) and lower (l) strips of a strip model that represents a spot weld with a gap and a bend in a lap-shear specimen as schematically shown in Figure 6.8(a) can be obtained from Equations (6.51)-(6.58) as

$$\sigma_{uo} = (\sigma_{uo})_{S^*} + (\sigma_{uo})_{T^*} \quad (6.61)$$

$$\sigma_{ui} = (\sigma_{ui})_{S^*} + (\sigma_{ui})_{T^*} \quad (6.62)$$

$$\sigma_{li} = (\sigma_{li})_{S^*} + (\sigma_{li})_{T^*} \quad (6.63)$$

$$\sigma_{lo} = (\sigma_{lo})_{S^*} + (\sigma_{lo})_{T^*} \quad (6.64)$$

It should be noted that the shear stresses τ_u and τ_l for spot welds with gaps and bends are similar to those for the spot welds with ideal geometry and can be obtained from Equations (6.42) and (6.43). Note also that once the normal structural stresses, σ_{ui} , σ_{uo} , σ_{li} and σ_{lo} , and shear stresses, τ_u and τ_l , for a spot weld with a gap and a bend in a lap-shear specimen are obtained from Equations (6.61)-(6.68), (6.42) and (6.43), the stress intensity factor and J integral solutions for spot welds with the gap and bend joining two sheets of similar or dissimilar materials with equal thickness or different thicknesses can be easily obtained from the equations listed in Section 6.2.

6.4. Three-dimensional finite element models

In this investigation, three-dimensional finite element models for resistance spot welds and spot friction welds with different weld geometries are conducted under lap-shear loading conditions. A general description of these models is reported in this section while the details for each model will be reported later. In the finite element analyses, the weld nugget and base metals are assumed to be linear elastic isotropic materials. Two types of materials, aluminum and steel, are considered in the finite element computations. The Young's moduli of the aluminum and steel sheets are taken as 68.9 GPa and 207 GPa, respectively. The Poisson's ratios of the aluminum and steel sheets are taken as 0.33 and 0.30, respectively. The commercial finite element program ABAQUS [39] is employed to perform the computations. Second-order quarter point crack-tip elements with collapsed nodes are used to model the $1/\sqrt{r}$ singularity near the crack front. Here r represents the radial distance to the crack front. The stress intensity factor and J integral solutions are directly computed

by ABAQUS. The computational stress intensity factor solutions are obtained based on the interaction integral method for cracks under mixed-mode loading conditions (Shih and Asaro [40]). It should be noted that the contact of the crack faces near the welds was not modeled in this investigation as the critical locations of the welds are subjected to positive K_I (or K_1) conditions.

It should be noted that the components K_1^A and K_2^A of the complex stress intensity factor solution $\mathbf{K}^A = K_1^A + iK_2^A$ obtained directly from ABAQUS are defined such that the stresses (σ_y, τ_{xy}) at a small distance r ahead of an interface crack tip are characterized by \mathbf{K}^A as

$$\sigma_y + i\tau_{xy} = \frac{K_1^A + iK_2^A}{\sqrt{2\pi r}} r^{i\varepsilon} \quad (6.65)$$

The K_1 and K_2 solutions as defined in Equation (6.18) are related to the K_1^A and K_2^A solutions as defined in Equation (6.65) as

$$K_1 = K_1^A \cos(\varepsilon \ln t) - K_2^A \sin(\varepsilon \ln t) \quad (6.66)$$

$$K_2 = K_1^A \sin(\varepsilon \ln t) + K_2^A \cos(\varepsilon \ln t) \quad (6.67)$$

Therefore, the K_1 and K_2 solutions for spot welds joining two sheets of dissimilar materials reported in this investigation are obtained from Equations (6.66) and (6.67) with the K_1^A and K_2^A solutions directly computed by ABAQUS.

A schematic plot of a half of a lap-shear specimen with a spot weld and the boundary conditions employed in the finite element models is shown in Figure 6.9. Note that $2a$ represents the diameter of the spot weld. In the finite element models reported later, the length L , the overlap length V , the half width b , and the upper

and lower sheet thicknesses t_u and t_l are based on the dimensions of the available specimens and testing fixture. The critical locations of the weld are marked as A, C and D in the figure (and also in Figure 6.2). As shown in Figure 6.9, a uniform displacement in the $+x$ direction is applied along the interfacial surface between the upper sheet and the doubler on the right edge surface of the specimen. Also, the displacements in the x , y and z directions for the interfacial surface between the doubler and the lower sheet on the left edge surface of the specimen are fixed. Due to symmetry, only a half of the lap-shear specimen is modeled. The displacement in the y direction of the symmetry plane, the xz plane, of the specimen is constrained to represent the symmetry conditions due to the loading conditions. Note that the three-dimensional finite element meshes employed in this investigation are evolved from the mesh reported in Wang et al. [14]. As shown later, the meshes near the crack front along the nugget circumference of the welds are refined to assure reasonable aspect ratios of the three-dimensional solid elements.

The resultant reaction forces F_x , F_y and F_z in the x , y and z directions, respectively, for the interfacial surface between the doubler and the lower sheet on the left edge of the specimen are directly calculated by ABAQUS. The numerical results indicate that F_y and F_z are negligibly small when compared to F_x . The force F_x is then used as the applied lap-shear load F in the analytical stress intensity factor and J integral solutions as discussed earlier. Note that the other geometric parameters employed in the finite element computation and in the analytical solutions for each model are the same for the purpose of comparison. It should be emphasized the analytical stress intensity factor and J integral solutions reported in this investigation

are obtained from the analytical solutions developed in Section 6.2 that employed the closed-form structural stress solutions presented in Section 6.3.

6.5. Validation of analytical stress intensity factor and J integral solutions for spot welds with ideal geometry in lap-shear specimens

Figures 6.10(a) and 6.10(b) show a three-dimensional finite element mesh and a close-up view of the mesh near the weld, respectively, for a half of a lap-shear specimen with a spot weld joining two sheets of equal thickness of $t_u = t_l = 0.65$ mm. For this finite element model, the length L ($= 77.3$ mm), the overlap length V ($= 47.1$ mm), the half width b ($= 18.9$ mm) and the weld diameter $2a$ ($= 6.4$ mm) are based on the dimensions of the lap-shear specimens as in Wang et al. [14]. The three-dimensional finite element mesh has 37,338 second-order solid elements. The boundary conditions are also shown in Figure 6.10(a). Two crack tips, marked as A and B, are also shown in Figure 6.10(b). Two finite element computations based on the mesh shown in Figures 6.10(a) and 6.10(b) were conducted. The finite element model for a weld with steel as the upper and lower sheet materials is denoted as the Fe/Fe-0.65/0.65 weld. The finite element model for a weld with aluminum and steel as the upper and lower sheet materials, respectively, is denoted as the Al/Fe-0.65/0.65 weld. It should be noted that the results presented in the following are obtained from the same applied lap-shear loads.

Figure 6.10(c) shows the normalized K_I , K_{II} and K_{III} solutions as functions of θ for the crack front along the nugget circumference of the Fe/Fe-0.65/0.65 weld based on our three-dimensional finite element computation and the analytical solutions. Note that the angular location θ is defined in Figure 6.3. It should be

noted that the order of θ is reversed in the figures reported in this paper to be consistent with the definition of the angular location θ and the geometry/loading as shown in Figure 6.10(a). Note also that the K_I , K_{II} and K_{III} solutions shown in Figure 6.10(c) are normalized by the K_2 solution at point A ($\theta = 0^\circ$) obtained from the finite element computation for the Al/Fe-0.65/0.65 weld (as shown later in Figure 6.10(d)). As shown in Figure 6.10(c), the analytical K_I , K_{II} and K_{III} solutions agree very well with the results obtained from the finite element computation. As shown in Figure 6.10(c), based on the analytical solutions and the finite element computation, the maximum values of the K_I solution are located at point A ($\theta = 0^\circ$) and point B ($\theta = 180^\circ$), the maximum values of the K_{II} solution are located at point A ($\theta = 0^\circ$), and the maximum values of the K_{III} solution are located at point C ($\theta = 90^\circ$). Note that the distributions of the K_I and K_{III} solutions are symmetric with respect to the y axis ($\theta = 90^\circ$) and the distributions of the K_{II} solution are anti-symmetric with respect to the y axis ($\theta = 90^\circ$). The results in Figure 6.10(c) also indicate that K_{II} is the dominant stress intensity factor for the Fe/Fe-0.65/0.65 weld under lap-shear loading conditions. Note that the distributions of the stress intensity factor solutions along the nugget circumference as shown in Figure 6.10(c) are quite similar to those shown in Radaj et al. [5] and Wang et al. [14].

Figure 6.10(d) shows the normalized K_1 , K_2 and K_3 solutions as functions of θ for the crack front along the nugget circumference of the Al/Fe-0.65/0.65 weld based on our three-dimensional finite element computation and the analytical solutions. Note that the K_1 , K_2 and K_3 solutions shown in Figure 6.10(d) are normalized by

the K_2 solution at point A ($\theta = 0^\circ$) obtained from the finite element computation. As shown in Figure 6.10(d), the analytical K_1 , K_2 and K_3 solutions agree very well with the results obtained from the finite element computation. As shown in Figure 6.10(d), based on the analytical solutions and the finite element computation, the maximum values of the K_1 and K_2 solutions are located at point A ($\theta = 0^\circ$) and the maximum values of the K_3 solution are located at point C ($\theta = 90^\circ$). Note that the distributions of the K_1 solutions are not symmetric with respect to the y axis ($\theta = 90^\circ$) and the distributions of the K_2 solution are not anti-symmetric with respect to the y axis ($\theta = 90^\circ$) due to different upper and lower sheet materials. The results in Figure 6.10(d) also indicate that K_2 is the dominant stress intensity factor for the Al/Fe-0.65/0.65 weld under lap-shear loading conditions. A comparison of Figures 6.10(c) and 6.10(d) indicates that the K_{III} and K_3 solutions for both welds are quite similar to each other.

Figure 6.10(e) shows the normalized J integral solutions as functions of θ for the crack fronts along the nugget circumferences of the Fe/Fe-0.65/0.65 weld and the Al/Fe-0.65/0.65 weld based on our three-dimensional finite element computations and the analytical solutions. Note that the J integral solutions shown in Figure 6.10(e) are normalized by the J integral solution at point A ($\theta = 0^\circ$) obtained from the finite element computation for the Al/Fe-0.65/0.65 weld. As shown in Figure 6.10(e), for both welds, the analytical J integral solutions agree very well with the results obtained from the finite element computations. For the Fe/Fe-0.65/0.65 weld, as shown in Figure 6.10(e), based on the analytical solutions and the finite element

computation, the maximum values of the J integral solution are located at point A ($\theta = 0^\circ$) and point B ($\theta = 180^\circ$). Also, the distributions of the J integral solution are symmetric with respect to the y axis ($\theta = 90^\circ$). For the Al/Fe-0.65/0.65 weld, as shown in Figure 6.10(e), based on the analytical solutions and the finite element computation, the maximum values of the J integral solution are located at point A ($\theta = 0^\circ$). Also, the J integral solutions at point A ($\theta = 0^\circ$) are about 2.5 times of those at point B ($\theta = 180^\circ$). As shown in Figure 6.10(e), the J integral solution at point A ($\theta = 0^\circ$) for the Al/Fe-0.65/0.65 weld is about 2.5 times of that for the Fe/Fe-0.65/0.65 weld, whereas the J integral solutions at point B ($\theta = 180^\circ$) for both welds are nearly the same.

The finite element mesh shown in Figures 6.10(a) and 6.10(b) is modified to investigate the effects of the sheet thickness on the stress intensity factor and J integral solutions. Figures 6.11(a) and 6.11(b) show a three-dimensional finite element mesh and a close-up view of the mesh near the weld, respectively, for a half of a lap-shear specimen with a spot weld joining two sheets with $t_u = 0.65$ mm and $t_l = 1.30$ mm. For this finite element model, the length L (= 77.3 mm), the overlap length V (= 47.1 mm), the half width b (= 18.9 mm) and the weld diameter $2a$ (= 6.4 mm) are based on the dimensions of the lap-shear specimens as in Wang et al. [14]. The three-dimensional finite element mesh has 55,388 second-order solid elements. The boundary conditions are also shown in Figure 6.11(a). Two crack tips, marked as A and B, are also shown in Figure 6.11(b). Three finite element computations based on the mesh shown in Figures 6.11(a) and 6.11(b) were conducted. The finite element model for a weld with steel as the upper and lower sheet materials is denoted

as the Fe/Fe-0.65/1.30 weld. The finite element model for a weld with aluminum and steel as the upper and lower sheet materials, respectively, is denoted as the Al/Fe-0.65/1.30 weld. The finite element model for a weld with steel and aluminum as the upper and lower sheet materials, respectively, is denoted as the Fe/Al-0.65/1.30 weld.

Figure 6.11(c) shows the normalized K_I , K_{II} and K_{III} solutions as functions of θ for the crack front along the nugget circumference of the Fe/Fe-0.65/1.30 weld based on our three-dimensional finite element computation and the analytical solutions. Note that the K_I , K_{II} and K_{III} solutions shown in Figure 6.11(c) are normalized by the K_2 solution at point A ($\theta = 0^\circ$) obtained from the finite element computation for the Al/Fe-0.65/0.65 weld as shown in Figure 6.10(d) for the purpose of comparison. As shown in Figure 6.11(c), the analytical K_I , K_{II} and K_{III} solutions agree very well with the results obtained from the finite element computation. As shown in Figure 6.11(c), based on the analytical solutions and the finite element computation, the maximum values of the K_I and K_{II} solutions are located at point A ($\theta = 0^\circ$) and the maximum values of the K_{III} solution are located at point C ($\theta = 90^\circ$). Note that the distributions of the K_I solutions are not symmetric with respect to the y axis ($\theta = 90^\circ$) and the distributions of the K_{II} solution are not anti-symmetric with respect to the y axis ($\theta = 90^\circ$) due to the different upper and lower sheet thicknesses. The results in Figure 6.11(c) also indicate that K_{II} is the dominant stress intensity factor for the Fe/Fe-0.65/1.30 weld under lap-shear loading conditions. A comparison of Figures 6.10(c) and 6.11(c)

indicates that the increase of the lower sheet thickness t_l does not change significantly the K_I and K_{II} solutions at point A ($\theta = 0^\circ$) for the welds.

Figure 6.11(d) shows the normalized K_1 , K_2 and K_3 solutions as functions of θ for the crack front along the nugget circumference of the Al/Fe-0.65/1.30 weld based on our three-dimensional finite element computation and the analytical solutions. Note that the K_1 , K_2 and K_3 solutions shown in Figure 6.11(d) are normalized by the K_2 solution at point A ($\theta = 0^\circ$) obtained from the finite element computation for the Al/Fe-0.65/0.65 weld as shown in Figure 6.10(d). As shown in Figure 6.11(d), the analytical K_1 , K_2 and K_3 solutions agree very well with the results obtained from the finite element computation. As shown in Figure 6.11(d), based on the analytical solutions and the finite element computation, the maximum values of the K_1 and K_2 solutions are located at point A ($\theta = 0^\circ$) and the maximum values of the K_3 solution are located at point C ($\theta = 90^\circ$). The results in Figure 6.11(d) also indicate that K_2 is the dominant stress intensity factor for the Al/Fe-0.65/1.30 weld under lap-shear loading conditions. A comparison of Figures 6.10(d) and 6.11(d) indicates that the increase of the lower sheet thickness t_l does not change significantly the K_1 and K_2 solutions at point A ($\theta = 0^\circ$) for the welds.

Figure 6.11(e) shows the normalized K_1 , K_2 and K_3 solutions as functions of θ for the crack front along the nugget circumference of the Fe/Al-0.65/1.30 weld based on our three-dimensional finite element computation and the analytical solutions. Note that the K_1 , K_2 and K_3 solutions shown in Figure 6.11(e) are normalized by the K_2 solution at point A ($\theta = 0^\circ$) obtained from the finite element computation for

the Al/Fe-0.65/0.65 weld as shown in Figure 6.10(d). As shown in Figure 6.11(e), the analytical K_1 , K_2 and K_3 solutions agree very well with the results obtained from the finite element computation. As shown in Figure 6.11(e), based on the analytical solutions and the finite element computation, the maximum values of the K_1 and K_2 solutions are located at point B ($\theta = 180^\circ$) and the maximum values of the K_3 solution are located at point C ($\theta = 90^\circ$). The results in Figure 6.11(e) also indicate that K_2 is the dominant stress intensity factor for the Fe/Al-0.65/1.30 weld under lap-shear loading conditions. A comparison of Figures 6.11(c), 6.11(d) and 6.11(e) indicates that the K_{III} and K_3 solutions for the three welds are quite similar to each other.

Figure 6.11(f) shows the normalized J integral solutions as functions of θ for the crack fronts along the nugget circumferences of the Fe/Fe-0.65/1.30 weld, the Al/Fe-0.65/1.30 weld and the Fe/Al-0.65/1.30 weld based on the finite element computations and the analytical solutions. Note that the J integral solutions shown in Figure 6.11(f) are normalized by the J integral solution at point A ($\theta = 0^\circ$) obtained from the finite element computation for the Al/Fe-0.65/0.65 weld as shown in Figure 6.10(d). As shown in Figure 6.11(f), the analytical J integral solutions for all three welds agree very well with the results obtained from the finite element computations. Also, the distributions of the J integral solution are not symmetric with respect to the y axis ($\theta = 90^\circ$) due to different materials and thicknesses. As shown in Figure 6.11(f), based on the analytical solutions and the finite element computations, the maximum values of the J integral solutions for the Fe/Fe-0.65/1.30 and Al/Fe-0.65/1.30 welds are located at point A ($\theta = 0^\circ$) and the

maximum values of the J integral solutions for the Fe/Al-0.65/1.30 weld are located at point B ($\theta = 180^\circ$).

As shown in Figure 6.11(f), the J integral solution at point A ($\theta = 0^\circ$) for the Al/Fe-0.65/1.30 weld is about 2.5 times of that for the Fe/Fe-0.65/1.30 weld, whereas the J integral solutions at point B ($\theta = 180^\circ$) for both welds are nearly the same. As shown in Figure 6.11(f), the J integral solution at point B ($\theta = 0^\circ$) for the Fe/Al-0.65/1.30 weld is about 2.5 times of that for the Fe/Fe-0.65/1.30 weld, whereas the J integral solutions at point A ($\theta = 0^\circ$) for both welds are nearly the same. In summary, as shown in Figures 6.10 and 6.11, the results obtained from the three-dimensional finite element computations validate the analytical stress intensity factor and J integral solutions for the crack fronts along the nugget circumferences of spot welds with ideal geometry joining two sheets of similar or dissimilar materials with equal or different thicknesses in lap-shear specimens based on the new closed-form structural stress solutions presented in Section 6.3.1.

6.6. Effects of weld geometry on fracture mechanics parameters for resistance spot welds and spot friction welds in lap-shear specimens

6.6.1. Aluminum 6111 resistance spot welds

Figure 6.12(a) shows an optical micrograph of the cross section along the symmetry plane of an aluminum 6111 resistance spot weld before testing. Aluminum 6111-T4 sheets with the nominal thicknesses of $t_u = 1.34$ mm and $t_l = 1.54$ mm are used to make the weld shown in Figure 6.12(a). As shown in the figure, the gray area represents the weld nugget where the upper and lower sheet materials were melt and solidified. Note that the weld and base metal have different gray levels. As shown in

Figure 6.12(a), the top surface of the upper sheet and the bottom surface of the lower sheet around the weld nugget were deformed due to the electrode indentation. Two notches, marked as N1 and N2, can be seen in the figure. The notches extend into the weld and become cracks. The locations of the crack tips are marked in the figure. As shown in Figure 6.12(a), the effective thicknesses t'_u ($= 1.3$ mm) and t'_l ($= 1.5$ mm) are measured at the crack tips of the weld. Note that the central portion of the weld nugget, schematically marked as region I in Figure 6.12(a), contains voids which are defects of this particular weld due to the resistance spot welding process.

Figure 6.12(b) show a close-up view of a three-dimensional finite element mesh near the aluminum 6111 resistance spot weld shown in Figure 6.12(a). For this finite element model, the length L ($= 76.4$ mm), the overlap length V ($= 25.4$ mm), the half width b ($= 12.7$ mm) and the weld diameter $2a$ ($= 6.7$ mm) are based on the dimensions of the 6111 resistance spot welds in lap-shear specimens and testing fixture. The three-dimensional finite element model has 13,284 second-order solid elements. Two crack tips, marked as A and B, are also shown in Figure 6.12(b). Note that the voids in region I as shown in Figure 6.12(a) are not modeled in this model. In order to examine the effects of this weld geometry of the aluminum 6111 resistance spot weld, another three-dimensional finite element analysis for an equivalent spot weld joining two aluminum sheets of effective thicknesses t'_u ($= 1.3$ mm) and t'_l ($= 1.5$ mm) is conducted. Note that the effective thicknesses t'_u and t'_l are also used as the upper and lower sheet thicknesses in the analytical solutions.

Figure 6.12(c) shows the normalized K_I , K_{II} and K_{III} solutions as functions of θ for the aluminum 6111 resistance spot weld shown in Figure 6.12(a) and for the

equivalent spot weld joining two aluminum sheets of $t'_u = 1.3$ mm and $t'_l = 1.5$ mm based on our three-dimensional finite element computations. Note that the angular location θ is defined in Figure 6.3. Note also that the K_I , K_{II} and K_{III} solutions shown in Figure 6.12(c) are normalized by the K_{II} solution at point A ($\theta = 0^\circ$) obtained from the finite element computation for the equivalent spot weld. As shown in Figure 6.12(b), the K_I , K_{II} and K_{III} solutions for the aluminum 6111 resistance spot weld and the equivalent spot weld are nearly the same. The results in Figure 6.12(c) also indicate that K_{II} is the dominant stress intensity factor for the aluminum 6111 resistance spot weld under lap-shear loading conditions. The J integral solutions for the aluminum 6111 resistance spot weld and the equivalent spot weld are nearly the same and are not reported here.

In order to examine the effects of the voids marked as region I in Figure 6.12(a) and for the later discussion on the effects of the central hole of spot friction welds, the finite element mesh shown in Figure 6.12(b) is modified by removing the central portion of the weld nugget which contains the voids. Figure 6.12 (d) shows a close-up view of the modified finite element mesh near the weld. Note that the modified mesh shown in Figure 6.12(d) is obtained from the original mesh shown in Figure 6.12(b) by removing a cylinder of a radius of 1.5 mm and a depth of 2.1 mm, measured from the top surface of the upper sheet. The modified mesh is then employed in another finite element analysis. Figure 6.12(e) shows the normalized K_I , K_{II} and K_{III} solutions as functions of θ for the aluminum 6111 resistance spot weld obtained from the finite element computations based on the original and modified meshes. Note that the K_I , K_{II} and K_{III} solutions shown in Figure 6.12(e)

are normalized by the K_{II} solution at point A ($\theta = 0^\circ$) obtained from the finite element computation for the equivalent spot weld as shown in Figure 6.12(c) for the purpose of comparison. As shown in Figure 6.12(e), the K_I , K_{II} and K_{III} solutions obtained from the finite element computations based on the original and modified meshes are nearly the same. The J integral solutions for both models are also nearly the same and are not reported here. Based on the finite element computations, the central portion of the weld nugget that contains the voids appears not to affect the stress intensity factor and J integral solutions for the crack front along the nugget circumference of the aluminum 6111 resistance spot weld.

It should be noted that the distributions of the stress intensity factor and J integral solutions based on the analytical solutions and the finite element computation for the equivalent spot weld are nearly the same and are not reported here. Since the gap and bend, represented by parameters g and e , for the aluminum 6111 resistance spot weld are relatively small when compared to the nominal sheet thicknesses, the effects of the gap and bend are not discussed here. In summary, the geometries of the electrode indentation and voids of the aluminum 6111 resistance spot weld as shown in Figure 6.12(a) appear not to affect the fracture mechanics parameters for the crack front along the nugget circumference of the weld in the lap-shear specimen when compared to the analytical solutions for the weld with ideal geometry as long as the effective thicknesses of the weld are used in the theoretical and numerical models.

6.6.2. Aluminum 5754 spot friction welds

Figure 6.13(a) shows an optical micrograph of the cross section along the symmetry plane of an aluminum 5754 spot friction weld before testing. Aluminum 5754-O sheets with a nominal thickness of $t_u = t_l = 2.0$ mm are used to make the weld shown in Figure 6.13(a). As shown in the figure, the indentation profile reflects the general shape of the threaded probe pin and the concave shoulder of the tool. The bottom surface of the lower sheet is almost flat. The area near the central hole represents the fine grain stir zone where the upper and lower sheets are well bonded possibly due to high pressure and large plastic deformation. Two notches, marked as N1 and N2, can be seen in the figure. The notches extend into the weld and become cracks. The locations of the crack tips are marked in the figure. The effective sheet thicknesses $t'_u = 1.70$ mm and $t'_l = 2.06$ mm are measured at the crack tips of the weld as shown in Figure 6.13(a).

Figure 6.13(b) show a close-up view of a three-dimensional finite element mesh near the aluminum 5754 spot friction weld shown in Figure 6.13(a). For this finite element model, the length L ($= 101.6$ mm), the overlap length V ($= 25.4$ mm), the half width b ($= 12.7$ mm) and the weld diameter $2a$ ($= 7.2$ mm) are based on the dimensions of the aluminum 5754 spot friction welds in lap-shear specimens tested in Tran et al. [27,28]. The three-dimensional finite element model has 18,639 second-order solid elements. Two crack tips, marked as A and B, are also shown in Figure 6.13(b). In order to examine the effects of this weld geometry of the aluminum 5754 spot friction weld, another three-dimensional finite element analysis for an equivalent spot weld joining two aluminum sheets of effective thicknesses t'_u ($= 1.70$ mm) and

t'_l ($= 2.06$ mm), is conducted. Note that the effective thicknesses t'_u and t'_l are also used as the upper and lower sheet thicknesses in the analytical solutions.

Figure 6.13(c) shows the normalized K_I , K_{II} and K_{III} solutions as functions of θ for the aluminum 5754 spot friction weld shown in Figure 6.13(a), for the equivalent spot weld joining two aluminum sheets of $t'_u = 1.70$ mm and $t'_l = 2.06$ mm based on our three-dimensional finite element computations, and the analytical solutions for the equivalent spot weld. Note that the angular location θ is defined in Figure 6.3. Note also that the K_I , K_{II} and K_{III} solutions shown in Figure 6.13(c) are normalized by the K_{II} solution at point A ($\theta = 0^\circ$) obtained from the finite element computation for the equivalent spot weld. As shown in Figure 6.13(c), the K_I , K_{II} and K_{III} solutions obtained from the finite element computations for the aluminum 5754 spot friction weld and the equivalent spot weld, and the results obtained from the analytical solutions for the equivalent spot weld are quite similar to each other. As shown in Figure 6.13(c), the K_I solution at point A ($\theta = 0^\circ$) obtained from the finite element computation for the equivalent spot weld is about 5% larger than that obtained from the analytical solutions, while the K_{II} solutions at point A ($\theta = 0^\circ$) obtained from the finite element computation and the analytical solutions are nearly the same. Also, the K_I solution at point A ($\theta = 0^\circ$) obtained from the finite element computation for the 5754 spot friction weld is about 8% smaller than that obtained from the analytical solutions, while the K_{II} solutions at point A ($\theta = 0^\circ$) obtained from the finite element computation for the 5754 spot friction weld is about 9% larger than that obtained from the analytical solutions. As shown in

Figure 6.13(c), the K_I and K_{II} solutions at point B ($\theta = 180^\circ$) obtained from the finite element computations for the 5754 spot friction weld and the equivalent spot weld, and the results obtained from the analytical solutions are nearly the same. The results in Figure 6.13(c) also indicate that K_{II} is the dominant stress intensity factor for the aluminum 5754 spot friction weld under lap-shear loading conditions. The J integral solutions obtained from both models are nearly the same and are not reported here.

Note that the central hole due to the tool probe pin indentation can be seen in Figure 6.12(a). In order to examine the effects the central hole, the finite element mesh for the 5754 spot friction weld shown in Figure 6.13(b) is modified by filling the central hole to a thickness of t'_u . Figure 6.13(d) shows a close-up view of the modified finite element mesh near the weld. The modified mesh is then employed in another finite element analysis. Figure 6.13(e) shows the normalized K_I , K_{II} and K_{III} solutions as functions of θ for the 5754 spot friction weld obtained from the finite element computations based on the original and modified meshes. Note that the K_I , K_{II} and K_{III} solutions shown in Figure 6.13(e) are normalized by the analytical K_{II} solution at point A ($\theta = 0^\circ$) obtained from the finite element computation for the equivalent spot weld as shown in Figure 6.13(c). As shown in Figure 6.13(e), the K_I , K_{II} and K_{III} solutions obtained from the finite element computations based on the original and modified meshes are nearly the same. Note that the J integral solutions obtained from both models are also nearly the same and are not reported here. Based on the finite element computations, the central hole due to the tool probe pin

indentation in the aluminum 5754 spot friction weld nugget appears not to affect the stress intensity factor and J integral solutions for the crack front along the nugget circumference of the weld.

As shown in Figure 6.13(c), the stress intensity factor and J integral solutions for the aluminum 5754 spot friction weld in the lap-shear specimen can be obtained by using the analytical solutions employed the effective thicknesses t'_u and t'_l measured at the crack tips of the weld. Since the gap and bend, represented by parameters g and e , for the aluminum 5754 spot friction weld are relatively small when compared to the nominal sheet thicknesses, the effects of the gap and bend are not discussed here. In summary, the complex weld geometry of the aluminum 5754 spot friction weld as shown in Figure 6.13(a) appears not to significantly affect the fracture mechanics parameters for the crack front along the nugget circumference of the weld in the lap-shear specimen when compared to the analytical solutions for the weld with ideal geometry as long as the effective thicknesses of the weld are used in the theoretical and numerical models. Note that a similar investigation for the aluminum 6111 spot friction weld tested in Tran et al. [27,28] also indicates that the complex weld geometry of the aluminum 6111 spot friction weld appears not to significantly affect the fracture mechanics parameters for the crack front along the nugget circumference of the weld in the lap-shear specimen when compared to the analytical solutions for the weld with ideal geometry.

6.6.3. Dissimilar Al/Fe spot friction welds

Figure 6.14(a) shows an optical micrograph of the cross section along the symmetry plane of an Al/Fe spot friction weld before testing. Aluminum 6000 series alloy and coated steel sheets with the nominal thicknesses of $t_u = 1.3$ mm and $t_l = 0.8$ mm, respectively, are used to make the weld shown in Figure 6.14(a). As shown in the figure, the indentation profile reflects the general shape of the smooth probe pin and the concave shoulder of the tool. Note that the tool probe pin penetrated partially into the upper sheet. The bottom surface of the lower sheet appears to be slightly bent. Two notches, marked as N1 and N2, can be seen in the figure. The notches extend into the weld and become cracks. The locations of the crack tips are marked in the figure. Note that the flashes on the top surface of the upper sheet near the tool shoulder indentation and the rises of the upper sheet material near the central hole due to the concave geometry of the tool shoulder are also observed in the figure. Note also that the effective thicknesses $t'_u = 0.83$ mm and $t'_l = 0.78$ mm are measured at the crack tips of the weld shown in Figure 6.14(a).

Figure 6.14(b) shows a close-up view of a three-dimensional finite element mesh near the dissimilar Al/Fe spot friction weld shown in Figure 6.14(a). For this finite element model, the effective length L ($= 100$ mm), the overlap length V ($= 30$ mm), the half width b ($= 15$ mm) and the weld diameter $2a$ ($= 9.7$ mm) are based on the dimensions of the dissimilar Al/Fe spot friction welds in lap-shear specimens and testing fixture of Tran and Pan [35]. The three-dimensional finite element model has 16,803 second-order solid elements. Two crack tips, marked as A and B in Figure 6.14(b), are also shown in the figure. In order to examine the effects of this complex

weld geometry of the Al/Fe spot friction weld, another three-dimensional finite element analysis for an equivalent spot weld joining an upper aluminum sheet of effective thickness t'_u ($= 0.83$ mm) and a lower steel sheet of effective thickness t'_l ($= 0.78$ mm) is conducted. Note that the effective thicknesses t'_u and t'_l are also used as the upper and lower sheet thicknesses in the analytical solutions.

Figure 6.14(c) shows the normalized J integral solutions as functions of θ for the Al/Fe spot friction weld shown in Figure 6.14(a), for the equivalent spot weld joining an aluminum sheet of $t'_u = 0.83$ mm and a steel sheet of $t'_l = 0.78$ mm based on our three-dimensional finite element computation, and the results based on the analytical solutions for the equivalent spot weld. In general, as indicated in Equation (6.18), the K_1 and K_2 solutions for an interface crack depend on the choice of a characteristic length. For convenient presentation, only the J integral solutions, which are independent of the choice of the characteristic length, for the Al/Fe spot friction weld are presented in Figures 6.14(c) and 6.15(b). The K_1 and K_2 solutions for the Al/Fe spot friction weld will be reported in Figure 6.16(b). Note that the J integral solutions shown in Figure 6.14(c) are normalized by the J integral solution at point B ($\theta = 180^\circ$) obtained from the finite element computation for the Al/Fe spot friction weld. As shown in the figure, the distributions of the J integral solution for the equivalent spot weld obtained from the analytical solutions and the finite element computation are quite similar. However, the distribution of the J integral solution for the Al/Fe spot friction weld is quite different from those for the equivalent spot weld based on the finite element computation and the analytical solutions. As shown in Figure 6.14(c), the maximum values of the J integral solutions for the equivalent

spot weld based on the finite element computation and the analytical solutions are located at point A ($\theta = 0^\circ$). In contrast, the maximum value of the J integral solution for the Al/Fe spot friction weld is located at point B ($\theta = 180^\circ$). As shown in Figure 6.14(c), the maximum values of the J integral solutions at point A ($\theta = 0^\circ$) based on the finite element computation and the analytical solutions for the equivalent spot weld are about 2.5 times of those at point B ($\theta = 180^\circ$). Also, the maximum value of the J integral solution at B ($\theta = 180^\circ$) for the Al/Fe spot friction weld is about 5 times of that at point A ($\theta = 0^\circ$) as shown in Figure 6.14(c). In summary, the complex weld geometry of the Al/Fe spot friction weld as shown in Figure 6.14(a) appears to strongly affect the fracture mechanics parameters for the crack front along the nugget circumference of the weld in the lap-shear specimen when compared to the analytical solutions for the weld with ideal geometry.

In order to investigate the effects of different features of the weld geometry of the Al/Fe spot friction weld shown in Figure 6.14(a) on the fracture mechanics parameters for the crack front along the nugget circumference of the weld in the lap-shear specimen in details, the finite element mesh shown in Figure 6.14(b) is modified into different meshes. First, the central hole due to the tool probe pin indentation is filled with aluminum until a thickness of t'_u . The J integral solutions obtained from the finite element computations based on the mesh shown in Figure 6.14(b) and the modified mesh with the filled central hole are nearly the same and are not reported here. The central hole therefore appears not to affect the stress intensity factor and J integral solutions for the crack front along the nugget circumference of the weld based on the finite element computations. Figure 6.15(a) shows different

three-dimensional finite element meshes for the Al/Fe spot friction welds in lap-shear specimens. The bold arrows in Figure 6.15(a) schematically show the resultant applied loads. In Figure 6.15(a), mesh A is used to model the Al/Fe spot friction weld based on the micrograph shown in Figure 6.14(a). Mesh B is used to examine the effects of the flashes on the top surface of the upper sheet near the tool shoulder circumference due to the expulsion of the upper sheet material resulting from the tool indentation, and the rises of the upper sheet material near the central hole due to the concave geometry of the tool shoulder. Mesh C is used to investigate the effects the gap between the upper and lower sheets. Mesh D is used to examine the effects of the bend of the upper and lower sheets near the weld. Mesh E is used to model an ideal or equivalent spot weld joining an aluminum sheet to a steel sheet in a lap-shear specimen with the effective thicknesses, t'_u and t'_l , and without any complex geometry to investigate only the effects of the non-uniform upper sheet thickness.

In Figure 6.15(a), the gap between the upper and lower sheets is represented by the parameter g ($= 0.267$ mm) between the top surface of the lower sheet and the bottom surface of the upper sheet where the lap-shear loads applied. Also, the bend of the sheets near the weld is represented by the offset distance e ($= 0.267$ mm) between the interfacial surface and the top surface of the lower sheet where the lap-shear load applied. As shown for meshes A and B, the loading directions are slightly inclined due to the realignment of the lap-shear specimen when mounted in the lap-shear testing fixture due to the presence of the gap between the upper and lower sheets. For meshes C, D and E, the loads are applied in the horizontal direction. For mesh C, the action line of the applied loads has an offset distance e with respect to

the interfacial surface. In meshes D and E, the action line of the lap-shear loads passes through the interfacial surface. Two crack tips, marked as crack tip A and crack tip B, are also shown in mesh A. Meshes A, B, C, D and E are then employed in other finite element analyses.

Figure 6.15(b) shows the normalized J integral solutions for the Al/Fe spot friction weld obtained from the finite element computations based on the meshes marked as A, B, C, D and E in Figure 6.15(a). The J integral solutions shown in Figure 6.15(b) are normalized by the J integral solution at point B ($\theta = 180^\circ$) obtained from the finite element computation based on mesh A. Mesh B is obtained from mesh A by removing the flashes and rises. As shown in Figure 6.15(b), the J integral solutions obtained from the finite element computation based on mesh B is nearly the same as those based on mesh A. Also, the maximum values of the J integral solution based on meshes A and B are located at point B ($\theta = 180^\circ$). The flashes on the top surface of the upper sheet and the rises of the upper sheet material in the nugget due to the indentation of the concave tool shoulder appear not to significantly affect the J integral solutions for the crack front along the nugget circumference of the Al/Fe spot friction weld in the lap-shear specimen. Therefore, the flashes are removed in meshes C and D as shown in Figure 6.15(a).

As shown in Figure 6.15(a), mesh C is obtained from mesh A by removing the flashes and by moving the parts of the upper sheet outside the weld a distance of g in the downward direction to fill the gap between the upper and lower sheets. As shown in Figure 6.15(b), the trends of the distributions of the J integral solutions obtained from the finite element computations based on mesh A and mesh C are quite similar.

However, the J integral solution at point A ($\theta = 0^\circ$) based on mesh C is about 45% larger than that based on mesh A, whereas the J integral solution at point B ($\theta = 180^\circ$) based on mesh C is about 38% smaller than that based on mesh A. Also, the maximum value of the J integral solution based on mesh C is located at point B ($\theta = 180^\circ$). As shown in Figure 6.15(b), the gap between the upper and lower sheets appears to strongly affect the J integral solutions for the crack front along the nugget circumference of the Al/Fe spot friction weld in the lap-shear specimen.

Mesh D in Figure 6.15(a) is used to investigate the effects of the bend near the weld, represented by the offset distance e between the interfacial surface and the top surface of the lower sheet where the lap-shear load applied. Mesh D is obtained from mesh C by straightening the upper and lower sheets outside the nugget circumference. As shown in Figure 6.15(b), the J integral solution at point A ($\theta = 0^\circ$) based on mesh D is about 83 % larger than that based on mesh C, whereas the J integral solution at point B ($\theta = 180^\circ$) based on mesh D is about 48% smaller than that based on mesh C. It should be noted that the maximum value of the J integral solution based on mesh D is located at point A ($\theta = 0^\circ$). As shown in Figure 6.15(b), the bend of the sheets near the weld appears to strongly affect the J integral solutions for the crack front along the nugget circumference of the Al/Fe spot friction weld in the lap-shear specimen.

As shown in mesh D, the upper sheet has a nominal thickness of $t_u = 1.3$ mm far away the weld nugget and an effective thickness $t'_u = 0.83$ mm at the crack tip of the weld. Not that the rises of the upper sheet material in the weld nugget appear not to affect the J integral solutions as discussed earlier. Mesh E in Figure 6.15(a) is used

to model an ideal spot weld without any complex geometry joining an aluminum sheet of $t'_u = 0.83$ mm and a steel sheet of $t'_l = 0.78$ mm to investigate only the effects of the non-uniform upper sheet thickness as shown in mesh D. As shown in Figure 6.15(b), the distribution of the J integral solutions obtained from the finite element computations based on mesh D and mesh E are similar. The deviation of the J integral solutions at point B ($\theta = 180^\circ$) based on mesh D and mesh E is most likely due to the non-uniform upper sheet thickness as shown in mesh D. In summary, as shown in Figure 6.15(b), among the complex features of the geometry of the Al/Fe spot friction weld, the gap and the bend are the two important geometric parameters that strongly affect the fracture mechanics parameters for the crack front along the nugget circumference of the Al/Fe spot friction weld in the lap-shear specimen.

As discussed earlier, the complex weld geometry of the Al/Fe spot friction can be mainly characterized by the gap and bend. Therefore, the analytical structural stress solutions developed in Section 6.3.2 for spot welds with gaps and bends in lap-shear specimens can be used to estimate the stress intensity factor K_1 , K_2 , K_3 and J integral solutions for the Al/Fe spot friction weld in the lap-shear specimen. Figure 6.16(a) shows the normalized J integral solutions for the Al/Fe spot friction weld and the equivalent spot weld based on the finite element computations and analytical solutions derived from the structural stress solutions for the spot weld with the gap and bend in the lap-shear specimen. The J integral solutions shown in Figure 6.16(a) are normalized by the J integral solution at point B ($\theta = 180^\circ$) obtained from the finite element computation based on mesh A. As shown in Figure 6.15(a) for mesh A, the upper sheet of the Al/Fe spot friction weld has a non-uniform thickness.

Therefore, both nominal sheet thicknesses ($t_u = 1.28$ mm, $t_l = 0.8$ mm) and effective sheet thicknesses ($t'_u = 0.83$ mm, $t'_l = 0.78$ mm) are used in the analytical solutions. As shown in Figure 6.16(a), the trends of the distributions of the J integral solutions obtained from the finite element computation and the analytical solutions with consideration of the gap and bend are quite similar. The analytical solutions predicted very well the critical location where the maximum value of the J integral solution is located. As shown in Figure 6.16(a), the J integral solution at point B ($\theta = 180^\circ$) obtained from analytical solutions with consideration of the gap and bend employed the nominal sheet thicknesses is about 84% of that obtained from the finite element computation. Therefore, the analytical solutions developed for the spot weld with the gap and bend in the lap-shear specimen may be used to approximately obtain the J integral solutions for the crack front along the nugget circumference of the Al/Fe spot friction weld in the lap-shear specimen.

Figure 6.16(b) shows the normalized K_1 , K_2 and K_3 solutions as functions of θ for the Al/Fe spot friction weld based on the finite element computation and the analytical solutions. Figure 6.16(c) shows the in-plane phase angle ω , defined in Equation (6.25), as a function of θ for the Al/Fe spot friction weld based on the finite element computation and the analytical solutions. Note that the K_1 , K_2 and K_3 solutions shown in Figure 6.16(b) are normalized by the K_1 solution at point B ($\theta = 180^\circ$) obtained from the finite element computation for the Al/Fe spot friction weld. It should also be noted that the analytical solutions shown in Figures 6.16(b) and 6.16(c) are based on the structural stress solutions for spot welds with the gap and bend in lap-shear specimen as developed in Section 6.3 and the nominal sheet

thicknesses. As shown in Figure 6.16(b), based on the finite element computation and the analytical solutions, the maximum values of the K_1 and K_2 solutions are located at point B ($\theta = 180^\circ$). Based on the finite element computation, the K_1 solution at point B ($\theta = 180^\circ$) is about 4 times of the K_2 solution. The results in Figure 6.16(b) also indicate that K_1 is the dominant stress intensity factor at point B ($\theta = 180^\circ$) for the Al/Fe spot friction weld in the lap-shear specimen. As shown in Figures 6.16(b) and 6.16(c), the general trends for the K_1 , K_2 , K_3 solutions and the phase angle ω based on the analytical solutions and the finite element computation are quite similar. However, the values of K_1 , K_2 and ω at point A ($\theta = 0^\circ$) and point B ($\theta = 180^\circ$) based on the analytical solutions and the finite element computation are different. The deviation of the results obtained from the finite element computation and the analytical solutions is most likely due to the effects of the other features of the complex weld geometry and the assumptions of the strip model with the spot weld idealized as a rigid inclusion as discussed later. However, the analytical results shown in Figure 6.16 can identify the important geometric parameters that strongly affect the fracture mechanics parameters for the crack front along the nugget circumference of the Al/Fe spot friction weld.

6.7. Discussions

It should be noted that the stress intensity factor solutions shown in Figures 6.10(c), 6.10(d), 6.11(c), 6.11(d) and 6.11(e) are normalized by the same value and the J integral solutions shown in Figures 6.10(e) and 6.11(f) are normalized by the same value for the purpose of comparison. As shown in these figures, the maximum

values of the stress intensity factor and J integral solutions for the spot welds with ideal geometry are located at point A ($\theta = 0^\circ$) and/or point B ($\theta = 180^\circ$). Therefore, the effects of the Young moduli, E_u and E_l , and thicknesses, t_u and t_l , of the upper (u) and lower (l) sheets on the stress intensity factor and J integral solutions at point A ($\theta = 0^\circ$) and point B ($\theta = 180^\circ$) are discussed here based on the results obtained from the finite element computations and the analytical solutions as shown in Figures 6.10 and 6.11.

As shown in Figure 6.10(c) for the Fe/Fe-0.65/0.65 weld and in Figure 6.10(d) for the Al/Fe-0.65/0.65 weld, and as shown in Figure 6.11(c) for the Fe/Fe-0.65/1.30 weld and in Figure 6.11(d) for the Al/Fe-0.65/1.30 weld, when E_u decreases, the K_1 and K_2 solutions at point A ($\theta = 0^\circ$) increase, while the K_1 and K_2 solutions at point B ($\theta = 180^\circ$) decrease. As shown in Figures 6.10(e) and 6.11(f), when E_u decreases, the J integral solution at point A ($\theta = 0^\circ$) significantly increases, while the J integral solution at point B ($\theta = 180^\circ$) does not change significantly. Similarly, as shown in Figure 6.11(c) for the Fe/Fe-0.65/1.30 weld and in Figure 6.11(e) for the Fe/Al-0.65/1.30 weld, when E_l decreases, the K_1 and K_2 solutions at point A ($\theta = 0^\circ$) decrease, while the K_1 and K_2 solutions at point B ($\theta = 180^\circ$) slightly increase. As shown in Figure 6.11(f), when E_l decreases, the J integral solution at point A ($\theta = 0^\circ$) slightly increases, while the J integral solution at point B ($\theta = 180^\circ$) does not change significantly.

As shown in Figure 6.10(c) for the Fe/Fe-0.65/0.65 weld and in Fig.11(c) for the Fe/Fe-0.65/1.30 weld, and as shown in Figure 6.10(d) for the Al/Fe-0.65/0.65 weld

and in Figure 6.11(d) for the Al/Fe-0.65/1.30 weld, when t_l increases, the K_1 and K_2 solutions at point A ($\theta = 0^\circ$) are nearly the same, while the K_1 and K_2 solutions at point B ($\theta = 180^\circ$) significantly decrease. As shown in Figures 6.10(e) and 6.11(f), when t_l increases, the J integral solutions at point A ($\theta = 0^\circ$) are nearly the same, while the J integral solutions at point B ($\theta = 180^\circ$) significantly decrease. By simply rotating the finite element model shown in Figure 6.11 by an angle 180° around the y axis, it can be seen that when t_u increases, the K_1 , K_2 and J integral solutions at point A ($\theta = 0^\circ$) significantly decrease, while the K_1 , K_2 and J integral solutions at point B ($\theta = 180^\circ$) are nearly the same. The differences in the J integral solutions for the Al/Fe-0.65/1.30 and Fe/Al-0.65/1.30 welds as shown in Figure 6.11(f) are due to the combined effects of the Young modulus and the sheet thickness.

In summary, for spot welds in lap-shear specimens where the lap-shear loads apply on the upper right leg and the lower left leg of the specimen, point A and point B denote for the crack tips on the right side and the left side, respectively, on the cross section along the symmetry plane of the welds. Based on the results obtained from the theoretical and numerical models, the K_1 and K_2 solutions at point A increase when t_u decreases, E_u decreases and E_l increases. The K_1 and K_2 solutions at point B increase when t_l decreases, E_u increases and E_l decreases. Also, the J integral solution at point A increases when E_u and t_u decrease, and appears not to be significantly sensitive to the change of E_l and t_l . Similarly, the J integral solution at point B increases when E_l and t_l decrease, and appears not to be significantly sensitive to the change of E_u and t_u .

It should be noted that the analytical stress intensity factor and J integral solutions for spot welds with ideal geometry joining two sheets of different materials and thicknesses as listed in the previous sections are complicated and lengthy in nature. For engineering applications, it may be preferred to approximately obtain the stress intensity factor and J integral solutions at point A and point B based on simple formulae. Here, we attempt to approximate the stress intensity factor and J integral solutions at point A and point B for spot welds with ideal geometry joining two sheets of different materials and thicknesses based on the K_I , K_{II} and J integral solutions at point A and point B or spot welds with ideal geometry joining two sheets of identical material and equal thickness as shown in Equations (6.44), (6.45) and (6.6) with $\theta = 0^\circ$ and $\theta = 180^\circ$, respectively. The K_I , K_{II} and J integral solutions at point A for the $E/E - t_u/t_l$ weld (joining two sheets of Young modulus E and thicknesses t_u and t_l) can be approximated as the K_I , K_{II} and J integral solutions at point A, respectively, for the $E/E - t_u/t_u$ weld (joining two sheets of Young modulus E and equal thickness t_u). Similarly, the K_I , K_{II} and J integral solutions at point B for the $E/E - t_u/t_l$ weld can be approximated as the K_I , K_{II} and J integral solutions at point B, respectively, for the $E/E - t_l/t_l$ weld (joining two sheets of Young modulus E and equal thickness t_l). The J integral solution at point A for the $E_u/E_l - t_u/t_l$ weld (joining two sheets of Young moduli, E_u and E_l , and thicknesses, t_u and t_l) can be approximated as the J integral solution at point A for the $E_u/E_u - t_u/t_u$ weld (joining two sheets of Young modulus E_u and equal thickness t_u).

Similarly, the J integral solution at point B for the $E_u/E_l - t_u/t_l$ weld can be approximated as the J integral solution at point B for the $E_l/E_l - t_l/t_l$ weld (joining two sheets of Young modulus E_l and equal thickness t_l). These approximations of the stress intensity factor and J integral solutions at point A and point B appear to be plausible since the upper right leg and lower left leg of the lap-shear specimen with a spot weld are the main load-carrying parts. Finally, for the $E_u/E_l - t_u/t_l$ weld with $E_u \leq E_l$ (or similarly with $E_u \geq E_l$), it is recommended to select the sheet thicknesses t_u and t_l such that $t_u \geq t_l$ (or similarly with $t_u \leq t_l$) to minimize the maximum values of the K_1 , K_2 and J integral solutions.

As discussed earlier, the numerical results obtained from the three-dimensional finite element computations for spot welds with ideal geometry in lap-shear specimens confirm the accuracy of the analytical stress intensity factor and J integral solutions for spot welds joining two sheets of similar or dissimilar sheet materials with equal or different thicknesses. As discussed earlier, the numerical results obtained from the finite element computations indicate that the complex weld geometries of the aluminum 6111 resistance spot weld and aluminum 5754 spot friction weld appear not to affect the stress intensity factor and J integral solutions for the crack fronts along the nugget circumferences of the welds in lap-shear specimens when compared to the analytical solutions for the welds with ideal geometry. However, the numerical results obtained from the finite element computations indicate that the complex weld geometry, gap and bend of the Al/Fe spot friction weld appear to strongly affect the stress intensity factor and J integral

solutions for the crack front along the nugget circumference of the weld in the lap-shear specimen when compared to the analytical solutions for the weld with ideal geometry.

It should be noted that the analytical stress intensity factor and J integral solutions developed in this investigation are based on the new closed-form structural stress solutions for a rigid inclusion in a finite square plate subjected to a lap-shear load and a coach-peel load developed in Lin and Pan [18]. However, for welds in automotive structural components under complex loading conditions, the deformation of the weld may deviate from that of a rigid inclusion. In this case, the structural stresses based on the rigid inclusion assumption may not give accurate stress intensity factor and J integral solutions for the crack fronts along the nugget circumferences of the welds (Lin et al. [16]; Lin and Pan [18]). It should be noted that based on the computational results, portions of the sheets along the nugget circumferences in lap-shear specimens contact each other under loading conditions. As in Lin and Pan [18], contact is not considered in both analytical and finite element analyses in this investigation. Therefore, negative values of the K_I (and K_{II}) solutions were seen in some results reported earlier.

It should be noted that the effective sheet thicknesses t'_u and t'_l were employed in the analytical solutions for the spot friction welds shown in Figures 6.13(d) and 6.14(c). In general, the analytical solutions based on the nominal sheet thicknesses t_u and t_l should also be considered since the upper sheet thickness is non-uniform. In this investigation, the analytical solutions employed the nominal sheet thicknesses t_u and t_l for aluminum 6111 resistance spot weld and aluminum 5754 spot friction

weld are not presented due to the fact that results are quite similar. Based on the numerical and analytical results reported in this investigation, for the given pair of upper and lower sheets of nominal thicknesses t_u and t_l used to make the spot friction welds, the welds with the larger effective thicknesses, t'_u and t'_l , and a larger weld diameter D_c will have smaller stress intensity factor solutions at the critical locations of the welds. Consequently, these welds will have better performance in term of fatigue lives. As discussed in Tran et al. [44], the effective thicknesses t'_u and t'_l will be larger for spot friction welds made at shorter processing times. However, the failure load of the spot friction weld increases when the processing time increases due to a larger weld diameter D_c . This remark may be useful for the selection of the optimal processing parameters for strength and fatigue failure of spot friction welds. Also, the gap and bend should be minimized to avoid the negative effects on the fracture mechanics parameters for the welds under lap-shear loading conditions.

It should be noted that lap-shear specimens are commonly used to investigate the mechanical behavior of spot welds under shear dominant loading conditions. Note that the maximum values of the K_1 , K_2 and J integral solutions obtained from the finite element computation for the Al/Fe spot friction weld are located at point B ($\theta=180^\circ$) as shown in Figure 6.16. Also, the numerical results shown in Figure 6.16(b) indicate that the Al/Fe spot friction weld in the lap-shear specimen is under mode I dominant loading conditions at point B ($\theta=180^\circ$). The mode I dominant loading condition for the Al/Fe spot friction weld in the lap-shear specimen is due to

the complex geometry, gap and bend of the Al/Fe spot friction weld as discussed earlier. As shown in Tran and Pan [35], the fatigue crack initiating at the crack tip marked as point B ($\theta = 180^\circ$) and propagating along the interfacial surface between the aluminum and steel sheets appears to be the dominant fatigue crack that caused the final failure of the Al/Fe spot friction welds in lap-shear specimens under cyclic loading conditions. The agreement between the numerical results and the experimental observation for the Al/Fe spot friction weld suggests that the stress intensity factor and J integral solutions at the critical locations of the Al/Fe spot friction welds may be used as appropriate parameters to correlate the experimental fatigue data for the Al/Fe spot friction welds in different types of specimens (Tran and Pan [35]). Further investigation is needed to fully understand the effects of the Al/Fe spot friction weld geometry and the loading conditions on the fracture mechanics parameters for the weld.

6.8. Conclusions

In this paper, the effects of weld geometry and sheet thickness on the fracture mechanics parameters for the crack fronts along the nugget circumferences of resistance spot welds and spot friction welds between similar and dissimilar sheet materials in lap-shear specimens are investigated based on a combined theoretical and numerical approach. The analytical stress intensity factor and J integral solutions for spot welds with ideal geometry, gap and bend joining two sheets of different materials and thicknesses in lap-shear specimens are first developed based on the strip model and the new structural stress solutions for a rigid inclusion in a finite square

plate subjected to a lap-shear load and a coach-peel load (Lin and Pan [18]). The numerical results obtained from the three-dimensional finite element analyses for spot welds with ideal geometry in lap-shear specimens are then used to validate the accuracy of the analytical solutions. Three-dimensional finite element models based on the micrographs of the cross sections along the symmetry planes of an aluminum 6111 resistance spot weld, an aluminum 5754 spot friction weld, and a dissimilar Al/Fe spot friction weld are conducted to obtain accurate stress intensity factor and J integral solutions for the crack fronts along the nugget circumferences of these welds under lap-shear loading conditions. The numerical results indicate that the complex weld geometries of the aluminum 6111 resistance spot weld and aluminum 5754 spot friction weld appear not to affect the stress intensity factor and J integral solutions when compared to the analytical solutions for the welds with ideal geometry. However, the complex weld geometry of the Al/Fe spot friction weld appears to strongly affect the stress intensity factor and J integral solutions when compared to the analytical solutions for the weld with ideal geometry. The numerical results indicate that the gap between the upper and lower sheets and the bend near the weld are the important geometric parameters that strongly affect the fracture mechanics parameters for the Al/Fe spot friction weld in the lap-shear specimen. The analytical stress intensity factor and J integral solutions for spot welds with the gap and bend agree with the results obtained from the three-dimensional finite element computation for the Al/Fe spot friction weld under lap-shear loading conditions. Finally, the results obtained from the theoretical and numerical analyses and the experimental observations are correlated.

Appendix B

The expressions for the factors a_j and b_j ($j = 1, 2, 3, 4$) given in Equations (6.22) and (6.23) are (Zhang [39])

$$a_1 = \frac{\cosh(\pi\varepsilon)\sqrt{t_u}}{2\sqrt{3(1+\eta)(1+4\eta\delta+6\eta\delta^2+3\eta\delta^3)}(1+\tan^2\omega)} \times \left[\frac{(1+4\eta\delta+9\eta\delta^2+6\eta\delta^3)\tan\omega}{\sqrt{1+2\eta\delta(2+3\delta+2\delta^2)+\eta^2\delta^4}} - \sqrt{3} \right] \quad (\text{B.1})$$

$$a_2 = -\frac{\cosh(\pi\varepsilon)\sqrt{t_u}}{2\sqrt{3(1+\eta)(1+4\eta\delta+6\eta\delta^2+3\eta\delta^3)}(1+\tan^2\omega)} \times \left[\frac{(1+4\eta\delta+3\eta\delta^2)\tan\omega}{\sqrt{1+2\eta\delta(2+3\delta+2\delta^2)+\eta^2\delta^4}} + \sqrt{3} \right] \quad (\text{B.2})$$

$$a_3 = \eta \frac{\cosh(\pi\varepsilon)\sqrt{t_u}}{2\sqrt{3(1+\eta)(1+4\eta\delta+6\eta\delta^2+3\eta\delta^3)}(1+\tan^2\omega)} \times \left[\frac{\delta(1-2\eta\delta-3\eta\delta^2)\tan\omega}{\sqrt{1+2\eta\delta(2+3\delta+2\delta^2)+\eta^2\delta^4}} + \sqrt{3}(2+\delta) \right] \quad (\text{B.3})$$

$$a_4 = -\eta\delta \frac{\cosh(\pi\varepsilon)\sqrt{t_u}}{2\sqrt{3(1+\eta)(1+4\eta\delta+6\eta\delta^2+3\eta\delta^3)}(1+\tan^2\omega)} \times \left[\frac{(1+4\eta\delta+3\eta\delta^2)\tan\omega}{\sqrt{1+2\eta\delta(2+3\delta+2\delta^2)+\eta^2\delta^4}} + \sqrt{3} \right] \quad (\text{B.4})$$

$$b_1 = \frac{\cosh(\pi\varepsilon)\sqrt{t_u}}{2\sqrt{3(1+\eta)(1+4\eta\delta+6\eta\delta^2+3\eta\delta^3)}(1+\tan^2\omega)} \times \left[\frac{(1+4\eta\delta+9\eta\delta^2+6\eta\delta^3)}{\sqrt{1+2\eta\delta(2+3\delta+2\delta^2)+\eta^2\delta^4}} + \sqrt{3}\tan\omega \right] \quad (\text{B.5})$$

$$b_2 = -\frac{\cosh(\pi\varepsilon)\sqrt{t_u}}{2\sqrt{3(1+\eta)(1+4\eta\delta+6\eta\delta^2+3\eta\delta^3)}(1+\tan^2\omega)} \times \left[\frac{(1+4\eta\delta+3\eta\delta^2)}{\sqrt{1+2\eta\delta(2+3\delta+2\delta^2)+\eta^2\delta^4}} - \sqrt{3}\tan\omega \right] \quad (\text{B.6})$$

$$b_3 = \eta \frac{\cosh(\pi\varepsilon)\sqrt{t_u}}{2\sqrt{3(1+\eta)(1+4\eta\delta+6\eta\delta^2+3\eta\delta^3)}(1+\tan^2\omega)} \times \left[\frac{\delta(1-2\eta\delta-3\eta\delta^2)}{\sqrt{1+2\eta\delta(2+3\delta+2\delta^2)+\eta^2\delta^4}} - \sqrt{3}(2+\delta)\tan\omega \right] \quad (\text{B.7})$$

$$b_4 = -\eta\delta \frac{\cosh(\pi\varepsilon)\sqrt{t_u}}{2\sqrt{3(1+\eta)(1+4\eta\delta+6\eta\delta^2+3\eta\delta^3)}(1+\tan^2\omega)} \times \left[\frac{(1+4\eta\delta+3\eta\delta^2)}{\sqrt{1+2\eta\delta(2+3\delta+2\delta^2)+\eta^2\delta^4}} - \sqrt{3}\tan\omega \right] \quad (\text{B.8})$$

Note that the expressions shown in Equations (B.1)-(B.8) are for the case of $\delta \leq 1$. If $\delta > 1$, one should rotate the strip model shown in Figure 6.9(b) by an angle of 180° to represent the same physical system but with $\delta < 1$. It should also be noted the factors a_j and b_j ($j = 1, 2, 3, 4$) are functions of η , δ , ε , t_u and ω . Here, the parameter ω is a function of the material properties and δ . The parameter ω is obtained from numerical calculations and can be found in the Appendices of Suo and Hutchinson [40] and Zhang [39].

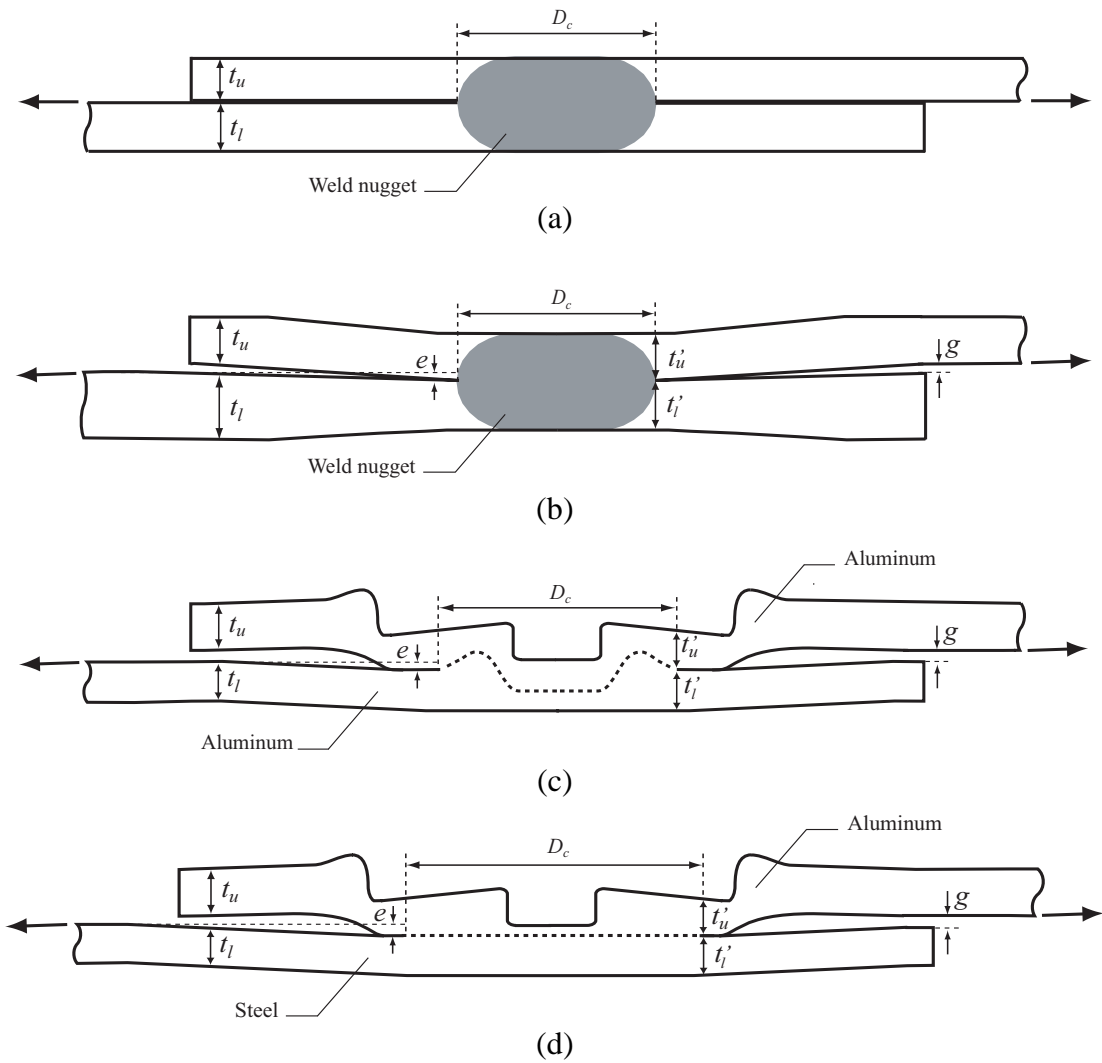


Figure 6.1 Schematic plots of (a) a spot weld with ideal geometry, (b) a resistance spot weld with electrode indentation, gap and bend, (c) an aluminum spot friction weld with complex geometry, gap and bend, (d) a dissimilar Al/Fe spot friction weld with complex geometry, gap and bend under lap-shear loading conditions.

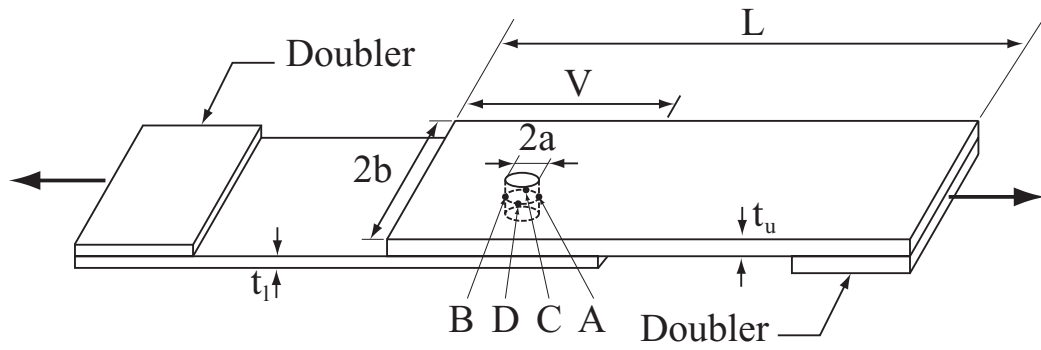


Figure 6.2 A schematic plot of a lap-shear specimen with a spot weld idealized as a circular cylinder under the resultant applied forces shown as the bold arrows.

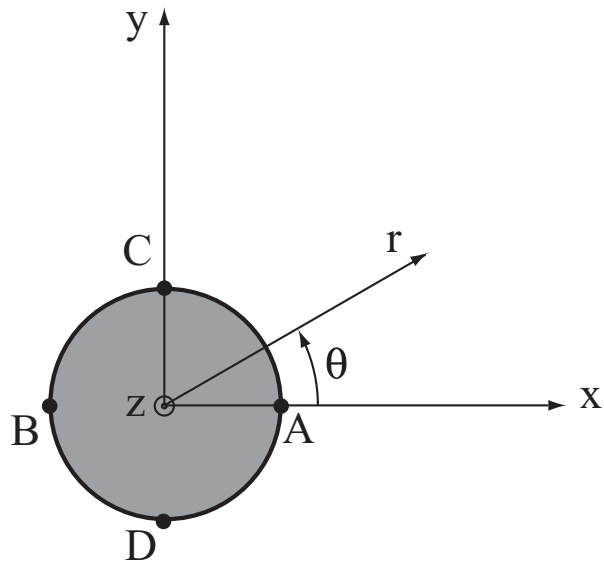


Figure 6.3 A schematic plot of a top view of the weld nugget (modeled as a rigid inclusion) in the upper sheet of the spot weld specimen with the cylindrical and Cartesian coordinate systems centered at the center of the upper half of the weld nugget.

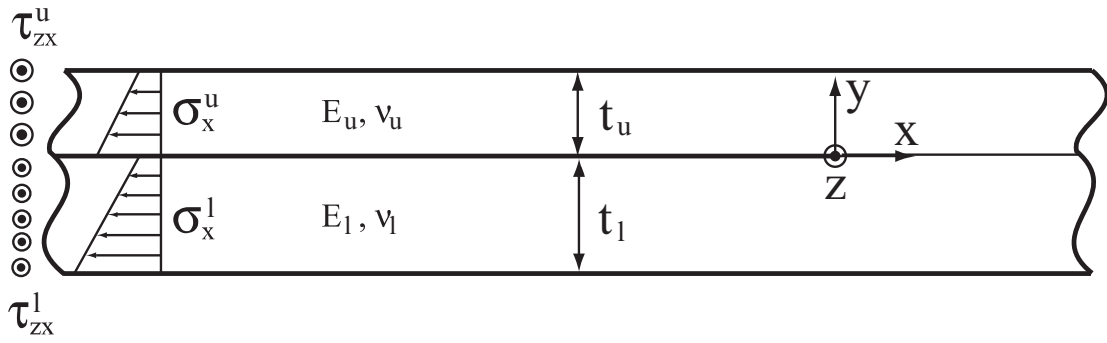


Figure 6.4 A two-dimensional model of two infinite strips made of different materials and thicknesses with the connection under plane strain loading conditions.

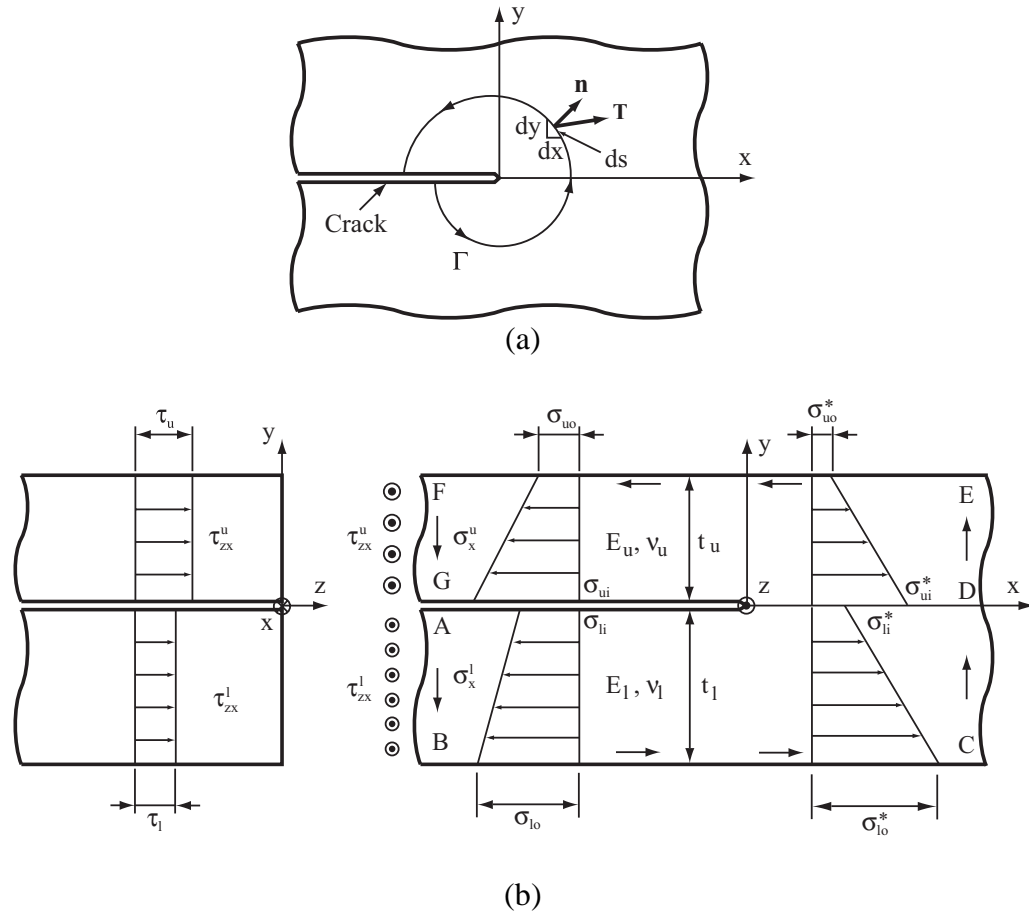


Figure 6.5 (a) A crack with contour Γ surrounding a crack tip, (b) the front and side views of the left half of the strip model. The normal stresses σ_{ui} , σ_{uo} , σ_{li} and σ_{lo} represent the normal stresses for line \overline{FG} and line \overline{AB} , the normal stresses σ_{ui}^* , σ_{uo}^* , σ_{li}^* and σ_{lo}^* represent the normal stresses for line \overline{DE} and line \overline{CD} at the inner (*i*) and outer (*o*) surfaces of the upper (*u*) and lower (*l*) strips, respectively. The shear stresses τ_u and τ_l represent the shear stress τ_{zx}^u of the upper (*u*) and lower (*l*) strips for line \overline{FG} and line \overline{AB} , respectively. The outside boundary line $\overline{ABCDEFG}$ is considered as the contour Γ for the *J* integral.

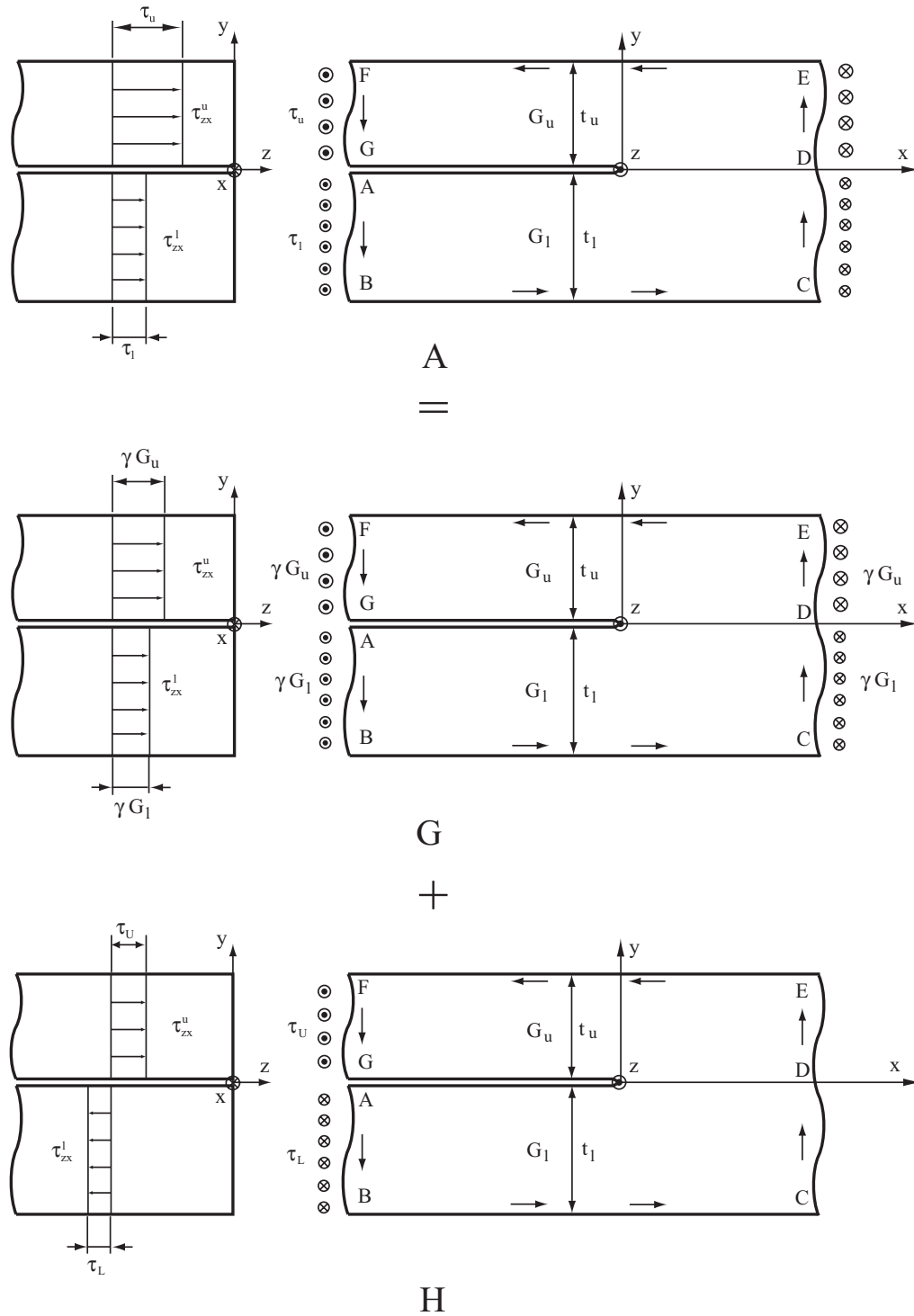
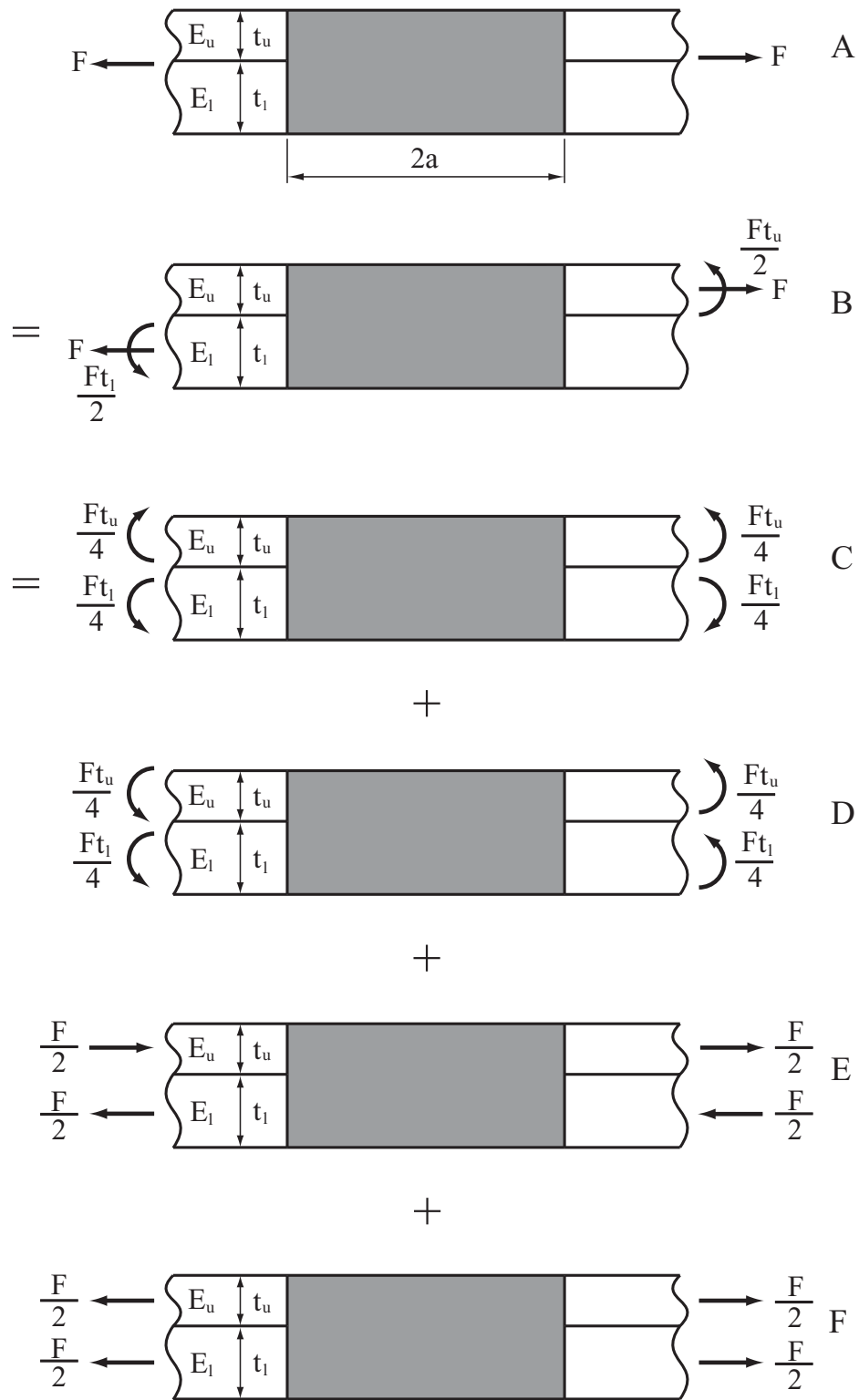


Figure 6.6 The decomposition process of the general out-of-plane shear stress distribution of a strip model. Model A represents a spot weld under general out-of-plane shear loading conditions. The general out-of-plane shear loading conditions of model A are decomposed into the two loading conditions shown in models G and H.



(a)

(to be continued on the next page)

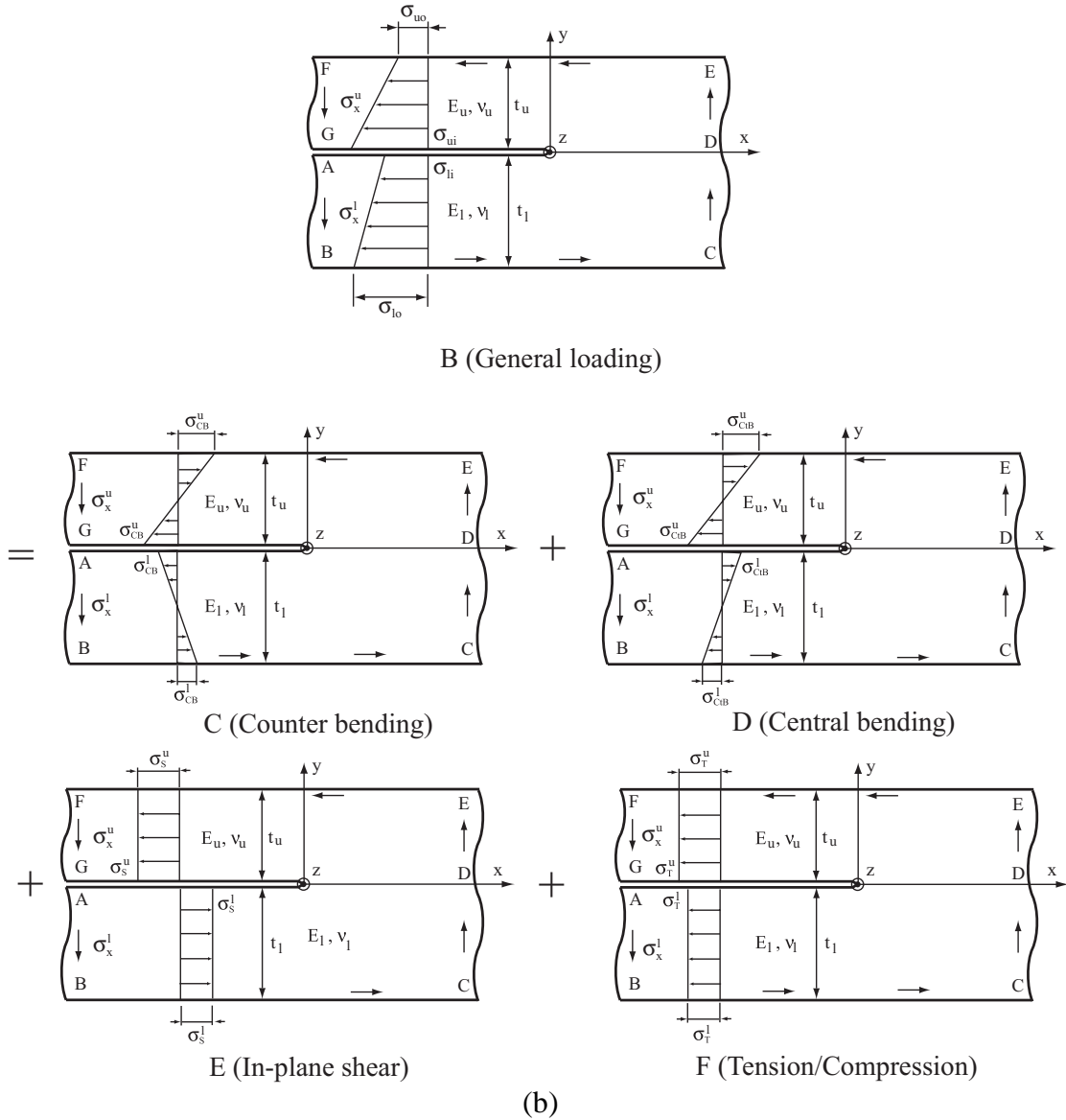
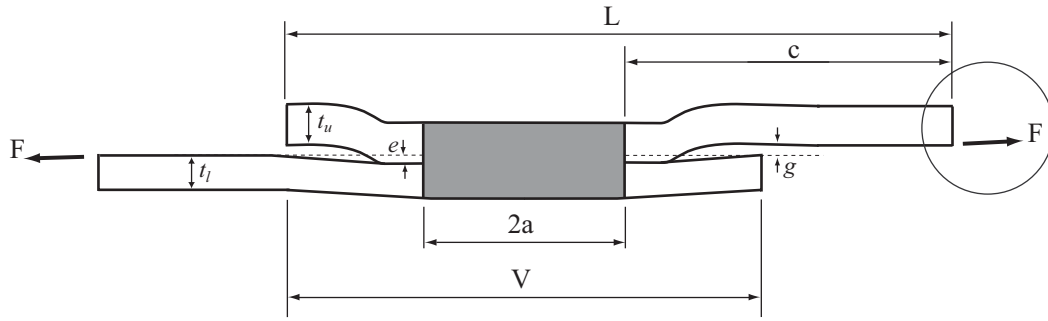


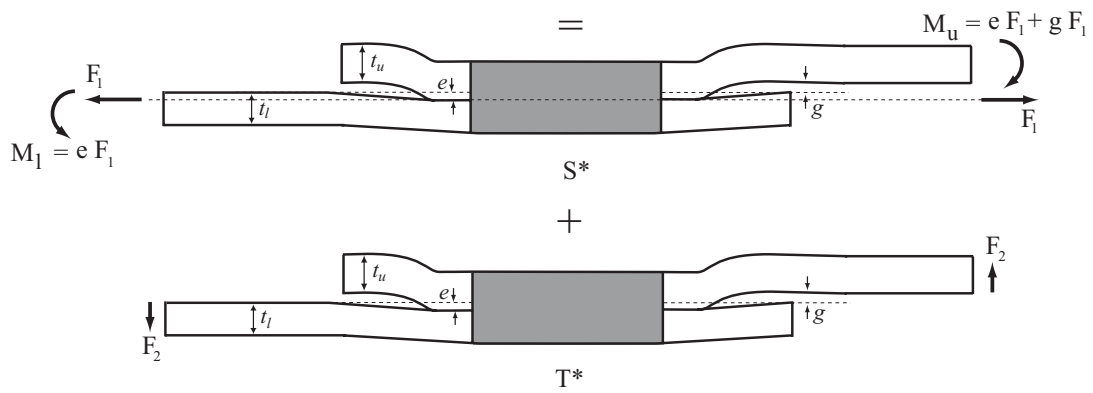
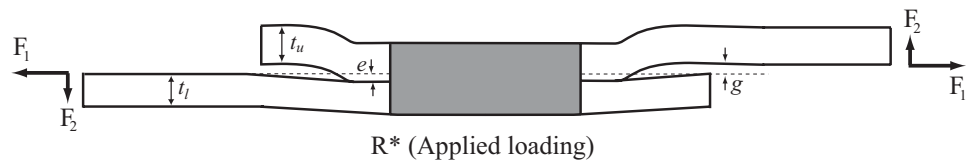
Figure 6.7 (a) The decomposition process of the lap-shear loading condition of a lap-shear specimen, (b) the decomposition process of the general normal structural stress distributions of a strip model. The gray-shaded areas represent the rigid inclusions. Model A represents a spot weld under lap-shear loading conditions. Model B represents a spot weld under an equivalent loading condition of model A. The forces, moments and general distributions of the normal structural stress of model B are decomposed into four simple loading conditions: counter bending, central bending, shear, and tension, marked as models C, D, E, and F, respectively.



(a)

$$\phi = \frac{g}{2L-V}$$

(b)



(c)

(to be continued on the next page)

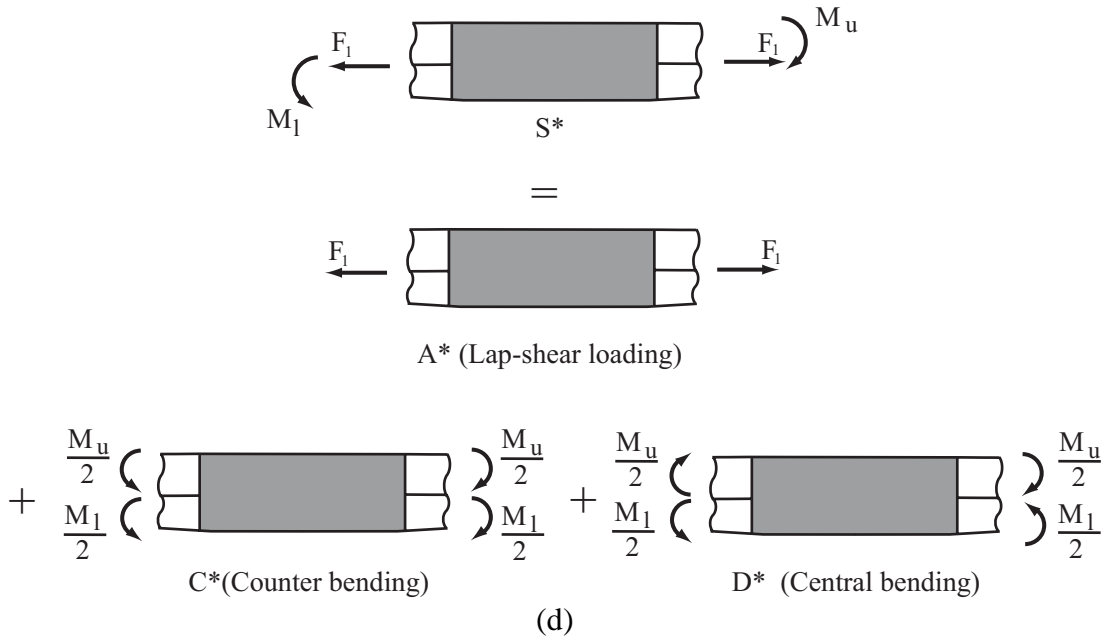


Figure 6.8 (a) A schematic plot of a spot weld with a gap and a bend in a lap-shear specimen under the applied forces F marked as the bold arrows, (b) a schematic plot of the applied loading condition near the right edge surface of the specimen, (c) the decomposition process of the loading conditions for the spot weld with the gap and bend in a lap-shear specimen, (d) the decomposition process of the general lap-shear loading conditions. Model R* represents a spot weld with the gap and bend in a lap-shear specimen under the applied forces of F_1 and F_2 . The forces in model R* are decomposed into the two loading conditions as shown in models S* and T*. The forces and moments in model S* are decomposed into three simple loading conditions: lap-shear loading, counter bending and central bending, marked as models A*, C* and D*, respectively.

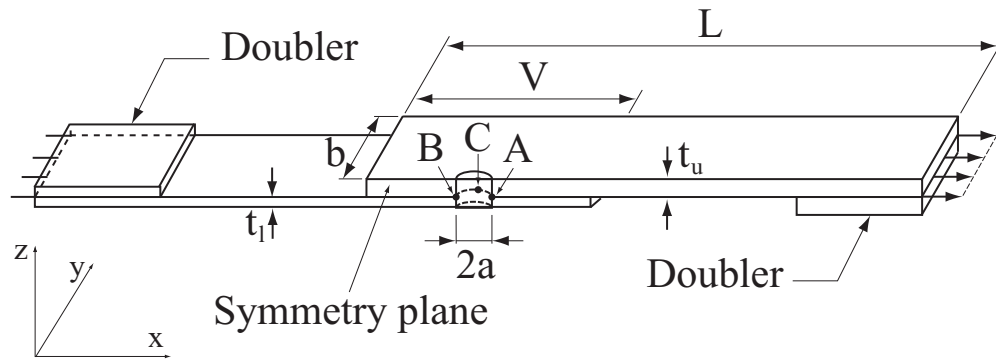
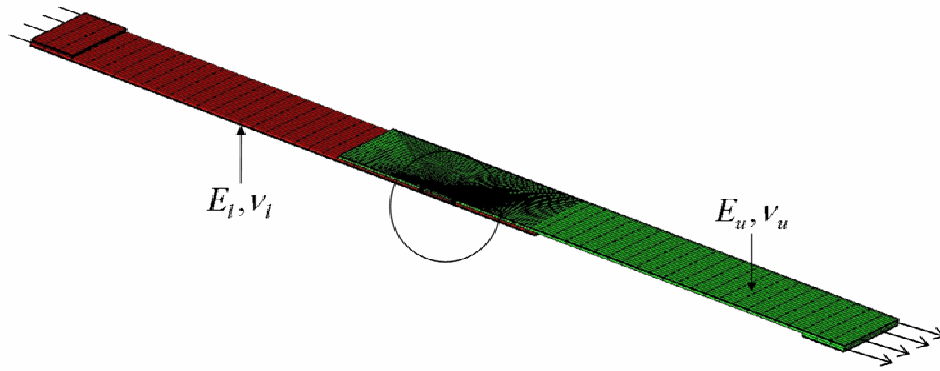
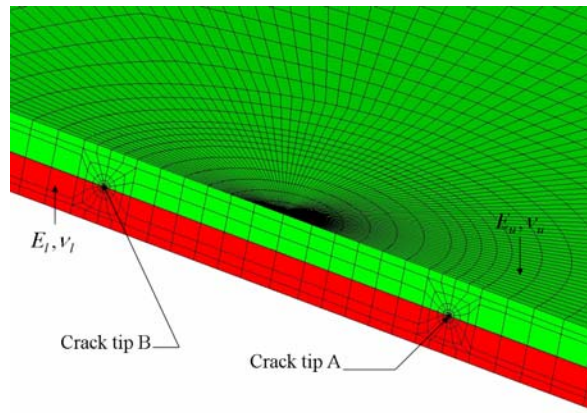


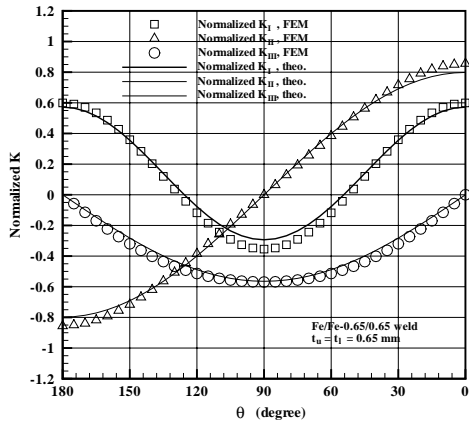
Figure 6.9 A schematic plot of a half of a lap-shear specimen with a spot weld and the boundary conditions employed in the finite element models.



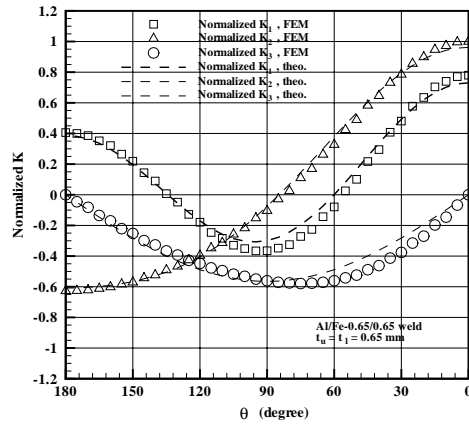
(a)



(b)

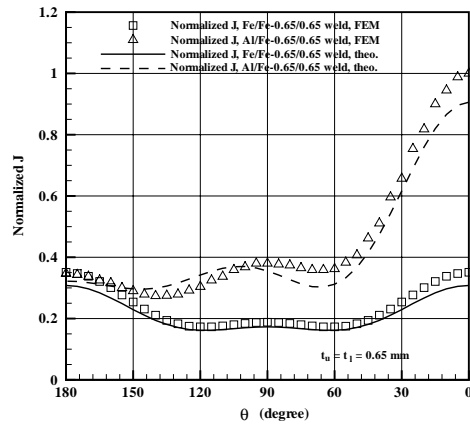


(c)



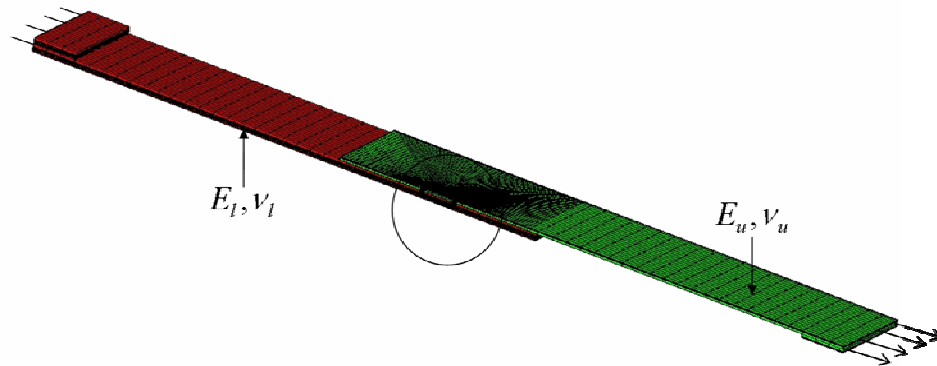
(d)

(to be continued on the next page)

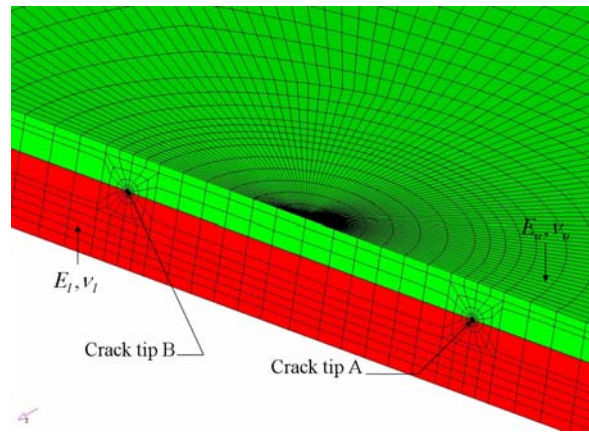


(e)

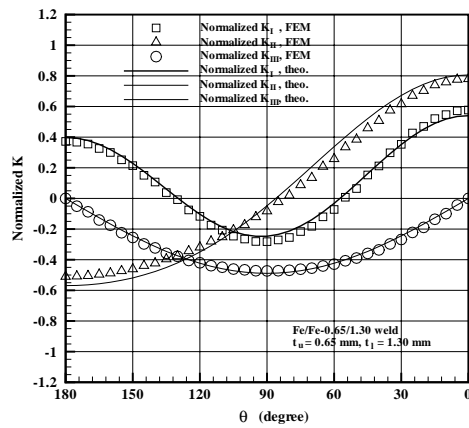
Figure 6.10 (a) A three-dimensional finite element mesh for a half of a lap-shear specimen with a spot weld joining two sheets of equal thickness of $t_u = t_l = 0.65 \text{ mm}$, (b) a close-up view of the mesh near the weld, (c) the normalized K_I , K_{II} and K_{III} solutions as functions of θ for the crack front along the nugget circumference of the Fe/Fe-0.65/0.65 weld, (d) the normalized K_1 , K_2 and K_3 solutions as functions of θ for the crack front along the nugget circumference of the Al/Fe-0.65/0.65 weld, (e) the normalized J integral solutions as functions of θ for the crack fronts along the nugget circumferences of the Fe/Fe-0.65/0.65 weld and the Al/Fe-0.65/0.65 weld.



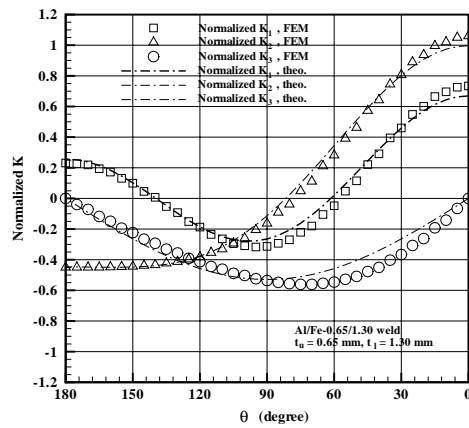
(a)



(b)

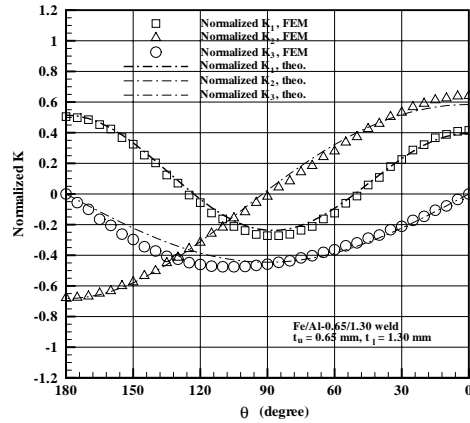


(c)

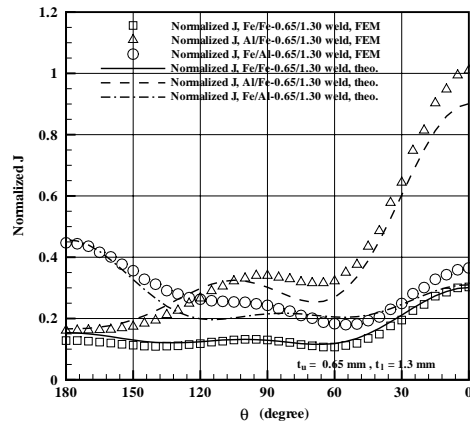


(d)

(to be continued on the next page)

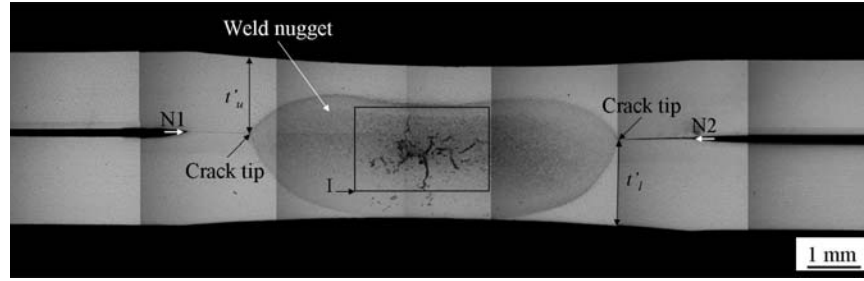


(e)

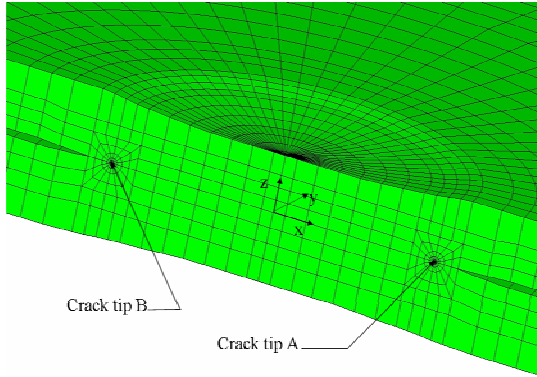


(f)

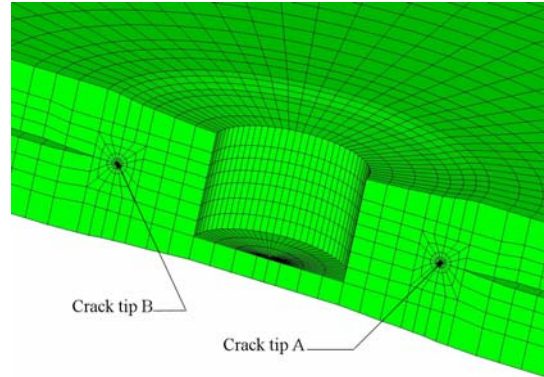
Figure 6.11 (a) A three-dimensional finite element mesh for a half of a lap-shear specimen with a spot weld joining two sheets of thicknesses $t_u = 0.65$ mm and $t_l = 1.3$ mm, (b) a close-up view of the mesh near the weld, (c) the normalized K_I , K_{II} and K_{III} solutions as functions of θ for the crack front along the nugget circumference of the Fe/Fe-0.65/1.30 weld, (d) the normalized K_1 , K_2 and K_3 solutions as functions of θ for the crack front along the nugget circumference of the Al/Fe-0.65/1.30 weld, (e) the normalized K_1 , K_2 and K_3 solutions as functions of θ for the crack front along the nugget circumference of the Fe/Al-0.65/1.30 weld, (f) the normalized J integral solutions as functions of θ for the crack fronts along the nugget circumferences of the Fe/Fe-0.65/1.30 weld, the Al/Fe-0.65/1.30 weld and the Fe/Al-0.65/1.30 weld.



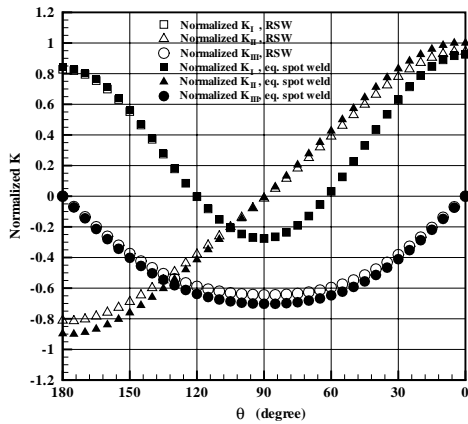
(a)



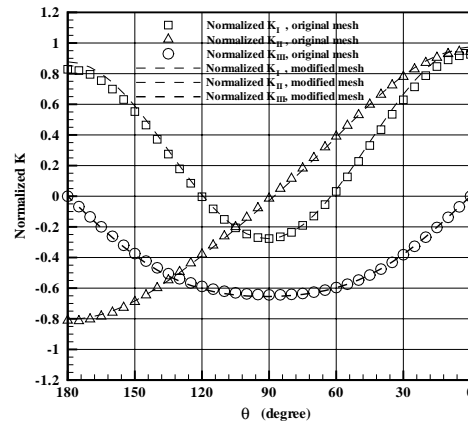
(b)



(d)

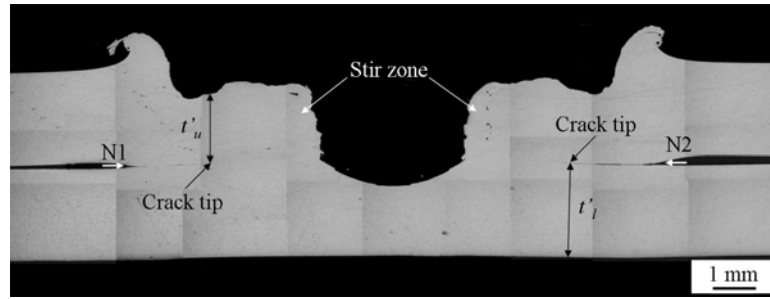


(c)

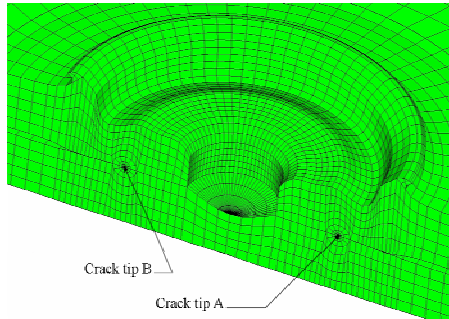


(e)

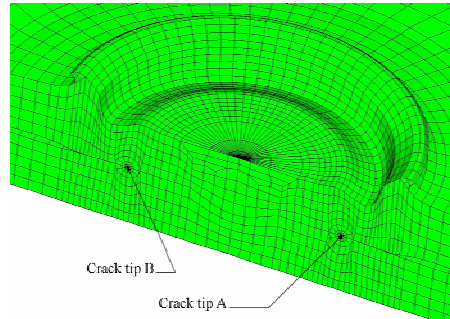
Figure 6.12 (a) An optical micrograph of the cross section along the symmetry plane of an aluminum 6111 resistance spot weld before testing, (b) a close-up view of a three-dimensional finite element mesh near the weld, (c) the normalized K_I , K_{II} and K_{III} solutions as functions of θ for the aluminum 6111 resistance spot weld and for the equivalent spot weld joining two aluminum sheets of $t'_u = 1.3$ mm and $t_l = 1.5$ mm based on the finite element computations, (d) a close-up view of a modified finite element mesh near the weld, (e) the normalized K_I , K_{II} and K_{III} solutions obtained from the finite element computations based on the original and modified meshes as functions of θ .



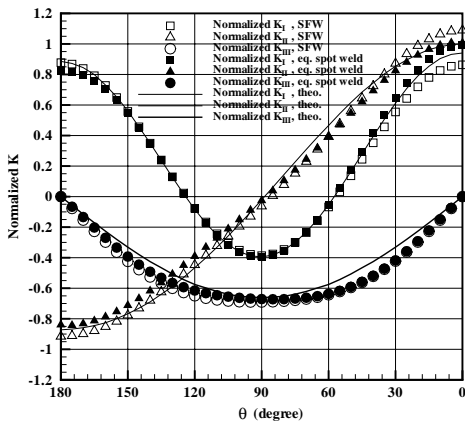
(a)



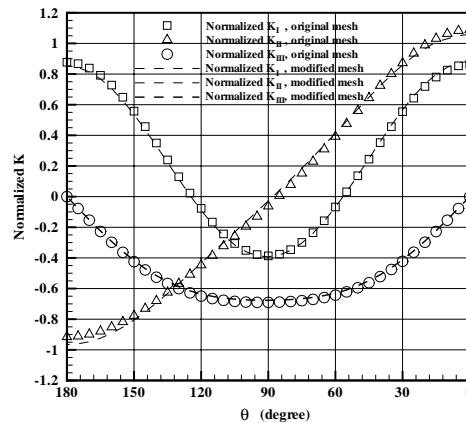
(b)



(d)

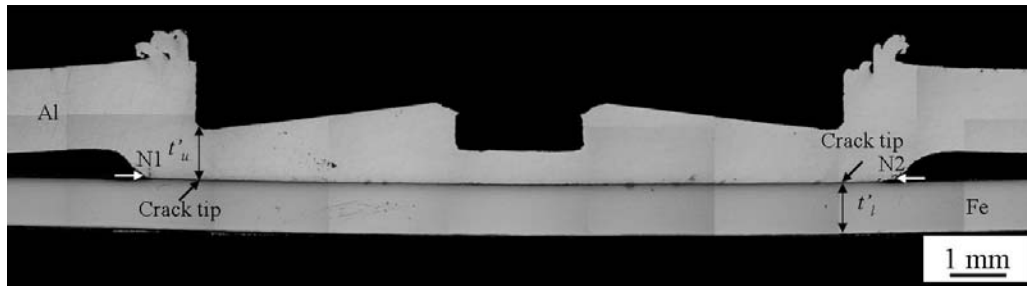


(c)

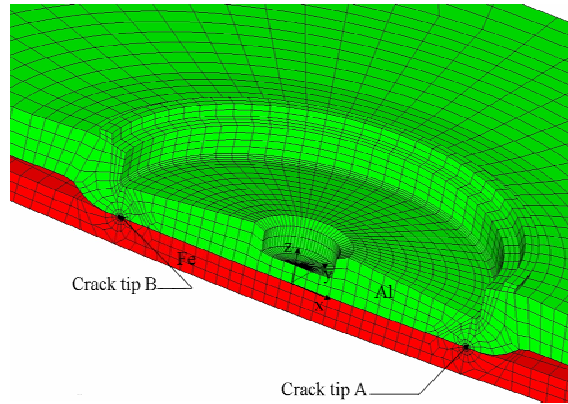


(e)

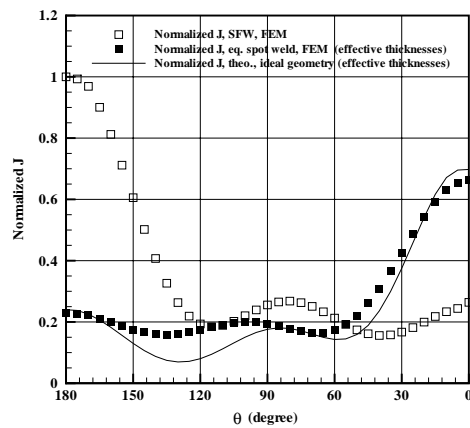
Figure 6.13 (a) An optical micrograph of the cross section along the symmetry plane of an aluminum 5754 spot friction weld before testing, (b) a close-up view of a three-dimensional finite element mesh near the weld, (c) the normalized K_I , K_{II} and K_{III} solutions as functions of θ for the aluminum 5754 spot friction weld, for the equivalent spot weld joining two aluminum sheets of $t'_u = 1.70$ mm and $t'_l = 2.06$ mm based on the finite element computations, and the results based on the analytical solutions for the equivalent spot weld, (d) a close-up view of a modified finite element mesh near the weld, (e) the normalized K_I , K_{II} and K_{III} solutions obtained from the finite element computations based on the original and modified meshes as functions of θ .



(a)

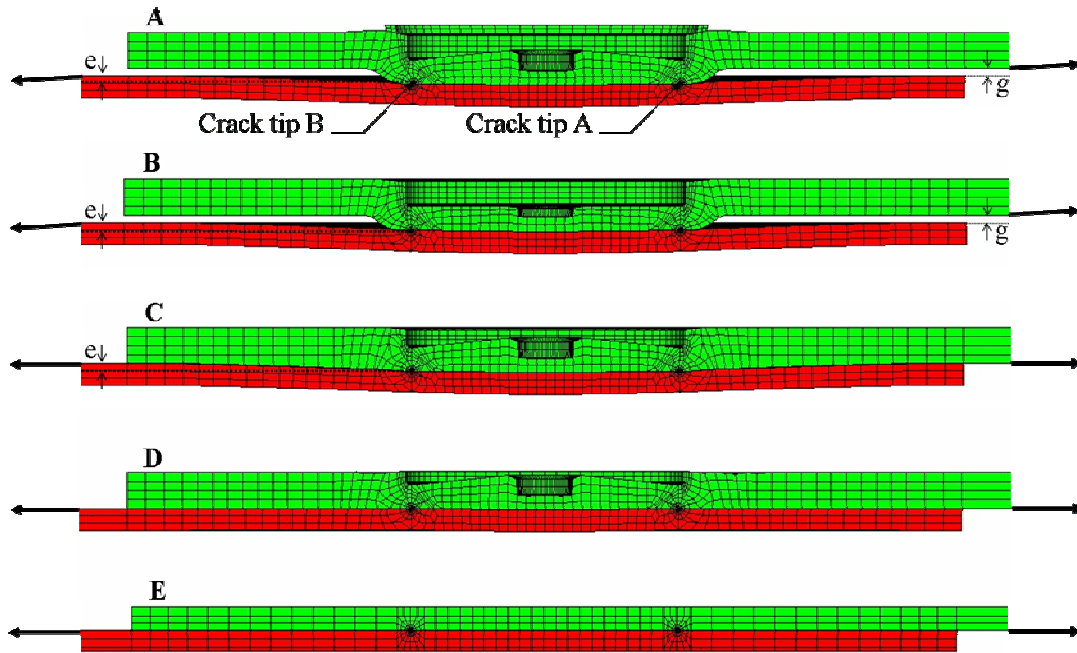


(b)

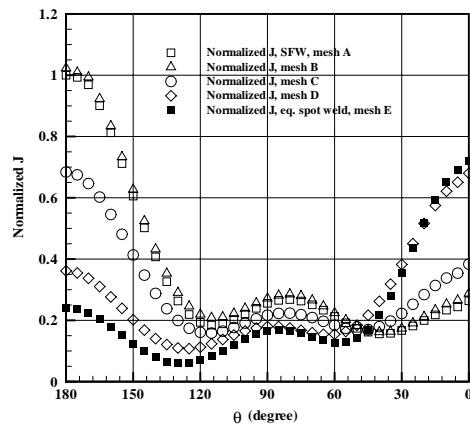


(c)

Figure 6.14 (a) An optical micrograph of the cross section along the symmetry plane of a dissimilar Al/Fe spot friction weld between an aluminum sheet and a coated steel sheet, (b) a close-up view of a three-dimensional finite element mesh near the weld, (c) the normalized J integral solutions as functions of θ for the Al/Fe spot friction weld, for the equivalent spot weld joining an aluminum sheet of $t'_u = 0.83$ mm to a steel sheet $t'_l = 0.78$ mm based on the finite element computations, and the results based on the analytical solutions for the equivalent spot weld.

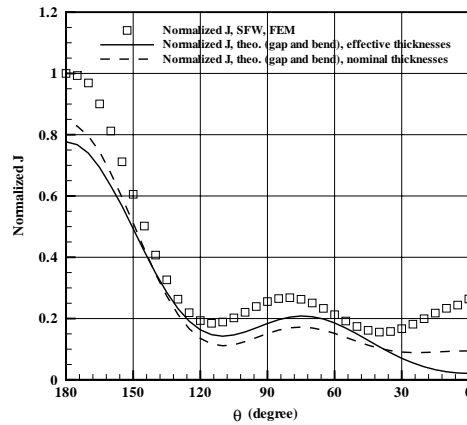


(a)

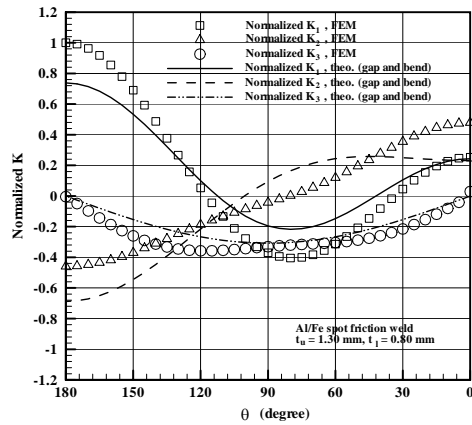


(b)

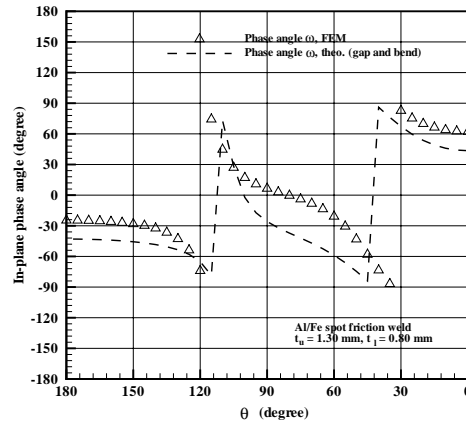
Figure 6.15 (a) Three-dimensional finite element meshes for the Al/Fe spot friction welds in lap-shear specimens, (b) the normalized J integral solutions for the Al/Fe welds obtained from the finite element computations based on meshes A, B, C, D and E. Mesh A is used to model the Al/Fe spot friction weld based on the micrograph shown in Figure 6.14(a). Mesh B is obtained from mesh A by removing the flashes and rises. Mesh C is obtained from mesh A by removing the flashes and by filling the gap between the upper and lower sheets. Mesh D is obtained from mesh C by straightening the upper and lower sheets. Mesh E is used to model an ideal spot weld joining an aluminum sheet to a steel sheet.



(a)



(b)



(c)

Figure 6.16 (a) The normalized J integral solutions, (b) the normalized K_1 , K_2 and K_3 solutions, (c) the in-plane phase angle ω as functions of θ for the Al/Fe spot friction weld based on the finite element computation and the analytical solutions for the equivalent spot weld based on the structural stress solutions with consideration of the gap and bend.

References

- [1] Zhang S. Approximate stress intensity factors and notch stress for common spot welded specimens. *Welding Research Supplement* 1999;78:173s-179s.
- [2] Pook LP. Fracture mechanics analysis of the fatigue behavior of spot welds. *Int J Fract* 1975;11:173-176.
- [3] Pook LP. Approximate stress intensity factors obtained from simple plane bending theory. *Eng Fract Mech* 1979;12:505-522.
- [4] Radaj D. Stress singularity, notch stress and structural stress at spot welded joints. *Eng Fract Mech* 1989;34:495-506.
- [5] Radaj D. Design and analysis of fatigue resistant welded structures. Abington: Halsted Press; 1990.
- [6] Radaj D, Zhang S. Stress intensity factors for spot welds between plates of unequal thickness. *Eng Fract Mech* 1991;39:391-413.
- [7] Radaj D, Zhang S. Simplified formulae for stress intensity factors of spot welds. *Eng Fract Mech* 1991;40:233-236.
- [8] Radaj D, Zhang S. Stress intensity factors for spot welds between plates of dissimilar materials. *Eng Fract Mech* 1992;42:407-426.
- [9] Sheppard SD. Estimation of fatigue propagation life in resistance spot welds. In: Mitchell MR, Landgraf RW, editors. *Advances in Fatigue Lifetime Predictive Techniques*, Vol. 2. ASTM STP 1993;1211:169-185.
- [10] Swellam MH, Banas G, Lawrence FV. A fatigue design parameter for spot welds. *Fatigue Fract Eng Mater Struct* 1994;17:1197-1204.
- [11] Zhang S. Stress intensities at spot welds. *Int J Fract* 1997;88:167-185.
- [12] Zhang S. Fracture mechanics solutions to spot welds. *Int J Fract* 2001;112:247-274.
- [13] Wang D-A, Lin S-H, Pan J. Stress intensity factors for spot welds and associated kinked cracks in cup specimens. *Int J Fatigue* 2005;27:581-598.
- [14] Wang D-A, Lin P-C, Pan J. Geometric functions of stress intensity factor solutions for spot welds in lap-shear specimens. *Int J Solids Struct* 2005;42:6299-6318.
- [15] Lin S-H, Pan J, Wung P, Chiang J. A fatigue crack growth model for spot welds in various types of specimens under cyclic loading conditions. *Int J Fatigue* 2006;28:792-803.

- [16] Lin P-C, Wang D-A, Pan J. Mode I stress intensity factor solutions for spot welds in lap-shear specimens. *Int J Solids Struct* 2007;44:1013-1037.
- [17] Lin P-C, Pan J. Closed-form structural stress and stress intensity factor solutions for spot welds under various types of loading conditions. *Int J Solids Struct* 2008;45:3396-4020.
- [18] Lin P-C, Pan J. Closed-form structural stress and stress intensity factor solutions for spot welds in commonly used specimens. *Eng Fract Mech* 2008;75:5187-5206.
- [19] Thornton PH, Krause, AR, Davies, R G. The aluminum spot weld. *Welding J* 1996;75:101s-108s.
- [20] Gean A, Westgate SA, Kucza JC, Ehrstrom JC. Static and fatigue behavior of spot welded 5182-O aluminum alloy sheet. *Welding J* 1999;78:80s-86s.
- [21] Sakano R, Murakami K, Yamashita K, Hyoe T, Fujimoto M, Inuzuka M, Nagao Y, Kashiki H. Development of spot FSW robot system for automobile body members. In: *Proceedings of the 3rd international symposium of friction stir welding*, Kobe, Japan, September 27-28, 2001.
- [22] Iwashita T. Method and apparatus for joining. US Patent 6601751 B2, August 5, 2003.
- [23] Lin P-C, Lin S-H, Pan J, Pan T, Nicholson JM, Garman, MA. Microstructures and failure modes of spot friction welds in lap-shear specimens of aluminum 6111-T4 sheets. SAE Technical Paper No. 2004-01-1330, Society of Automotive Engineers, Warrendale, PA: 2004.
- [24] Lin P-C, Pan J, Pan T. Fracture and fatigue mechanisms of spot friction welds in lap-shear specimens of aluminum 6111 sheets. SAE Technical Paper No. 2005-01-1247, Society of Automotive Engineers, Warrendale, PA:2005.
- [25] Lin P-C, Pan J, Pan T. Fatigue failures of aluminum 6111 spot friction welds under cyclic loading conditions. SAE Technical Paper No. 2006-01-1207, Society of Automotive Engineers, Warrendale, PA:2006.
- [26] Lin P-C, Pan J, Pan T. Failure modes and fatigue life estimations of spot friction welds in lap-shear specimens of aluminum 6111-T4 sheets, Part 1: Welds made by a concave tool. *Int J Fatigue* 2008;30:74-89.
- [27] Lin P-C, Pan J, Pan T. Failure modes and fatigue life estimations of spot friction welds in lap-shear specimens of aluminum 6111-T4 sheets, Part 2: Welds made by a flat tool. *Int J Fatigue* 2008;30:90-105.

- [28] Tran V-X, Pan J, Pan T. Fatigue behaviors of aluminum 5754-O spot friction welds in lap-shear Specimen. SAE Technical Paper No. 2008-01-1139, Society of Automotive Engineers, Warrendale, PA:2008.
- [29] Tran V-X, Pan J, Pan T. Fatigue behavior of aluminum 5754-O and 6111-T4 spot friction welds in lap-shear specimens. *Int J Fatigue* 2008;3:2175-2190.
- [30] Tran V-X, Pan J. Investigation of the fatigue behavior of dissimilar spot friction welds between different aluminum 5754-O and 7075-T6 sheets, to be submitted for publication in *Int J Fatigue*, 2009.
- [31] Carle, D., Blount, G. The suitability of aluminium as an alternative material for car bodies. *Mater Design*, 1999;20:267-272.
- [32] Sakurai, T. The latest trends in aluminum alloy sheets for automotive body panels. *Kobelco Technology Review*, No. 28, October, 2008. http://www.kobelco.co.jp/english/ktr/pdf/ktr_28/022-028.pdf
- [33] Mazda Motor Corporation. Mazda develops world's first steel and aluminum joining technology using friction heat. Mazda Press Release, June 2, 2005.
- [34] Gendo T, Nishiguchi K, Asakawa M, Tanioka S. Spot friction welding of aluminum to steel. SAE Technical Paper No. 2007-01-1703. Society of Automotive Engineers, Warrendale, PA:2007.
- [35] Tran V-X, Pan J, Pan T. Fatigue behavior of dissimilar spot friction welds between aluminum and coated steel sheets in lap-shear and cross-tension specimens. SAE Technical Paper No. 2009-01-0036, Society of Automotive Engineers, Warrendale, PA:2009.
- [36] Rice JR. A path independent integral and the approximate analysis of strain concentration by notches and cracks. *J Appl Mech* 1968;35:379-386.
- [37] Smelser RE, Gurtin ME. On the J-integral for bi-material bodies. *Int J Fract*, 1977;13:382-384.
- [38] Rice JR, Shih GC. Plane problems of cracks in dissimilar media. *J Appl Mech* 1965;32:418-423.
- [39] Zhang S. Stress intensities derived from stresses around a spot weld. *International Journal of Fracture* 1999;99:239-257.
- [40] Suo Z, Hutchinson JW. Interface crack between two elastic layers. *Int J Fract* 1990;43:1-18.
- [41] ABAQUS. User's Manual for Version 6.5, ABAQUS, Inc., Providence, RI:2004.
- [42] Shih, CF, Asaro RJ. Elastic-plastic analysis of cracks on bimaterial interfaces: Part I – Small scale yielding. *J Appl Mech* 1988;55:299-316.

- [43] Rice JR. Elastic fracture mechanics concepts for interfacial cracks. *J Appl Mech* 1988;55:98-103.
- [44] Tran V-X, Pan J, Pan T. Effects of processing time on strengths and failure modes of dissimilar spot friction welds between aluminum 5754-O and 7075-T6 sheets. *J Mater Process Technol* 2009; 209:3724-3739.

CHAPTER VII

CONCLUSIONS

In Chapter II, the fatigue behavior of aluminum 5754-O and 6111-T4 spot friction welds in lap-shear specimens is investigated based on experimental observations and two fatigue life estimation models. Optical micrographs of the 5754 and 6111 welds made by a concave tool and a flat tool, respectively, before and after failure under quasi-static and cyclic loading conditions are examined. The micrographs show that the failure modes of the 5754 and 6111 welds under quasi-static and cyclic loading conditions are quite different. Under quasi-static loading conditions, both types of welds mainly fail from the nearly flat fracture surface through the nugget. Under low-cycle loading conditions, both types of welds mainly fail from the kinked crack through the upper sheet thickness and the fracture surface through the nugget. Under high-cycle loading conditions, both types of welds mainly fail from the kinked cracks through the upper and lower sheet thicknesses.

Based on the experimental observations of the partially failed welds, the failures of the 5754 welds made by the concave tool under cyclic loading conditions appear to be dominated by kinked cracks that initiate from the original crack tips and propagate through the upper sheet with a reduced thickness. The failure of the 6111 welds made by the flat tool under low-cycle loading conditions appears to be dominated by kinked cracks that initiate from the original crack tips and propagate through the upper sheet

with a reduced thickness. However, the failure of the 6111 welds made by the flat tool under high-cycle loading conditions appears to be dominated by kinked cracks that initiate from the original crack tips and propagate through the lower sheet thickness. Based on the experimental observations of the paths of the dominant kinked fatigue cracks, a kinked fatigue crack growth model of Newman and Dowling [1] and Lin et al. [2] based on the Paris law and the stress intensity factor solutions for finite kinked cracks is adopted to estimate the fatigue lives of both types of welds. Also, a structural stress model based on the closed-form structural stress solutions at the critical locations of the welds, defined as the locations where the dominant kinked fatigue cracks are initiated, is developed to estimate the fatigue lives of both types of welds. The fatigue life estimations based on the kinked fatigue crack growth model and the structural stress model with parameters obtained from three-dimensional finite element analyses and experimental stress-life fatigue data agree well with the experimental results for the aluminum 5754 and 6111 spot friction welds in lap-shear specimens.

In Chapter III, the effects of the processing time on the strengths and failure modes of dissimilar 5754/7075 and 7075/5754 spot friction welds between aluminum 5754-O and 7075-T6 sheets are investigated by experiments. Dissimilar 5754/7075 and 7075/5754 welds made at different processing conditions were tested under lap-shear loading conditions. The experimental results indicate that the failure loads of both types of welds in lap-shear specimens increase when the processing time increases for the given ranges of the processing time. The maximum failure load of the 7075/5754 welds is about 40% larger than that of the 5754/7075 welds. Selected optical and scanning electron micrographs of both types of welds made at different processing times before and after

failure are examined. The micrographs show different weld geometries and different failure modes of the welds made at different processing times. The micrographs show that cracking in the 5754/7075 and 7075/5754 welds made at different processing times was initiated at the original crack tips and grew along the interfacial surface between the two deformed sheet materials. However, these cracks did not continue to grow along the interfacial surfaces but propagate through the deformed sheet materials near the central holes at the final stage of the specimen failure. The failure modes of the dissimilar 5754/7075 and 7075/5754 spot friction welds are quite complex and appear to strongly depend on the geometry and strength of the interfacial surface between the two deformed sheet materials. The optimal processing times of 3.8 sec and 6.5 sec to maximize the failure loads of the 5754/7075 and 7075/5754 welds, respectively, under lap-shear loading conditions are identified. The failure load, the displacement at the failure load and the energy dissipation to separate the specimen for the 7075/5754 weld at the optimal processing time are higher than those for the 5754/7075 weld at the optimal processing time.

In Chapter IV, the fatigue behavior of dissimilar 5754/7075 and 7075/5754 spot friction welds made at the optimal processing times (as identified in Chapter III) in lap-shear and cross-tension specimens is investigated based on experimental observations and three fatigue life estimation models. Optical micrographs of the 5754/7075 and 7075/5754 welds before and after failure under quasi-static and cyclic loading conditions are examined to understand the fracture and failure mechanisms of the welds. The micrographs show that the 5754/7075 welds in lap-shear specimens mainly fail from the kinked cracks through the lower sheet thickness under cyclic loading conditions. Also,

the 7075/5754 welds in lap-shear specimens mainly fail from the kinked cracks through the lower sheet thickness and from the fracture surfaces through the upper sheet thickness under cyclic loading conditions. The micrographs show that the 5754/7075 and 7075/5754 welds in cross-tension specimens mainly fail from the fracture surfaces along the interfacial surfaces and in the upper sheet materials under cyclic loading conditions.

Based on the experimental observations of the paths of the dominant fatigue cracks, three fatigue life estimation models are adopted and developed to estimate the fatigue lives of the welds. The kinked fatigue crack growth model and the structural stress model as developed in Chapter II are adopted to estimate the fatigue lives of the 5754/7075 and 7075/5754 welds in lap-shear specimens. A through-nugget fatigue crack growth model based on the closed-form stress intensity factor solutions for the through-nugget cracks and the Paris law for the fatigue crack propagation is developed to estimate the fatigue lives of the 5754/7075 and 7075/5754 welds in cross-tension specimens. The fatigue life estimations based on the kinked fatigue crack growth model, the structural stress model and the through-nugget fatigue crack growth model with parameters obtained from three-dimensional finite element analyses and experimental stress-life fatigue data agree well with the experimental results. Finally, the effective stress intensity factor and J integral solutions at the critical locations of the welds obtained from three-dimensional finite element analyses appear to be good fracture mechanics parameters to correlate the experimental fatigue data for the 5754/7075 and 7075/5754 welds in lap-shear and cross-tension specimens.

In Chapter V, the fatigue behavior of dissimilar Al/Fe spot friction welds between aluminum 6000 series alloy and coated mild steel sheets in lap-shear and cross-tension

specimens is investigated based on experiments and three-dimensional finite element analyses. Optical micrographs of the Al/Fe welds after failure under quasi-static and cyclic loading conditions show that the Al/Fe welds in lap-shear and cross-tension specimens mainly fail along the interfacial surface between the aluminum and steel sheets. Three-dimensional finite element analyses based on the micrograph of the cross section along the symmetry plane of the weld before testing were conducted to obtain accurate stress intensity factor and J integral solutions for the crack fronts along the nugget circumferences of the welds under lap-shear and cross-tension loading conditions. The numerical results indicate that K_1 is the dominant stress intensity factor for the Al/Fe spot friction welds in lap-shear and cross-tension specimens. The results obtained from the finite element computations correlate well with those obtained from the experimental observations. The numerical results suggest that the in-plane effective stress intensity factor and J integral solutions at the critical locations of the welds obtained from three-dimensional finite element analyses may be used as fracture mechanics parameters to correlate the experimental fatigue data for the Al/Fe spot friction welds in lap-shear and cross-tension specimens.

In Chapter VI, the effects of weld geometry and sheet thickness on the fracture mechanics parameters for the crack fronts along the nugget circumferences of resistance spot welds and spot friction welds between similar and dissimilar sheet materials in lap-shear specimens are investigated based on a combined theoretical and numerical approach. The analytical stress intensity factor and J integral solutions for spot welds with ideal geometry, gap and bend joining two sheets of different materials and thicknesses in lap-shear specimens are first developed based on the strip model and the

new structural stress solutions for a rigid inclusion in a finite square plate subjected to a lap-shear load and a coach-peel load (Lin and Pan [3]). The numerical results obtained from the three-dimensional finite element analyses for spot welds with ideal geometry in lap-shear specimens validated the accuracy of the analytical solutions.

For spot welds in lap-shear specimens where the lap-shear loads apply on the upper right leg and the lower left leg of the specimen, point A and point B denote for the original crack tips on the right side and the left side, respectively, on the cross section along the symmetry plane of the weld. Also, the Young moduli and thicknesses of the upper (u) and lower (l) sheets are denoted as E_u and E_l , and t_u and t_l , respectively. Based on the results obtained from the theoretical and numerical models, the K_1 and K_2 solutions at point A increase when t_u decreases, E_u decreases and E_l increases. The K_1 and K_2 solutions at point B increase when t_l decreases, E_u increases and E_l decreases. Also, the J integral solution at point A increases when E_u and t_u decrease, and appears not to be significantly sensitive to the changes of E_l and t_l . Similarly, the J integral solution at point B increases when E_l and t_l decrease, and appears not to be significantly sensitive to the changes of E_u and t_u .

The K_I , K_{II} and J integral solutions at point A for the $E/E - t_u/t_l$ weld (joining two sheets of Young modulus E and thicknesses t_u and t_l) can be approximated as the K_I , K_{II} and J integral solutions at point A, respectively, for the $E/E - t_u/t_u$ weld (joining two sheets of Young modulus E and equal thickness t_u). Similarly, the K_I , K_{II} and J integral solutions at point B for the $E/E - t_u/t_l$ weld can be approximated as the

K_I, K_{II} and J integral solutions at point B, respectively, for the $E/E - t_l/t_l$ weld (joining two sheets of Young modulus E and equal thickness t_l). The J integral solution at point A for the $E_u/E_l - t_u/t_l$ weld (joining two sheets of Young moduli, E_u and E_l , and thicknesses, t_u and t_l) can be approximated as the J integral solution at point A for the $E_u/E_u - t_u/t_u$ weld (joining two sheets of Young modulus E_u and equal thickness t_u). Similarly, the J integral solution at point B for the $E_u/E_l - t_u/t_l$ weld can be approximated as the J integral solution at point B for the $E_l/E_l - t_l/t_l$ weld (joining two sheets of Young modulus E_l and equal thickness t_l).

Three-dimensional finite element models based on the micrographs of the cross sections along the symmetry planes of an aluminum 6111 resistance spot weld, an aluminum 5754 spot friction weld, and a dissimilar Al/Fe spot friction weld are then conducted to obtain accurate stress intensity factor and J integral solutions for the crack fronts along the nugget circumferences of these welds under lap-shear loading conditions. The numerical results indicate that the complex weld geometries of the aluminum 6111 resistance spot weld and aluminum 5754 spot friction weld (as shown in Chapter II) appear not to affect the stress intensity factor and J integral solutions when compared to the analytical solutions for the welds with ideal geometry. However, the complex weld geometry of the Al/Fe spot friction weld (as shown in Chapter V) appears to strongly affect the stress intensity factor and J integral solutions when compared to the analytical solutions for the weld with ideal geometry. Different three-dimensional finite element models based on the meshes that represent different features of the weld geometry are conducted. The numerical results indicate that the gap between the upper and lower

sheets and the bend near the weld are the important geometric parameters that strongly affect the fracture mechanics parameters for the Al/Fe spot friction weld in the lap-shear specimen. The analytical stress intensity factor and J integral solutions for spot welds in lap-shear specimens with consideration of the gap and bend agree with the results obtained from the three-dimensional finite element computation for the Al/Fe spot friction weld in the lap-shear specimen. The results obtained from the theoretical and numerical analyses correlated well with the experimental observations.

References

- [1] Newman JA, Dowling NE. A crack growth approach to life estimation of spot-welded lap joints. *Fatigue Fract Eng Mater Struct* 1998;21:1123-1132.
- [2] Lin S-H, Pan J, Wung P, Chiang J. A fatigue crack growth model for spot welds in various types of specimens under cyclic loading conditions. *Int J Fatigue* 2006;28:792-803.
- [3] Lin P-C, Pan J. Closed-form structural stress and stress intensity factor solutions for spot welds in commonly used specimens. *Eng Fract Mech* 2008;75:5187-5206.